eman ta zabal zazu

Universidad del País Vasco

Euskal Herriko Unibertsitatea

First principles simulations of sodium-based battery materials

Oier Arcelus

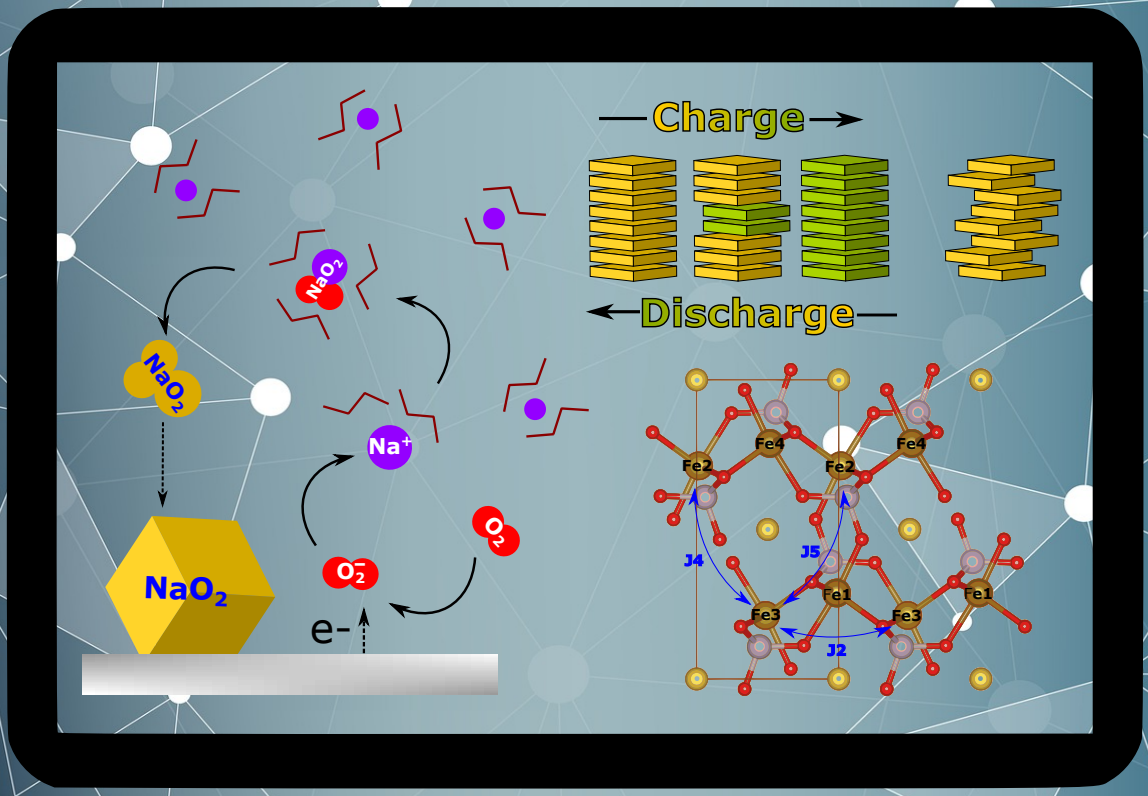

2019

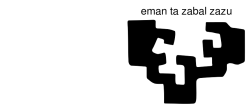

Universidad del País Vasco / Euskal Herriko Unibertsitatea

Doctoral Thesis

First principles simulations of sodium-based battery materials

Author:
Oier Arcelus Elcorobarrutia

Thesis Supervisor:
Dr. Javier Carrasco Rodríguez
UPV/EHU Supervisor:
Prof. Andrés Arnau Pino

A thesis submitted in fulfillment of the requirements for the degree of Doctor of Physics

October 4, 2019

Abstract

From portable electronic systems to the electric vehicle, electrical energy storage (batteries) has become of utmost importance on human technological development process. However, current technologies often fall short in terms of their energy storage capabilities, which make them non-viable for many applications, e.g., high-autonomy electric vehicles and solving grid-unbalance issues related to the fluctuations in renewable energy generation. This requires searching new chemical systems capable of storing far more energy than present technologies. This search is costly, specially when experimental trial and error is involved. In this regard, *first-principles* methods offer the possibility of running realistic simulations to effectively gain fundamental understanding into relevant processes on battery materials, and inform experimental researchers in their endeavor. In this thesis, we employ first-principles simulations to gain insight into a promising group of new post Li-based batteries, that base their operation in the use of sodium (Na) as the active electrochemical element. Concretely, we perform simulations on two different types of sodium based systems, Na-air and Na-ion batteries.

First, we examine the main discharge product of Na-air batteries, sodium superoxide (NaO_2), at different levels of dimensionality (small clusters, extended surfaces, and bulk material) to calculate its electronic structure and stability. We see that NaO_2 is insulating in all cases, which supports the proposed solution mediated charge-discharge mechanism, where NaO_2 forms small aggregates in solution, to then precipitate in a conductive carbon support, or viceversa. From the stability point of view, we find that small $(NaO_2)_n$ clusters prefer to adopt 3D configurations faster than their lithium counterparts, which prefer ring-shaped structures. This, in combination with the solution mediated discharge mechanism, could explain the cubic shaped particle observed on Na-air batteries, when compared to the toroidal particles of Li-air batteries. Regarding the selection of the electrolyte solvent, we compare the electrochemical performance of three glymes of increasing length; 1,2-Dimethoxyethane '$C_4H_{10}O_2$' (DME), 2-Methoxyethyl ether '$C_6H_{14}O_3$' (DEGDME), and Tetra ethylene glycol dimethyl ether '$C_{10}H_{22}O_5$' (TEGDME); at different salt concentrations and current densities. Aided by Density Functional Theory (DFT) calculations we helped index the relevant infrared (IR) peaks that are affected by the interaction with Na^+ ions and studied the energetic properties of different $[Na\text{-}(M)_n]^+$ complexes. We see that different cycling conditions lead

to different optimal solvent choices. At low salt concentrations the big solvation structure of DME prevents Na^+ ions from forming ion-pairs easily. TEGDME binds Na^+ ions too strongly and makes it difficult to desolvate them. DEGDME offers a good balance between binding strength and small solvation structure. At higher salt concentrations, the solvation structures of both DME and DEGDME are similar, so the weaker binding in DME improves its cycling performance relative to DEGDME. At high current densities the viscosity of the solvent appears to dominate the process, and DME is the better choice.

Secondly, we shift our focus to Na-ion batteries. Particularly we examine the energetics of P $\leftrightarrow$ O transformations, that appear on the charge-discharge process of Na-ion batteries when layered transition-metal oxides are used as cathodes. We focus on the prototypical P2-Na_xVO_2 system (where x = 0, 0.25, 0.333, 0.5, 0.666, and 1), and analyze the energetics of rigid glidings of transition-metal layers in P2 $\leftrightarrow$ O2 transformations by transition-state search methods. We see that the energetic barriers associated to such gliding processes are linearly correlated with the amount of Na (x) intercalated in the system, and their energetics are dominated by electrostatic interactions. More importantly, we find that different local coordination of Na ions within the transition-metal layers results in high- or low-energy transition states within gliding, which means that strategies such as selectively populating certain Na sites, or inducing Na/vacancy disordering could effectively block these unwanted transformations.

Third, we calculate the magnetic properties of sodium iron phosphate ($NaFePO_4$), which is a promising cathode material for Na-ion batteries. We focused on two known polymorphs of $NaFePO_4$, the maricite phase (m-phase) and the tryphlite phase (t-phase). By combining density functional theory and model Hamiltonians parametrized by Wannier functions, we obtain the isotropic magnetic exchange interactions between magnetic centers as well as higher order Dzyaloshinskii-Moriya interactions. We conclude that reproducing the experimental magnetic structure in the m-phase remains a challenge as the model fails to capture long-ranged magnetic interactions, which seem crucial in stabilizing the $\mathbf{q} = (1/2, 0, 1/2)$ magnetic structure. Instead the model predicts an incommensurate magnetic ordering $\mathbf{q} = (0.36, 0, 0)$ which would mean that the m-phase could allow for the magnetoelectric effect. In the t-phase, our models correctly stabilize the experimental magnetic ground state, which also allows for the magnetoelectric effect. We put forward that these emerging effects could negatively affect batteries exposed to high magnetic fields, as the subsequent electric polarization could result in undesirable fluctuations in the operational voltage.

Laburpena

Energia elektrikoa batzeko gailuak (bateriak) zeresan handikoak bihurtu dira giza garapen teknologikoan, gailu elektroniko eramangarrien eta ibilgarritasun iraunkor eta berdearen munduan batez ere. Alabaina, gaur egungo teknologiak motz geratzen dira euren energia biltzeko gaitasunean, beraz, aplikazio askotan baliagarritasuna galtzen dute, adibidez, autonomia handiko ibilgailu elektrikoetan eta energia berriztagarriek sortzen dituzten fluktuazioak kontrolatzeko ahalmenean. Arazo hauek sistema kimiko berriak ikertzeko beharra dakarte, energia biltzeko gaitasun handiagoa dutenak alegia. Ikerketa hau garestia da, bereziki froga eta errorea prozesuan nahasita badago. *Lehen printzipioetan* oinarritutako kalkuluak zeresan handia dute gai honen inguruan. Besteak beste, aukera ematen digute baterietan erabilgarriak izan daitezken materialen inguruan simulazio errealistak egiteko, horrela, garrantzizkoak diren prozesu fisikoei buruzko oinarrizko ulermena lortzeko. Modu honetan, ikertzaile esperimentalei irizpide fisikoak emanez, material berrien garapena erraztu daiteke. Tesi honetan bateria talde konkretu bat aztertu dugu, sodioa (Na) litioaren (Li) ordez erabiltzen duena. Konkretuki, simulazioak bi bateria azpitaldetan banatu ditugu: Na-aire eta Na-ioi bateriak. Tesi honen helburua bi sistema hauen inguruan dauden galdera irekiei erantzun bat ematea da.

Hasteko, Na-aire baterien deskargaren produktu nagusia, sodio superoxidoa (NaO_2), aztertu dugu dimentsionalitate maila ezberdinetan ('kluster' txikiak, gainazalak eta 'bulk' materiala). Atal honetan NaO_2-aren propietate elektroniko eta energetikoak ikertu ditugu. Propietate elektronikoen aldetik, NaO_2-a isolatzaile elektrikoa dela ikusi dugu, dimentsionalitate maila guztietan. Honek, literaturan proposaturiko mekanismoetako bat sostengatzen du, soluzioan oinarritutako karga eta deskarga mekanismoa konkretuki. Mekanismo honen arabera, deskarga prozesuan NaO_2-ak kluster txikiak sortzen ditu soluzioan. Ondoren, eroale elektrikoa den karbonozko matrize batean prezipitatzen da NaO_2 partikula handiagoak sortuz. Alderantzizko prozesuan NaO_2-a disolbatu egiten da, partikulen tamaia txikituz. Klusterren egonkortasun energetikoari dagokionez, ikuten da $(NaO_2)_n$ kluster txikiak 3D estrukturak sortzea nahiago dutela, litiozko kluster txikiekin konparatuta. Azken hauek eraztun itxurako estrukturak osatzen dituzte. Honek, soluzionan oinarritutako mekanismoarekin batera, Na-airezko baterietan ikusten diren partikula kubikoen sorrerari azalpena eman diezaioke. Disolbatzailearen aukerari dagokionez, 'glimak' deritzen hiru disolbatzaileren joera elektrokimikoak konparatu ditugu, 'kate' luzeera ezberdinetakoak; 1,2-Dimetoxietanoa '$C_4H_{10}O_2$' (DME),

2-Metoxietil eterra '$C_6H_{14}O_3$' (DEGDME), eta Tetraetileno glicol dimetil eterra '$C_{10}H_{22}O_5$' (TEGDME); gatz kontzentrazio eta korronte dentsitate ezberdinetan. DFT kalkuluak lagunduta, Na^+ ioien interakzioaren ondorioz, disolbatzaileen infragorri espektruetan ikusten diren aldaketak indexatu ditugu. $[Na\text{-}(M)_n]^+$ konplexuen propietate energetikoak ere aztertu ditugu. Ondoren, baldintza elektrokimikoek disolbatzaileen joera nola aldatzen duten ikusi dugu. Gatz kontzentrazio txikietan DMEaren solbatze egitura oso handia da, honek ioi bikoteak erraztasunez sortzea galerazten du. Bestetik, TEGDMEak Na^+ ioiak indartsuki lotzen ditu, beraz ioien desolbazioa eragozten da. DEGDMEak aldiz, konpromisu egokia erakusten dut indar ertaineko lotura eta solbatze egitura txiki baten artean. Gatz kontzentrazio altuetan bestetik, DMEaren eta DEGDMEaren solbatze egituren tamainak antzekoak dira, beraz DMEak sortzen dituen lotura ahulagoek sistemaren errendimendu elektrokimikoa hobetzen dute. Korronte dentsitatea altua denean, disolbatzailearen biskositatea da garrantzitsua. Kasu honetan, DMEa da aukera egokia.

Bigarrengoz, Na-ioizko bateriak aztertu ditugu, P $\leftrightarrow$ O transformazio parasitikoak konkretuki, katodo modura erabiltzen diren trantsizio metalezko oxido laminarretan agertzen direnak. Lan honetan P2-Na_xVO_2 sistema ikertu dugu (non $x = 0$, 0.25, 0.333, 0.5, 0.666, 1), trantsizio metal geruzen mugikortasunaren energetika aztertuz P2 $\leftrightarrow$ O2 transformazioetan. Barrera energetiko hauek linearki hazten dira sodio kontzentrazioa (x) handituz, eta, beraz, Na eta V-aren arteko aldaratze elektrostatikoa handituz. Interesgarriki, ikusi dugu energia langa hauen magnitudea Na/bakante konfigurazioaren arabera asko aldatzen dela, energia altuko edo baxuko trantsizio konfigurazioak sortuz. Honela, eztabaidatu dugu nola, sodio okupazio konkretu batzuk mesedetuz, P2 $\leftrightarrow$ O2 transformazioak blokeatzea posible dela, adibidez Na/bakanteen desordena sortuz.

Azkenik, sodio burdin fosfatoaren ($NaFePO_4$) propietate magnetikoak aztertu ditugu. $NaFePO_4$-a, Na-ioi baterietan katodo modura erabiltzen den material interesgarri bat da. Konkretuki, $NaFePO_4$-ak sortzen dituen bi polimorfo ikertu ditugu; marizita (m) fasea, eta triflita (t) fasea. Dentsitate funtzionalaren teoria eta modelo hamiltondarrak erabilita, burdin atomoen arteko akoplamendu magnetiko isotropikoak eta Dzyaloshinskii-Moriya interakzioak kalkulatu ditugu. Ondorioztatu dugu m-fasearen estruktura magnetiko esperimentala erreproduzitzea erronka bat izaten jarraitzen duela. Gure modelo hamiltondarrak ez baititu helmen handiko interakzioak modu egokian jasotzen. Interakzio hauek oso garrantzitsuak dirudite $\mathbf{q} = (1/2, 0, 1/2)$ orden esperimentala lortzeko. Aldiz, gure kalkuluek $\mathbf{q} = (0.36, 0, 0)$ ordena aurresaten dute, m-fasean efektu magnetoelektrikoa ahalbidetuz. Bestetik, gure kalkuluek t-fasearen ordenamentu magnetiko esperimentala modu egokian aurresaten dute. Ordenamentu honek ere efektu magnetoelektrikoa ahalbidetzen du. Emaitza hauek garrantzizkoak dira, besteak beste, bateriek eremu magnetiko altuekiko esposizioa duten aplikazioetan, eremu elektriko baten sorrera

espontaneoak arazoak ekarri ditzakeelako, baterien boltaiaren fluktuazioaren bitartez.

Resumen

Los dispositivos de almacenamiento eléctrico (baterías) son, hoy por hoy, indispensables en el proceso de desarrollo tecnológico humano, habiendo habilitado la industria de la electrónica portátil y siendo clave en el desarrollo del coche eléctrico. No obstante, las tecnologías actuales se quedan cortas en cuanto a su capacidad de almacenamiento de energía, haciendolas inviables para aplicaciones críticas en el mundo moderno, tales como: vehículos eléctricos de gran autonomía y baterías integradas en la red eléctrica, que solucionarían los desequilibrios generados por las fuentes de energía renovables. Éstas aplicaciones requieren, por tanto, de nuevos sistemas químicos capaces de almacenar mucha más energía que las tecnologías actuales. Sin embargo, la búsqueda de alternativas es costosa, especialmente debido a que el proceso convencional de búsqueda suele implicar procedimientos de ensayo y error. Los métodos de cálculo basados en *primeros principios*, en concreto la teoría funcional de densidad (o DFT), ofrecen la posibilidad de acelerar este tipo de investigaciones. En esta tesis centramos nuestra atención en un tipo concreto de baterías basadas en sodio (Na) en vez de litio (Li) como elemento electroquímicamente activo. Concrétamente, nos concentramos en dos tipos de baterías: Las Na-aire y Na-ión.

Esta tesis se divide en seis capítulos; en el primero y segundo se da una introducción general de la motivación del trabajo presentado y de los métodos teóricos usados. Los tres siguientes capítulos presentan los resultados, discusión y principales conclusiones obtenidas, intentando dar respuesta a ciertas preguntas abiertas sobre los procesos que conciernen al funcionamiento de las baterías Na-aira y Na-ión. Los tres capitulos en concreto se dividen en los siguientes temas. I) Caracterización de la estructura electrónica y del proceso de formación del superóxido de sodio (NaO_2); y la selección del disolvente para mejorar el rendimiento de las baterías de Na-aire. II) Mecanismos de cambios de secuencia de apilamiento (transformaciones de fase) en cátodos de óxidos laminares de metales de transición (OLMT), que plagan los procesos de carga y descarga en baterías de Na-ión. III) Propiedades magnéticas y fenómenos emergentes derivados de las mismas, en materiales polianiónicos frecuentemente usados como materiales de inserción de iones de sodio. En el último capitulo se dan las conclusiones generales de esta tesis.

TEMA I: Baterías de Na-aire

Introducción:

Las baterías de metal-aire son una nueva tecnología de almacenamiento de energía eléctrica prometedora, ya que pueden, en teoría, almacenar mucha más energía que los actuales sistemas basados en procesos de intercalación iónica. Las baterías de metal-aire usan el oxígeno del aire o de un tanque de oxígeno acoplado a la batería mediante una reacción de reducción de oxígeno (ORR). Por ejemplo, la capacidad de una batería real de litio-aire, cuyo producto de descarga es el peróxido de litio (Li_2O_2), se situa entre los 450 y 600 Wh/kg, tres veces más que una batería convencional de litio-ión, y en la zona útil para su uso en el vehículo eléctrico. No obstante, esta tecnología no está exenta de problemas. En concreto, la descomposición del cátodo de carbono y los diferentes disolventes orgánicos, altos sobrepotenciales de carga y reacciones parasitarias, entre otras, evitan que estas baterías ciclen más allá de los 100 ciclos. Estos problemas han incentivado la consideración de otros metales alcalinos tales como el sodio o el potasio para baterías metal-aire.

En concreto, las baterías de sodio-aire funcionan del mismo modo que sus equivalentes de litio, la diferencia es que, en este caso, el superóxido de sodio (NaO_2) es accesible como producto de descarga, a pesar de no ser termodinámicamente estable en comparación al peróxido. La formación de NaO_2 es ventajosa ya que implica sobrepotenciales de carga y descarga muy bajos, lo cual mejora la eficiencia coulómbica de la batería. No obstante, muchos de los problemas presentes en las baterías de litio-aire siguen apareciendo en las sodio-aire, dada la alta reactividad del anión superóxido O_2^-.

En este tema se analiza la estructura electrónica del NaO_2 a varios niveles de dimensionalidad (bulk, superficies y pequeños agregados), para desvelar el mecanismo de transporte eléctrico en los productos de descarga. También se analiza la geometría y estabilidad de estos pequeños agregados que pueden estar presentes en el inicio de la descarga de la batería, y pueden, en última instancia, determinar la morfología de los productos de descarga. Finalmente, se analiza cómo el uso de la diglima como disolvente mejora la ciclabilidad de las baterías de sodio-aire al compararlos con sus equivalentes de 'cadena corta' (dimetoxietano) y 'cadena larga' (tetraglima) en ciertos régimenes de concentración de sal e intensidad de carga y descarga.

Análisis y resultados:

Para el análisis DFT de la estructura electrónica y estabilidad energética del NaO_2 en el bulk, superficie (100) y pequeños agregados, se ha usado el paquete de software llamado Vienna Ab Initio Simulation Package (VASP). Uno de los mayores problemas del DFT reside en que el funcional que recoge

efectos puramente cuánticos, tales como las interacciones de canje y correlación, es desconocido. Este problema se trata de manera parcial mediante diferentes aproximaciones tales como la aproximación local de densidad (LDA) o la aproximación del gradiente generalizado (GGA). En este trabajo usamos una de las variaciones más famosas del GGA llamado el funcional de Perdew-Burke-Ernzerhof (PBE) y un funcional híbrido llamado Heyd-Scuseria-Ernzerhof (HSE06) que incluye explícitamente una porción de la interacción de canje.

En todos los niveles de dimensionalidad el análisis de la densidad de estados electrónicos demuestra que el funcional PBE falla al describir los estados antienlazantes del superóxido. Debido a la falta de interacción de canje en PBE, los electrones sufren una fuerte auto-interacción repulsiva parasitaria. En consecuencia, los estados energéticos ocupados (estados de valencia) se desestabilizan moviéndose a energías más altas y colapsando con los estados vacíos. Debido a esto, en todos los casos el funcional PBE predice un estado fundamental semi-metálico en el NaO_2. En cambio, el funcional híbrido HSE06 describe corréctamente el carácter aislante del NaO_2, separando los estados antienlazantes del superóxido con una separación (gap) entre estados llenos y estados vacíos de 2.0 eV. Nótese que el mecanismo de formación de NaO_2 puede ocurrir de varias maneras. Una posibilidad es que el NaO_2 se forme mediante la reducción directa del oxígeno en la propia superficie del NaO_2, esto requeriría de suficiente conductividad eléctrica y sería el escenario que el uso del PBE predeciría. La otra posibilidad es que el oxígeno se reduzca en el soporte y se disuelva en el electrolito formando pares iónicos de Na^+ y O_2^-, para luego precipitar en el soporte y formar los productos de descarga. Este parece ser el mecanismo correcto según los cálculos HSE06 y en acuerdo con la evidencia experimental.

Por otro lado, las observaciones indican que la morfología de los productos de descarga cambia en el caso de baterías de litio-aire y sodio-aire. El peróxido de litio, que se forma mediante un intermediario de superóxido de litio, forma partículas en forma de toroide. En cambio, el NaO_2 forma cubos con superficies estequiométricas (100). Los cálculos con HSE06 revelan que este fenómeno se puede racionalizar en base a la tendencia que tienen los metales alcalinos más pesados como el sodio o el potasio a formar pequeños agregados de superóxido tridimensionales; en comparación a los agregados de superóxido de litio que energéticamente prefieren formar agregados planares (en forma de anillos) más grandes. También se demuestra que las interacciones que gobiernan la estabilidad de estos agregados son mayoritariamente electrostáticas.

Desde un punto de vista más fundamental, los superóxidos de metales alcalinos también son materiales interesantes. Los estados moleculares antienlazantes de la molécula superóxido se ven afectados, por ejemplo, por el acoplo spin-orbita, típicos de elementos más pesados que el oxígeno. Ciertas fases pueden, por consiguiente, resultar ser multiferroicas. La conclusión general

es que los superóxidos son sistemas de electrones 2p altamente correlacionados. En consecuencia, también se han calculado los acoplos magnéticos entre centros moleculares de superóxidos. Los cálculos revelan que estos acoplos varían dependiendo de la orientación relativa de los superóxidos, y son mayoritariamente antiferromagnéticos. El mecanismo que gobierna estos acoplos magnéticos es la interacción de supercanje de Anderson (1959).

Otra parte importante en el funcionamiento de las baterías de sodio-aire es la selección del disolvente orgánico usado en el electrolito. En este caso se ha usado el paquete de software llamado FHI-aims con el funcional híbrido B3LYP. Las observaciones sugieren que entre la familia de las 'glimas', existe un compromiso entre glimas de cadena corta (dimetoxietano) y cadena larga (tetraglima), obteniendo los mejores resultados de ciclabilidad cuando se usa el compuesto intermedio (diglima). En los cálculos se simulan complejos de iones de sodio ($[\text{Na-(M)}_n]^+$) solvatados con estos disolventes. Se han calculado los modos de vibración y el espectro infrarrojo de estos complejos en función del número de moléculas (n) usadas para formarlo. Nuestros resultados coinciden mayoritariamente con los espectros experimentales y han ayudado a indexar los modos de vibración correspondientes a los picos observados experimentalmente. Los cálculos de energias de formacion de los complejos tambien coinciden con las medidas de calorimetría experimentales. La conclusión es que la esfera de solvatación de glimas de cadena corta es muy grande, por lo que, a concentraciones bajas de sal, de-solvatar un ión de sodio es cinéticamente desfavorable. Además , las glimas de cadena larga se enlazan muy fuertemente con los iones de Na^+, por lo que de-solvatarlos es energéticamente desfavorable. El uso del compuesto intermedio como la diglima, es óptimo a concentraciones bajas ya que el número de solvatación no es tan grande como en el dimetoxietano, ni el enlace es tan fuerte como en la tetraglima. En cambio, a mayores concentraciones de sal, los números de solvatación de los tres disolventes se equiparan, favoreciendo el ciclado en el dimetoxietano.

TEMA II: Transformaciones de fase en óxidos laminares de metales de transición

Introducción:

Las baterías de ión-sodio son una alternativa interesante para baterías estacionarias a gran escala, donde el coste, la durabilidad y seguridad son requerimientos clave. A diferencia del litio, el sodio es un elemento muy abundante en la Tierra lo que lo hace más económico y sostenible. Por otro lado, el sodio no forma aleaciones con el aluminio, por lo que es posible usar colectores de corriente más baratas que los típicos de cobre. Las limitaciones de las baterías de ión sodio residen en el hecho de que el sodio es un elemento más pesado y su potencial redox es 0.3 V más bajo que el del litio, por lo que es prácticamente

imposible competir con las baterías de litio en densidad energética.

Los materiales catódicos más prometedores para baterías de ión sodio son las estructuras polianiónicas (de las que hablaremos más adelante) y los óxidos laminares de metales de transición (OLMT). Estos últimos son particularmente interesantes por su alta capacidad y bajo coste. Estructuralmente estos compuestos se dividen en dos familias: On y Pn. La letra señala si los átomos de sodio se encuentran en una coordinación octaédrica (O) o prismática (P), y el número (n) el número de capas que forman la secuencia de apilamiento periódica del cristal. Uno de los retos más importantes en la aplicabilidad de estos materiales es su estabilidad. Esto es una consecuencia de las transformaciones de fase (P $\leftrightarrow$ O) que plagan la carga y descarga de estas baterías y que pueden, en última instancia, comprometer su integridad estructural y su capacidad. En este Tema se simulan los procesos de deslizamiento de las capas mediante DFT, en un sistema laminar sencillo, la fase P2 del oxido laminar de vanadio (P2-$NaVO_2$).

Análisis y resultados:

Las simulaciones DFT, al igual que en el Tema I, se han llevado a cabo con el paquete de software VASP. En este caso hemos usado un funcional que ha sido desarrollado muy recientemente, llamado SCAN. De modo adicional, al estar simulando materiales laminares, se espera que las interacciones de largo alcance tipo van der Walls estén presentes. Es importante, entonces, capturar estas interacciones que no están presentes por si solas en el funcional SCAN, acoplándolo al método rVV10. Se ha probado que este método SCAN+rVV10 supera en precisión al resto de funcionales, en múltiples compuestos, incluyendo materiales laminares. Para el modelado de cambios de fase P2 $\leftrightarrow$ O2 del $NaVO_2$, nos concentramos en los momentos iniciales de estas transiciones. La aproximación más sencilla es considerar el movimiento de una sola capa emparedada entre dos bloques del cristal prístino en la fase P2, de modo que dos interfaces son modificadas durante la transformación estructural. Aquí asumimos que mover más de una capa a la vez es mucho menos favorable energéticamente. El método de Nudged Elastic Band (NEB) se ha usado adicionalmente para obtener los caminos de mínima energía y la configuración del estado de transición en los procesos de deslizamiento de las capas del óxido de vanadio.

Para empezar, se simulan los procesos de deslizamiento de capas en la estructura P2-VO_2, sin iones de sodio. El cálculo de la energía interfacial debido a las interfaces creadas por el deslizamiento de capas se computa como la diferencia de energía entre el cristal prístino y el cristal que contiene una capa que ha sido trasladada por un vector $\mathbf{R}$. Se calculan las energías interfaciales en una red densa de 400 vectores de translación $\mathbf{R}$, que abarcan fracciones discretas de los vectores de celda paralelos a las capas. De esta manera se construyen mapas de contorno que representan una superficie de energía por

la cual se puede derivar el camino de mínima energía. Este mapa revela una transformación de fase sin barrera de energía entre la fase P2 y la O2, a lo largo del vector $\mathbf{R} = (1/3, 2/3, z)$ o cualquier otro equivalente bajo rotaciones del grupo de simetría C_6. Vemos entonces que la fase O2 es termodinámicamente estable cuando no hay sodio intercalado en el sistema. Esto coincide con otros materiales laminares que tienden a transformar a la fase O2 cuando están en altos estados de carga.

Al empezar a incluir iones intercalados entre las capas de metales de transición, se observa que, en el momento en el que el sodio se introduce, se genera una barrera en el camino que conecta la fase P2 y O2. Otra observación es que para todos los contenidos de sodio considerados (Na_xVO_2, x = 0.25, 0.333, 0.5, 0.666, y 1) la barrera para el deslizamiento de la capa de una transformación P2 $\rightarrow$ O2 crece de manera lineal con el contenido de sodio, y la fase O2 se vuelve cada vez menos estable energéticamente. Otro factor a tener en cuenta es que en una fase P2, el sodio puede ocupar dos sitios prismáticos diferentes. Dependiendo del sitio que ocupan, la barrera del deslizamiento de capas cambia. De hecho, se calcula que cuando existen iones de sodio en ambos sitios prismáticos (el caso x = 0.5) la barrera del deslizamiento es el doble de alta en comparación al caso en el que los iones de sodio ocupan solo sitios prismáticos que comparten esquinas con los octaedros de VO_6. Esta diferencia es visible analizando la coordinación de los iones de sodio en el estado de transición. En el caso de la barrera alta, los iones de sodio son forzados a ocupar sitios tetraédricos inestables, mientras que si un reordenamiento previo de los iones ocurre es posible evitar estos sitios tetraédricos, resultando en barreras más bajas. Es importante mencionar que la barrera de la difusión del sodio para la reordenación, es dos veces más pequeña que el deslizamiento de las capas y, por tanto, es cinéticamente accesible durante la transformación de fase.

Como ya hemos mencionado, uno de los retos de los OLMT consiste en mejorar su estabilidad estructural, para mejorar la retención de capacidad. Interesa, entonces, tratar de buscar estrategias que sean capaces de suprimir las transformaciones de fase que involucran cambios en la secuencia de apilamiento de las capas de metales de transición, tales como las transformaciones vía deslizamiento de capas en transformaciones P $\leftrightarrow$ O. Una estrategia convencional para evitar estas transformaciones es limitar la cantidad de sodio que se extrae del sistema, que resulta en una pérdida de capacidad para la batería. Estos cálculos sugieren una estrategia efectiva para bloquear estas transformaciones de fase. Se ve que, a bajos contenidos de sodio, todos los sodios ocupan sitios que derivan en barreras bajas. Una posible estrategia sería encontrar la manera de hacer que los sodios ocupen otros tipos de sitios cristalográficos que derivan en barreras más altas. Una estrategia empleada para alterar los ordenamientos del sodio en los OLMT es sustituir parcialmente los metales de transición por otros elementos electroquímicamente inactivos. Se especula que inducir un mayor desorden de sodio-vacante (mediante la sustitución de

metales de transición) incrementa la probabilidad de encontrar microestados en los que el sodio ocupa sitios cristalográficos que inducen a su vez mayores barreras para la transformación de fases, mejorando así la estabilidad y en última instancia el rendimiento de la batería.

TEMA III: Propiedades magnéticas de materiales catódicos en baterías de Na-ión

Introducción:

En el Tema II, hemos mencionado como las baterías de Na-ión son una alternativa prometedora para aplicaciones en sistemas de almacenamiento eléctrico a gran escala y de cómo existen dos familias principales para materiales catódicos; los OLMT, y los compuestos polianiónicos. Estos últimos se basan en estructuras que combinan unidades tetraédricas aniónicas $(XO_4)^{n-}$ u otras derivadas a partir de estas (siendo X = Si, As, S, P, Mo, W...), y poliedros de MO_x (siendo M un metal de transición). Su interés como posibles materiales en baterías de Na-ión se debe a la conjunción de una serie de factores. Los aniones moleculares $(XO_4)^{n-}$ son muy inductivos e hibridizan muy levemente con los centros redox de metales de transición, por lo que permiten extraer un mayor voltaje. También, son materiales muy diversos y estables estructuralmente por lo que permiten explorar una infinidad de estructuras para su uso potencial en baterías.

A parte de su buen funcionamiento electroquímico, otras facetas interesantes de este tipo de materiales han sido exploradas en menor medidas. Por ejemplo, los compuestos polianiónicos basados en metales de transición albergan electrones $3d$ altamente correlacionados, cuyas propiedades magnéticas resultan en propiedades emergentes exóticas y de alto interés tecnológico, tales como la magnetoelectricidad y la multiferroicidad. El origen de estos fenómenos es consecuencia de acoplamientos magnéticos por caminos M-O-M y M-O-X-O-M, entre centros magnéticos de metales de transición. Este tema se centra en calcular las propiedades magnéticas de dos polimorfos $NaFePO_4$, la fase triflita (t) y la maricita (m), usando cálculos a primeros principios y hamiltonianos modelos.

Análisis y resultados:

Como ya hemos mencionado el $NaFePO_4$ cristaliza en dos polimorfos diferentes. La fase 'm' es la termodinámicamente estable y muestra similitudes con los óxidos de perovskitas distorsionadas ortorrómbicamente. La fase 't' es estructuralmente análoga al $LiFePO_4$. Experimentalmente se observa que el t-$NaFePO_4$ presenta el mismo orden antiferromagnético (AFM) que el $LiFePO_4$. Por otro lado, el m-$NaFePO_4$ forma una superestructra magnética con un vector de propagación $\mathbf{q} = (1/2,0, 1/2)$, lo cual implica interacciones magnéticas que compiten entre ellas en el sistema. Este caso es bastante interesante ya que existen muchos ejemplos de manganitas ortorrómbicas con este tipo de

interacciones complejas que rompen la simetría de inversión del sistema y dan efectos multiferróicos como resultado.

Para el análisis de estas interacciones magnéticas se han combinando los paquetes de software Quantum-ESPRESSO y Wannier90, para derivar completamente a primeros principios los parámetros necesarios para construir un Hamiltoniano modelo de Hubbard, que incluye las interacciones de un solo electron y las interacciones repulsivas entre electrones. Estas últimas son difíciles de tratar por lo que se ha empleado el método *constrained random-phase approximation* (cRPA). Después de construir el modelo, se ha solucionado usando el método de Hartree-Fock de campo medio (MFHF). Ésta es la aproximación más sencilla posible que trata las correlaciones electrónicas como un campo medio, no obstante, se calcula que, al estar los centros magnéticos muy distorsionados, el campo cristalino rompe la degeneración de los niveles atómicos, por lo que es razonable asumir que la función de onda está definida por un solo determinante de Slater, y, por lo tanto, el método MFHF es adecuado.

Otro factor a tener en cuenta es la manera de tratar la interacción de canje tal y como ya hemos mencionado en el Tema I. En principio, las interacciones entre electrones derivadas del cRPA contienen gran parte de las interacciones tanto de canje como de correlación (XC). No obstante, aproximaciones como el LDA o el GGA también incluyen, en cierto grado, las interacciones XC. Esto introduce un problema de doble conteo, en el que estamos sumando la misma interacción en dos partes diferentes del modelo. Para mitigar el problema, se han definido tres esquemas diferentes. En el Esquema 1 se ha usado la parte de un solo electrón tal y como está, pero se usa la parametrización esférica de la interacción entre electrones, de manera que evitamos contar dos veces la parte no-esférica de la interacción XC. En el Esquema 2, se ha eliminado por completo la interacción XC de la parte de un solo electrón y se usa la totalidad de la interacción XC de la parte inter-electrónica. En el Esquema 3, se ha usado el método *linear muffin-tin orbital* LMTO en la aproximación de esferas atómicas que, aunque es un método más primitivo para definir la estructura electrónica, está mayoritariamente exento del problema del doble conteo.

Una vez solucionado el modelo con MFHF, se han calculado las interacciones isotrópicas magnéticas en el régimen del supercanje de Anderson y con el teorema de la fuerza local, mediante la fórmula de Lietchenstein. Después se ha derivado el orden magnético que predicen estas interacciones. Empezando por el m-$NaFePO_4$, ambos regímenes resultan en interacciones magnéticas muy parecidas con una temperatura de Curie-Weiss de -90 K, cerca del valor experimental de -83 K.

La siguiente pregunta es si estas interacciones reproducen el orden magnético

experimental, con vector de propagación $\mathbf{q}$ = (1/2,0,1/2). Para esto analizamos la estabilidad de los ordenamientos magnéticos A y C (en la misma notación que en las perovskitas) con respecto a excitaciones inconmesuradas de spin. Considerando el valor calculado de las interacciones entre electrones (U), se ha visto que el ordenamiento A es estable con respecto a cualquier otra excitación. Al reducir manualmente la fuerza de la interacción U, en cambio, el ordenamiento A deja de ser estable, a cambio del ordenamiento C. Por otro lado, se estabilizan ondas de spin que corresponden al aumento de interacciones AFM a lo largo de la dirección ortorrómbica 'c', teniendo el mínimo de energía en el vector inconmesurado $\mathbf{q}$ = (0,0,0.36). Del mismo modo la dispersión que estabilizaría una superestructura a lo largo de la dirección 'a' es prácticamente plana, lo cual sugiere que no hay interacciones magnéticas de largo alcance en esta dirección, incluso cuando se reduce el valor de U. Esta predicción es opuesta a la superestructura observada experimentalmente $\mathbf{q}$ = (1/2,0, 1/2), de modo que el origen microscópico de este ordenamiento magnético es aún desconocido. Uno de los posibles problemas es que, al reducir el valor de la U, la teoría del supercanje de Anderson empieza a fallar y se requieren órdenes de perturbación superiores. Estas interacciones de mayor alcance se hacen llamar super-super canje y operan vía caminos M-O-M-O-M y M-O-X-O-M-O-X-O-M, los cuales podrían reforzar las interacciones AFM en la dirección 'a', y finalmente estabilizar la superestructura experimental. Por último, cabe mencionar que si el vector de propagación fuese $\mathbf{q}$ = (0,0,0.36), el m-$NaFePO_4$ sería multiferróico, y se sugiere explorar esta idea más a fondo de manera experimental.

A pesar de ser una estructura más compleja, el cálculo del t-$NaFePO_4$ ha resultado ser mucho más sencillo. Otra vez, las interacciones magnéticas calculadas entre 'Esquemas' son muy parecidas y aunque la temperatura de Curie-Weiss esté sobre-estimada por un factor de 1.5-2, la temperatura de Néel calculada entra en el rango 34-68 K, siendo consistente con el valor experimental de 50 K. La estructura magnética AFM experimental también está bien reproducida por estos valores. Adicionalmente, y a diferencia de la fase 'm', el t-$NaFePO_4$ sitúa los centros magnéticos fuera de los centros de inversión de su grupo espacial *Pnma*. Por esta razón, un ordenamiento sencillo AFM, sin necesidad de estabilizar ondas de spin con vectores de propagación inconmesurados (como en la fase 'm'), puede inducir multiferroicidad. Éste parece ser el caso con el t-NaFePO4, cuyo ordenamiento magnético AFM combina las simetrías de inversión espacial y temporal ($\hat{IT}$) del sistema y, por tanto, puede albergar fenómenos multiferróicos.

Estos fenómenos son relevantes por su interés tecnológico en sensores, filtros electrónicos, osciladores de alta sensibilidad y demás componentes electrónicos, así como otras aplicaciones más experimentales relacionadas con la spintrónica,. Estos resultados también podrían ser relevantes en el campo de las baterías. Por ejemplo, acondicionar un sistema de baterías cerca de generadores y motores elétricos; u otros dispositivos que son capaces de generar campos

magnéticos elevados, podría ser dañino para la batería si la respuesta del cátodo a estos campos magnéticos es generar polarización eléctrica (magneto-electricidad).

Acknowledgements

First of all, I would like to express my gratitude to my thesis supervisor, Dr. Javier Carrasco, for giving me the opportunity of working with him. It first started as a Summer Internship. From this, he gave me the chance to do the Master's thesis, which I undoubtedly accepted. Finally, it lead to these wonderful 4 years of studies, working on this PhD thesis. His availability to informal discussion has really made my life as a PhD student simple and, most importantly, amusing. I also would like to thank him for having the confidence for giving me the opportunity to be involved in different collaborations.

I thank the host of my extended stays at the National Institute of Materials Science in Japan, Dr. Igor V. Solovyev. His cheerful character was really inspiring and I really learned a lot about model Hamiltonians. My only regret is that we could not finish that climb to Mt. Shirane because of the weather conditions, I will be back for sure. Of course, my stay would have not been the same without the support of Dr. Sergey A. Nikolaev. Both scientifically and personally, I learned a lot from you, and life in Japan would have been much more boring without your presence. Thanks to Dr. Akihiro Tanaka, he allowed the second visit, and he always showed keen to help me with everything. Thanks also to Shingo-san and Dr. Towhid Chowdhury for the awesome, afterwork, friday times. I will not forget you.

My thanks also go to Prof. Nicolas Suaud, for out collaboration with wave function based calculations, and Dr. Nagore Ortiz-Vitoriano for offering the experimental connection, alongside collaborators of Oak Ridge National Lab, which is part of this thesis.

I would also like to thank to my institute, CIC Energigune, for the economical support and for all the years that I spent here doing battery research. Without a doubt, a bright future holds for this growing project. Obviously, a good institute must necessarily be conformed with good people. That's why my thanks go to all the good friends I've made here: Jon, Itziar, Ane, Edu, Oier, Jaione, Guillermo, Giorgio, Xabi, Maria (all of them), Fran, Angel, Carlos, Silvia, Juanlu, Iciar, Nebil, Iñaki... Either in the coffe breaks, pintxopotes, parties, beach, or dinners, you have made this time at the CIC as enjoyable as it can be. Thanks to all of them, and to those I forgot, to whom I apologize.

I thank the Department of Education of the Basque Government for the economical support through a Predoctoral grant (PRE-2016-1-0044), and to the

computing facilities that I could access during these years: i2Basque, Arina cluster, Barcelona Supercomputing Center, and Tirant.

Thanks to all of my friends from outside the work environment. Eskerrik asko 'Indignos' guztiei: Olano, Escribano, Manex, Josu, eta Raul. Unibertsitate garaiak ezinobeak izan ziren benetan, eta, orain gutxiagotan ikusten garen arren, elkartzen garen bakoitzean denbora ez dela pasatu dirudi. Cómo no, estos agradecimientos no pueden acabar sin mencionar a mi gente: Beñat, Mikel, Koldo, Xabi, Diego, Alex, Unai, y Pablo. Aquellos que conozco desde que soy pequeño y que siempre están ahí, dispuestos a amenizar las tardes y las noches, para hacerme desconectar cuando más lo necesito. Mi mano siempre estará tendida para vosotros.

Finally, I want to give my wholehearted gratitude to the most important people of my life. Eskerrik asko zuei, familia, Aita eta Ama, zuengatik nago hemen, eta horregatik egongo naiz betirako zuekin zorretan. Eskerrik asko nire bizitzako konstantea, nire sostengu eta babesa izateagatik. Zugatik, Aita, izan dut gauzen zergatia ezagutzeko jakinmina. Zugatik, Ama, izan dut behar nuen diziplina honera heltzeko. Eskerrik asko, osaba-izebak, lehengusu-lehengusinak, Mikel, Ane eta Kirmutz bereziki, familiaz harro sentitzeko soberan arrazoi emateagatik. A ti, Yuly, gracias por el tiempo que hemos pasado estos años, has sido mi apoyo y compañera, lejos o cerca, en los altos y en los bajos. Por muchos años más.

Contents

List of Publications

Publications Featured in this Thesis

- O. Arcelus, C. Li, T. Rojo, and J. Carrasco. Electronic Structure of Sodium Superoxide Bulk, (100) Surface, and Clusters using Hybrid Density Functional: Relevance for Na-O_2 Batteries. *J. Phys. Chem. Lett.* 2015, **6**, 2027-2031
- O. Arcelus, N. Suaud, N. A. Katcho, and J. Carrasco. Insight from first principles into the stability and magnetism of alkali-metal superoxide nanoclusters. *J. Chem. Phys.* 2017, **146**, 184301
- O. Arcelus, S. Nikolaev, J. Carrasco, and I. Solovyev. Magnetism of $NaFePO_4$ and related polyanionic compounds. *Phys. Chem. Chem. Phys.* 2018, **20**, 13497-13507
- O. Arcelus and J. Carrasco. Atomistic Insight into Glide-Driven Phase Transformations in Layered Oxides for Sodium-Ion Batteries: A Case Study on Na_xVO_2. *ACS Appl. Mater. Interfaces* 2019, **11**, 12562-12569

Other Publications

- T. Deng, W. Zhang, O. Arcelus, J.-G. Kim, J. Carrasco, S. J. Yoo, W. Zheng, J. Wang, H. Tian, H. Zhang, X. Cui, and T. Rojo. Atomic-level energy storage mechanism of cobalt hydroxide electrode for pseudocapacitors. *Nat. Comm.* 2017, **8**, 15194
- U. Arrieta, N. A. Katcho, O. Arcelus, and J. Carrasco. First-Principles Study of Sodium Intercalation in Crystalline Na_xSi_{24} ($0 \leq x \leq 4$) as Anode Material for Na-ion Batteries. *Sci. Reports.* 2017, **7**, 5350
- T. Deng, W. Zhang, O. Arcelus, D. Wang, X. Shi, X. Zhang, J. Carrasco, T. Rojo, and W. Zheng. Vertically co-oriented two dimensional metal-organic frameworks for packaging enhanced supercapacitive performance. *Comm. Chem.* 2018, **1**, 6
- H- Zhang, O. Arcelus, and J. Carrasco. Role of asymmetry in the physiochemical and electrochemical behaviors of perfluorinated sulfonimide anions for lithium batteries: A DFT study. *Electrochem. Acta* 2018, **280**, 290-299

- L. Dai, O. Arcelus, L. Sun, H. Wang, H. Zhang, J. Carrasco, W. Zhang, and J. Tang. An Embedded 3D Li+ Channels in Water-in-Salt Electrolyte to Package Flexible Supercapacitor and Lithium-ion Batteries. *J. Mater. Chem. A* 2019, (Accepted Manuscript)

Ama, Aita eta Maite ditudanak...

Chapter 1

Introduction

1.1 Motivation

Historically, energy consumption has been closely related to demographic growth. In particular, since the start of the industrialization period, global population has seen a seven-fold increase. Continuing with this trend, although all of the so-called 'first world' countries have mostly stabilized their populations, many other 'developing' countries are expected to keep growing. Recent estimates say that the global population will finally stabilize in 2050 at 9.22 billion. This introduces an energetic dual challenge; on the one hand, 80% of the global population still lives under the 100 GJ (gigajoules) per capita threshold [1], that the United Nations Human Developing Index sets as the point above which substantial increases in well-being and human development are present. This means that the majority of the world still aims at increasing their energetic capabilities. On the other hand, given our current technologies, this perspective is necessarily linked to an increase in fossil fuel consumption, thus increasing the CO_2 emissions and worsening the climate problem. Another issue comes from the fact that fossil fuel reservoirs will eventually deplete. Assuming the population stabilization at 9.2 billion and no reforms into energy consumption habits, studies suggest that fossil fuel supply (accounting for all coal, gas, uranium, and crude oil) is guaranteed until 2100 based on known reserves [2]. This is definitely less imminent than other, more 'catastrophic', estimates [3]. However, in relation to the percentage of human population striving to reach the 100 GJ threshold, this is already an issue for the climate. Indeed, if we were to meet the climate targets with respect to carbon emissions, i.e., keeping the average global temperature increase bellow 2 °C (as negotiated in the UN Paris Agreement), we should leave about two thirds of our known reserves untouched [4] to only hold a 50% chance of being successful.

Apart from the impact of carbon emissions on the climate, the use of fossil fuels also represents a public health issue. For instance, air pollutants in urban areas generated by vehicle exhaust emissions were directly responsible for 385000

premature deaths in 2015 globally [5]. Global average life expectancy is also reduced by 2 years because of the air pollution [6], specially affecting the most vulnerable populations in poor urban areas.

Solving all these issues requires from transitioning our actual model into clean, renewable energy sources and transportation. In this context, the development of electrical energy storage devices (batteries) offers great opportunities in the technological development process. Well-known technologies, such as the Li-ion batteries, which are based on the intercalation of alkaline lithium ions into rigid host structures, have allowed the surge of portable electronics and communications technologies. Far from these achievements, batteries offer also the possibility of substituting the use of fossil fuels in transportation, with the still incipient Electric Vehicle (EV) technology, and solving the grid unbalance issues caused by fluctuations in energy generation of renewable power sources [7, 8]. Yet such a diverse range of applications implies the need for very different battery requirements depending on intended use and operating conditions. Additionally, the increasing demand of lithium and the limited availability of lithium salt precursors, has pushed research into finding new battery materials and chemistries, which has become a thriving field of research in the last decade [9–13].

In particular, sodium based battery materials look promising. Sodium is abundant and evenly distributed on the Earth's crust, which makes it more economical and sustainable than lithium [14]. In addition, lithium forms alloys with aluminum at low voltages, so Li-ion batteries use more expensive copper as an anode current collector; sodium does not present this issue, and cost-effective aluminum current collectors can be readily used in sodium based batteries [15]. Yet, the use of sodium has an intrinsic specific energy penalty as Na ions are heavier and larger than Li ions. Furthermore, the standard redox potential of the Na^+/Na^0 couple relative to the standard hydrogen electrode is about 0.3 V higher than the corresponding Li^+/Li^0 potential; this implies that sodium based batteries always fall short in terms of energy density with respect to their lithium counterparts. Thus, current research efforts in Na based batteries focuses on achieving competitive specific energies, capacities and operating voltages. To this end, understanding the physical processes behind these technologies will be very valuable to inform future materials design strategies.

1.2 Basic battery components

Batteries are electric energy storage (EES) devices made up of smaller electrochemical units called *cells*. Batteries are either *primary* or *secondary*. The former are disposable and cannot be recharged, while the latter are rechargeable and can be used many times. Alkali-ion batteries lie within this group,

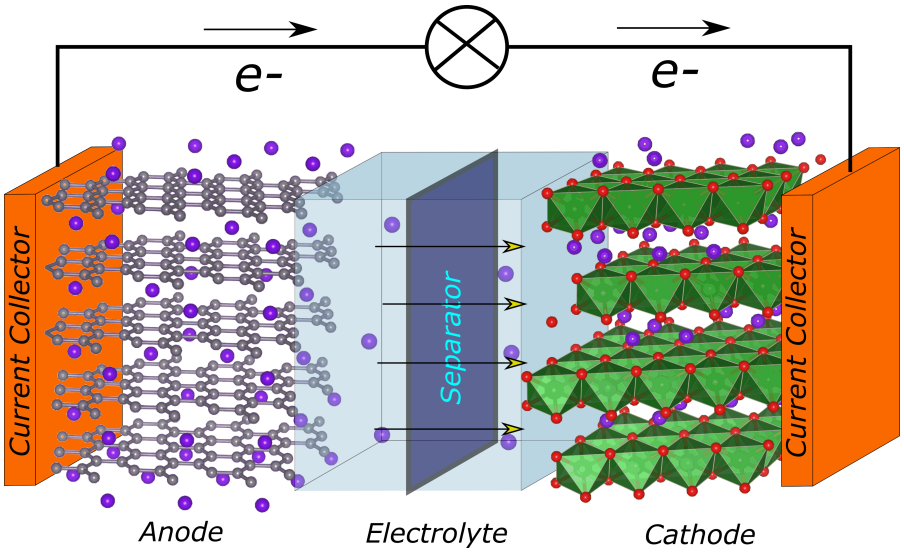

FIGURE 1.1: Schematic representation of the typical Li-ion cell, with a Li_xC anode and a Li_xCoO_2 layered oxide cathode. The electrons moving from the anode to cathode represent the discharge process.

and we will focus this introduction on them. Cells are built up of a number of components that are listed here and shown in Figure 1.1:

- *Negative electrode:* Often (but wrongly) called *anode*, it is the component of the cell that loses electrons when discharging, i.e., it gets *oxidized*. During charge, the negative electrode accepts electrons, i.e., it gets *reduced*. The use of the word *anode* is technically wrong since this word is used for the electrode where oxidation occurs. Thus, the negative electrode is only an anode during discharge. However due to the extended use of the word, we will generally refer to the negative electrode as *anode*.

- *Positive electrode:* Also called *cathode*, it is the component that gains electrons when discharging, i.e., it gets *reduced*. During charge, it loses electrons, i.e., it gets *oxidized*. Similar to anodes, the positive electrode is only the cathode when discharging the battery. Regardless, we will still generally refer to it as *cathode*.

- *Electrolyte:* It is an ionic conductor that provides the means by which the ion charge transfer occurs. An electrolyte usually comprises a liquid *solvent* containing dissolved chemicals, typically *salts*, that ensure sufficient ionic conductivity. When the anode is oxidized and the cathode reduced (discharge), dissolved positively charged ions move towards the cathode and

negatively charged ions move towards the anode, thus compensating the excess (or lack) of electric charge in both electrodes.

- *Separator:* It is the component that physically separates the anode and the cathode. It prevents internal short circuit by electrically insulating both electrodes, while allowing for ionic charge diffusion in the electrolyte.

- *Current collectors:* They are the components that are adhered to both electrodes to act as an electronic conductor in which to put contacts on. The current collectors do not take part into the electrochemical reaction, i.e., they do not get reduced or oxidized.

1.3 Functional properties of a battery

Throughout this thesis we will sparely reference some functional properties of batteries, it is worth therefore defining them here, to get a better general understanding of what makes a battery competitive. Figure 1.2 shows a schematic of the typical charge/discharge voltage curves that are measured when testing electrochemical cells, and includes all the basic information about the performance of the battery, which can be characterized by the following properties.

- *Cell voltage:* During operation, a battery delivers electronic current as the result of spontaneous redox reactions that occur at a given potential in discharge (V_{dis}). In charge, an external potential difference (V_{ch}) must be applied so that the inverse redox reactions occurs. These voltages change depending on the internal battery resistance (R_{in}) to the corresponding ionic current (I_i), that induce charge (discharge) overpotentials with ohmic behavior, $\eta_{dis} = I_{dis}R_{in}$ ($\eta_{ch} = I_{ch}R_{in}$). Such that:

$$V_{dis} = V_{oc} - \eta_{dis}(q, I_{dis}). \tag{1.1}$$

$$V_{ch} = V_{oc} + \eta_{ch}(q, I_{ch}). \tag{1.2}$$

where V_{oc} is the open-circuit voltage and q is the state of charge (the amount of charge that has been moved between the electrodes). V_{oc} is a constant magnitude, which means that it does not depend on the load of the external circuit. In other words, it is the *equilibrium potential difference* when the device is disconnected from any circuit, and therefore, it is independent of internal resistances and currents. Equations 1.1 and 1.2 show that V_{oc} is the maximum (minimum) voltage one gets (needs to apply) when discharging (charging) a battery. Of course, in the same way no real mechanical machine

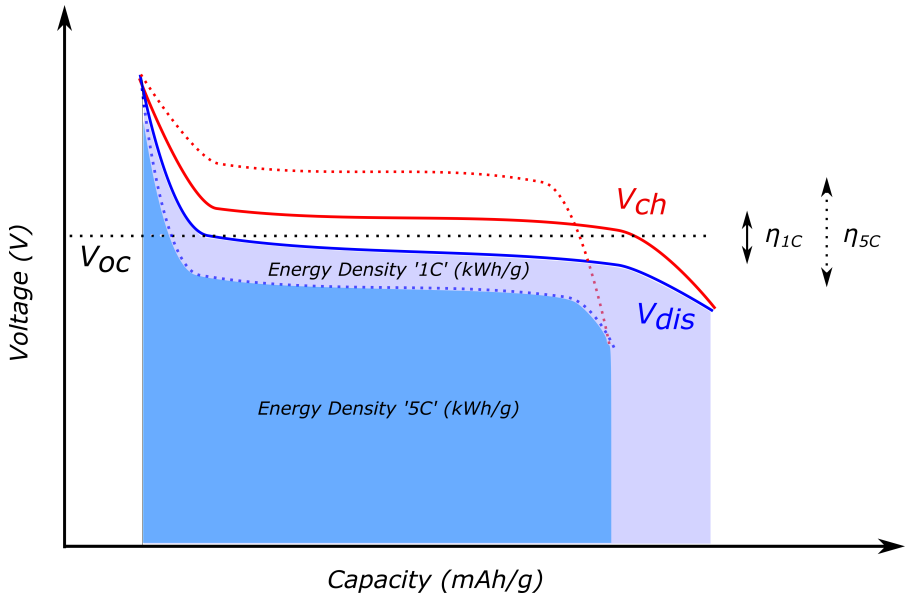

FIGURE 1.2: Schematic representation of the CV (capacity/voltage) curves of a typical electorchemical cell. Blue (red) curves represent the charge (discharge) curves. Curves at different C rates are shown in solid ('1C') and pointed ('5C') lines. The overpotetials (η) at different rates are shown as the vertical distance between the red and blue curves. The open-circuit voltage (V_{oc}) is shown as the horizontal pointed black line. Note that these values are strictly pictorical, just to qualitatively present the response of the cell to different charge/discharge rates. Energy densities are presented as the integrated area bellow the discharge curves.

exists without friction, no battery exists without internal resistances. Therefore, the difference between V_{dis} and V_{ch} is always finite. This difference is called the total overpotential (η) that results in efficiency losses that are related to internal resistive factors. It is, therefore, of technological interest to reduce η as much as possible. Another design principle related to this is to find systems where V_{oc} is high, as higher voltages indicates a higher capacity to store energy.

- *Reversible capacity:* It specifies the amount of charge, measured in ampere-hours (Ah) or miliampere hours (mAh) that a cell can reversibly deliver, at a particular rate. It is a measure of quantity, and therefore, a higher value the larger the amount of electrochemically active material the battery has, regardless of its weight or volume. When this value is normalized by

weight or volume, it is referred to as *gravimetric capacity* or *volumetric capacity*, respectively. The *theoretical capacity* is the maximum possible charge an electrode can deliver in the ideal case that all of the active material is reversibly used in the charge/discharge process, without any degradation mechanism.

- *C rate:* It is a measure of the constant current, on charge or discharge, that a cell can hold for 1 hour until it gives all the capacity away. The applied currents are then measured relative to this 'C' unit. Therefore, charging or discharging a battery at 'C/2' rate should take 2 hours, 'C/10' should take 10 hours, ect. Again, this is the idealized scenario, as the battery is subject to limitations regarding the ionic and electronic conductivities of the electrodes and electrolyte. This means that if high rates are used, because of internal resistances, an incomplete utilization of the active material will occur, followed by the subsequent loss of capacity and lowering of the use time. At low rates, the contrary may happen.

- *Energy density:* Relates to the quantity of electrical energy in watt hours (Wh) or kilowatt hours (kWh) that the cell can hold at a particular rate. It can again be normalized by weight (*gravimetric energy density*) or by volume (*volumetric energy density*) of the active material. It gives the combined relation between capacity and voltage.

Summing up, fast conductance (low η), high capacity, lightweight, small, and high voltage are the properties that make electrode and electrolyte materials suitable for batteries. Other *very* important factors to take into account are; *cost*, coming from the availability and abundance of raw materials, ease of synthesis, scalability, etc.; *safety*, concerning the use of electrodes that produce internal short circuits, dangerous degradation mechanisms resulting in high temperatures that lead into fire risks, etc.; and *environmental friendliness*, regarding the toxicity of the materials used, recoverability, net carbon emissions related to the battery production activity, etc. However, all these aspects, although crucial, lie outside of what the 'functional properties' of a battery are. Therefore, a full assessment of all the possible factors that make a battery feasible is outside of the scope of this introduction.

1.4 Working principles of a battery

In this section we briefly introduce the electronic band alignments (as shown in Figure 1.3) of different cell systems as a way of fundamentally looking at batteries [16]. Figure 1.3a shows the ideal case for a battery, where the electron chemical potential of the anode (μ_A) lies just bellow the lowest unoccupied molecular orbital (LUMO) of the electrolyte. Similarly, the cathode's μ_C lies above the electrolyte highest occupied molecular orbital (HOMO). This scenario, prevents the oxidation and reduction of the electrolyte itself, which

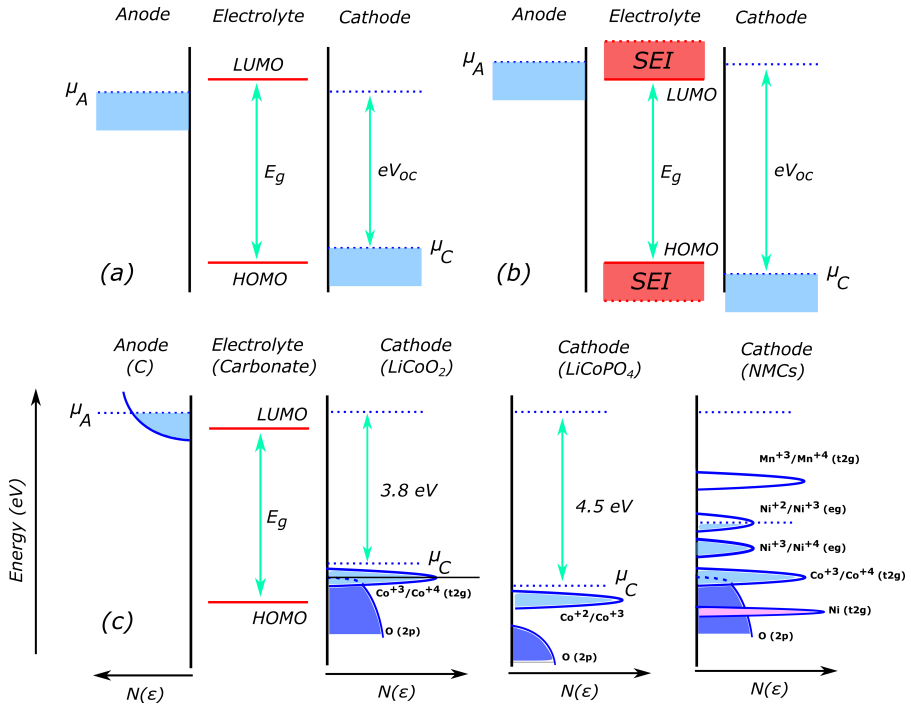

FIGURE 1.3: (a) and (b) are the electronic band alignments of different possible cell systems. N(ϵ), shown in (c), is the electronic density of states (DOS) of the electrodes.

would lead to irreversible electrolyte degradation and safety issues. When the circuit is opened, the system is in equilibrium at a given electrochemical potential difference, V_{oc}, which we already introduced and is defined as:

$$V_{oc} = \frac{\mu_A - \mu_C}{e}. \tag{1.3}$$

When the circuit is closed, during discharge, electrons will spontaneously flow from the higher potential electrode (anode) to the lower potential electrode (cathode). During charge, external power must be applied to set μ_C higher than μ_A to make electrons flow in the opposite direction. An scenario similar to what is shown in Figure 1.3b is also possible. In this case, it may happen that because μ_A (μ_C) is above (below) the electrolyte LUMO (HOMO), the formation of a Solid Electrolyte Interface (SEI) layer occurs at both the cathode and the anode surface, through chemical reactions involving electrolyte salts, electrochemically active material, and electrode surfaces. This prevents the anode (cathode) from reducing (oxidizing) the electrolyte, however, it increases the internal resistance for ionic conduction and results in

an overall loss of capacity upon cycling, since the SEI grows bigger with each charge/discharge cycle, and the electroactive material is gradually lost. Still, many commercial batteries operate through the formation of an SEI layer, and controlling its formation and morphology is of utmost importance in the design of battery systems. The open-circuit voltage is still calculated as in Equation 1.3.

Lastly, Figure 1.3c shows the diagram of the typical C/$LiCoO_2$ cell, as represented in Figure 1.1, in a discharged state. This cell is composed by a graphite (C) anode and a layered $LiCoO_2$ cathode, with a carbonate-based electrolyte, with a voltage window, E_g (typically $\sim$ 5 V), that limits the maximum voltage a cell can deliver before it starts decomposing. As already explained, μ_A is higher than μ_C, where the latter is located just above the Co 3d state manifold of t_{2g} symmetry. Since μ_A is above the electrolyte LUMO, this battery will work through the formation of a SEI layer at the anode surface. In the discharged state, all Co ions will be on a +3 oxidation state, with the 3d (t_{2g}) bands completely occupied. When charging, Li ions start leaving the layered Li_xCoO_2 framework, and Co^{+3} will start oxidizing to Co^{+4} accordingly, thus emptying the 3d state manifold. Notice here the overlap of the O 2p states in the lower half of the Co 3d band. At $x \leq 0.5$, when half of the cobalt is oxidized, the added holes start to be trapped on O 2p states, and it becomes impossible to continue oxidizing Co^{+3} to Co^{+4}. Additionally, those holes locate themselves in O 2p states of peroxide molecules at the particle surface, finally leading to an irreversible loss of O_2 by oxygen evolution and the subsequent degradation of the electrode. Therefore, practical C/Li_xCoO_2 cells usually limit the amount of extracted lithium from the cathode ($0.5 \leq x \leq 1$). This is indeed a common practice in a number of different cathode materials, but it inevitably results in lower capacities.

There are several strategies that can be used to circumvent this issue, for example, by trying to lower the top of the O 2p band, which can be done by substituting the oxide ions (O^{-2}) by more polarizing polyanion units (PO_4^{-3}), as is the case of $LiCoPO_4$. This allows for fully oxidizing the redox centers in the cathode and increasing the voltage with respect to their oxide counterparts [17], as can be seen in Figure 1.3c. Another strategy consists of using a mixture of metals in a $LiCoO_2$ type layered structure. For example, EV manufacturers, such as Nissan and BMW use layered Nickel-Manganese-Cobalt oxides (NMCs) for their Nissan Leafs and BMW i3's, while Nickel-Cobalt-Aluminum oxides (NCAs) are currently being used by Tesla for the Models 'S' and 'X' [18]. In the case of NMCs, the corresponding ratios of transition metals allow for the functionalization of their electrochemical properties. As can bee seen in Figure 1.3c, these hosts contain Mn^{+4}, which is electrochemically inactive, but the strong Mn-O bonds offer great thermal and cycling stability with the downside of capacity loss. Ni 3d states do not overlap with O 2p states, and therefore they can be fully oxidized from Ni^{+2} to Ni^{+4}, yielding high capacities without oxygen degradation. However, high Ni contents

are related to structural degradation, as Ni^{+2} is known to form antisite defects by occupying sites in the Li containing layers, Ni^{+4} is also known to be highly reactive towards organic electrolytes [19]. High Co containing NMCs are known to offer good rate capabilities [20], however they still suffer from the intrinsic limitations that we already addressed for $LiCoO_2$ cathodes. Because of these competing issues, commercial cells for EVs use NMC-111, i.e, $LiNi_{0.333}Mn_{0.333}Co_{0.333}O_2$, as the $\sim$ 4 V cathode material, because it offers a good compromise between capacity, rate performance, and structural stability. However, current research efforts aim at increasing the nickle content to form other compounds such as NMC-311, NMC-811, etc.

Although we presented the general case for commercial, widespread, Li-ion batteries, the same operation principles still hold for Na-based batteries, which is the main focus of this thesis. Indeed, research on Na-based batteries have been mostly done based on previous knowledge generated from Li-based ones because of the chemical similarity of both elements. Here we include all the chemistries, such as Na-ion [21, 22], Na-air [12, 23], Na-S [24, 25], ect., the former two being covered in the following chapters. However, we note that, usually, the larger size and different bonding of sodium leads to different electrochemical behavior in comparison to their lithium counterparts [26, 27].

1.5 The role of atomistic first-principles simulation methods

The former sections have been dedicated to explaining which are the main functioning principles and characteristics of rechargeable batteries and which is the basic rationale behind designing better batteries. We saw that finding adequate materials for batteries is far from trivial. It requires from a delicate balance between compounds whose electrochemical potentials lie within a narrow voltage window, maximize their potential differences, maintain their ability to store the maximum amount of alkaline ions, have good conductivity, ect. This is a 'find a needle in the haystack' problem, and a very expensive one indeed, especially when the search is done by trial and error. In this quest of finding high-performance materials, computational first-principles methods, concretely density functional theory (DFT), plays an important role in helping predicting and characterizing the structures and properties of materials at the atomic scale [28], because they can offer insight into atomic and electronic scale processes without the need of experimental inputs. These 'computer experiments' can then be used to aid experimentalist, either by predicting candidate materials suitable for interesting applications, or by providing a physical interpretation to experimental results. In the field of battery materials, exciting contributions have been made in this respect. In the following we proceed to briefly mention some of the battery properties that are predicted

by DFT. For the interested reader, the following references [29–32] give a more in-depth description of the recent advances in the field.

DFT calculations generally require an input of the crystalline (or molecular) atomic structure of the material of interest. After this, several atomic or electronic processes are simulated keeping track of their electronic and energetic changes. The differences between these changes are then used to extract several properties, such as, open-circuit voltages, thermodynamical stability, magnetic couplings, ionic diffusion, spatial charge localization, vibrational properties, ect.

To better illustrate the significance of first principles methods in battery applications, let us introduce a general Na-ion intercalation cathode (Na_xMO_2, where M is a transition-metal), which undergoes the following reversible reaction:

$$Na_xMO_2 \leftrightarrow Na_yMO_2 + (x-y)(Na^+ + e^-). \tag{1.4}$$

When the battery is in equilibrium, the dissolved Na^+ and the corresponding electron e^- are in equilibrium with the anodic electrode. If we choose metallic sodium to be the anode, then we will only need to compute the DFT energies of three different crystal structures; (i) Na_xMO_2, (ii) Na_yMO_2, and (iii) Na (metal). The difference between these energies will give us the reaction free energy, which can easily be transformed into the open-circuit voltage in the following way:

$$V_{oc} = -\frac{\Delta G}{ze} \approx -\frac{E[Na_xMO_2] - E[Na_yMO_2] - (x-y)E[Na]}{(x-y)e}. \tag{1.5}$$

Here, ΔG is approximated as ΔE, which is the difference between the internal energies calculated by DFT at T = 0 K, without accounting for entropic, vibrational, or pressure effects. Also, $x - y$ is the amount of Na extracted from the host cathode. Note that this equation is the equivalent to the one represented in the Equation 1.3, as it is no more than the difference between electrochemical potentials of the active ions in both electrodes.

Cathode materials also need to be good ionic conductors. DFT calculations can also be used to calculate energetic barriers for ionic diffusion inside the cathode hosts. Figure 1.4 shows a pictorial example of how these barriers are calculated with DFT. From these barriers one can obtain an approximation of the rate at which these types of diffusion events occur, and from there the chemical diffusivity can be obtained. One could also use these rates as inputs for other larger microscopic models, for example in kinetic Monte Carlo (kMC) simulations.

Generally, we showed a few examples of what can DFT calculations contribute to characterizing battery materials, but the range of possible applications is much larger [29–31]. Indeed, many success stories of DFT predicted, and

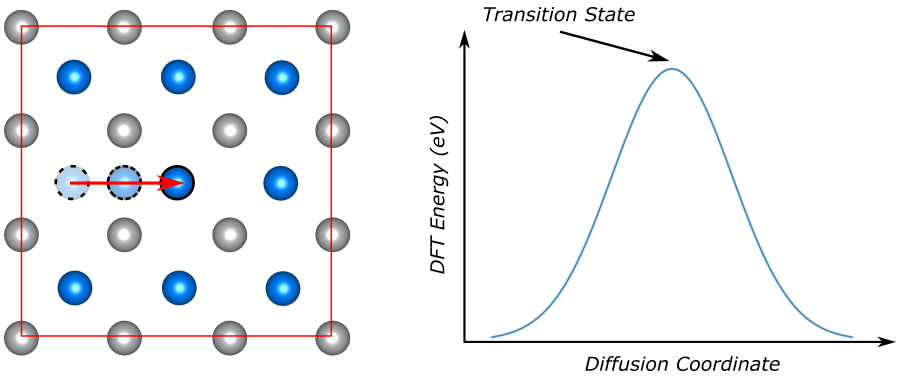

FIGURE 1.4: (left) Schematic representation of a body-centered cubic crystal structure with two different atoms. The computational cell is shown red. The red arrow indicates the direction in which the blue atom is moved to occupy a vacancy in the center of the cell, leaving a vacancy behind. (right) Hypothetical DFT energy related to such diffusion process. The top of the curve represents the energy of the transition state (TS), shown as the interstitial blue atom in the middle of the red arrow on the left hand side figure.

experimentally confirmed, battery materials exist [28], making it an exciting field of research for the coming years, where synergies between experimental and theoretical research will be key to push major advances in energy related materials.

1.6 Structure of the Thesis

This thesis has been written by addresing several open questions about different Na based battery systems using first-principles simulations. Thus, each Chapter is meant to be read independently from each other (with some cross reference), where the results and conclusions about a particular battery material are self-contained within them.

Chapter 2 includes a brief summary of the theoretical background of the methods used to perform the simulations for this Thesis. Chapter 3 contains all the simulations performed on Na-air battery systems. The reader will find an electronic, energetic and structural characterization of the battery discharge products, and an atomic insight onto the effect of the solvent on the battery performance. Chapter 4 presents the results on phase transformations on layered oxide cathodes for Na-ion batteries. Lastly, Chapter 5 contains the

simulations about the magnetic properties of polyanionic cathodes for Na-ion batteries, with an extra section for theoretical methods that are unique to this Chapter.

Chapter 2

Theoretical Background

2.1 Schrödinger's equation and the Born Oppenheimer approximation

The Schrödinger's equation provides a first-principles description of matter based on quantum mechanics. Solving it provides the full information of the many body system under study, including time. However, when dealing with static properties of atoms, molecules, or condensed matter, we can simply focus on the time-indendent Schrödinger's equation:

$$\hat{H}\,|\Psi\rangle = E\,|\Psi\rangle\,. \tag{2.1}$$

where $\hat{H}$ is the Hamiltonian operator, E is the total energy of the system, and $|\Psi\rangle$ is the eigenvector of the Hamiltonian operator that refers to the many-body wave-function. Ignoring relativistic effects, for a system with N interacting electrons and M nuclei, $\hat{H}$ is expressed as follows:

$$\hat{H} = -\sum_{i}^{N}\frac{\nabla_i^2}{2} - \sum_{j}^{M}\frac{\nabla_j^2}{2M_j} - \sum_{i,j}^{N,M}\frac{Z_j}{\mid \mathbf{r}_i - \mathbf{R}_j \mid} + \frac{1}{2}\sum_{i,i'}^{N}\frac{1}{\mid \mathbf{r}_i - \mathbf{r}_{i'} \mid} + \\ + \frac{1}{2}\sum_{j,j'}^{M}\frac{Z_j Z_{j'}}{\mid \mathbf{R}_j - \mathbf{R}_{j'} \mid}. \tag{2.2}$$

The first two terms are the kinetic energies of electrons and nuclei, respectively. The third and fourth terms correspond to the attractive electron-nuclei and the repulsive electron-electron interactions, whereas the last term accounts for the repulsive nucleus-nucleus interaction.

Solving Equation 2.1 yields the many-body wave-function, which depends on the coordinates of the electrons $\mathbf{r}_i$ and nuclei $\mathbf{R}_i$:

$$\langle \mathbf{r}_1, ..., \mathbf{r}_N, \mathbf{R}_1, ..., \mathbf{R}_M | \Psi \rangle = \Psi(\mathbf{r}_1, ..., \mathbf{r}_N, \mathbf{R}_1, ..., \mathbf{R}_M). \tag{2.3}$$

From a practical viewpoint, Equation 2.1 is impossible to be solved analytically for any system bigger than a handful of particles. And, therefore, Equation 2.1 can only be solved considering certain approximations. For instance, the mass of the proton is approximately 1800 times larger than that of the electron, the Born-Oppenheimer (BO) approximation [33] states that because of this mass difference, the coupling between nuclei and electrons is such that electrons react instantaneously to nuclear movement. This enables important simplifications as discussed below.

The Hamiltonian (Equation 2.2) can be written as $\hat{H} = \hat{T}_{nuc} + \hat{H}_{el}$, where $\hat{H}_{el}$ holds all interactions apart from the nuclear kinetic energy. Here, the electronic Hamiltonian depends parametrically on $\{\mathbf{R}\}$, and it can be solved separately as:

$$\hat{H}_{el}\psi^n_{el}(\{\mathbf{r}\};\{\mathbf{R}\}) = E^n_{el}(\{\mathbf{R}\})\psi^n_{el}(\{\mathbf{r}\};\{\mathbf{R}\}). \tag{2.4}$$

This gives the electronic eigenfunctions $\psi^n_{el}(\{\mathbf{r}\};\{\mathbf{R}\})$. The semicolons express that the nuclear positions are parameters. These eigenfunctions form an orthogonal basis

$$\langle\psi^n_{el}|\psi^m_{el}\rangle = \delta_{mn} = \int d\mathbf{r}_1 ... d\mathbf{r}_N \; \psi^n_{el}(\{\mathbf{r}\};\{\mathbf{R}\})^*\psi^m_{el}(\{\mathbf{r}\};\{\mathbf{R}\}). \tag{2.5}$$

And the complete wave-function (2.3) can be expanded in this basis:

$$\Psi(\{\mathbf{r}\},\{\mathbf{R}\}) = \sum_n F_n(\{\mathbf{R}\})\psi^n_{el}(\{\mathbf{r}\};\{\mathbf{R}\}), \tag{2.6}$$

where the expansion coefficients F_n depend on the nuclear positions. Note that the total wave-function does not depend now parametrically on $\{\mathbf{R}\}$. Plugging the total wave-function in Equation 2.1, projecting over another electronic state, and reordering its terms; we obtain the following equation:

$$\sum_n \langle\psi^m_{el}|\,\hat{T}_{nuc}\,|\psi^n_{el}\rangle\, F_n(\{\mathbf{R}\}) + (E^m_{el}(\{\mathbf{R}\}) - E)F_m(\{\mathbf{R}\}) = 0. \tag{2.7}$$

The first term in Equation 2.7 represents the coupling between electrons and nuclei. If we consider now the BO approximation, the off-diagonal elements vanish and result in a set of uncoupled nuclear equations of motion:

$$[\hat{T}_{nuc} + E^m_{el}(\{\mathbf{R}\})]F_m(\{\mathbf{R}\}) = EF_m(\{\mathbf{R}\}). \tag{2.8}$$

The complexity of the problem is greatly reduced with this important simplification. But still, solving the electronic Hamiltonian, $\hat{H}_{el}$, is too complex to be treated exactly for any chemical system of actual interest. Therefore, further approximations are commonly needed.

2.2 Wave-function methods

2.2.1 Hartree-Fock approximation

In analytically unsolvable problems, the variational principle is a handy tool. The main concept behind this principle is that the energy obtained from a trial wave-function (Ψ') will always be higher than the actual ground-state energy (E_0). Therefore, the full minimization of the energy functional with respect to all allowed N-body wave-functions, will eventually give the correct solution to the ground-state:

$$E[\Psi'] > E_0 = \min_{\Psi} E[\Psi]. \tag{2.9}$$

We can further assume our trial electron wave-function Ψ to be defined by a Slater determinant (Equation 2.10), i.e., an antisymmetrized product of single electron wave-functions $\psi_i(\mathbf{x})$, which are themselves a product of a spatial orbital and a spin functions. Here $\mathbf{x}$ contains both the real-space coordinates ($\mathbf{r}$) and spin coordinates (s).

$$\Psi_{HF} = \frac{1}{\sqrt{N!}} \begin{vmatrix} \psi_1(\mathbf{x}_1) & \psi_2(\mathbf{x}_1) & \cdots & \psi_N(\mathbf{x}_1) \\ \psi_1(\mathbf{x}_2) & \psi_2(\mathbf{x}_2) & \cdots & \psi_N(\mathbf{x}_2) \\ \vdots & \vdots & \ddots & \vdots \\ \psi_1(\mathbf{x}_N) & \psi_2(\mathbf{x}_N) & \cdots & \psi_N(\mathbf{x}_N) \end{vmatrix}. \tag{2.10}$$

The Hartree-Fock (HF) approximation [34] is based on a constrained search over all of the orthonormal orbitals $\psi_i(\mathbf{x})$ that minimize $E[\Psi]$ for an approximated Ψ_{HF}. The scalar product of the wave-function $\langle\Psi_{HF}|\Psi_{HF}\rangle$ is equal to 1 and, therefore, the expectation value for the energy is given by:

$$E_{HF} = \langle\Psi_{HF}|\hat{H}|\Psi_{HF}\rangle = \sum_{i}^{N} H_i + \frac{1}{2}\sum_{ii'}^{N}(J_{ii'} - K_{ii'}). \tag{2.11}$$

Here, the first summation contains the single particle energies, which includes the kinetic energy and the interaction with the nuclei. The second term is expressed as the difference between the Coulomb interaction of the electron densities ($J_{ii'}$) and the exchange term ($K_{ii'}$), which arises from the antisymmetry of the many-body wave-function. They have the following form:

$$H_i = \int \psi_i^*(\mathbf{x})\Big[-\frac{\nabla^2}{2} + \sum_{j}^{M}\frac{Z_j}{\mid \mathbf{r} - \mathbf{R_j} \mid}\Big]\psi_i(\mathbf{x})d\mathbf{x}. \tag{2.12}$$

$$J_{ii'} = \int\int \psi_i^*(\mathbf{x})\psi_i(\mathbf{x})\frac{1}{\mid \mathbf{r} - \mathbf{r}' \mid}\psi_{i'}(\mathbf{x}')\psi_{i'}^*(\mathbf{x}')d\mathbf{x}d\mathbf{x}'. \tag{2.13}$$

$$K_{ii'} = \int\int \psi_i^*(\mathbf{x})\psi_{i'}(\mathbf{x})\frac{1}{\mid \mathbf{r}-\mathbf{r}' \mid}\psi_i(\mathbf{x}')\psi_{i'}^*(\mathbf{x}')d\mathbf{x}d\mathbf{x}'. \tag{2.14}$$

These three equations show that the HF energies can be evaluated as a functional of single one electron wave-functions $\psi_i(\mathbf{x})$. The minimization search over these orbitals will therefore result in the ground-state energy. This is done subject to orthonormality conditions

$$F_{HF} = E_{HF} + \sum_{i,j}\varepsilon_{ij}\left\langle\psi_i|\psi_j\right\rangle. \tag{2.15}$$

And results in the HF differential equations:

$$\hat{F}_{HF}\psi_i(\mathbf{x}) = \epsilon\psi_i(\mathbf{x}). \tag{2.16}$$

$$\hat{F}_{HF} = -\frac{1}{2}\nabla^2 + \sum_j^M \frac{Z_j}{\mid \mathbf{r}-\mathbf{R_j} \mid} + \sum_{i'}^N \int \frac{\psi_{i'}(\mathbf{x}')\psi_{i'}^*(\mathbf{x}')}{\mid \mathbf{r}-\mathbf{r}' \mid}d\mathbf{x}' - \hat{K}. \tag{2.17}$$

In Equation 2.17 the four terms correspond to the kinetic, electron-nucleus, eletron-electron Coulomb and exchange ($\hat{K}$) interaction operators, respectively.

$\hat{K}$ corresponds to a purely non-local interaction, which means that operating $\hat{K}$ on $\psi_i(\mathbf{x})$ will now depend on the value of ψ_i on all of the points of space:

$$\hat{K}\psi_i(\mathbf{x}) = \sum_{i'}^N \int \frac{\psi_{i'}^*(\mathbf{x}')\psi_{i'}(\mathbf{x})}{\mid \mathbf{r}-\mathbf{r}' \mid}\psi_i(\mathbf{x}')d\mathbf{x}'. \tag{2.18}$$

Note that the definition of $\hat{F}_{HF}$ depends on the solutions of Equation 2.16, and therefore, its solution is self-consistent. A very detailed review of the method can be found in the book by Yang and Parr [35].

The most important benefit of the HF approximation in modern quantum chemistry is that it exactly nullifies the so-called self-interaction error (SIE). In particular, the exchange interaction in the HF framework is treated exactly, and an important equality arises when $i = i'$, as can be seen in Equations 2.13-2.14, which is $J_{ii} = K_{ii}$. This means that the parasitic repulsive interaction that an electron feels with the field that is generated by all the electrons, and therefore, by itself, is fully compensated by the exchange term.

2.2.2 Multi-configurational approaches

The limitations of the HF approximation comes from the fact that the true wave-function of a system is never represented by a single determinant and, therefore, the energy of the system will always differ from the true energy. The error between the real and the HF derived energy is called the correlation energy.

The most straightforward approach to evaluate the correlation energy is to consider a linear mixing of all possible determinantal wave-functions, which could in theory capture all the correlation energy of a system. This is the so-called configuration-interaction (CI) approach [36]. Yet, notice that the number of single determinants increases exponentially with the number of orbitals and electrons considered, and the problem becomes quickly intractable.

Ways to circumvent this issue comes from treating a selected set of orbitals (called active orbitals) with CI, while the rest of orbitals are considered inactive (if occupied) or virtual (if unoccupied). The complete active-space self-sonsistent field (CASSCF) [37] is one of the various methods used in this framework. At this point, the remaining correlation, also called dynamical-correlation, is brought by single and double electron-hole excitations, between active, and inactive (or virtual) states, obtained from a multi-determinantal treatment such as CASSCF. These residual correlations, which are very important in low-energy phenomena, such as magnetism, can be treated perturbatively at the second order, for example with the n-electron valence state perturbation theory (NEVPT2) [39–41] or the complete active-space perturbation theory (CASPT2) [42, 43]; or variationally (diagonalizing the single and double configuration interaction space (SDCI)). This last approach is still to computationally demanding, however one may get rid of the 2 electron - 2hole inactive excitations (from the inactive to the virtual orbitals) and apply CI to an even more reduced configurational space. This method is known as the difference-dedicated configuration interaction (DDCI). Figure 2.1 schematically summarize the different kind of excitations that can be considered.

The methods described in this section, which are going to be used in this work, are not the only ones to generate multi-determinantal spaces. But describing the whole state of the art of the wave-function based methods is far beyond the scope of this general introduction. More detailed information on related topics can be found in the following review papers [38, 44–46].

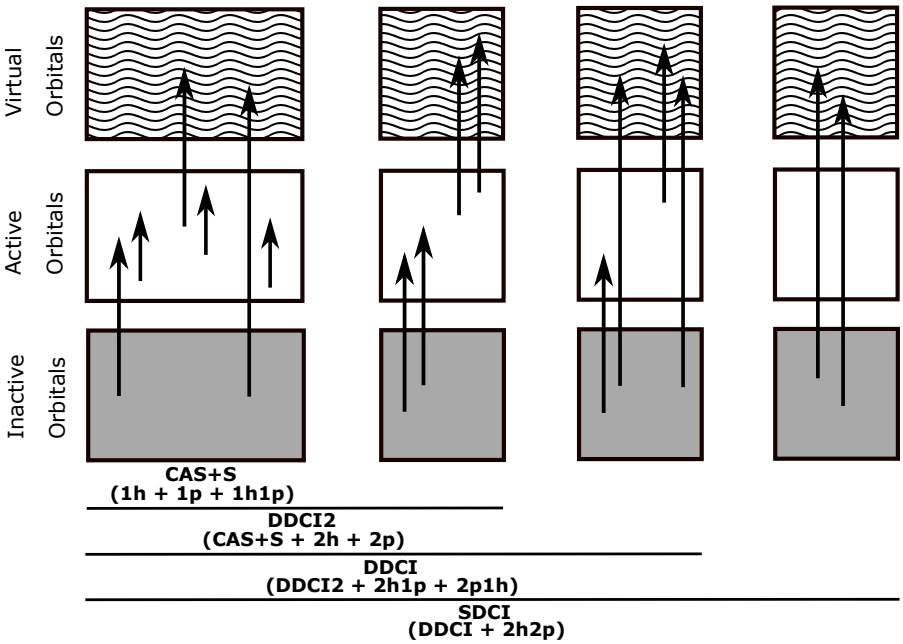

FIGURE 2.1: All possible single and double electron and hole excitations between active, inactive and virtual orbitals, that are added to the CAS space for CI analysis. This figure is based on the review by Malrieu *et. al.* [38].

2.3 Density Functional Theory

The ever increasing complexity of the N-body wave-function makes complex systems hard to model. Density function theory enables the complicated wave-function to be replaced by a much simpler quantity, the electron density $n(\mathbf{r})$:

$$n(\mathbf{r}) = N \int d\mathbf{r_2}...d\mathbf{r_N} \Psi^*(\mathbf{r}, \mathbf{r_2}, ..., \mathbf{r_N}) \Psi(\mathbf{r}, \mathbf{r_2}, ..., \mathbf{r_N}). \tag{2.19}$$

However, we first need to know how different observables are written as functions of electron densities. For this, we introduce the electron density matrices:

$$n_1(\mathbf{r}, \mathbf{r}') = N \int d\mathbf{r_2}...d\mathbf{r_N} \Psi^*(\mathbf{r}, \mathbf{r_2}, ..., \mathbf{r_N}) \Psi(\mathbf{r}', \mathbf{r_2}, ..., \mathbf{r_N}). \tag{2.20}$$

where the $n(\mathbf{r})$ is contained in the diagonal elements $\mathbf{r} = \mathbf{r}'$. We also define the pair density matrix as:

$$n_2(\mathbf{r}, \mathbf{r}') = \frac{N(N-1)}{2} \int d\mathbf{r_3}...d\mathbf{r_N} \Psi^*(\mathbf{r}, \mathbf{r}', ..., \mathbf{r_N}) \Psi(\mathbf{r}, \mathbf{r}', ..., \mathbf{r_N}). \tag{2.21}$$

Note that Equations 2.20 and 2.21 do not involve spin coordinates for simplicity. The full details on density matrices can be found in Chapter 2 of the book by Yang and Parr [35].

The expectation value of the electronic Hamiltonian, $\hat{H}_{el}$ in Equation 2.4, can be now described in terms of electron- and pair-density matrices.

$$E = \langle \hat{H}_{el} \rangle = -\frac{1}{2} \int d\mathbf{r} \nabla^2_{\mathbf{r}} [n_1(\mathbf{r}, \mathbf{r}')]_{\mathbf{r}=\mathbf{r}'} + \int d\mathbf{r} V_{ext}(\mathbf{r}) n(\mathbf{r}) + \\ + \int d\mathbf{r} d\mathbf{r}' \frac{n_2(\mathbf{r}, \mathbf{r}')}{\mid \mathbf{r} - \mathbf{r}' \mid}. \quad (2.22)$$

The three terms in this formula represent the kinetic energy, the electron-nucleus potential and the electron-electron potential, respectively. The electron-electron potential is written with a classical Coulombic repulsion term and a non-classical interaction term. The known form of the classical term suggests that the pair-density matrix can be written as:

$$n_2(\mathbf{r}, \mathbf{r}') = \frac{1}{2} n(\mathbf{r}) n(\mathbf{r}') [1 + h(\mathbf{r}, \mathbf{r}')]. \quad (2.23)$$

where $h(\mathbf{r}, \mathbf{r}')$ is the pair-correlation function, and contains all non-classical effects of the electron-electron interactions. If we replace this expression into Equation 2.22, we obtain:

$$E = T[n(\mathbf{r})] + \int d\mathbf{r} V_{ext}(\mathbf{r}) n(\mathbf{r}) + J[n(\mathbf{r})] + K[n(\mathbf{r})]. \quad (2.24)$$

where E corresponds to the sum of the kinetic, electron-nucleus, classical electron-electron repulsion and non-classical electron-electron terms, respectively. All this procedure has led us to an exact expression of the energy from density matrices. Nonetheless, the kinetic energy, $T[n(\mathbf{r})]$, and the non-classical electron-electron energy, $K[n(\mathbf{r})]$, (also called exchange-correlation energy) terms turned out to be utterly problematic to define. Many trials to approximate these terms were carried out by L. H. Thomas, E. Fermi and P. Dirac [47–49], but none of them had satisfactory results. It was not until 1964 that Hohenberg and Kohn changed the panorama with their simple and elegant theorems.

2.3.1 The Hohenberg-Kohn theorems

1^{st} **Theorem. The use of $n(\mathbf{r})$ as a base variable**: *The external potential $V_{ext}(\mathbf{r})$ is determined, within a trivial additive constant, by the electron density $n(\mathbf{r})$.*

1^{st} **Corolary**: Since $V_{ext}(\mathbf{r})$ is uniquely determined by $n(\mathbf{r})$,

the wave-function Ψ is completely determined by the ground-state electron density $n_0(\mathbf{r})$. Thus, all the properties of the ground-state can be derived from our base variable.

2^{nd} **Theorem. Density analog to the variational principle**: *For a trial electron density $n(\mathbf{r})$, being the total energy of the system a functional of the density $E[n]$, the global minimization of the total energy functional will deliver the exact ground-state energy.*

$$E_0 \leq E[n] = \int V_{ext}(\mathbf{r}) n(\mathbf{r}) d\mathbf{r} + F[n]. \tag{2.25}$$

Where the unknown universal functional $F[n] = T[n] + V_{ee}[n]$, is proved to exist.

2^{nd} **Corolary**: Equation 2.25 would be exact for the ground-state if the exact form of $F[n]$ was known. Therefore, the total energy functional is sufficient to determine the ground-state energy and density.

2.3.2 Kohn-Sham approach

We have seen that an energy functional exists, which is exact for the ground-state and is solely defined by the electron density. However, it is composed by an unknown functional $F[n]$, that includes the kinetic energy and the full electron-electron interactions. In 1965 Kohn and Sham proposed a novel approach for dealing with this universal functional [50]. The method consists of using a basis of one electron orbitals ψ_i to compute the kinetic energy to a good accuracy and leaving a small residual correction (presumably) to be handled separately. The kinetic energy is written as a special case of a more general formulation, and holds true for a wave-function that describes a *non-interacting* N electron system.

$$T_s[n(\mathbf{r})] = -\frac{1}{2} \sum_i^N \int d\mathbf{r} \psi_i^*(\mathbf{r}) \nabla_{\mathbf{r}}^2 \psi_i(\mathbf{r}). \tag{2.26}$$

And the electron density

$$n(\mathbf{r}) = \sum_i^N \mid \psi_i(\mathbf{r}) \mid^2 . \tag{2.27}$$

The problem now is that given a density $n(\mathbf{r})$ we need to know a unique decomposition of orbitals from which T_s is calculated. Kohn and Sham defined a *non-interacting reference system* whose ground-state density is exactly n and has a unique decomposition in terms of these orbitals ψ_i (KS orbitals). The equations that define the eigenvalues ε_i and eigenfunctions ψ_i of this reference

system are:

$$[-\frac{1}{2}\nabla^2 + V_s(\mathbf{r})]\psi_i = \varepsilon_i\psi_i. \tag{2.28}$$

As a result of solving Equation 2.28, the kinetic energy and the density are defined exactly in Equations 2.26 and 2.27. What Kohn and Sham achieved was to define an auxiliary system of N non-interacting particles, in such a way that for any given density n, where an external potential with that same *interacting* particle density n exists, it also exists another potential V_s yielding the same *non-interacting* density n, for which the kinetic energy T_s is exact.

If we now invoke the universal functional from the 2^{nd} Hohemberg-Kohn theorem and rewrite it with $T_s[n(\mathbf{r})]$ as the kinetic energy component we define:

$$F[n(\mathbf{r})] = T_s[n(\mathbf{r})] + J[n(\mathbf{r})] + E_{XC}[n(\mathbf{r})]. \tag{2.29}$$

where T_s; J and E_X; and E_C can be though of as 0^{th}, 1^{st}, and 2^{nd} (and above) order terms for the expansion of the universal functional F. Note that the third term is different to the functional K in Equation 2.24, because it also includes the residual correction due to the kinetic energy being that of a non-interacting system. And as we have already seen the total energy functional will be defined as:

$$E[n(\mathbf{r})] = F[n(\mathbf{r})] + \int V_{ext}(\mathbf{r})n(\mathbf{r})d\mathbf{r}. \tag{2.30}$$

Similar to the HF approximation we can now search for the KS orbitals that minimize the energy functional under orthonormality conditions:

$$\frac{\delta}{\delta\psi_i^*(\mathbf{r})}[E[n(\mathbf{r})] - \sum_i^N \varepsilon_i \langle\psi_i|\psi_i\rangle] = 0. \tag{2.31}$$

A more detailed derivation can be found in Ref. [35]. From this minimization search we are left with a set of N one-particle Kohn-Sham differential equations of the type:

$$[-\frac{1}{2}\nabla^2 + V_{eff}(\mathbf{r})]\psi_i = \varepsilon_i\psi_i. \tag{2.32}$$

This set of equations define a system of N non-interacting particles moving in an effective external potential of the type:

$$V_{eff}(\mathbf{r}) = V_{ext}(\mathbf{r}) + \int d\mathbf{r}\frac{n(\mathbf{r})}{\mid \mathbf{r} - \mathbf{r}' \mid} + V_{XC}(\mathbf{r}). \tag{2.33}$$

Where the exchage-correlation potential is defined as:

$$V_{XC}(\mathbf{r}) = \frac{\delta E_{XC}[n(\mathbf{r})]}{\delta n(\mathbf{r})}. \tag{2.34}$$

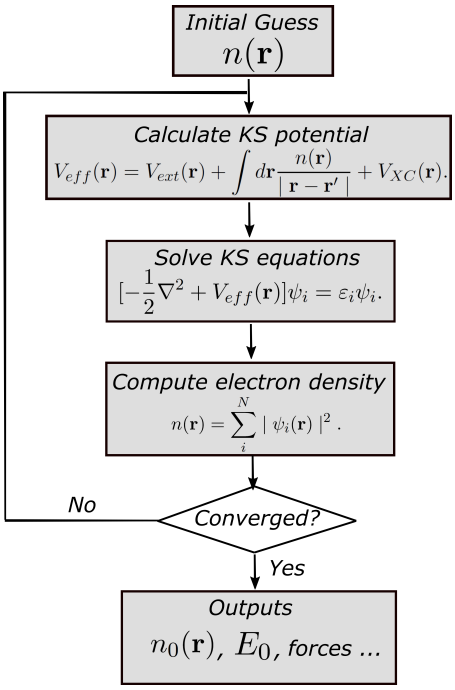

FIGURE 2.2: Scheme of the iterative process that has to be followed to solve the KS equations.

Therefore if we set the potential of the auxiliary non-interacting particle system (2.28) $V_s = V_{eff}$, Equations 2.28 and 2.32 merge, and solving the set of 'N' KS equations will give the ground-state density $n(\mathbf{r})$ which has a correspondence mapping to the interacting system of external potential V_{ext}. This ground-state density will then be used to calculate the ground-state properties of the system. Notice that the effective potential depends on $n(\mathbf{r})$ itself. The solution to the KS equations (2.32) must therefore be solved iteratively (Figure 2.2).

The KS equations are in principle exact, and are able to include all the exchange-correlation effects of electrons. This is different from the HF approximation, in that the latter is approximated by definition. Yet the exact form of E_{XC} is unknown. The main task then resides on finding an appropriate expression for E_{XC} that correctly describes the system under study.

2.3.3 LDA, GGA, and meta-GGA functionals

The first approximation is to use the exchange-correlation functional E_{XC} of an uniform electron gas. The so called local density approximation (LDA), where E_{XC} takes the following form:

$$E_{XC}^{LDA}[n] = \int d\mathbf{r} n(\mathbf{r}) \varepsilon_{xc}(n(\mathbf{r})), \tag{2.35}$$

where $\varepsilon_{xc}(n(\mathbf{r}))$ indicates the exchange-correlation energy density of a uniform electron gas of density $n(\mathbf{r})$, which can be split into two parts:

$$\varepsilon_{xc}(n(\mathbf{r})) = \varepsilon_x(n(\mathbf{r})) + \varepsilon_c(n(\mathbf{r})), \tag{2.36}$$

where $\varepsilon_x(n(\mathbf{r}))$ represents the exchange energy per electron in a uniform gas of a particular density and its explicit form was derived by Dirac in 1930 [48]:

$$\varepsilon_x(n(\mathbf{r})) = -\frac{3}{4}\left(\frac{3}{\pi}\right)^{1/3} n(\mathbf{r})^{1/3}. \tag{2.37}$$

However, there is not such analytical expression for the correlation energy $\varepsilon_c(n(\mathbf{r}))$. Instead some accurate Monte Carlo calculations exist for the correlation energy [51], as well as some other interpolated analytical expressions [52, 53].

In short, LDA replaces the E_{XC} of a non-uniform electron system with the one of a uniform electron gas, with the density value of an infinitesimal volume portion of the non-uniform electron distribution. So the Equation 2.35 sums the individual contributions of the uniform electron gas E_{XC} in each portion of the space.

Hence, LDA is a good approach to deal with systems with little electron localization. However it fails in systems where electron localization is high, such as atoms, molecules, and strongly correlated materials. It also tends to overestimate the valence-band energies because it fails at capturing the full effect of the exchange interaction and does not nullify the electron self-interaction and, therefore, it systematically underestimates band gaps. It also tends to overestimate bonding energies and, therefore, underestimates bond-lengths.

The next logical step to improve LDA is to consider not only the exchange and correlation contributions of a uniform electron gas of density $n(\mathbf{r})$ at a given position $\mathbf{r}$, but also to consider the values of the density at the vicinity of that position (semi-local approximation). In this case the gradient of the density, $\nabla n(\mathbf{r})$ accounts (to some extent) for the inhomogeneities of the density. This

is the generalized gradient approximation (GGA):

$$E_{XC}^{GGA}[n] = \int d\mathbf{r} f(n(\mathbf{r}), |\nabla n(\mathbf{r})|). \tag{2.38}$$

In this case, similar to what happens in LDA, E_{XC} can be split in two terms:

$$E_{XC}^{GGA}[n] = E_{X}^{GGA}[n] + E_{C}^{GGA}[n]. \tag{2.39}$$

There are many expressions for this gradient dependent kernel. For example, the Becke, Lee, Yang, and Parr parameterization (BLYP) [54, 55]; the Perdew-Yang 91 (PW91) [56]; and the Perdew-Burke-Ernzerhof (PBE) [57] which is going to be used in this Thesis.

A further improvement to the GGA functionals is to also include the second derivative of the electron density. This is the so-called meta-GGA (mGGA) approach. In practice the orbital kinetic energy density is used, written using the occupied KS orbitals:

$$\tau(\mathbf{r}) = \frac{1}{2} \sum_{i}^{N} \mid \nabla \psi_i(\mathbf{r}) \mid^2 . \tag{2.40}$$

The E_{XC} functional can then be written as:

$$E_{XC}^{mGGA}[n] = \int d\mathbf{r} f(n(\mathbf{r}), |\nabla n(\mathbf{r})|, \tau(\mathbf{r})). \tag{2.41}$$

Note that now, the energy functional depends not only on the density, but also on the KS orbitals explicitly included in it. Again, the kernel f is unknown: There are two approaches to write its functional form. Empirical approaches, where parameters of f are fitted based on large molecular databases, such as the Minnesota functionals MXXL (M06L [58], revM06L [59], M11L [60], MN12L [61], MN15L [62]). And purely nonempirical approaches that are formulated satisfying exact constraints of the functionals without empirical parameters, such as, TPSS [63], revTPSS [64], θ-GGA [65], and SCAN [66]. In particular the strongly constrained and appropriately normed (SCAN) functional is used in some of the calculations that appear in this Thesis.

2.3.4 Hybrid functionals

Hybrid functionals are a further extension to improve the accuracy and transferability of the aforementioned approximations. They are based on mixing a percentage (α) of HF exact exchange energy (see Section 2.2), in the exchange-correlation functional from DFT.

$$E_{XC}^{hyb} = \alpha E_{X}^{HF} + (1-\alpha) E_{X}^{DFT} + E_{C}^{DFT}. \tag{2.42}$$

In this Thesis we used the B3LYP [67, 68] and the HSE (Heyd Scuseria Ernzerhof)[69] functionals. B3LYP is the most popular hybrid functional between quantum chemists, and takes the following form:

$$E_{XC}^{B3LYP} = (1-\alpha)E_X^{LDA} + \alpha E_X^{HF} + \alpha_X E_X^{B88} + \alpha_C E_C^{LYP} + (1-\alpha_C)E_C^{LDA}. \tag{2.43}$$

where the three parameters are set to $\alpha = 0.2$, $\alpha_X = 0.72$, and $\alpha_C = 0.81$; E_X^{B88} [55] and E_C^{LYP} [54] are GGA type exchange and correlation functionals; and E_C^{LDA} is the LDA correlation term as obtained by Vosko, Wilk, Nusair [52].

The HSE functional depends on two parameters: the percentage of exact exchange included (α), and the screening parameter (ω), which represents an inverse lenght parameter that separates the short- and long-range (SR and LR) contributions of the exact exchange interactions. The HSE functional considers the exact HF exchange at SR, while the rest of the LR interactions are treated with PBE, thus reducing the computational cost significantly.

$$E_{XC}^{HSE} = \alpha E_X^{HF,SR}(\omega) + (1-\alpha)E_X^{PBE,SR}(\omega) + E_X^{PBE,LR}(\omega) + E_C^{PBE}. \tag{2.44}$$

Particularly, we use the HSE06 version [70], with $\alpha = 0.25$ and $\omega = 0.11$.

To sum up, the exact treatment of the exchange interaction using HF exchange offers a way of partially solving the self-interaction problem. It therefore improves the description of many molecules and solids, in terms of bond-lenghts, HOMO-LUMO gaps (band gaps), vibrational frequencies, etc. However, it still depends on empirical parameters, so it is not a purely *ab-initio* approach.

2.4 Non-local long-ranged van der Waals corrections

The exchange-correlation functionals discussed so far are strictly (semi-)local, except hybrid functionals that further include the non-local exchange interaction that accounts for the problem of self-interaction. However, all of these approximations fail at describing long-ranged electron correlation effects, which are important to correctly describe non-covalent bonding, such as, for instance, binding in molecular crystals [71–73], absorption of molecules on surfaces [74–76], structural description of ionic liquids [77, 78], and liquid water [79–81].

Long-range interactions can actually be included in a number of ways. For instance, using high level methods that involve random-phase approximation (RPA) [82–84], quantum monte-carlo (QMC) [85], and many-body perturbation theory (MBPT) [86]. But these approaches, although accurate, are too computationally demanding for large systems.

Alternatively, long-range interactions can also be included by developing explicitly non-local density functionals of the form:

$$E_{nl}^{c} = \frac{1}{2}\int d\mathbf{r}\int d\mathbf{r}' n(\mathbf{r}) f(\mathbf{r},\mathbf{r}') n(\mathbf{r}'), \tag{2.45}$$

where the specific form of f could take different forms, such as the vdW-DF [87–89] and vdW-DF2 [90] functionals of Lundqvist and co-workers, or the more recent rVV10 Vydroov and van Voorhis functionals [91–93] (which we will use in this Thesis). One could also optimize the performance of the van der Waals (vdW) inclusive exchange-correlation functionals by keeping the vdW-DF form of E_{nl}^{c}, and selecting other exchange and correlation parts different from what is proposed in vdW-DF, as in the case of optPBE-vdW and optB88-vdW density functionals of Klimes and co-workers [94].

Another possibility is correcting the DFT energy *a posteriori* for the missing dispersion effects. This is the so-called DFT-D approach, which was first described by Grimme *et. al.* [95] and where the dispersion energy takes the following form:

$$E_{disp} = -\frac{1}{2}\sum_{A}^{N}\sum_{B}^{N}\sum_{\mathbf{R}}\frac{C_{6AB}}{|\mathbf{r}^{A,0}-\mathbf{r}^{B,\mathbf{R}}|^{6}} f_{damp}(|\mathbf{r}^{A,0}-\mathbf{r}^{B,\mathbf{R}}|), \tag{2.46}$$

where the summation runs over all pair of atoms A (located at the home unit cell $\mathbf{L} = 0$) and B (located at any other $\mathbf{L}$); C_6 parameters are dispersion coefficients which are generally tabulated from atomic polarizabilities; and f_{damp} is the damping function that avoids the energy to diverge when atoms are too close to each other. Specifically, Equation 2.46 is known as the DFT-D2 method [96]. Other latter expressions include higher order dispersion interactions (higher than the C_6 appearing in Equation 2.46), as is the case of the DFT-D3 approach [97]. Other methods use the concept of atoms-in-molecules to calculate the C_6 parameters, as in the Tkatchenko-Scheffler (TS) method [98]. The selection of the damping function also changes the effectiveness of the correction.

2.5 Basis sets

Regardless of the chosen DFT functional, the next step is always to solve the KS differential equations (Equation 2.32). Numerically, these KS orbitals (ψ_i) must be expressed in a specific basis set ($\{\phi_p\}$):

$$\psi_i = \sum_{p}^{P} c_p^i \phi_p. \tag{2.47}$$

And then, the Equation 2.32 could be written in matrix form in the following manner:

$$(\mathbf{H} - \varepsilon_i \mathbf{S})\mathbf{c}^i = 0. \tag{2.48}$$

where $\mathbf{H}$ is the Hamiltonian matrix in the basis $\{\phi_p\}$; $\mathbf{S}$ is the overlap matrix, which, in the case of having an orthonormal basis, equals to the identity matrix ($\mathbf{S} = \mathbb{I}$); and ε_i and $\mathbf{c}^i$ are the eigenvalues and eigenvectors containing the expansion coefficients of each ψ_i. Note that the basis size (P) is infinite, so in practice, one should reduce the basis to a finite size (P'). In order to find an appropriate reduced basis set, we should select basis functions that are both *efficient* (few basis functions are needed for the expansion of the orbitals ψ_i) and *unbiased* (the basis functions are sufficiently general so as to represent any kind of orbitals). This is of course a compromise between computational cost and generality, and different basis sets can be used for different systems.

2.5.1 Bloch's theorem and the plane-wave basis set

In the case of crystalline solids it is useful to notice that they can be described from a Bravais lattice, which specifies a real-space periodic array in which the repeating units of the crystal are arranged in positions $\mathbf{R}$[1], forming identical fragments of volume called unit cells. These unit cells can be formed by atoms, molecules, or clusters of atoms. Cosidering that such a repeating array of atoms generates a potential, $V(\mathbf{r})$, with the corresponding Bravais lattice periodicity:

$$V(\mathbf{r} + \mathbf{R}) = V(\mathbf{r}), \tag{2.49}$$

the Hamiltonian of such systems is also periodic. The Bloch's theorem states that the one electron eigenfunctions of such Hamiltonians are written as:

$$\psi_{n\mathbf{k}}(\mathbf{r}) = e^{i\mathbf{k}\mathbf{r}} u_{n\mathbf{k}}(\mathbf{r}). \tag{2.50}$$

or:

$$\psi_{n\mathbf{k}}(\mathbf{r} + \mathbf{R}) = e^{i\mathbf{k}\mathbf{R}} \psi_{n\mathbf{k}}(\mathbf{r}). \tag{2.51}$$

where $\mathbf{k}$ is the wave vector of the electrons, n is the band index and $u_{n\mathbf{k}}(\mathbf{r}) = u_{n\mathbf{k}}(\mathbf{r} + \mathbf{R})$. Notice that the wave vector $\mathbf{k}$ can always be confined to the first Brillouin zone (1BZ). This is because any wave vector $\mathbf{k}'$ outside the first Brillouin zone can be written as:

$$\mathbf{k}' = \mathbf{k} + \mathbf{G}, \tag{2.52}$$

where $\mathbf{G}$ is the reciprocal lattice vector [2]. It is also important to note that the Bloch states are orthonormal for different wave vectors $\mathbf{k}$.

[1] $\mathbf{R} = n_1\mathbf{a}_1 + n_2\mathbf{a}_2 + n_3\mathbf{a}_3, n_i \in \mathbb{N}$ and $\mathbf{a}_i$ are vectors of the unit cell.
[2] $\mathbf{G} = k_1\mathbf{b}_1 + k_2\mathbf{b}_2 + k_3\mathbf{b}_3, k_i \in \mathbb{N}$ and $\mathbf{b}_i$ are vectors of the reciprocal unit cell.

Any eigenfunction that is periodic with the Bravais lattice, can be expanded in plane waves with that same periodicity conditions. It is therefore natural to use this basis to expand the periodic function $u_{n\mathbf{k}}(\mathbf{r})$, which is indeed a convenient approach because of its conceptual simplicity and ease of implementation:

$$u_{n\mathbf{k}}(\mathbf{r}) = \sum_{\mathbf{G}} c_{\mathbf{G}}^{n,\mathbf{k}} e^{i\mathbf{G}\mathbf{r}}. \tag{2.53}$$

Then, the Bloch states in the plane wave basis are written as:

$$\psi_{n\mathbf{k}}(\mathbf{r}) = \frac{1}{\sqrt{\Omega}} \sum_{\mathbf{G}} c_{\mathbf{G}}^{n,\mathbf{k}} e^{i(\mathbf{G}+\mathbf{k})\mathbf{r}}. \tag{2.54}$$

where Ω is the unit cell volume and normalizes $\psi_{n\mathbf{k}}(\mathbf{r})$. So, the next step is now to solve Equation 2.47 in this basis for each wave vector $\mathbf{k}$ independently (the Hamiltonian matrix is block-diagonal in $\mathbf{k}$) and get the coefficients $c_{\mathbf{G}}^{n,\mathbf{k}}$.

Again, the practical implementation of this basis set consists of truncating the size of the Hamiltonian matrix. As we saw earlier, the basis set on which we are expanding the eigenfunctions of the Hamiltonian, belongs to a Hilbert space of infinite dimensions. In our case, the reciprocal lattice is infinite, and so are the set of reciprocal lattice vectors $\{\mathbf{G}\}$ and the size of the basis of plane-waves. We then truncate the size of the basis set by selecting a maximum kinetic energy cutoff for the plane-waves:

$$E_{cutoff} \geq |\langle \mathbf{k} + \mathbf{G}_{max}^{\mathbf{k}}| - \frac{1}{2}\nabla^2 |\mathbf{k} + \mathbf{G}_{max}^{\mathbf{k}}\rangle| = \frac{1}{2}|\mathbf{k} + \mathbf{G}_{max}^{\mathbf{k}}|^2. \tag{2.55}$$

where $\mathbf{G_{max}}$ is the largest reciprocal lattice vector that gives a kinetic energy right below the maximum cutoff, which could be different for each $\mathbf{k}$ in the 1BZ.

Moreover, it follows from the Bloch's theorem with the Born-Von Karman boundary conditions [99] that the number of allowed wave vectors in the 1BZ is equal to the number of sites in the crystal. This means that in the 1BZ there are approximately 10^{23} allowed wave vectors. This number, although not infinite, makes the practical computation of so many Hamiltonian blocks untractable. Therefore, only few wave vectors $\mathbf{k}$ are usually selected to construct a *K-point* grid in the 1BZ, trying to include the most relevant points of the 1BZ.

But, is the plane-wave basis *efficient* and *unbiased*? It is surely unbiased as it is the natural consequence of the Bloch's theorem and has been proven to work in a variety of crystalline solids. Yet, further approximations are needed to achieve computational efficiency. In this regard, the *pseudopotentials* approach, first introduced in the 1930s by Hans Hellmann [100, 101], has been the most effective way of implementing the plane-wave basis for practical calculations. In the following, we provide a brief introduction to the

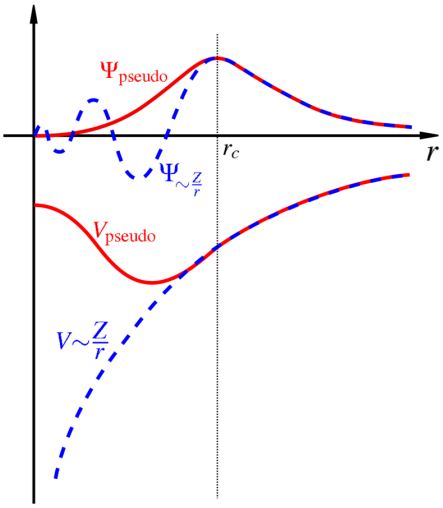

FIGURE 2.3: Scheme of a pseudopotential approach.The pseudopotential, V_{pseudo}, and the corresponding wavefunction, Ψ_{pseudo}, are shown in red. The real attractive potential $\frac{Z}{r}$ of the nucleus and the corresponding wavefunction, $\Psi_{\frac{Z}{r}}$, are the dashed blue curves. r_c corresponds to the cutoff radius.

pseudopotential approach.

2.5.2 Pseudopotentials

The wavefunctions of inner electrons (core electrons) in atoms oscillate a lot more than outer electrons (valence electrons). In consequence, an enormous amount of plane-waves are needed to correctly describe the oscillation of core electron wavefunctions, i.e. their cutoff energy in Equation 2.55 is very large.

In principle, we can assume that the valence electrons are quite shielded by the core electrons, and the latter do not usually participate in the chemistry of materials. Therefore, one can replace the potential associated to core electrons by a *pseudopotential*. As shown in Figure 2.3, pseudopotentials are designed to yield smooth wavefunctions near the nucleus. Then, above some cutoff radius, r_c, the pseudopotential smoothly varies to match the real potential for valence electrons. In this way, the total amount of needed plane-waves can be vastly reduced.

A good pseudopotential is determined by its *softness* and *transferability*. A pseudopotential is soft when few plane-waves are needed to describe the

pseudo-wavefunctions. It is transferable when the pseudopotential is general enough so as to be used in a variety of chemical environments. Over the years different approaches to constructing pseudopotentianls have been proposed: ultra-soft pseudopotentials (USPP) [102–104], norm-conserving pseudopotentials (NCPP) [105], and projector augmented wave method (PAW) [106, 107]. The two latter approaches are going to be used in this Thesis as implemented in the Quantum-ESPRESSO (QE) [108, 109] package for NCPPs and the Vienna ab-initio simulation package (VASP) [110–113] for PAW potentials.

2.5.3 Numeric atomic orbital basis

In previous subsections 2.5.1 and 2.5.2, we discussed the expansion of KS orbitals of a periodic crystal in terms of a delocalized plane-wave basis. However, choosing other basis sets may be advantageous in a variety of cases. In particular, atom centered, localized numerical atomic orbitals (NAOs) are another convenient way to select a basis set to expand the wavefunctions of solids and molecules. NAOs are written as:

$$\phi_n(\mathbf{r}) = \frac{u_n(r)}{r} Y_{lm}(\theta, \varphi). \tag{2.56}$$

where $Y_{lm}(\theta, \varphi)$ are complex spherical harmonics, and $u_n(r)$ (n is a combined index of l, m and atomic sites) are tabulated numerical solutions of a radial Schrödinger-like equation of the type:

$$[-\frac{1}{2}\frac{d^2}{dr^2} + \frac{l(l+1)}{r^2} + v_n(r) + v_{cut}(r)]u_n(r) = \epsilon_n u_n(r), \tag{2.57}$$

where $v_n(r)$ is obtained from the self-consistent solution of KS equations of a free isolated atom, and $v_{cut}(r)$ is a confinement potential that ensures that the tails of the atomic orbitals are strictly zero above a given cutoff radius r_c. This guarantees that different atomic orbitals do not overlap between distant regions of space, and enables the use of very efficient linear-scaling O(N) numerical solvers. Solving these equations yields *minimal basis* of radial functions for which the all-electron treatment of systems becomes straightforward, as the oscillations of the wavefunctions near the nucleus are naturally described within the numerical solutions of $u_n(r)$. Of course a basis set constructed from free atom numerical radial solutions is not good enough to accurately model the intricacies of chemical bonding in molecules and solids, and more basis functions should be included on top of the minimal basis.

The FHI-aims package [114–119], which we use in this Thesis, implements NAO basis in terms of this minimal basis and further expands the basis functions in a hierarchical manner by successively adding pre-constructed radial functions (hydrogen-like, cation-like, atom-like, etc.) and looking for the one that gives the best single improvement of the energy. In this way, each added

function to enlarge a given basis already contains all the rest of 'lower-level' basis functions, and the energy systematically converges with the successive addition of basis functions of higher hierarchy. This hierarchy is organized in element-specific *tiers*. Typically, *tier1* basis are well suited for fast pre-relaxations and give accurate forces and geometries. However, *tier2* basis are needed in order to achieve meV level converged results. Moreover, on top of the '*tier*' hierarchy, another element-specific hierarchy of predefined settings (density of integration grids, maximum order of the multiple expansion of the density and so on) can be set as *light*, *tight*, or *really-tight*.

This same approach can be generalized to periodic boundary conditions by defining the Bloch orbitals (see Subsection 2.5.1) with real space basis functions as:

$$\psi_{n\mathbf{k}}(\mathbf{r}) = \sum_{\mathbf{R}} e^{i\mathbf{k}(\mathbf{R}+\mathbf{r}_j)} \phi_n(\mathbf{r}-\mathbf{R}), \tag{2.58}$$

where $\mathbf{r}_j$ is the position of site j starting from the origin of the unit cell in position $\mathbf{R}$. Equation 2.58 verifies the Bloch condition (Equation 2.51), and the wavevectors $\mathbf{k}$ are those allowed by Born-Von Karman boundary conditions.

2.6 Maximally localized Wannier functions

An alternative representation to plane-waves and localized basis functions are the so-called Wannier functions, which were first introduced by G. Wannier in 1937 [120]. These orbitals depend on the band index n and on the cell index of the direct lattice $\mathbf{R}$, and come from the realization that a Bloch function, with a fixed $\mathbf{r}$ is periodic in the reciprocal lattice. Such function has therefore a Fourier series in plane waves with wavevectors in the direct lattice $\mathbf{R}$:

$$\psi_{n\mathbf{k}}(\mathbf{r}) = \sum_{\mathbf{R}} e^{i\mathbf{k}\mathbf{R}} w_{n\mathbf{R}}(\mathbf{r}), \tag{2.59}$$

with the Fourier coefficients given by:

$$w_{n\mathbf{R}}(\mathbf{r}) = \frac{V}{(2\pi)^3} \int_{BZ} d\mathbf{k}\; e^{-i\mathbf{k}\mathbf{R}} \psi_{n\mathbf{k}}(\mathbf{r}), \tag{2.60}$$

where V is the volume of the unit cell and the integration is done over the 1BZ. Note that Equation 2.59 is very similar to Equation 2.58, provided that ϕ is not necessarily a NAO but any other localized atomic function; and, $w_{n\mathbf{R}}(\mathbf{r})$ depends on $\mathbf{r}$ and $\mathbf{R}$ only through its difference $(\mathbf{r}-\mathbf{R})$ [99]. However, Wannier functions $w_{n\mathbf{R}}(\mathbf{r})$ differ from atomic orbitals $\phi(\mathbf{r}-\mathbf{R})$ in that Wannier functions form a complete orthogonal set.

2.6.1 Gauge freedom

The similarity of w functions to ϕ orbitals makes one think that Wannier functions are also well localized as atomic orbitals are. However, an important problem arises from the strong non-uniqueness of Wannier functions due to the freedom to apply any unitary transformation to Bloch orbitals at each $\mathbf{k}$, and still get another legitimate set of Bloch orbitals. For the case of a single separated band, a Bloch orbital in band n could be transformed as:

$$\tilde{\psi}_{n\mathbf{k}}(\mathbf{r}) = e^{i\varphi_n(\mathbf{k})}\psi_{n\mathbf{k}}(\mathbf{r}), \tag{2.61}$$

with $\varphi_n(\mathbf{k})$ being any real function with the reciprocal lattice periodicity. For the case of having a manifold of N bands, where many internal band crossings and degeneracies may occur, this set of unitary transformations can be expressed with the unitary matrix $U_{mn}^{(\mathbf{k})}$ [121]. And the resulting Bloch orbitals are then expressed as:

$$\tilde{\psi}_{n\mathbf{k}}(\mathbf{r}) = \sum_{m}^{N} U_{mn}^{(\mathbf{k})}\psi_{m\mathbf{k}}(\mathbf{r}). \tag{2.62}$$

The corresponding Wannier functions are then expressed as:

$$w_{n\mathbf{R}}(\mathbf{r}) = \frac{V}{(2\pi)^3}\int_{BZ} d\mathbf{k}\; e^{-i\mathbf{k}\mathbf{R}} \sum_{m}^{N} U_{mn}^{(\mathbf{k})}\psi_{m\mathbf{k}}(\mathbf{r}). \tag{2.63}$$

This freedom of obtaining equally valid Bloch orbitals by such unitary transformations is called 'gauge freedom'. As a result, the choice of the 'gauge' for the Bloch functions will result in different Wannier functions, and not all of them will be well localized, as we assumed in the previous section.

An important advance to solve this issue was first introduced by Marzari and Vanderbilt [121], where they imposed the condition of 'maximal localization' of the Wannier functions as the way of selecting a particular 'gauge' of Bloch functions. This method is based on the minimization of the spread functional with respect to the unitary transformations $U_{mn}^{(\mathbf{k})}$, which switching to the braket notation is written as:

$$\Omega = \sum_{n} \left[\langle n\mathbf{0}|\, r^2\, |n\mathbf{0}\rangle - \langle n\mathbf{0}|\, \mathbf{r}\, |n\mathbf{0}\rangle^2\right] = \sum_{n} \left[< r^2 >_n - < \mathbf{r} >_n^2\right]. \tag{2.64}$$

This minimization allows for extracting well-localized Wannier functions, which are called maximally localized Wannier functions (MLWFs). As a consequence, we will also have 'maximally smooth' Bloch functions in $\mathbf{k}$-space, which allow to interpolate any $\mathbf{k}$-dependent property up to virtually any arbitrarily fine $\mathbf{k}$-point grid. This procedure therefore offers a useful post-processing tool, implemented in the Wannier90 code [122], for first-principle

electronic structure calculations. It can be used to efficiently calculate many system properties, from electronic transport to the microscopic polarization of condensed matter. Moreover, as presented in this Thesis, the MLWFs can be used as basis functions for the construction of model Hamiltonians, for strongly correlated and magnetic systems. A more detailed description of the capabilities of MLWFs can be found in this Review [123]. Full details about the method can be found in the work of Marzari, Souza, and Vanderbilt [121, 124].

2.7 Ionic relaxations and transition states

In previous sections we explained how to solve the electronic Hamiltonian of Equation 2.4. Now we briefly comment on how to minimize the energy $E(\{\mathbf{R}\})$, that parametrically depends on atomic positions $\{\mathbf{R}\}$.

All of the electronic structure calculation codes that we have used in this Thesis (VASP, Quantum-Espresso, and FHI-aims), implement their own versions of known minimization algorithms based on the calculation of interatomic forces using the Hellman-Feynman theorem [125].

In this way one relaxes atomic positions so that the forces between atoms reach almost zero values and, at that point, we can say that the atomic structure is at its minimum of $E(\{\mathbf{R}\})$. However, there is no way of actually telling whether this minimum is a global minimum of the system or not. These algorithms are also unable to find saddle points in $E(\{\mathbf{R}\})$ that correspond to transition states between two local minima, and are of uttermost interest to analyze energetic pathways in chemical reactivity and phase transitions. The dimer [126] and the nudged elastic band (NEB) methods [127–129], are broadly used approaches designed to locate these transition state structures. Specifically, in this Thesis we have employed the NEB method.

2.7.1 Nudged elastic band method

The NEB method [127–129], is a useful tool for finding transition states and minimum energy paths (MEPs) between two known local minima (initial and final states). The method consists of setting an elastic band with $N+1$ images ($[\mathbf{R_0}, ..., \mathbf{R_N}]$), where the initial and final states are given by the local energy minima $\mathbf{R_0}$ and $\mathbf{R_N}$. The NEB method acts over the images with forces that are a sum of two components for each image i: The spring force along the tangent of the band $\mathbf{F}^k_{i\parallel}$, and the 'real' DFT calculated force perpendicular to the tangent $\mathbf{F}^r_{i\perp}$. So the total force is written as:

$$\mathbf{F}_i = \mathbf{F}^k_{i\parallel} + \mathbf{F}^r_{i\perp} = \mathbf{F}^k_{i\parallel} - \nabla E(\mathbf{R}_i)_\perp, \tag{2.65}$$

where the true force is represented as:

$$\nabla E(\mathbf{R}_i)_\perp = \nabla E(\mathbf{R}_i) - \nabla E(\mathbf{R}_i) \cdot \hat{\tau}_i, \tag{2.66}$$

where $E(\mathbf{R})$ is the electronic energy of the system for a given atomic configuration $\mathbf{R}$ and $\hat{\tau}_i$ is a normalized vector that points in the direction of the local tangent at image i. The spring force is represented as:

$$\mathbf{F}^k_{i\parallel} = k(|\mathbf{R}_{i+1} - \mathbf{R}_i| - |\mathbf{R}_i - \mathbf{R}_{i-1}|)\hat{\tau}_i. \tag{2.67}$$

The spring force ensures that images have a constant spacing between them, and the true force will bring the images towards a MEP where the saddle point is at. Note that to converge the MEP, the images must communicate the forces between them, so all the images need to be optimized simultaneously. An important limitation of the NEB method is that the actual saddle point hardly ever corresponds to any of the considered images and, therefore, the transition-state structures remains unknown.

The climbing-image nudged elastic band (CI-NEB) method [127] is a more refined approach that enables one to keep the shape of the MEP, but rigorously converge an image to the saddle point structure. The method consists of running a conventional NEB, and after some iterations identifying the highest energy image i_{max} (climbing-image). Then the force in this image is given by:

$$\begin{aligned}\mathbf{F}_{i_{max}} = -\nabla E(\mathbf{R}_{i_{max}}) + 2\nabla E(\mathbf{R}_{i_{max}})_\parallel = -\nabla E(\mathbf{R}_{i_{max}}) + \\ + 2\nabla E(\mathbf{R}_{i_{max}}) \cdot \hat{\tau}_{i_{max}} \hat{\tau}_{i_{max}}.\end{aligned} \tag{2.68}$$

Note that the climbing-image is no longer affected by spring forces. And the extra force $2\nabla E(\mathbf{R}_{i_{max}})_\parallel$ parallel to the tangent, makes the image to converge to the saddle point.

Chapter 3

Sodium-air Batteries

This chapter is devoted to investigating systems of interest for Na-air batteries. First we consider the study of discharge products consisting of sodium superoxide (NaO_2) small clusters, extended surfaces, and bulk material. Then we explore the solvation of Na ions in glyme solvents. This study allows us to understand the early stages of nucleation on discharge by analyzing the thermodynamical stability of small NaO_2 clusters, and their electronic structure. Also, the study of solvation effects of sodium ions provide fundamental understanding on the observed differences on the cyclability when using different glyme solvents on the electrolyte.

3.1 Introduction

Current Li-ion batteries are reaching their limit in terms of energy density. For example, typically, Li-ion batteries provide energy densities between 100 and 200 Wh/kg, and lifetimes of 1000 cycles [18, 130, 131]. These values hinder the development of 'urgent' technologies such as the EV. Taking into account that the energy density of gasoline is $\sim$ 13000 Wh/kg, and that the efficiency of an internal combustion engine is of 12.6%, the usable specific energy of gasoline is of 1700 Wh/kg [132]. This numbers, even considering the increase in efficiency of electricity driven motors [132], is too large for offering an efficient and cost-effective usage of commercial Li-ion batteries in EV applications.

Metal-air batteries are an attractive alternative to intercalation-based batteries because they can theoretically store far more energy than most competing technologies [133]. Unlike intercalation batteries, metal-air batteries uses the oxygen of the air (ideally), or an oxygen reservoir such as a tank, via an oxygen reduction reaction (ORR), and an oxygen evolution reaction (OER), that happens at the cathode support (typically carbon). In particular, the Li-air technology has received an increased research interest [134, 135], with many research groups trying to push forward this technology towards automotive

applications. A Li-air battery works by using a Li-metal anode, and reversibly forming and decomposing lithium peroxide (Li_2O_2) in the cathode. Li-metal has a theoretical energy density of 11680 Wh/kg, very close to gasoline, and in the discharged state Li_2O_2 has a theoretical energy density of around 3500 Wh/kg, which is an order of magnitude larger than that of Li-ion batteries and even larger than the effective 'tank-to-wheel' energy density from gasoline (1700 Wh/kg). Realistically, conservative estimates on the energy density of a practical Li-air battery suggest values around 450-600 Wh/kg. While these values are much lower than the theoretical ones, they are still promising, as they are good enough for a real EV battery. However, important technical challenges stop researches from unlocking the full potential of this technology [136].

On the one hand, superoxide and peroxide anions are extremely reactive, and essential components for the battery tend to decompose during cycling, especially the organic electrolytes [137, 138] and the carbon cathode support [139]. Shuttle effect of redox mediators and side reactions of contaminants in the air such as H_2O and CO_2 are also a source of parasitic reaction products that limit the safety, stability and cycle life of the battery [140–142].

On the other hand, there are problems related to the poor Coulombic efficiency due to high polarization effects, especially high charge overpotentials [27], that reduce the efficiency of the battery to quantities lower than 80% even using precious metal catalysts [143]. Another issue is that the overpotentials and charge-discharge capacities strongly depend on the charge-discharge rates [144], and usually the large capacities that are observed in Li-air cells are due to the low-rate operation of the battery. All these factors prevent Li-air batteries from reaching more than a few hundreds of cycles at acceptable rates [143], and, therefore, limit the overall energy density of a real Li-air battery.

Recent efforts to solve these issues have allowed increasing the cycle lifetime of Li-air batteries by careful tuning of the redox chemistry and selection of materials [145–147], but many of the problems are still present. These challenges have prompted a surge of research for alternatives to lithium. In particular, substitution of lithium by other alkali metals such as sodium [12] and potassium [148] has been given attention lately.

Interestingly, research on Na-air batteries has shown that they work similarly to Li-air batteries but some of the inherent problems of Li chemistry can be mitigated when replacing Li by Na. Na-air batteries are comprised of a Na-metal anode, a sodium conducting organic electrolyte, and carbon air cathode. The oxygen reduces at the cathode and reacts with solvated sodium ions to reversibly form sodium superoxide (NaO_2), in contrast to lithium peroxide (Li_2O_2).

$$Na^+ + O_2 + e^- \leftrightarrow NaO_2. \tag{3.1}$$

Note that the theoretical energy density of NaO_2 is of 1108 Wh/Kg. Despite

being three times smaller than Li_2O_2, it is big enough to be of technological interest, and is, in fact, the only plausible way of using sodium, alongside with very recent room-temperature Na-Sulfur batteries [24], for high energy density applications. Moreover, there are certain beneficial aspects that make Na-air batteries specially attractive, because they can potentially circumvent some of the base level problems with Li-air batteries. For instance, the chemistry of the cell is 'cleaner' in the Na-O_2 systems [27]. In Li-air batteries Li_2O_2 is the only thermodynamically stable product, whereas in the Na-air system, while sodium peroxide (Na_2O_2) is thermodynamically stable at ambient conditions the formation of NaO_2 is kinetically preferred [149], and should result in smaller overpotentials. Indeed, in 2013 Hartmann *et. al.* [23], successfully constructed a room temperature Na-air battery where NaO_2 was formed as the sole discharge product, with cubic particles of sizes between 1-50 μm. Those batteries worked surprisingly well, with very low charge-discharge overpotentials (< 100 meV), and high Coulombic efficiencies ($> 95\%$) [23, 150]. Na-air batteries immediately solve some of the issues with the Li-air technology, and could therefore retain more of their theoretical energy density. There are also some cost benefits to choosing sodium over lithium.

However, there are still important practical challenges to be solved: (i) understanding the formation of secondary sodium peroxide (Na_2O_2) and sodium peroxide dihydrate ($Na_2O_2{\cdot}2H_2O$) during discharge [150–153], (ii) electrolyte and carbon cathode decomposition by superoxide reactivity, (iii) decomposition of Na-metal anodes, (iv) understanding the ORR-OER reaction at the carbon cathode, (v) mitigating capacity loss and poor cylcability due to electrolyte interaction with O_2^- species. In this chapter we aim at providing new physical insights into some of these issues using DFT calculations.

In addition to their interest in metal-air batteries, alkali-metal superoxides are also interesting magnetic materials from a fundamental viewpoint [154–156]. The antibonding $2p$ molecular orbital of superoxide anions (O_2^-) enable NaO_2 to evince, for example, spin-orbital coupling, which is usually attributed to heavier elements than oxygen [157–159]. Some phases of NaO_2 could even be multiferroic as proposed by Solovyev and co-workers [160]. A common conclusion of these studies is that superoxides are, in general, strongly correlated $2p$ electron systems, with electronic and magnetic structures significantly affected by the relative orientation of O_2^- species within the crystal lattice. This originates a rich variety of spin orderings when considering different polymorphs or temperature dependence. In this chapter we will also analyze the magnetic properties of NaO_2 clusters and provide fundamental insight to better understand the magnetic properties of these $2p$ systems.

3.2 Energetic, electronic and magnetic properties of NaO_2

In Na-air batteries capacity loss is strongly related to the underlying crystal growth mechanism of the discharge product NaO_2. It is therefore important to clarify whether O_2 is reduced at the carbon cathode, or directly on NaO_2 surface sites [161]. Considering the former mechanism, the O_2^- anion should dissolve in the electrolyte and diffuse, to then form NaO_2 in solution, and precipitate onto the growing NaO_2 crystal. This dissolution and precipitation processes may involve small clusters in the nucleation and initial stages of crystal growth, and therefore, understanding the nature of the stabilizing interactions in these systems is of particular importance. On the contrary, if the latter mechanism is dominant, it would imply that NaO_2 has sufficient electrical conductivity, either intrinsic, or polaron based [162]. It is also important to note that electrical conductivity may occur at concrete levels of dimensionality, as has been predicted for Li_2O_2 [163]. In this section we examine therefore the electronic structure of a range of materials models including bulk, surfaces, and small clusters of NaO_2. And for comparison, we extend the study also to LiO_2 and KO_2 systems.

3.2.1 Computational methods

Spin-polarized DFT calculations have been performed using the PBE [57] functional and the HSE06 [69, 70] hybrid density functional with 25% of exact HF exchange. The VASP 5.3 code [110–113] has been used, where the core electrons have been replaced with PBE-based PAW potentials [107]. The Li ($2s^1$), Na ($2p^6 3s^1$), K ($3p^6 4s^1$), and O ($2s^2 2p^4$) electrons were explicitly treated as valence electrons, where their wavefunctions were expanded in plane waves with an energy cutoff of 500 eV. All geometries were relaxed with a residual force threshold of 0.02 eV/Å. The **k**-points in the 1BZ and the simulation cells used depend on the type of model used to calculate the relevant properties of interest.

Regarding the choice of the percentage of exact HF exchange (α), it is well known that adjusting its value can lead to improved calculated properties, especially bandgaps [164, 165]. For nonmetallic solids, a good ansatz is to obtain α as the inverse of the static dielectric constant [166–168]. Here, in order to asses the effect of the α on our results, the formation of energy of a $(NaO_2)_2$ dimer from the aggregation of two monomers (Figure 3.1a) and the simplest case of the HOMO-LUMO gap of a single NaO_2 monomer (Figure 3.1b), has been considered as function of α. Values of α ranging from 0.25 up to 0.48 have been considered, as previously proposed to describe bulk Li_2O_2 [169], and more recently also for Na_2O_2 and NaO_2 [170]. The formation

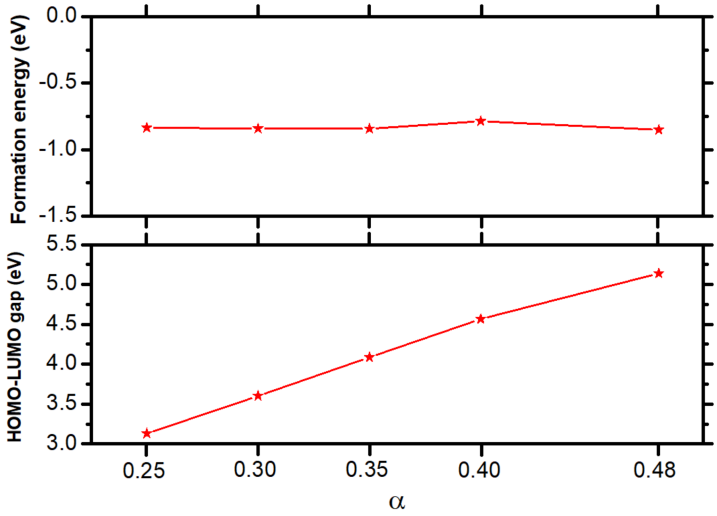

FIGURE 3.1: (a) Formation energy of a $(NaO_2)_2$ dimer and (b) HOMO-LUMO gap of a NaO_2 monomer as a function of α.

energy is shown to be rather insensitive to changes in α, with changes no bigger than 50 meV. Additionally, Figure 3.1b shows that the HOMO-LUMO gap increases linearly when increasing α, as usually observed [165]. Overall, given the lack of a clear reference for small $(NaO_2)_n$ clusters, and for the sake of settling a common calculation framework for all models (bulk, surfaces, and clusters), a value of $\alpha = 0.25$ has been chosen, which is routinely considered as the standard for HSE06 calculations.

3.2.2 Bulk NaO_2

Between 196 and 223 K, NaO_2 crystallizes in the cubic $Pa\bar{3}$ space group (pyrite phase), with O_2^- molecular bond axes parallel to the $\langle 111 \rangle$ directions as shown in Figure 3.2a. When heating above 223 K, O_2^- species freely rotate to have a $Fm\bar{3}m$ symmetry [171]. Such O_2^- disorder is then expected to occur in Na-air cells under working conditions. However, for simplicity, in this study the NaO_2 structures have been approximated to that of the ordered pyrite phase. The structure was optimized using a 5×5×5 **k**-point mesh, which ensures a convergence within 0.001 Å. And the magnetization was initialized ferromagnetically as 1 μ_B/O_2^-. The optimized equilibrium lattice parameters and atomic positions with PBE and HSE06 yield a cubic cell with lattice parameters ($a_{PBE} = 5.509$ Å and $a_{HSE06} = 5.487$ Å) close to the experimental value (5.460 Å) [171]. The O_2 bond lenghts are also very similar between the

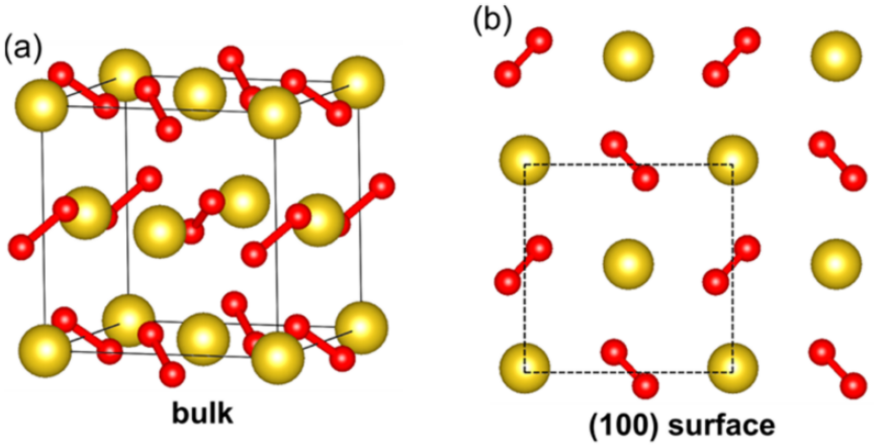

FIGURE 3.2: Optimized structures of (a) $Pa\bar{3}$ NaO_2 bulk, and (b) top view of a NaO_2(100) surface. Yellow and red spheres are Na and O atoms, respectively.

two functionals: 1.354 Å (PBE) and 1.326 Å (HSE06). However, the electronic structure between PBE and HSE06 differs significantly. Figure 3.3a shows the partial density of states (PDOS) projected onto the p orbitals of oxygen atoms using PBE. If one considers the molecular orbital (MO) diagram of the O_2^- molecule (Figure 3.3c) and following the simplified case for a NaO_2 monomer as shown in Figure 3.3d-e, the low-energy states that appear around 4.5 to 6.0 and 6.0 to 7.0 eV below the Fermi level (E_F) corresponds to σ_g- and π_u-like bonding MOs, respectively. The empty states above 4.2 eV are σ_u^*-like antibonding MOs, whereas the π_g^*-like antibonding MOs appears around the E_F. We see that NaO_2 is insulating in the spin-up channel, but spin-down π_g^*-like states form a narrow, half-filled band, which would make NaO_2 a half-metallic system. A similar electronic structure has already been reported by Solovyev *et. al.* using LDA calculations [172]. However switching to HSE06 (Figure 3.3b) splits the degeneracy of π_g^* states, resulting in one fully occupied band right below E_F and one empty state around 2.0 to 2.5 eV above it. This is twice as large as the calculation reported by Lee and coworkers [173].

Later calculations show that rotations of the O_2^- species, that lower the symmetry from $Pa\bar{3}$ to $Fm\bar{3}m$ because of room temperature operation, leave the bandgap of 2.0 eV nearly unchanged [174]. Moreover, other later calculations involving more advanced many body perturbation theory methods, such as the HSE-G0W0, push the bandgaps even further, up to 5.30 eV [170]. Therefore, these results predict an insulating character for bulk NaO_2, since intrinsic electron conduction at room temperature is not possible. Additionally, Yang

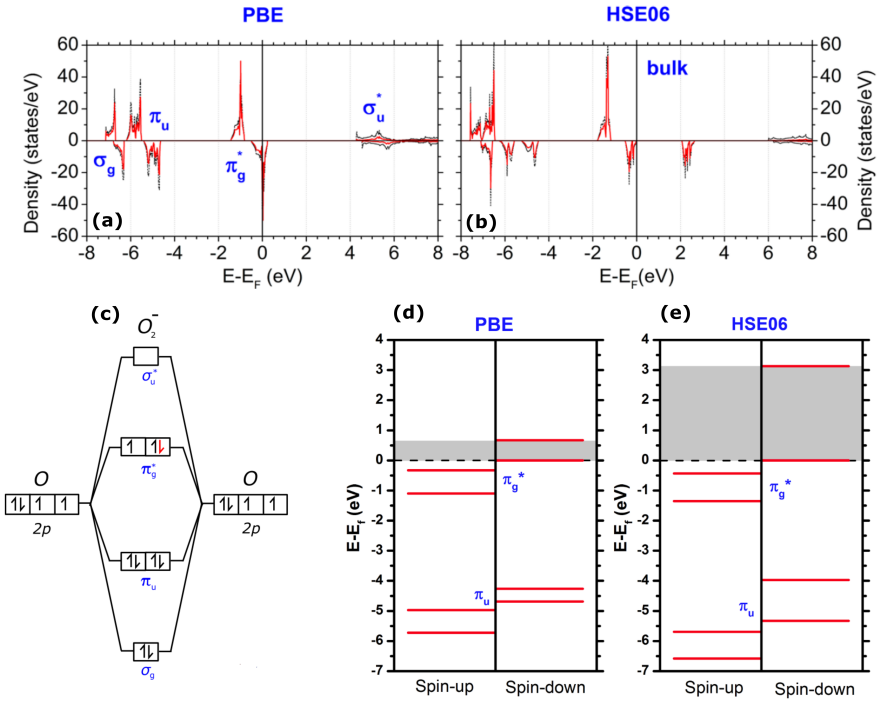

FIGURE 3.3: Density of states for bulk NaO_2 with the two considered functionals (a) PBE and (b) HSE06. The black dashed (red solid) lines are the total DOS (PDOS projected on the p states of oxygen atoms). Positive (negative) values correspond to spin up (down) states. (c) schematic representation of the MO diagram for a superoxide anion. The KS eigenstates of a NaO_2 monomer are represented using (d) PBE and (e) HSE06, where the energy zero is E_F. The gray band highlights the HOMO-LUMO gap.

et. al. [170] calculated the electronic conductivity through electron-hole polaron, and charged vacancy diffusion. Their calculations indicate that NaO_2 has a low electron-hole polaron conductivity, around 6-7 orders of magnitude smaller than what is estimated to be necessary to meet performance targets in Li-air cells [169]. Their results also indicate that charge transport through a combination of positive oxygen dimer vacancies and negative sodium vacancies, is 10 orders of magnitude higher than in Na_2O_2 or Li_2O_2. However, typical cathode supports for metal-air batteries, such as carbon, are ion-blocking which means that charge transfer in NaO_2 is not likely to occur through ion diffusion.

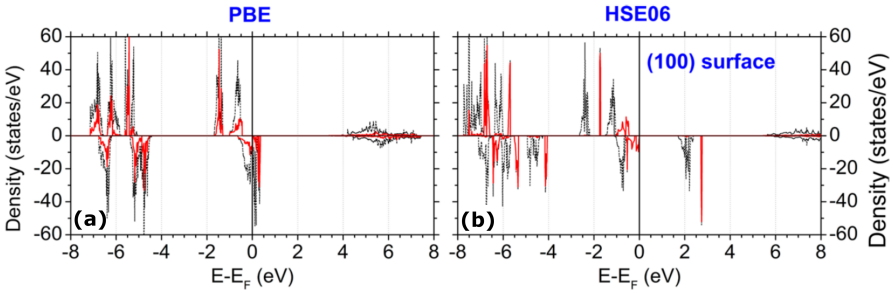

FIGURE 3.4: Density of states for the (100) surface of NaO_2 with the two considered functionals (a) PBE and (b) HSE06. The black dashed (red solid lines) are the total DOS (PDOS projected on the p states of oxygen atoms on the topmost surface layer). Positive (negative) values correspond to spin up (down) states.

3.2.3 (100) NaO_2 surface

Although we have shown that NaO_2 is a bulk insulator, surface states might still contribute to electronic conductivity. Conductive surface terminations have actually been proposed for stable surfaces of Li_2O_2 in Li-air batteries. Particularly, Radin *et.al.* [163, 169] identified non-stoichometric stable oxygen terminated (0001) and (1-100) surfaces, with conducting surface states. It is therefore interesting to examine if NaO_2 surfaces can also be conductive. Scanning Electron Microscopy (SEM) images from Hartmann *et. al.* [23], show that the discharge product of NaO_2 mainly consists of cube shaped particles, probably composed of stoichometric (100) facets. Indeed, Lee *et. al* [173] and Kang *et. al.* [175] reported that the stoichometric (100) is the most stable surface of pyrite NaO_2 at both oxidizing and reducing conditions. So we have calculated the electronic structure of the (100) surface.

A slab model cut along the (100) direction has been used (see Figure 3.2b), containing 5 atomic NaO_2 layers with the two bottom layers fixed at their bulk PBE-optimal positions. A vacuum of 14 Å has been considered between slabs along the 'c' direction. This ensures that spurious interactions between periodic images are negligible. It is noted that including more layers or larger vacuum regions does not significantly impact on the computed electronic properties. The **k**-point mesh used was 7×7×1 (5×5×1) for PBE (HSE06) calculations. The calculated layer-projected density of states (PDOS) using PBE is shown in Figure 3.4a. Like in bulk NaO_2, the spin-up states are insultaing, while the spin-down states show a half-metallic character. Moreover, the system is stabilized with ferromagnetic interactions arising from an unpaired π_g^* electron on each superoxide ion. Switching to HSE06, the insulating nature of the system is recovered (Figure 3.4b), with a bandgap for the three topmost

layers of the (100) surface (1.9 eV), which is very similar to that of the bulk phase (2.1 eV). This result suggests that the clean (100) surface is insulating as the bulk NaO_2. Note that for the surface O 2p states, a sharp peak appears at 2.7 eV above E_F, which indicates that the first layer not only is insulating but indeed helps to passivate the surface. Overall, this analysis reveals that particle morphologies that exhibit (100) surfaces [23], do not contribute to the conducting properties of NaO_2. Indeed it is shown by electrochemical atomic force microscopy (EC-AFM) experiments that when applying a bias to the cantilever tip in contact with the NaO_2 surface, no current is observed [174], which gives an experimental hint on the insulating nature of NaO_2; and reinforces the conclusion that a solution mediated discharge mechanism is more likely to occur, rather than a direct ORR on the NaO_2 surface.

It is useful to give a few caveats at this point. To begin with, although electronic conductivity through polaron hopping is small for both peroxide and superoxides, charged vacancy diffusion is about ten orders of magnitude higher for NaO_2 when compared to Na_2O_2. Due to the ion-blocking of the carbon support, this is not likely to be directly responsible for charge transfer. However, the concentration of carriers due to charged defects is also ten orders of magnitude higher in NaO_2 when compared to Na_2O_2 [170, 176]. The high concentration of charged carriers and fast ion kinetics in superoxides could, under operation conditions, facilitate desodiation from NaO_2, which could result in the formation of sodium poor phases ($Na_{1-x}O_2$) that could exhibit higher electronic conductivity, specially in the surface, as in the case of O-rich terminations in Li_2O_2 surfaces. On the other hand, our calculations and other works in the literature [170, 174, 176] only focus on the properties of NaO_2 but do not consider the carbon support, in particular the NaO_2/C interface is still rather unexplored. Among other things, the configuration of the NaO_2/C interface could result in band alignments such that electrons from the carbon cathode could be 'injected' into the conduction band of NaO_2 when an appropriate bias is applied, and therefore result in free electron transport.

In any case, the most straightforward conclusion supported by our calculations, and demonstrated by different experimental works [161, 174, 177–180] is that discharge products cannot form by direct ORR in the NaO_2 surface, but by a solution-mediated process where solvated NaO_2 agreggates precipitate on the carbon support forming the discharge products. Regarding oxidation of NaO_2 in the charge process, experimental results show conflicting conclusions. The work by Morasch *et. al.* [179] shows that NaO_2 oxidation occurs at the NaO_2/C interface, arguing that NaO_2 has sufficient electrical conductivity to allow for this. Lutz *et. al.* [180] with operando transmission electron microscopy (TEM) showed that in the charging process the dissolution of NaO_2 cubes starts from the outer part of the cube (interface between NaO_2 and electrolyte) and the size of the cubes steadily decrease. Our work and others [170, 173, 174, 176] support the latter conclusion. Because of the low electrical conductivity and high solubility of NaO_2 the most probable scenario is

a solution-mediated charging process. However, other possible mechanisms, such as sodium poor phases that enhance conductivity or the effect of band alignment in the NaO_2/C, which has not been studied theoretically and may have not been observed experimentally could still play a role in the charging mechanism proposed by Morasch *et. al.* [179].

3.2.4 Small NaO_2 clusters

From the previous discussions, we deduced that the most probable scenario is that the discharge happens by electrochemically produced NaO_2 soluble species, where, after saturation of the electrolyte small NaO_2 nuclei form on the electrode surface in the form of small $(NaO_2)_n$ clusters. Then, larger cubes are form by continuous deposition of NaO_2 species on the clusters [180]. The size and shape of these clusters might then significantly affect the electrochemical performance of Na-air batteries. Also, it is known that nanosized crystals often help to reduce transport path lengths or enhance electric field distributions [30]. Therefore, it is important to obtain physical insight into the stabilizing interactions between O_2^- and Na^+ species in small $(NaO_2)_n$ clusters, which govern the cluster geometries that ultimately control the particle morphology of the discharge products in Na-air batteries. In order to better analyze these interactions we also considered Li and K alkali metal ions to compare the properties of $(LiO_2)_n$ and $(KO_2)_n$ clusters with those of $(NaO_2)_n$. In particular, we focus on examining if reducing the dimensionality of these systems results in a reduction of the bandgap, enhancing their electronic conductivity. Additionally, we also took the chance to investigate other outstanding questions regarding the accurate description of highly correlated $2p$ electron systems within DFT, which are relevant to better understand interesting magnetic phenomena.

A. Geometries

We considered a range of alkali-metal superoxide clusters, $(MO_2)_n$ (M = Li, Na, and K, with n = 2-10) periodic models. To this end, variable cell shapes and sizes to accommodate each cluster have been used, so that a minimum vacuum of 10 Å is ensured as the separation between clusters of neighboring cells. All the calculations were performed at the Γ point and the formation energies were corrected with the zero-point energy (ZPE), computed from harmonic vibrational frequencies, which were calculated numerically by building the Hessian dynamical matrix through finite displacements of ±0.01 Å from the optimized structures. The rest of computational details can be found in Subsection 3.2.1. Following a previous study by Das *et. al.* [181], two main groups of structures have been considered: planar-ring and non-planar clusters. Non-planar clusters were generated by stacking planar-ring structures

or by considering bulk-truncated MO_2 geometries. Figure 3.5 shows all the computed clusters with their optimized lowest energy configurations. The notation used to label the non-planar clusters is $(MO_2)_n$-x×y(bulk), indicating that the cluster has been constructed from stacking planar-ring clusters of sizes x and y (trimming of the bulk structure). Figure 3.5 also shows the sizes of the computational boxes that were used in the calculations.

Regarding the spin states of the clusters, the coupling of the n unpaired electrons on the singly occupied π_g^*-like O_2^- orbitals (see Figure 3.3c-d-e) generates states with a ground-state spin projection along the quantization axis 'z', M_s. M_s values range from 0 to $n/2$ in the case of even n values and from 1/2 to $n/2$ in the case of odd n values. According to the topology and ferro/antiferromagnetic nature of the coupling between O_2^- species, M_s can take any value in this range. We found that the cluster geometries were nearly insensitive to different choices of M_s, and their relative energies were also very similar (<5 meV), with a few exceptions as shown in Figure 3.6. In general, the lowest-energy solution was the one with the smallest M_s value. From now on, we will only consider the most stable solution for each $(MO_2)_n$ cluster.

Looking at the structures of Figure 3.5 it is generally observed that optimized clusters generated by stacking planar rings of different sizes show more asymmetric structures than that of stacked rings of equal size. However, when changing the alkaline ion, the geometries of $(MO_2)_n$ clusters are qualitatively similar between them. For planar clusters, O_2^- species tend to be aligned in the direction normal to the plane of the cluster. On the other hand, O_2^- species in non-planar clusters are tilted, resulting in more compact, bulk-like structures. Another observation is that $(LiO_2)_n$ clusters are, in general, less symmetric than equivalent $(NaO_2)_n$ or $(KO_2)_n$ clusters. The selection of the exchange correlation functional does not significantly alter the geometries of the clusters either. For instance, differences between the PBE and HSE06 methods for O-O, M-O, and M-M distances are less than 0.05 Å.

Regarding the effect of the cluster size in the interatomic distances, is first observed that superoxide species are basically unperturbed by the cluster size, with O-O distances being nearly constant ($\sim$ 1.3 Å) as a function of the number of MO_2 monomer units within the cluster. In contrast, M-O and M-M interatomic distances (R_{M-O} and R_{M-M}, respectively) have a strong dependence with the cluster size. Figure 3.7 shows the mean R_{M-O} and R_{M-M} distances as a function of n for each alkali metal (M = Li, Na, and K). Looking at the planar-ring clusters one can see that R_{M-O} quickly increases with n up to $n = 3$, then it becomes nearly constant at around 1.9 Å for the increasingly sized clusters. Similarly, R_{M-M} also increases with the cluster size, but does not reach any constant value before the largest cluster size considered with HSE06 ($n = 8$). In the case of non-planar clusters, due to their antisymmetric nature, R_{M-O} and R_{M-M} show a more irregular dependence with cluster size n, when compared with planar rings. It is interesting to

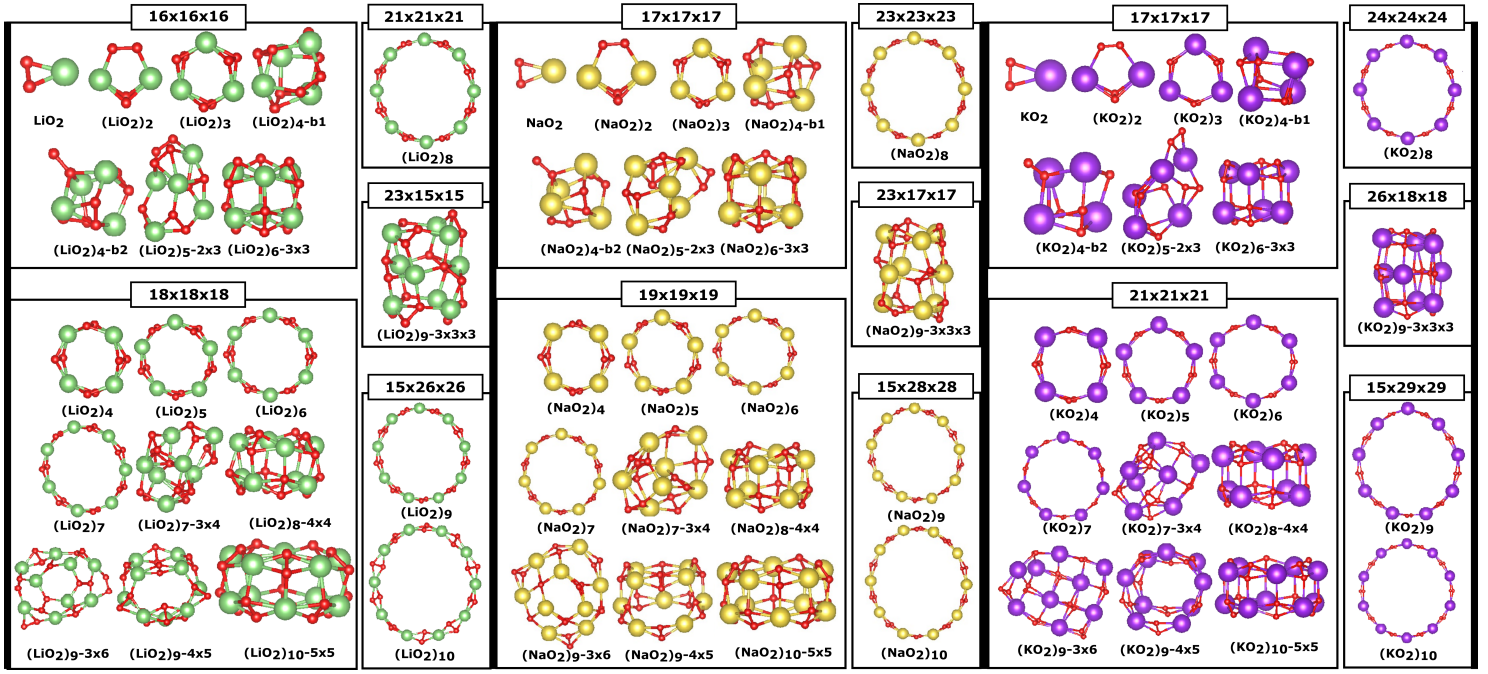

FIGURE 3.5: Optimized structures for the cluster models of (a) LiO_2, (b) NaO_2, and (c) KO_2. O atoms are shown in red. The dimensions of the simulation box are given above each group of clusters.

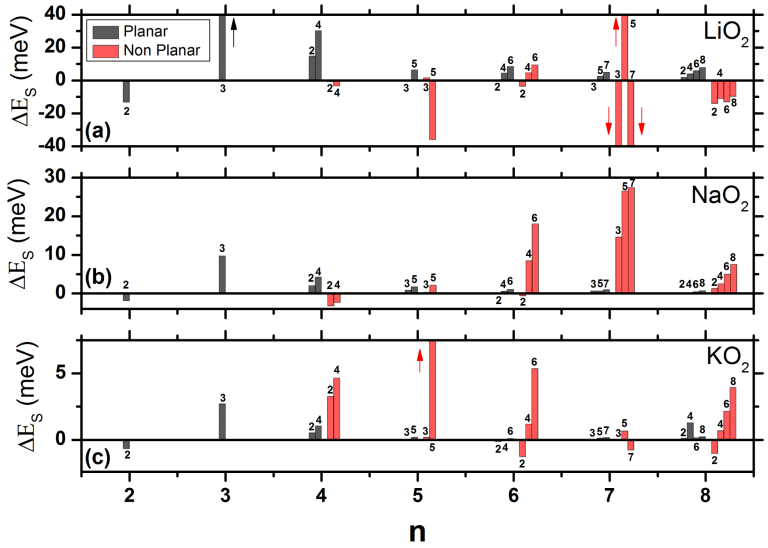

FIGURE 3.6: Energy differences among possible M_s values for $(LiO_2)_n$ (a), $(NaO_2)_n$ (b), $(KO_2)_n$ (c) as a function of the cluster size (n) using HSE06. The smallest M_s value 0 (1/2) for even (odd) values of n, is taken as the reference. Values for planar (non-planar) clusters are shown in black (red) bars. The numbers above or under the bars indicate the magnetization for each calculation.

note that non-planar cluster distances, R_{M-M} and R_{M-O} are closer to bulk distances than those of planar rings, as shown in Figures 3.7c-d for $(NaO_2)_n$ clusters. This is consistent with the fact the planar-rings are not compatible with the building blocks of MO_2 bulk, while non-planar geometries yield bulk-like structures.

B. Formation energies

In order to better understand the role of cluster size and morphology on the energetics and stabilizing interactions of the clusters, we considered the aggregation formation energy of n MO_2 to form a $(MO_2)_n$ cluster as:

$$E_f = \frac{E_n}{n} - E_1, \tag{3.2}$$

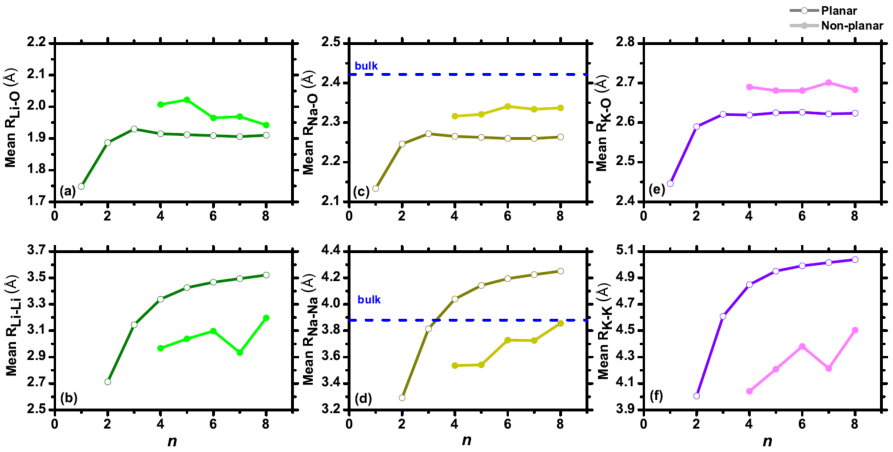

FIGURE 3.7: Interatomic distances R_{M-O} ((a), (c), and (e)) and R_{M-M} ((b), (d), and (f)) of optimized planar and non-planar $(MO_2)_n$ clusters using HSE06. Reprinted from *J. Chem. Phys.* **146**, 184301 (2017) [182], with the permission of AIP Publishing.

where E_n and E_1 are the total energies of a $(MO_2)_n$ cluster and a MO_2 monomer, respectively. Table 3.1 shows E_f of the most stable $(MO_2)_n$ planar-ring and non-planar clusters using both PBE and HSE06. Essentially, PBE and HSE06 yield very similar formation energies for $(NaO_2)_n$, $(KO_2)_n$ and planar-ring clusters; the largest difference being 65 meV/MO_2. Non-planar $(LiO_2)_n$ clusters present slightly larger differences up to 90 meV/(LiO_2).

The ZPE correction is calculated as:

$$E_f^{ZPE} = \frac{1}{n}(E_n + \frac{1}{2}\sum_i \hbar\omega_i) - (E_1 + \frac{1}{2}\sum_i \hbar\omega_i'), \tag{3.3}$$

where $\hbar\omega_i$, and $\hbar\omega_i'$ are the vibrational energies of the $(MO_2)_n$ clusters and MO_2 monomer, respectively. ZPE corrections increase the formation energies of $(NaO_2)_n$ clusters by around 20-40 meV/(NaO_2), as can bee seen in Table 3.1.

Figure 3.8 shows E_f as a function of the number on of MO_2 monomer within the cluster using HSE06. An important general observation is that the clusters become more stable as the cluster size increases. These results are consistent with the calculations on $(LiO_2)_n$ clusters (n = 1-12, 16, 18) reported by Das *et. al.* [181] and indicates a cooperative effect, this is to say, the number of M-O_2 bonds within the clusters further stabilizes the clusters themselves. It is

	PBE		HSE06	
Cluster	Planar	Non-Planar	Planar	Non-Planar
LiO_2	0		0	
$(LiO_2)_2$	-0.783		-0.718	
$(LiO_2)_3$	-1.100		-1.094	
$(LiO_2)_4$	-1.223	-1.089	-1.246	-1.058
$(LiO_2)_5$	-1.288	-1.295	-1.308	-1.205
$(LiO_2)_6$	-1.319	-1.209	-1.344	-1.271
$(LiO_2)_7$	-1.339	-1.342	-1.366	-1.290
$(LiO_2)_8$	-1.351	-1.277	-1.380	-1.349
NaO_2	0		0	
$(NaO_2)_2$	-0.831 (-0.819)		-0.837 (-0.824)	
$(NaO_2)_3$	-1.203 (-1.178)		-1.232 (-1.209)	
$(NaO_2)_4$	-1.317 (-1.292)	-1.266 (-1.245)	-1.349 (-1.327)	-1.272 (-1.250)
$(NaO_2)_5$	-1.368 (-1.343)	-1.341 (-1.321)	-1.402 (-1.379)	-1.332 (-1.307)
$(NaO_2)_6$	-1.394 (-1.369)	-1.429 (-1.407)	-1.429 (-1.407)	-1.422 (-1.404)
$(NaO_2)_7$	-1.411 (-1.386)	-1.478 (-1.456)	-1.447	-1.493
$(NaO_2)_8$	-1.422	-1.477 (-1.456)	-1.458	-1.504
KO_2	0		0	
$(KO_2)_2$	-0.636		-0.644	
$(KO_2)_3$	-1.002		-1.039	
$(KO_2)_4$	-1.079	-1.082	-1.120	-1.117
$(KO_2)_5$	-1.111	-1.110	-1.154	-1.132
$(KO_2)_6$	-1.127	-1.209	-1.171	-1.259
$(KO_2)_7$	-1.136	-1.240	-1.181	-1.285
$(KO_2)_8$	-1.142	-1.263	-1.187	-1.316

TABLE 3.1: Formation energies in $eV/(MO_2)$ of $(MO_2)_n$ clusters using PBE and HSE06 functionals. ZPE corrected values are shown in parenthesis.

also interesting to note that cooperative effects occurs for all three alkali-metal superoxide clusters.

Another observation is that small clusters prefer to form planar-ring structures, however, non-planar clusters become more stable above a certain value

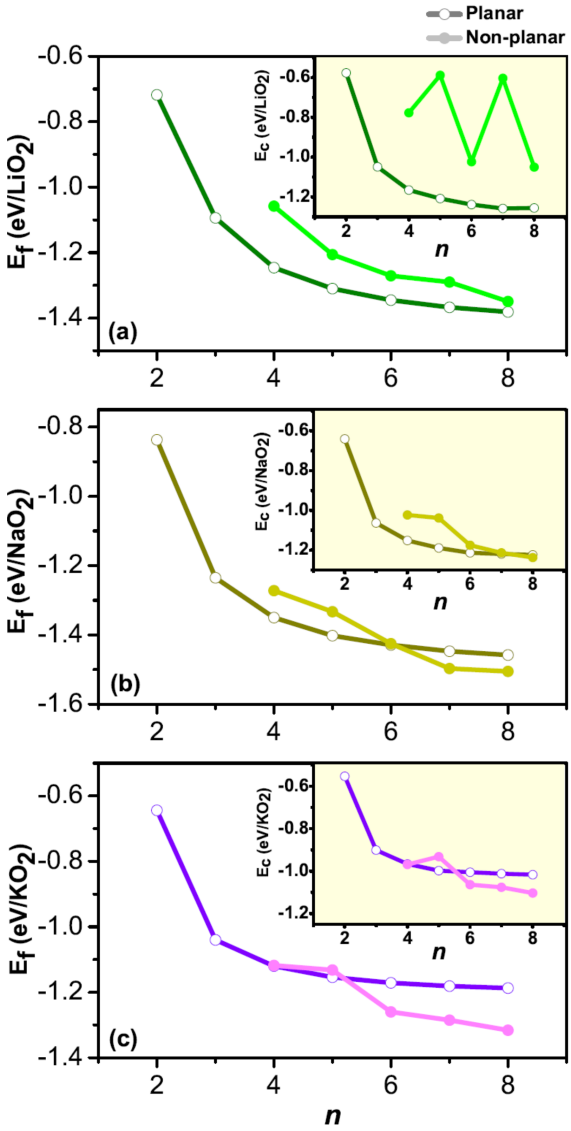

FIGURE 3.8: Formation energies of (a) $(LiO_2)_n$, (b) $(NaO_2)_n$, and (c) $(KO_2)_n$ clusters using HSE06 as a function of the number of MO_2 units (n) within each cluster. The insets show the corresponding Coulomb energy (E_C) as computed using Eq. (1.3). Reprinted from *J. Chem. Phys.* **146**, 184301 (2017) [182], with the permission of AIP Publishing.

of n. Interestingly, the location of this crossover point depends on the nature of the chosen alkali metal. For instance, one can see in Figure 3.8b that non-planar $(NaO_2)_n$ clusters onset at $n = 6$, while planar ring $(LiO_2)_8$ clusters still remain more stable than their non-planar counterparts (3.8a). This preference for non-planar structures appears earlier in $(MO_2)_n$ clusters with alkali metals of larger radii: $(KO_2)_n > (NaO_2)_n > (LiO_2)_n$.

A possible way of rationalizing this behavior is to analyze the highly ionic M-O_2 bonding from an electrostatic viewpoint. To this end, we computed the Coulomb formation energy, E_C of an $(MO_2)_n$ cluster as:

$$E_C = \frac{1}{n} \sum_{i>j} \frac{q_i q_j}{4\pi\epsilon_0 r_{ij}} - E_{C1}, \tag{3.4}$$

where q is the charge of $M^{\delta+}$ and $O^{\delta-}$ species, r is the distance between each pair of species within a cluster, and ϵ_0 is the vacuum dielectric constant. Because of the molecular character of O_2^- the repulsive intramolecular O-O interaction was purposefully eliminated. We use the Bader partitioning scheme [183–186] to compute q: $M^{0.8+}$ and $O^{0.4-}$. We found that these charges are rather insensitive to the cluster size and geometry and, therefore, the same values were used to calculate E_C for all of the clusters considered. The insets of Figure 3.8 show the values of E_C as a function of n for $(LiO_2)_n$, $(NaO_2)_n$, and $(KO_2)_n$ clusters. Generally, the value of E_C becomes increasingly negative with the size of the clusters, following a similar behavior to that of E_f, especially in the case of $(KO_2)_n$, $(NaO_2)_n$, and planar-ring $(LiO_2)_n$ clusters. Notice that the behavior of E_C of non-planar $(LiO_2)_n$ clusters is much more irregular with n, when compared to their sodium and potassium counterparts. The same happens with the values of E_f of non-planar $(LiO_2)_n$ clusters when using the PBE functional. In contrast, it seems that the exact exchange fraction included in HSE06 improves the description of the stability of non-planar lithium superoxide clusters.

These results indicate that electrostatics govern the stabilizing effect of increasing cluster size, as evidenced by the linear correlation shown in Figure 3.9. Notice that the green points in Figure 3.9 follow a much worse correlation when compared to $(NaO_2)_n$ and $(KO_2)_n$ clusters. So the stabilizing interactions in LiO_2 are a bit more complex than pure classical electrostatics. One can see that the electrostatic curves of planar-ring and non-planar clusters also have a crossover point for $(NaO_2)_n$ and $(KO_2)_n$ systems. As said, in the case of $(LiO_2)_n$ clusters, the situation is more complex, although it is clear that the crossover point should occur beyond $n = 8$. Additionally, the location of such crossover shows a similar trend to that analyzed for E_f curves: $(KO_2)_n > (NaO_2)_n > (LiO_2)_n$. It is clear, then, that for the most part, electrostatic interactions control the relative stability of planar-ring (2D) and non-planar (3D) clusters. As seen in Figure 3.7, the bigger the n, the larger the interatomic M-O distances and, as a consequence, the balance between attractive

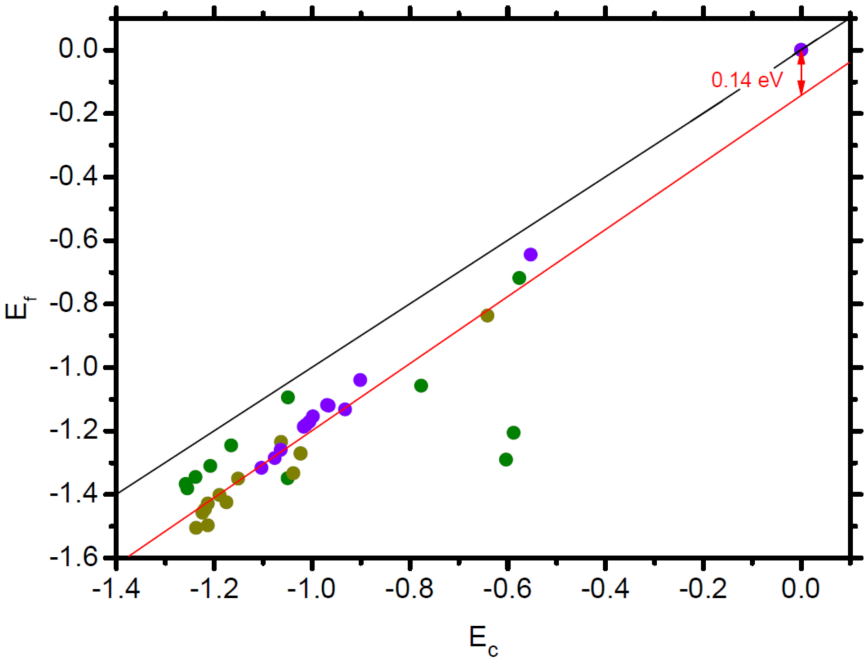

FIGURE 3.9: Formation energies calculated with HSE06 plotted versus electrostatic formation energies of point Bader charges (in eV/MO_2). Color code: Na in yellow, Li in green, and K in purple. The linear fit of all the points is shown in red whereas the expected correlation of a purely ionic cluster is shown in black.

and repulsive electrostatic interactions within the clusters of different geometries is altered. This balance can also be influenced by the choice of the alkali metal; in particular, larger alkali metals (such as K) have a stronger preference for forming 3D structures earlier than smaller ones (such as Li).

Regarding the relative magnitude of formation energies, $(NaO_2)_n$ clusters yield larger values than those of $(LiO_2)_n$ and $(KO_2)_n$ clusters, as can be seen in Table 3.1, with differences ranging from 0.08 to 0.27 eV/(MO_2). Such behavior is also a consequence of the electrostatic interactions governing the stability of the clusters. As can be seen in the insets of Figure 3.8, in general, the Coulomb energies of the $(NaO_2)_n$ clusters are systematically lower than those corresponding to $(LiO_2)_n$ and $(KO_2)_n$ clusters, especially in the case of non-planar clusters. Interestingly, these results suggest therefore that the electrostatic balance between $M^{\delta+}$ and $O^{\delta-}$ species is optimal for $(NaO_2)_n$ clusters.

C. Electronic and magnetic properties

After having analyzed the impact of cluster size and morphology in the previous section, we now focus on the electronic and magnetic properties. In this case, only $(NaO_2)_2$ clusters are analyzed. For studying the electronic properties, we computed the DOS of NaO_2 with DFT. And for the magnetic properties, the magnetic exchange coupling constants, J, where calculated between molecular magnetic centers O_2^- species using DFT and wave-function theory (WFT) calculations. For the sake of simplicity, magnetic properties were only calculated on $(NaO_2)_4$ clusters, where the effect of cluster morphology was examined by considering both planar-ring and non-planar structures. First we present the calculations done with DFT and then we discuss the WFT results. Finally, we provide a general overview and comparison between the two approaches.

DFT calculations: Looking at the DOS of non-planar $(NaO_2)_4$, $(NaO_2)_5$, $(NaO_2)_6$, $(NaO_2)_7$, and $(NaO_2)_8$ clusters (see Figure 3.10), it is possible, as in the case of the NaO_2 monomer (Figure 3.3), to classify the peaks as π_g^*, π_u, and σ_g-like orbitals. A key observation that differs from the case of the monomer is that, when using PBE for all non-planar clusters, the π_g^* orbitals around E_F range between -2 eV and 0.5 eV, having half-filled spin-down states with negligible HOMO-LUMO gaps, which leave the non-planar NaO_2 clusters half metallic. Switching to HSE06, however, the π_g^* spin-down states lift their degeneracy, resulting in fully occupied states right below E_F and placing the unnocupied states at 2.0-2.3 eV for non-planar $(NaO_2)_4$, $(NaO_2)_6$, $(NaO_2)_7$, and $(NaO_2)_8$. It is noted that for the $(NaO_2)_5$ a slightly lower HOMO-LUMO gap of 1.3 eV is predicted. This behavior is similar to that of NaO_2 bulk and (100) surfaces (see Figures 3.3a-b and 3.4), which further suggests the bulk-like behavior of non-planar $(NaO_2)_n$ clusters.

Planar clusters on the other hand, differ significantly from the non-planar ones in their electronic structure. Looking at the DOS of planar-ring $(NaO_2)_4$, $(NaO_2)_5$, and $(NaO_2)_6$ (see Figure 3.11); in all cases, PBE already splits the π_g^*-like states, opening a gap of approximately 0.5 eV (similar to the NaO_2 monomer). Using the HSE06 functional further broadens the separation between these levels from 0.5 to 3 eV, which is 1 eV more than the computed HOMO-LUMO gaps of non-planar clusters. Therefore, regarding the electronic conductivity of small $(NaO_2)_n$ clusters, our results predict that reducing the dimensionality of these systems does not help improving their intrinsic electronic conductivity and, therefore, the discussion of Subsections 3.2.2 and 3.2.3 still holds for small clusters.

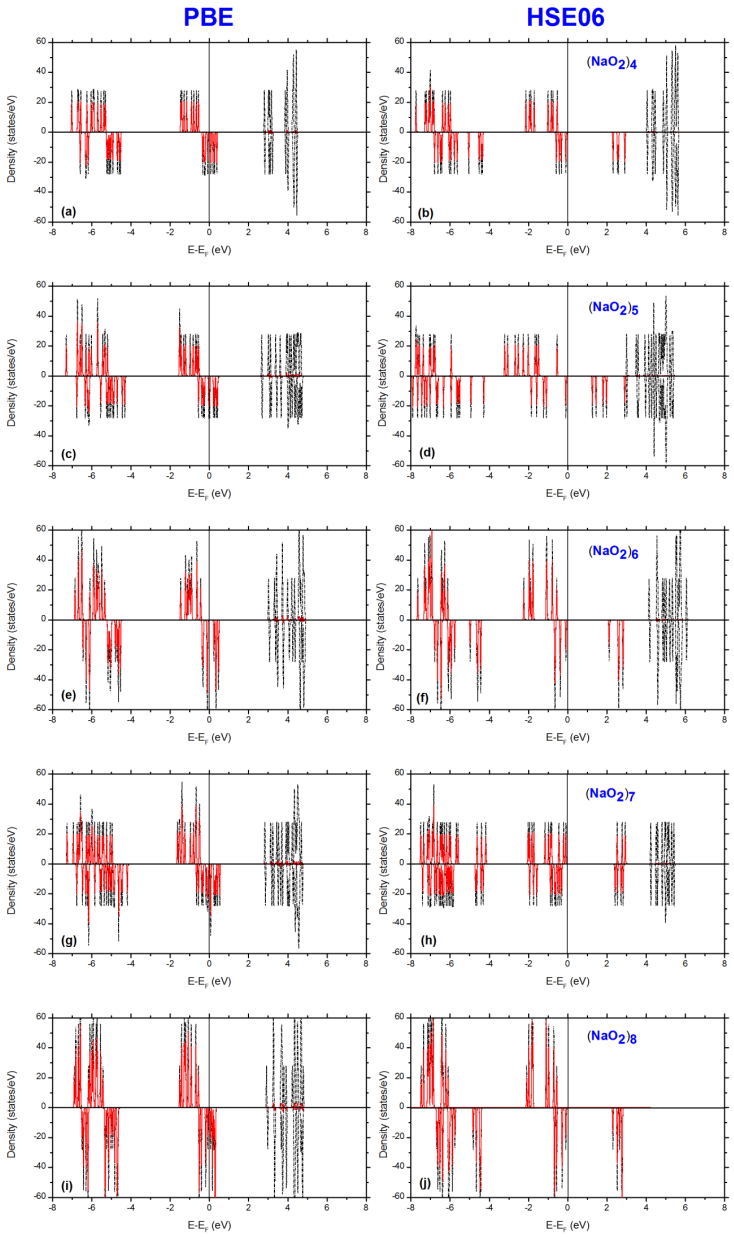

FIGURE 3.10: Density of states of non-planar $(NaO_2)_n$ clusters. (a,b) $(NaO_2)_4$ cluster, (c,d) $(NaO_2)_5$, and (e,f) $(NaO_2)_6$, (g,h) $(NaO_2)_7$, and (i,j) $(NaO_2)_8$ clusters. Red solid lines are the PDOS projected on the p orbitals of oxygen. Positive (Negative) values for spin up (down) states. PBE (HSE06) in the left (right) columns.

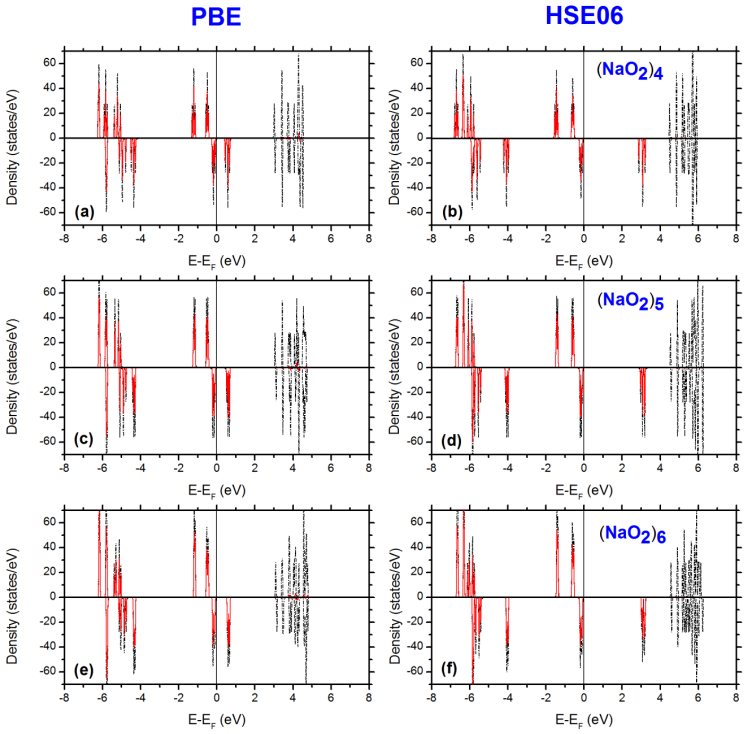

FIGURE 3.11: Density of states of planar-ring $(NaO_2)_n$ clusters. (a,b) $(NaO_2)_4$ cluster, (c,d) $(NaO_2)_5$, (e,f) $(NaO_2)_6$. Red solid lines are the PDOS projected on the p orbitals of oxygen. Positive (Negative) values for spin up (down) states. PBE (HSE06) in the left (right) columns.

Moving now to the analysis of the magnetic structure of $(NaO_2)_4$ clusters, it is noted that magnetic interactions in the system arises from the unpaired electron lying in π_g^*-like MOs. These MOs are well localized on O_2^- species. Indeed, when continuously adding MO_2 monomers, O states never hybridize which leads to nearly degenerated MOs. Especially, planar-ring clusters show sharp peaks in the same positions as the O $2p$ states in the NaO_2 monomer (see Figure 3.3), and a narrow energy dispersion of less than 0.4 eV (see Figure 3.11). Following the strategy proposed by Solovyev *et. al.* [172] eight MLWFs associated to each of the π_g^*-like MOs were constructed using PBE, for both planar-ring and non-planar $(NaO_2)_4$ clusters. The construction of MLWFs [121, 123, 124] was performed using the Wannier90 code [122] with the VASP2WANNIER90 interface implemented in VASP. The wannierization procedure was initialized using random projections, with the energy windows

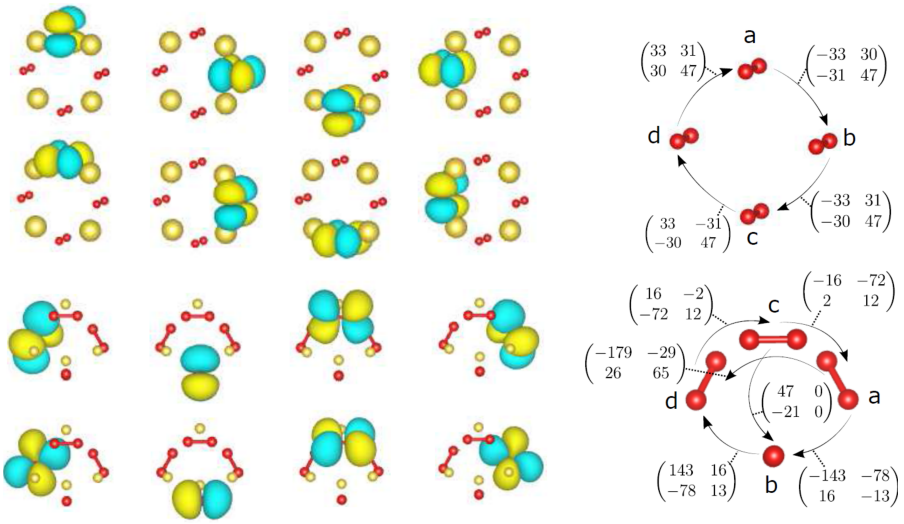

FIGURE 3.12: Representation of the eight MLWFs extracted from the π_g^*-like MOs in planar-ring (first two rows) and non-planar (third and fourth row) geometries. And transfer integrals (in meV), $t_{ij}^{pp'}$, on each $i-j$ bond (where $i, j = a, b, c, d$, and $i \neq j$) between $p-p'$ MOs of O_2^- species for planar-ring (top right) and non-planar (bottom right) clusters. The superoxide molecules involved in the electron transfer are schematically represented using arrows. The observed slight inequalities between the off-diagonal elements of all $t_{ij}^{pp'}$ matrices in the planar case and $t_{ad}^{pp'}$ in the non-planar case are due to small distorsions of the structure with respect to fully symmetric geometries, which occurred during DFT geometrical optimization and the underlying incapability of the wannierisation procedure to set the centers of the MLWFs in the exact molecular centers. Reprinted from *J. Chem. Phys.* **146**, 184301 (2017) [182], with the permission of AIP Publishing.

set so as to include all π_g^*-like states. The outputs are eight, well converged and well localized MLWFs, with a total spread of 9.8 (9.9) Å^2 for planar (non-planar) clusters, as can be seen in Figure 3.12. Then, the PBE Hamiltonian matrix elements were represented on the basis of the calculated MLWFs. This gave information about the 'molecular field', MF, (site diagonal elements) and the transfer integrals (off-diagonal elements) which allowed us to characterize a non-periodic Hubbard-type Hamiltonian as:

$$\hat{H} = \sum_{i \neq j, \sigma} \sum_{p,p' = \pi_g^*, \pi_{g'}^*} t_{ij}^{pp'} \hat{a}_{i\sigma p}^{\dagger} \hat{a}_{j\sigma p'} + \hat{H}_0, \tag{3.5}$$

where $\hat{H}_0 = \hat{H}_{MF} + \hat{H}_U$ contains the on-site terms of the MF splitting ($\hat{H}_{MF}$), given by:

$$\hat{H}_{MF} = \sum_{i,p,\sigma} \Delta_{ip}\ \hat{a}^{\dagger}_{i\sigma p}\hat{a}_{i\sigma p}, \tag{3.6}$$

where the summation runs over all sites and orbitals, and the Hubbard interaction ($\hat{H}_U$), which is given by:

$$\hat{H}_U = U \sum_{i,\sigma\neq\sigma',p} \hat{n}_{i\sigma p}\hat{n}_{i\sigma' p} + U' \sum_{i,\sigma\neq\sigma'} \sum_{p<p'} \hat{n}_{i\sigma p}\hat{n}_{i\sigma' p'} + \\ + (U' - J_H) \sum_{i,\sigma} \sum_{p<p'} \hat{n}_{i\sigma p}\hat{n}_{i\sigma p'}. \tag{3.7}$$

Here $\hat{a}^{\dagger}_{i\sigma p}$ ($\hat{a}_{j\sigma p'}$) are the creation (annihilation) operators acting at sites i (j) on Wannier orbitals, which include the spin (σ and σ') and orbital (p and p') degrees of freedom. The term $\hat{n}_{i\sigma p}$ represents the particle number operator, whereas Δ_{ip} is the value of the energy of the orbital p at site i, with respect to the most stable one, whose Δ_{ip} value is set to zero. Later in this Thesis more details about the construction of Hubbard Hamiltonians and their solutions will be given, for now it is enough to note that the one-body parts of Equation 3.5, i.e., the transfer integrals $t_{ij}^{pp'}$ and $\hat{H}_{MF}$, contain all the interactions which are present in DFT for the target bands. The transfer integrals are defined as $t_{ij}^{pp'} = \langle W_i^p | \hat{H}_{PBE} | W_j^{p'} \rangle$, where W_i^p represents the MLWFs that are associated with their corresponding π_g^*-like MOs. These transfer integrals are 2×2 matrices representing electron hoppings between two O_2^- molecular sites $i - j$ and MO pairs $p - p'$ of π_g^* symmetry, as defined in Figure 3.12. On the multi-orbital case, the Kanamori parameters are included [187], which represent the on-site intra- and inter- orbital Coulomb interactions U and U', accounting for the electron-electron repulsion when electrons at the same site occupy the same (intra) or different (inter) orbitals. The intra-molecular exchange interaction J_H is also included. Solovyev and Imada [188] showed that U can be obtained by combining constrained local density [189–192] and random phase [193] approximations (cLDA-RPA). For the case of the $Pa\bar{3}$ phase of NaO_2, the computed on-site parameters have the values of U = 3.65 eV and J_H = 0.61 eV. For such highly symmetric systems, the Coulomb interactions on orbitals of π_g^* symmetry are expected to be the same, this leads to Kanamori parameters that are linked by an identity, $U' = U - 2J_H$. For lower symmetry phases of NaO_2 bulk, such as the marcasite phase (Pnnm space group), Solovyev *et. al.* showed that even in this case, the Coulomb interactions of the π_g^*-like orbitals, which are expected to be different, do not change in more than 1% and can be neglected. Therefore, we approximated the Kanamori parameters (U, U', and J_H) of $(NaO_2)_4$ clusters to that of the $Pa\bar{3}$ phase.

PBE was used as a starting point to parameterize the one body part of the Hubbard Hamiltonian. This is because when adding some on-site Coulomb

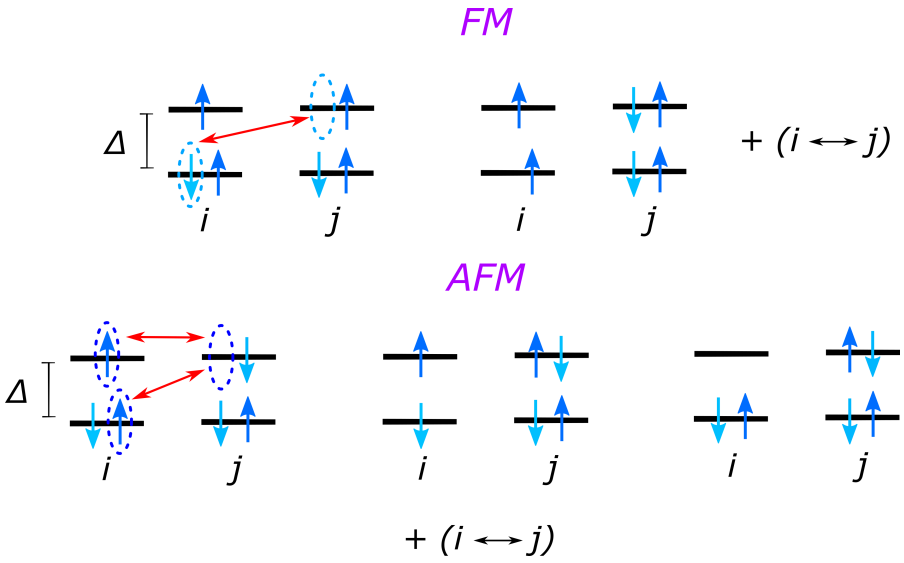

FIGURE 3.13: Scheme representing the ground state and excited state configurations on the process of hoppings of electrons between sites $i-j$ and π_g^* MOs of O_2^- species, for FM and AFM configurations. Blue (turquoise) represent spin up (down) electrons. Δ represents the energy level splitting between π_g^* MOs.

and exchange interactions on top of the selected functional, one should subtract the interactions of the same type that are already present in the functional, in order to avoid double counting the same terms. Using hybrid functionals, such as the HSE06, is problematic in this context, due to the underlying fraction of the non-local HF exchange and the strong non-sphericity of the local potential. This makes it not trivial to remove the same type of interactions from the on-site terms of the model.

The transfer integrals (Figure 3.12) are at least two orders of magnitude smaller than the on-site Kanamori parameters. Therefore it is possible to extract the spin exchange couplings J_{ij} between O_2^- species in sites i and j as second order perturbations with respect to these transfer integrals. This is called the superexchange theory of Anderson [194], and it consists of calculating the kinetic energy gains $T_{ij}^{\uparrow\uparrow}$ for the ferromagnetic (FM) and $T_{ij}^{\uparrow\downarrow}$ for the anti-ferromagnetic (AFM) configurations, on each pair of non-equivalent bonds $i-j$, as a consequence of the virtual hoppings of electrons from the space of occupied spin orbitals, to the subspace of unoccupied spin orbitals. The energy difference between both spin configurations of a given bond is then

mapped onto the following Heisenberg Hamiltonian:

$$H = -\sum_{i>j} J_{ij}\mathbf{S}_i\mathbf{S}_j, \tag{3.8}$$

with $S_i = S_j = \frac{1}{2}$. Therefore, the spin exchange couplings are computed as

$$J_{ij} = \frac{1}{2S^2}(T_{ij}^{\uparrow\downarrow} - T_{ij}^{\uparrow\uparrow}). \tag{3.9}$$

First the kinetic energy gains for $(NaO_2)_4$ planar clusters are calculated as follows. The $p_\parallel$ and $p_\perp$ are defined as the π_g^*-like MOs whose lobes point in the direction parallel and perpendicular to the center of the ring, respectively. The energy level splitting (Δ) between these MOs is 100 meV, with $p_\parallel$ MOs located at higher energies than $p_\perp$ MOs. As a consequence, at low temperature and a $\frac{3}{4}$ filling, $p_\perp$ MOs are expected to be fully occupied, whereas $p_\parallel$ MOs are half-occupied. This allows to define a ground-state wavefunction on the bond $i-j$ from the occupied orbitals in sites i and j. In the case of the FM configurations, as electrons do not change their spin upon hopping, only transitions from occupied $p_\perp$ states in site i to unnocupied $p_\parallel$ states in site j are allowed as can be seen in Figure 3.13. The allowed states involved in the process of virtual hoppings with a FM configurations are the following:

$$\begin{aligned}
|GS\rangle_{ij} &= |p_\perp\uparrow\rangle_i\,|p_\perp\downarrow\rangle_i\,|p_\parallel\uparrow\rangle_i\,|p_\perp\uparrow\rangle_j\,|p_\perp\downarrow\rangle_j\,|p_\parallel\uparrow\rangle_j \\
|1\rangle_{ij} &= |p_\perp\uparrow\rangle_i\,|p_\parallel\uparrow\rangle_i\,|p_\perp\uparrow\rangle_j\,|p_\perp\downarrow\rangle_j\,|p_\parallel\uparrow\rangle_j\,|p_\parallel\downarrow\rangle_j \\
|2\rangle_{ij} &= |p_\perp\uparrow\rangle_i\,|p_\perp\downarrow\rangle_i\,|p_\parallel\uparrow\rangle_i\,|p_\parallel\downarrow\rangle_i\,|p_\perp\uparrow\rangle_j\,|p_\parallel\uparrow\rangle_j
\end{aligned} \tag{3.10}$$

From non-degenerate second order perturbation theory the energy corrections to the $|GS\rangle_{ij}$, ground state of the bond $i-j$, are calculated for the FM configuration as:

$$T_{ij}^{\uparrow\uparrow} = -\frac{(t_{ij}^{p_\perp p_\parallel})^2 + (t_{ji}^{p_\perp p_\parallel})^2}{U - 3J_H + \Delta}, \tag{3.11}$$

where $U-3J_H+\Delta$ is the energy difference between $|GS\rangle$ and $\{|1\rangle, |2\rangle\}$, for the base unperturbed Hamiltonian $H_{MF}+H_U$, in the FM configuration. It arises from transferring one electron from site i to site j, leaving two remaining electrons in site i, but keeping the same spin in different MOs, as can be seen in Figure 3.13. In the case of the AFM configurations, two possible channels exist for the virtual hopping of one electron between sites i and j, when electrons from both $p_\perp$ and $p_\parallel$ MOs occupy the half-filled $p_\parallel$ MOs of the neighboring sites. The states involved in the process of virtual hoppings

with AFM configurations in the bond $i-j$ are the following:

$$\begin{aligned}
|GS\rangle_{ij} &= |p_\perp\uparrow\rangle_i\,|p_\perp\downarrow\rangle_i\,|p_\parallel\uparrow\rangle_i\,|p_\perp\uparrow\rangle_j\,|p_\perp\downarrow\rangle_j\,|p_\parallel\downarrow\rangle_j \\
|1\rangle_{ij} &= |p_\perp\downarrow\rangle_i\,|p_\parallel\uparrow\rangle_i\,|p_\perp\uparrow\rangle_j\,|p_\perp\downarrow\rangle_j\,|p_\parallel\uparrow\rangle_j\,|p_\parallel\downarrow\rangle_j \\
|2\rangle_{ij} &= |p_\perp\downarrow\rangle_i\,|p_\perp\uparrow\rangle_i\,|p_\parallel\uparrow\rangle_i\,|p_\parallel\downarrow\rangle_i\,|p_\perp\uparrow\rangle_j\,|p_\parallel\downarrow\rangle_j \\
|3\rangle_{ij} &= |p_\perp\uparrow\rangle_i\,|p_\perp\downarrow\rangle_i\,|p_\perp\uparrow\rangle_j\,|p_\perp\downarrow\rangle_j\,|p_\parallel\uparrow\rangle_j\,|p_\parallel\downarrow\rangle_j \\
|4\rangle_{ij} &= |p_\perp\uparrow\rangle_i\,|p_\perp\downarrow\rangle_i\,|p_\parallel\uparrow\rangle_i\,|p_\parallel\downarrow\rangle_i\,|p_\perp\downarrow\rangle_j\,|p_\perp\uparrow\rangle_j
\end{aligned} \tag{3.12}$$

Thus, the expression of the kinetic energy correction in the AFM configuration is written as:

$$T_{ij}^{\uparrow\downarrow} = -\frac{(t_{ij}^{p_\perp p_\parallel})^2 + (t_{ji}^{p_\perp p_\parallel})^2}{U - 2J_H + \Delta} - \frac{(t_{ij}^{p_\parallel p_\parallel})^2 + (t_{ji}^{p_\parallel p_\parallel})^2}{U}, \tag{3.13}$$

where $U-2J_H$ and U stand for the inter-orbital and intra-orbital Coulomb repulsion energies. The expression above could also be corrected to account for the effects of spin polarization of the doubly occupied MO due to the unpaired electrons [195, 196]. However, it is assumed that this effect is negligible compared to U and $U-2J_H+\Delta$.

The same procedure applies for the non-planar $(NaO_2)_4$ clusters. However, the extraction of J_{ij} values is more cumbersome. The planar ring $(NaO_2)_4$ cluster shows a D_{4h} symmetry, and all of the molecular O_2^- centers are equivalent by symmetry. Therefore, the value of the level splitting ($\Delta_i = \Delta$ for all i) is also equivalent for all sites. In contrast the lower C_s symmetry of the non-planar $(NaO_2)_4$ clusters result in a range of different energy splittings of π_g^*-like MOs for different sites.

For planar clusters, diagonal couplings ($J_{ac} = J_{bd}$, following the notation shown in Figure 3.12) are zero. Magnetic couplings between the nearest-neighbor superoxide centers are AFM and practically identical due to the underlying D_{4h} symmetry. For instance, the values of isotropic exchange couplings are the following, $J_{ab} = J_{bc} = J_{cd} = J_{da}$ = -1.95 meV for planar-ring $(NaO_2)_4$ clusters. In non-planar clusters, the dominant coupling is also AFM and occurs between molecular centers a and d (J_{ad} = -4.24 meV); the rest of couplings are FM: $J_{ac} = J_{cd}$ = 1.25 meV, $J_{ab} = J_{bd}$ = 1.32 meV, and J_{bc} = 0.1 meV.

WFT calculations: WFT calculations were also performed on $(NaO_2)_4$ clusters using the DFT structures optimized with HSE06. The methods used are described in the theoretical background Section 2.2.2. Basically, one has to construct a multi-determinantal space first, defined with CAS(N/m)SCF, where N are the number of electrons and m are the number of MOs considered. On top of this active space, the dynamical correlation energy is included perturbatively, with CASPT2 and NEVPT2; or variationally, with DDCI and

Planar-ring $(NaO_2)_4$						
Basis set	Method	T0	T1	T2	S0	S1
BS-1	NEVPT2	-3.33	-1.70	-1.65	-5.02	-1.75
BS-2	NEVPT2	-3.26	-1.68	-1.63	-4.92	-1.76
BS-1'	DDCI2	-3.15	-1.62	-1.57	-4.72	-1.61
BS-1'	DDCI	-2.24	-1.15	-1.11	-3.36	-1.14
BS-1'	DDCI2	-3.08	-1.58	-1.53	-4.62	-1.58
BS-1'	DDCI	-2.12	-1.09	-1.06	-3.23	-1.09
Non-planar $(NaO_2)_4$						
Basis set	Method	T0	T1	T2	S0	S1
BS-1	NEVPT2	-14.17	-4.98	-2.13	-17.32	-4.07
BS-2	NEVPT2	-17.46	-4.99	-2.29	-20.12	-4.73
BS-1'	DDCI2	-15.86	-2.95	1.20	-17.52	-0.09
BS-1'	DDCI	-9.60	0.93	5.25	-9.46	6.05
BS-2'	DDCI2	-16.79	-2.96	1.11	-18.30	-0.33
BS-2'	DDCI	-10.53	0.71	4.80	-10.36	5.35

TABLE 3.2: Calculated total energies in meV of the quintet (reference), triplets (T0, T1, and T2) and singlets (S0 and S1) at NEVPT2, DDCI2, and DDCI levels of theory, using CAS(4/4).

DDCI2.

CASSCF-NEVPT2 calculations were performed with the Orca 3.0.3 suite [197], whereas CASSCF-CASPT2 and DDCI calculations where calculated with Molcas 8.0 [198] and Casdi [199]. Two different atomic basis sets where used for Orca calculations: (i) cc-VDZ Na (including $4s3p1f$ orbital polarization functions) and O ($3s2p1d$); and (ii) cc-VTZ Na ($5s4p2d1f$) and O ($4s3p2d1f$) [200]. For Molcas and Casdi calculations, two relativistic contracted atomic natural orbital (ANO-RCC) basis sets were used: (i) ($4s3p1f$) for Na and O; and (ii) Na ($4s3p1f$) and O ($4s3p2d1f$) [201, 202]. These basis sets are labeled as BS-1, BS-2, BS-1' and BS-2', respectively.

In short, we evaluated the energy gaps between different 'global' (in the sense that treats the whole cluster as a quantum spin system, instead of individual bonds $i-j$ with single determinantal states as in the superexchange theory) magnetic multiplet structures of $(NaO_2)_4$ clusters. In this particular case we can generate a quintet (Q), three triplet (T0, T1, and T2), and two singlet (S0 and S1) spin states, which arise from the addition of the angular momentum

Planar-ring $(NaO_2)_4$						
Basis set	Method	T0	T1	T2	S0	S1
BS-1	NEVPT2	-3.18	-1.62	-1.58	-4.79	-1.65
BS-2	NEVPT2	-3.16	-1.62	-1.57	-4.75	-1.68
Non-planar $(NaO_2)_4$						
BS-1	NEVPT2	-14.66	-4.79	-2.13	-17.89	-3.77
BS-2	NEVPT2	-18.08	-4.90	-2.21	-20.83	-4.41

TABLE 3.3: Calculated total energies in meV of the quintet (reference), triplets (T0, T1, and T2) and singlets (S0 and S1) at NEVPT2, DDCI2, and DDCI levels of theory, using CAS(12/8). Among the 96 states generated only the six most stable ones are included.

of the four S = 1/2 centers, using the methods above: CASSCF, CASPT2, NEVPT2, DDCI2, and DDCI. Apart from the CAS(4/4), which only considers the single unpaired electron in each O_2^- center, all the π_g^*-like MOs were treated and their energy gaps were evaluated with the CAS(12/8)SCF and CAS(12/8)NEVPT2 methods. For shortness, only the calculations performed with NEVPT2, DDCI2, and DDCI calculations are shown in Table 3.2 for CAS(4/4) and Table 3.3 for CAS(12/8).

CAS(4/4)-based NEVPT2 and DDCI2 on planar $(NaO_2)_4$ clusters yield very similar energy gaps (Table 3.2), but they are 50% larger than those obtained with DDCI. Similar behavior is observed with non-planar $(NaO_2)_4$ clusters. Also, CAS(12/8)NEVPT2 calculations are in good agreement with those based on CAS(4/4); this means that the effect of the most stable π_g^* orbital on each O_2^- species can be accurately treated by means of single and double excitations on top of CAS(4/4)SCF wavefunctions and energies. CAS(12/8) also allow to estimate the energy splitting between the π_g^* MOs on O_2^- species, resulting in a gap of 500 meV for planar clusters (5 times larger than those derived from the Hubbard Hamiltonian shown in Equation 3.5). In non-planar clusters similar tendency is observed with the lowest transition energy between π_g^* orbitals, with a gap of 150 meV. In short, these preliminary results indicate the necessity of CAS(4/4)DDCI calculations to reach accurate values.

Moving to the evaluation of the magnetic couplings (J_{ij}) for a Heisenberg model (Equation 3.8) using WFT, an effective Hamiltonian is constructed using the DDCI wavefunctions and energies using the methods described in [38, 203, 204], and then this Hamiltonian is mapped with the matrix representation of Equation 3.8, providing a direct evaluation of the interaction among unpaired electrons in π_g^* MOs.

		$\mid t_{ij} \mid (meV)$		$J_{ij}(meV)$	
		PBE	CAS(3/4)DDCI	Superexchange	CAS(4/4)DDCI
Planar	Edges	47.0	46.0	-1.9	-1.1
Non-planar	ad	179.0	193.0	-4.2	-12.0
	ab = bd	78.0	100.0	1.3	2.7
	ac = cd	2.0	16.0	1.2	0.6
	bc	0.0	0.0	0.1	0.1

TABLE 3.4: Comparison of transfer integrals and magnetic exchange couplings between DFT- and WFT-based methods. The second column stands for the magnetic centers (O_2^- species) involved in the magnetic couplings.

For the planar-ring $(NaO_2)_4$ cluster, diagonal J_{ad} and J_{bc} terms are almost zero, whereas edge AFM couplings are almost identical ($J_{ab} = J_{bc} = J_{cd} = J_{da}$ = -1.1 meV). In contrast, non-planar $(NaO_2)_4$ clusters show a more complex behavior, the largest couplings are AFM between a and d centers (J_{ad} = -12.0 meV). The rest of exchange couplings are FM and significantly smaller, for instance, $J_{ab} = J_{bd}$ = 2.7 meV, and $J_{ac} = J_{cd}$ = 0.6 meV. Additionally, the electron transfer integrals, t_{ij}^{pp}, between singly occupied π_g^*-like MOs of $(NaO_2)_4$ clusters. In this instance we mapped a Hückel model Hamiltonian with an effective Hamiltonian constructed from CAS(3/4)DDCI (considering the clusters with one electron less) using basis set BS-2'. The values of the transfer integrals computed with WFT are given in Table 3.4.

Comparison between DFT and WFT results: The calculations based on DFT and WFT yield essentially very similar absolute values of the calculated transfer integrals as seen in Table 3.4. However, larger discrepancies are found between the two methods when it comes to the computed magnetic exchange couplings. The qualitative character of the interactions, regarding their AFM or FM nature, is correctly extracted by combining DFT, Hubbard model Hamiltonians and the superexchange theory, but the intensities are, in general, twice larger than those computed with WFT for planar-ring clusters, and significantly smaller for non-planar clusters (particularly, J_{ad}). One possible reason for such discrepancy is that it was assumed that the on-site Coulomb and exchange parameters (U, U', and J_H) for the clusters were the same as those derived for NaO_2 bulk using cLDA-RPA [160]. Indeed, Figure 3.14 shows that for small variations of U and J_H, it is possible to obtain superexchange couplings that are close to the ones calculated with DDCI. This is consistent with the fact that $(NaO_2)_4$ clusters should have slightly different on-site interaction parameters. However, the variation of U and J_H that is needed to extract the correct J_{ad} interaction, is much larger. This highlights the limitation of the underlying approximations made when constructing the

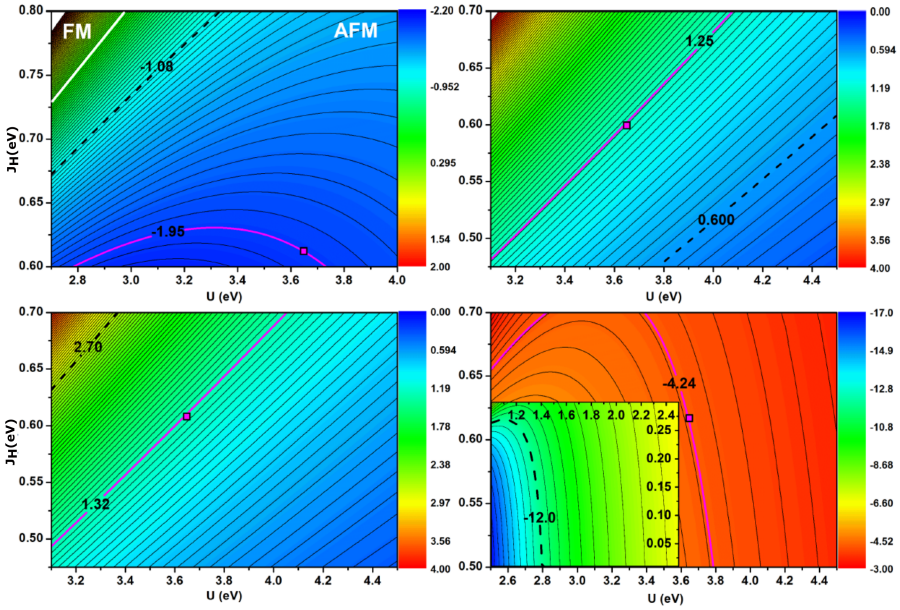

FIGURE 3.14: Contour map of the magnetic exchange parameters of $(NaO_2)_4$ clusters in meV obtained with superexchange theory. Exchange parameters for planar geometries (top-left) and non-planar geometries with values: $J_{ab} = J_{bd}$ (top-right), $J_{ac} = J_{cd}$ (bottom-left), and J_{ad} (bottom-right) as a function of on-site interaction parameters U and J_H. The color code represents the intensity of the magnetic coupling, and the palette is found at the right of each graph. Purple contour lines have the values of the coupling obtained with $U = 3.65$ eV and $J_H = 0.61$ eV values (purple square). Black dashed lines represent the reference values obtained with DDCI, within the parameter space of the superexchange model. White line represents the transition between AFM and FM couplings.

Hubbard model, and suggests that a more accurate model Hamiltonian should include further interaction parameters (e.g., inter-site Coulomb repulsive interactions of π_g^*-like electrons or MO and site dependencies with U and J_H parameters). Also, the relationship $U' = U - 2J_H$ is strictly valid in systems with cubic symmetry, which is not the case with the $(NaO_2)_4$ clusters.

It is noted that the exchange couplings are qualitatively consistent with the M_s values found for the most stable cluster structures computed with HSE06. As shown in Figure 3.6, the ground states of planar structures correspond to the smallest M_s values (the interactions are AFM). However, non-planar clusters

show a different trend in some cases. Interestingly, the largest coupling in non-planar $(NaO_2)_4$ clusters is AFM, while the rest of interactions are FM. This could lead to a M_s ground state different from 0, which would be consistent with the HSE06 calculations.

3.2.5 Conclusions

In conclusion, we have performed a series of DFT, WFT, and model Hamiltonian calculations, on NaO_2 systems of different dimensionalities, using bulk, slab, and cluster models. Regarding the DFT electronic structure, these results show the formation of a fully occupied spin-up and a half-filled spin-down antibonding π_g^* states associated with O_2^- species, in the valence band of all these systems. The conventional PBE approach predicts a half-metallic character for the bulk, (100) surface, and $(NaO_2)_n$ (n = 4, 5, 6, 7, and 8) clusters; however, it is found that for the correct description of such localized π_g^* states, the hybrid HSE06 functional is required. This result highlights the failure of conventional GGA approaches to describe the open-shell O $2p$ states in superoxide systems. Using HSE06 opens band (HOMO-LUMO) gaps of around 2 eV in all investigated systems, showing their insulating character. This result provides insight into the understanding of the electrocrystallization of NaO_2 in Na-air batteries. Concretely, the absence of intrinsic electron conducting pathways on (100) surfaces and clusters suggests a solution mediated nucleation process on discharge, were the electrolyte gets saturated with solvated NaO_2 species and then small $(NaO_2)_n$ clusters form to precipitate onto the carbon support. Regarding the charge process, the situation is a bit more controversial. While the lack of intrinsic electron conductivity still holds, fast ionic dynamics and the facile dissolution of the superoxide species in the electrolyte could lead to non-stoichiometric surface terminations, that could enhance electron conductivity as in the case of the conducting Li_2O_2 O-rich terminations. The effect of the band alignment in the NaO_2/C interface is another unexplored mechanism for enhancing electronic conductivity, that could inject electrons from the C support on the NaO_2 conduction band.

Regarding the structural and energetic investigation of the small clusters. DFT calculations were carried with PBE and HSE06 functionals in small $(MO_2)_n$ clusters (M = Li, Na, and K, with n = 2-8). The calculations show that metal-oxygen and metal-metal distances present a strong dependence with the cluster size. It is also found that increasing the cluster size results in thermodynamically downhill stabilization for both planar-ring and non-planar $(MO_2)_n$ clusters. Planar rings are favored over non-planar structures for small cluster sizes. For larger cluster sizes, however, non-planar geometries start to become energetically favored. Particularly, the exact crossover point for the stability of the non-planar clusters against the planar-rings depends on the nature of the alkali metal and shifts to smaller cluster sizes when moving from

LiO_2 to KO_2. This behavior is rationalized by means of electrostatic interactions in the highly ionic M-O_2 bonding. Concretely, it is shown that larger alkali metals, such as K, tend to stabilize non-planar clusters earlier than smaller ones, such as Li; which is particularly insightful when understanding the morphology of the discharge products in alkali-metal-air batteries. In principle, such high surface energy nuclei act as a template directing the crystallization of larger MO_2 particles. Non-planar clusters, ideally, have the necessary bulk-like features to nucleate the bulk material, while the planar-ring clusters do not. The observed trends suggest that NaO_2 and KO_2 allow forming small crystalline bulk nuclei at early stage, whereas LiO_2 promotes the formation of planar structures. As a consequence, the formation of larger crystalline, cubic particles would only be favored in the case of NaO_2 and KO_2, which is consistent with the observed growth of large crystalline particles in Na-air batteries [23, 150], as opposed to the behavior of Li-air cells [161].

Regarding the magnetic properties of $(NaO_2)_4$ clusters, the evaluation of isotropic exchange couplings J and the electron transfer integrals $\hat{t}$ between O_2^- species are sensitive to the underlying WFT method (CASSCF, NEVPT2, CASPT2, DDCI2, or DDCI). The accurate treatment of these electrons requires the computationally expensive DDCI calculations. Interestingly, combining cheaper approaches, such as DFT, model Hamiltonians and superexchange theory, one is able to obtain a good qualitative agreement with DDCI results. However, resolving quantitative discrepancies between J couplings probably requires the consideration of more sophisticated model Hamiltonians.

3.3 The role of Na^+ solvation in glyme-based electrolytes

As we already discussed, charge/discharge processes on Na-air batteries are likely to occur through solution mediated processes. The role of the electrolyte solvent is then really important, and often overlooked, for its effects in the energetics and kinetics of O_2^- dissolution and ion-pair formation. In the case of metal-air batteries, carbonate mixtures were first selected as solvents, because of previous experience based on Li-ion battery technologies. This was proven to be far from ideal as those solvents showed a propensity to decompose, for example, to Li_2CO_3 at the cathode interfaces of Li-air batteries. Therefore, more stable solvents were enabled [139, 205]. Consequently, new solvents will also be required for Na-air batteries. In particular, glyme solvents have been shown to be promising for metal-air batteries because of their higher stability in the presence of highly reactive superoxide radicals [206]. Moreover, glyme solvents of different lengths have been showed to hugely affect battery performance [178]. This section is dedicated to understanding the role of Na ion solvation in the performance of the battery, for three different glyme solvents 1,2-dimethoxyethane '$C_4H_{10}O_2$' (DME), 2-methoxyethyl ether '$C_6H_{14}O_3$' (DEGDME), and tetraethylene glycol dimethyl ether '$C_{10}H_{22}O_5$' (TEGDME), at different salt concentrations.

3.3.1 Computational Methods

We performed DFT calculation using the B3 exchange functional along with the LYP nonlocal correlation functional B3LYP [54, 207], implemented in the all-electron code FHI-aims with numeric atom centered orbital basis sets [118, 119]. Previous studies have shown that B3LYP-based calculations can accurately describe battery electrolytes [208–210]. The structures were generated using the builder tools of the molecular editor Virtual NanoLab. Different solvation configurations were considered by optimizing $[Na\text{-}(M)_n]^+$ complexes (where n = 1, 2, 3, 4 for M = DME; n = 1, 2, 3 for M = DEGDME; and n = 1, 2 for M = TEGDME) using a trust radius enhanced version of the Broyden-Fletcher-Goldfarb-Shanno optimization algorithm [211], where the forces where minimized until a 10^{-4}/Å threshold was achieved. The vibration modes and simulated IR spectra were calculated by finite differences with displacement values of 0.0025 Å. We placed a 20 cm^{-1} full width half maximum to simulate standard line broadening to the individual IR bands to better compare with experimental data. Because of the fairly big size of some of the complexes (up to 75 atoms in total), we used "ligth" settings and "tier2" standard basis sets in the FHI-aims code for Na, C, O, and H. Generally, "tight" settings should be used for calculating vibrational frequencies, particularly for O and H containing systems, as numerical noise might impact the calculated

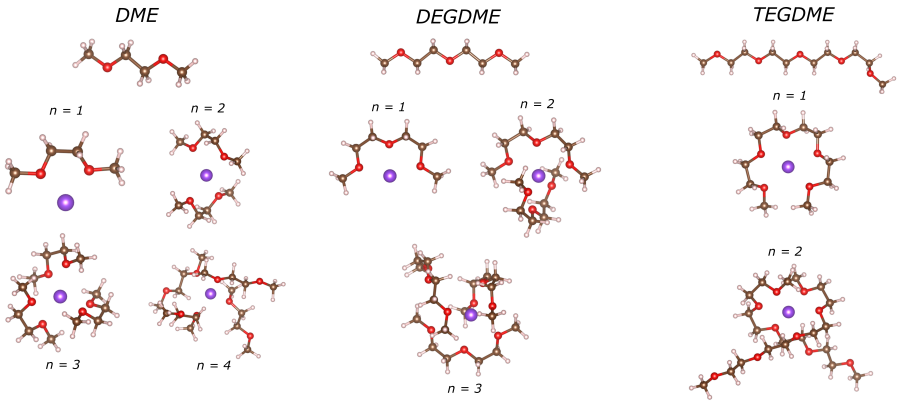

FIGURE 3.15: DFT optimized structures of DME, DEGDME, and TEDGME solvent molecules; and the corresponding Na complexes containing n glyme molecules. Color code: H (white), C (brown), O (red), and Na (purple).

modes, specially at high frequencies. Therefore, we first assessed the accuracy of our considered integration grids by calculating the vibrational modes of DME with both "light" and "tight" settings. In general we see that bellow the frequencies of interest (1200 cm^{-1}) the differences in mode frequencies are smaller than 1 cm^{-1}. We can therefore safely assume that the use of "light" setting is accurate enough on these systems.

3.3.2 Structures of solvation complexes

The initial structures for the optimization procedures were selected with the previous knowledge that glyme-based solvents generally prefer to curl when solvating alkaline ions [178, 212–214]. In this way we are able to maximize the amount of ion-O bonds, which compensates the energy penalty associated with the dihedral rotations around C-O and C-C bonds. We considered some plausible initial geometries and relax their structures. Figure 3.15 shows the most stable optimized geometries that we found. Note that isolated DME and DEGDME molecules are more stable in their linear configurations, unlike TEGDME molecules. Regarding the optimized structures, Na-O bonds generally increase in length with the amount of oxygen donor groups that are participating in bonding as shown in Table 3.5. In all studied cases, the maximum amount of O groups that were able to coordinate with Na^+ were six, even if more O groups were available. For instance, for DME it was not possible to use curled structures to maximize Na-O bonds beyond $n = 3$, as

	$< r >_{Na-O}$ (Å)				
n	0	1	2	3	4
DME		2.247	2.320	2.431	2.345
DEGDME		2.298	2.438	2.567	
TEGDME		2.418	2.473		
	$< r >_{C-O}$ (Å)				
DME	1.412	1.436	1.429	1.424	1.421
DEGDME	1.412	1.432	1.424	1.421	
TEGDME	1.412	1.427	1.419		
	$< r >_{C-C}$ (Å)				
DME	1.518	1.512	1.511	1.510	1.519
DEGDME	1.518	1.512	1.510	1.509	
TEGDME	1.515	1.512	1.514		

TABLE 3.5: Table of mean Na-O, C-O, and C-C bond distances for $[\text{Na-(M)}_n]^+$ complexes (M = DME, DEGDME, and TEGDME).

the optimizer would always form the $[\text{Na-(DME)}_3]^+$ complex, leaving the remaining DME molecule uncoordinated. Alternatively, considering only linear configurations, it was possible to further allocate four DME molecules in the complex as shown in Figure 3.15 at the cost of only forming four Na-O bonds. We note that in this case the Na-O bond distance is smaller. Similarly, in the case of DEGDME, maximizing Na-O bonds was only possible up to $n = 2$. When introducing an extra molecule in the complex, due to steric repulsion effects and the greater volume of each of the solvent molecules, one of the molecules would use its three oxygen donor groups, another molecule would use two, while the third would use only one, which is different to the $n = 3$ case of DME. Lastly, the TEGDME molecules are the largest of the three. In this case, already a single TEGDME molecules can nearly completely chelate the Na^+. When introducing the second TEGDME molecule, the most stable configuration that we found resembles that of the $[\text{Na-(DEGDME)}_2]^+$ complex featuring straight tails that leave two uncoordinated O donor groups per molecule.

3.3.3 Energetics of complexation

In this section, we calculated the reaction energies for the formation of the complexes shown in Figure 3.15. We considered two scenarios: the limit of infinitely dilute and saturated salt concentrations. The corresponding energy profiles are shown in Figure 3.16. The energy profile in black is obtained by

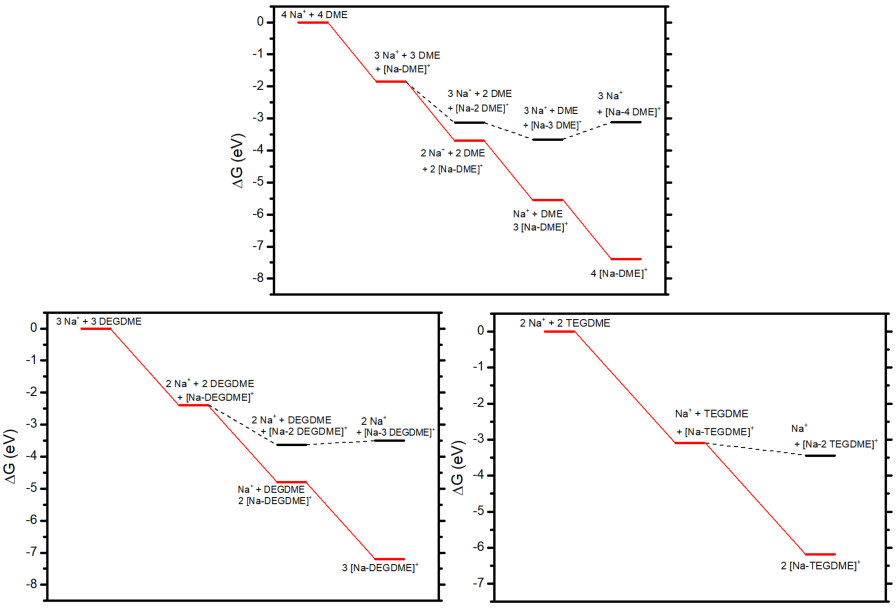

FIGURE 3.16: Simulated reaction energies for the formation of the $[Na—(M)_n]^+$ complex (black curve), or the formation of various $n[Na—(M)]^+$ complexes (red curve).

continuously adding solvent molecules to a given solvation complex, simulating the scenario in which many molecules are available to solvate a single Na ion (diluted limit). The red energy profile shows the energy gain (or loss) when a single solvent molecule chelates a single Na ion, simulating the saturated limit (without accounting for the salt counterion). The energies of the first step in both red and black curves are obtained as:

$$\Delta G_1^{r,b} = G([Na-M]^+) - G(M) - G(Na^+). \tag{3.14}$$

The successive steps in the red energy profile are just a repetition of the first step, i.e., $\Delta G_n^r = n\Delta G_1^r$, while for the black curve we consider the following:

$$\Delta G_n^b = G([Na-(M)_n]^+) - G([Na-(M)_{n-1}]^+) - G(M). \tag{3.15}$$

G is the Gibbs free energy of the complexes. Here, we approximate it as $G = E_{DFT} + F_{vib}(T) + F_{rot}(T)$ (with T = 298 K), where $F_{vib}(T)$ and $F_{rot}(T)$ are the vibration and rotational energy contributions, respectively. On the one hand, we observe that when continuously adding glyme molecules to a preformed $[Na\text{-}(M)_n]^+$ complex, the structure is further stabilized up to a threshold that decreases with the size of the solvent molecules: DME $n = 3$, DEGDME $n = 2$-3, and TEGDME $n = 1$-2. We note that previously proposed

structures based on molecular dynamics (MD) simulations [178] are consistent with our findings, specially the minima of the black energy profile in Figure 3.16. This is somewhat obvious, since smaller molecules allow for increasing stabilizing Na-O interactions without repelling each other, when compared to TEGDME, for instance, where a single molecule almost entirely chelates the Na ions, as already explained in the previous section. On the other hand, the red energy profile shows that it is thermodynamically preferred to chelate the Na ions to form various $[Na\text{-}(M)]^+$ complexes, where a single solvent molecule is present. These results qualitatively explain the decrease in coordination number upon increasing the salt concentration in the mixture, that is going to be introduced in the following sections. We must also note that at the more dilute limit, the experimental values for the solvation number do not coincide with the theoretical ones, which are underestimated. We argue that, although the black energy profiles show a minimum at values DME $n = 3$, DEGDME n = 2-3, TEGMDE n = 1-2, further increasing the amount of glyme molecules involved in the formation of the complex is still more favorable than not forming any complexes at all, so if we were to keep adding solvent molecules we would still get a thermodynamically favorable reaction. This of course would require explicitly including a second solvation shell and exploring the configurational space for such complex, which was not feasible for the purposes of this work.

3.3.4 Simulated IR spectra

The calculated vibrational spectra are shown in Figure 3.17. In particular two regions are shown: 1200-1000 cm^{-1} and 890-820 cm^{-1}, where the biggest shifts occur upon adding sodium. The regions correspond to changes in vibration frequencies of C-C and C-O bonds, concretely C-O-C stretches (1200-1000 cm^{-1}) and C-C-O bends/twists (890-820 cm^{-1}). Looking at the C-O-C stretch region, a red shift is clearly visible with respect to the neat glyme molecules, which suggest electron donation from the O groups to the Na ions. When continuing to add solvent molecules, i.e., simulating a decrease in salt concentration, a small blue shift is observed, which is consistent with the shortening of the C-O bonds with respect to $n = 1$ complexes. The first red shift is approximately of 80 cm^{-1}, 60 cm^{-1}, and 50 cm^{-1} for DME, DEGDME, and TEGDME, respectively. Turning to the C-C-O bend/twist region, there is a blue shift of about 10 cm^{-1} upon increasing the size of the complexes, which is consistent with the shortening of the C-C bonds shown in Table 3.5.

3.3.5 Comparison with experiments

In the last sections we presented the structural and energetic properties of different solvation complexes of Na ions with glyme solvents, as well as their

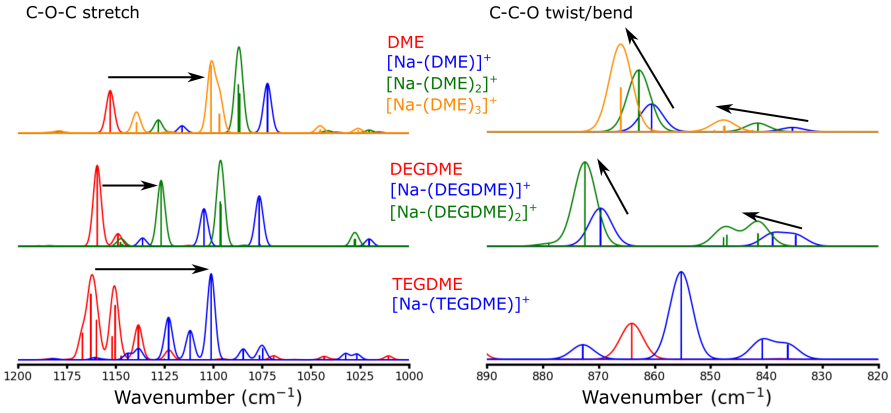

FIGURE 3.17: Simulated DFT infrared spectrum of the glyme molecules of Figure 3.15. Left-most plots highlight the C-O-C stretching region, while the right-most plots display the C-C-O bending/twisting modes.

simulated IR spectra. In this section we attempt to find connections between our results and the experiments that were done as part of a collaboration with Nagore Ortiz-Vitoriano and co-workers at Oak Ridge National Laboratory, in order to shed light into the cycling properties of these three glyme solvents in Na-air batteries.

In this work $NaClO_4$ is considered as salt additive, since the anion (ClO_4^-) is known to interact weakly with the solvent [215], and therefore its effect can be disregarded from the solvation of Na^+. This allows us for analyzing the structure of isolated Na^+ ions with respect to glyme length and studying their corresponding electrochemical responses. Experimentally, the coordination structure of Na^+ in the $NaClO_4$/DME-DEGDME-TEGDME solutions was estimated through fourier transformed infrared (FTIR) spectroscopy data, by fitting the vibrational modes that are sensitive to changes in the chemical environment due to ion coordination as presented in the simulated IR spectra in the previous section.

The experimental fits of the FTIR spectra show, in agreement with simulations, a C-O-C stretching region in the range of 1200-1000 cm^{-1} and a C-C-O bend/twist region between 890-800 cm^{-1}. The C-O-C stretching modes show a red shift with the increase of salt concentration, which are estimated to be of about 30 cm^{-1}, 25 cm^{-1}, and 21 cm^{-1}, for DME, DEGDME, and TEGDME, respectively. With respect to the simulations the red shift is smaller in magnitude, but the general tendency of decreasing red shifts for larger glyme molecules is conserved. In the C-C-O bend/twist region a blue shift of about

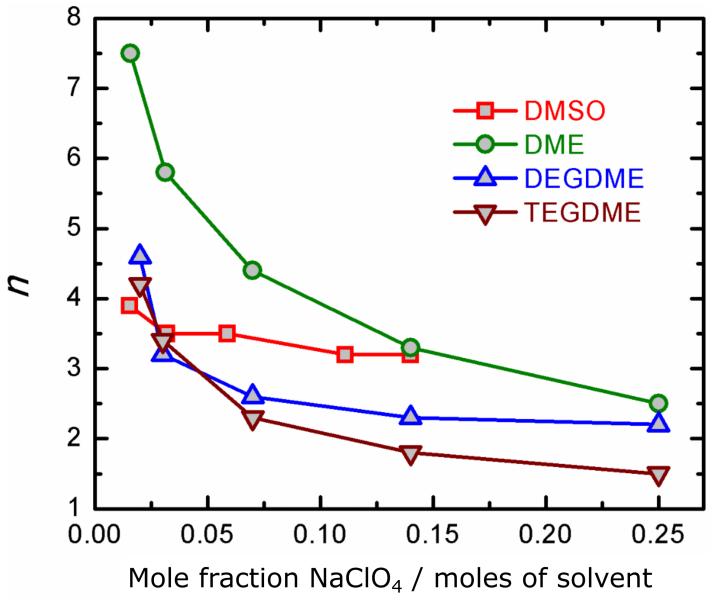

FIGURE 3.18: Apparent coordination number as a function of Na salt concentration.

8 cm^{-1} is observed, regardless of the solvent. This is due to the fact the increasing the electron donation from the donor O groups to the Na^+ weakens C-O bonds, increasing their bond length, and in turn shortens the C-C bonds and produces the blue shift. In our calculations this effect was not well captured, as one can see in Figure 3.17 the blue shift in the C-C-O bend/twist region happens with increasing the size of the complex, i.e., decreasing the salt concentration, while the reverse is observed experimentally. Indeed, Table 3.5 shows that while the weakening of the C-O bonds is well captured at high salt concentrations (see that the mean C-O bond distance is larger for smaller n values), correctly predicting the red shifts in the C-O-C stretching region, the C-C bonds also appear to get weaker, as their bond lengths also increase with smaller n values. The origin of this error could be due to the fact that we simulate isolated complexes on gas-phase, while in reality these complexes would exist in a liquid environment. The inclusion of an implicit solvent model, that accounts for electrostatic screening and steric effects by embedding the complexes in an effective dielectric medium, could solve this issue, however the FHI-aims package that we used still lacks the ability to perform structure optimizations with such implicit models.

By analyzing the area under the spectral FTIR signals it was possible to obtain the apparent coordination number n as a function of salt concentration as shown in Figure 3.18. It represents the number of solvent molecules that

are chemically affected by the Na^+ ions, not necessarily in the first solvation sphere, but generally participating in the charge screening. The apparent coordination numbers show an exponential decay, reaching a constant value at high salt concentrations. Dymethilsulfoxide '$(CH_3)_2SO$' (DMSO) is also shown as a baseline for comparing the glyme solvents. This results are reasonable and qualitatively captured through the energetics of our calculations as discussed in Section 3.3.2. Concretely, the dipole moments of DMSO, DME, DEGDME and TEGDME are 4.0 D, 1.6 D, 1.9 D, and 2.4 D, respectively, which means that charge screening is most effective in DMSO and weakest in DME, being n the smallest for DMSO and the largest for DME at low concentrations, and showing elongated decays in glyme solvents. Here, DEGDME reaches a constant value faster than the other glymes, while DME still does not reach a constant value. These results show that at low concentrations many DME molecules will be participating in the solvation of the Na^+, while almost half of those molecules are going to be present when using DEGDME or TEGDME. This will have some important implications on battery performance, as it becomes clear that establishing the right concentration of salt in a given solvent is important in order to optimize the electrochemical response of the system as we will see in the following section.

Not only the coordination number, but the stability of the Na^+ in the corresponding solvents will also play an important role on battery performance. In this collaboration, the enthalpies of dissolution of $NaClO_4$ in the three glyme solvents were also measured by calorimetry, showing that the dissolution becomes more exothermic for larger glyme solvents, being -23.33 kJ/mol, -40.02 kJ/mol, and -45.12 kJ/mol, for DME, DEGDME, and TEGMDE, respectively. This again pairs well with the calculated reaction energies for the formation of the complexes, specially one can see in Figure 3.16 that the first steps are most exothermic in TEGDME when compared to DME. Showing a greater stability of Na^+ in longer glymes, as more Na-O bonds are formed per solvent molecule.

3.3.6 Considerations on cycling performance

We now analyze the implications of the results discussed above in the operation of Na-air batteries. In the discharge process an important factor to consider is the chelating ability of the solvent, which is larger for larger chain glyme solvents as observed in the previous sections, arising from their greater ability to form Na-O bonds. Higher chelating ability means that Na^+ ions will become very stable in solution by forming $[Na\text{-}TEGDME]^+$ complexes, as demonstrated by calorimetry and DFT calculations. This should in principle favor a solution mediated process, where stable ion pairs are formed and then precipitated after saturation. This hypothesis, however, is not fully met [178], as XRD experiments show the formation of NaO_2 in DME and DEGDME based electrolytes, but not in TEGDME. The presence of

cube shaped discharge products is also observed with DME and DEGDME suggesting a solution mediated discharge process, while a film-like structure is observed with TEGDME. One possible reason is that, since high chelating ability solvents produce highly stable Na^+ complexes, Na^+ ions present high desolvation barriers. Therefore, it is possible that, once the TEGDME molecules chelate the Na^+ ions, they are not able to unbound them and, therefore, only a few ion pairs will be forming and desolvating during ORR near the cathode surface, forming film-like structures, blocking the surface with an insulating NaO_2 film, and inducing premature cell death. Considering shorter chain DME and DEGDME favors the desolvation process because the molecules interact more weakly with Na^+ ions, since they have less O donor groups. Other factors to take into account are the solubility of O_2^- (TEGDME<DEGDME<DME), which results in capacity increases. And the viscosity of the solvent (TEGDME>DEGDME>DME), which induces sluggish kinetics. Regarding the charge process, during OER, the discharge products of the electrode surface must be decomposed electrochemically and the formed species (Na^+ and O_2^-) must be restabilized in the electrolyte. Again, the chelating ability and the viscosity of the solvents will play an important role here.

Looking at how the solvation structure changes with the salt concentration and how the kinetic effects may impact battery performance, our experimental collaborators performed cyclability experiments in four different regimes, considering two salt concentrations (0.1 M and 1.5 M) and two current densities (65 $\mu A/cm^2$ and 120 $\mu A/cm^2$). At 0.1 M and 65 $\mu A/cm^2$ the cyclability of the three different solvents is as follows: DEGDME (29 cycles), DME (13 cycles), and TEGDME (no cycling, as discussed in the last paragraph). We attempt to explain these differences by reviewing the Gutmann's Donor Numbers (DN) of the three solvents, which relates to the capacity of the solvents to share electrons with the salt cations and, therefore, favor the dissolution of the salt. During ORR, effective charge screening by higher DN solvents reduces the Lewis acidity of the Na^+ ions, and increases the capacity to stabilize ion-pairs with soft bases such as O_2^-, favoring the formation of sodium superoxide (NaO_2) against sodium peroxide (Na_2O_2). During OER, high DN indicate a higher capacity of dissolving the discharge products and restabilizing the Na^+ ions in solution. Depending on the source, the values for the DN vary for the three glyme solvents, but generally it is clear that TEGDME has the smallest DN (12 kcal/mol [178] or 16.6 kcal/mol [216]), while DME (19 kcal/mol [178] or 20.0 kcal/mol [216]) and DEGDME (18 kcal/mol [178] or 24.0 kcal/mol [216]) have comparable values. It is then clear that DN is not the only factor explaining the almost two fold increase in the cyclability of DEGDME when compared to DME. For instance, the DN are values measured against the solvation of Sb^{+5} at a concentration of 1:1 (each solvent molecule is solvating one cation), and does not take into account other important factors such as the steric hydrance, the chelating ability, the ability of the solvent molecule to protect the cation, or the coordination structure of the solvent molecules,

0.1 M - 65 μA/cm^2	0.1 M - 120 μA/cm^2
- Best cyclability : DEGDME (29 cycles) > DME (13 cycles)	- Best cyclability : DEGDME (32 cycles) $\approx$ DME (30 cycles)
- Low n of DEGDME when compared to DME - Steric effects favor Na^+ desolvation on DEGDME	- Lower viscosity of DME improves cycling
1.5 M - 65 μA/cm^2	**1.5 M - 120 μA/cm^2**
- Best cyclability : DEGDME (31 cycles) > DME (24 cycles)	- Best cyclability : DME (46 cycles) > DEGDME (36 cycles)
- Similar n in both DME and DEGDME - Weaker DME binding to Na^+ favors desolvation	- Again lower viscosity of DME favors cycling in combination with weaker binding to Na^+

TABLE 3.6: Summary of the main contributing factors to the electrochemical performance of DME, DEGDME, and TEGDME solvents, at the four different salt concentration and current density regimes.

that we saw changing with the salt concentration. Particularly, in the regime of low salt concentration (0.1 M), there will be a greater number of solvent molecules solvating Na^+ when using DME, in contrast to DEGDME. This means that, effectively, a large amount of DME molecules have to move in order to precipitate the ion pairs.

Also, the coordination configuration for the same amount of solvent molecules is different as shown by DFT calculations. Looking at the case of $n = 3$, as already shown in previous sections, DME will use all its O donor groups to solvate Na^+, while in DEGDME, steric effects repel parts of the molecule out of the coordination structure, resulting in one of the molecules using the three O donor groups, other using two, and the last one using only one. Therefore, although DEGDME is considered to be a better chelating agent than DME, in the $n = 3$ case, only one molecule would act as such, while the other two would bind weakly. The desolvation is then favored for DEGDME when compared to DME at low salt concentrations.

At higher current densities (120 μA/cm^2), the cyclability of DME has a two fold increase, from 13 to 30 cycles, and DEGDME improves from 29 to 32

cycles. At high current densities the discharge products have less time to stabilize in the solvent and diffuse to the electrode surface. This fact is aggravated in DEGDME, because of its large viscosity (more than double than that of DME), and prevents sufficient diffusion of the species. Thus, at higher intensities, solvent viscosity probably plays a dominant role in the cycling behavior.

At higher concentrations (1.5 M) and low current densities, the cyclability improves for DME (24 cycles) and DEGDME (31 cycles). This may be the result of an increased ionic conductivity due to a higher concentration of Na^+. But again, the coordination structure may play an important role. For instance, as we already saw in Figure 3.18 the coordination number n decreases at high salt concentrations, approaching to the limit of $n = 2$ in both DME and DEGDME. In this new situation, only two DME molecules will be coordinated to the Na^+. Therefore, only four donor oxygens will be participating in the solvation of the cation. In the case of DEGDME, the solvation is stronger, as there are six donor oxygens that are able to solvate the Na^+. Thus, in the more dilute region, DME presents more difficulties to desolvate because of the big amount of molecules on the coordination structure when compared to DEGDME, but at higher concentrations desolvation becomes easier in DME. The slight improvement of the cyclability of DEGDME might be because, during charge, it still facilitates the disolution and stabilization of the species formed during the discharge process.

When increasing the current density, again the cyclability of both DME and DEGDME improves to 46 and 36 cycles, respectively. As already mentioned, the viscosity of the solvent is prone to dominate the higher current density regimes. To sum up, all the dominant effects at different operational regimes are contained in Table 3.6.

3.3.7 Conclusions

In this work we studied the energetic, structural, and electrochemical properties of three different glyme solvents (DME, DEGDME, and TEGDME), aiding experimentalists with simulations based on DFT calculations. From the simulations perspective, a range of plausible Na^+ solvation structures of the type $[Na\text{-}(M)_n]^+$ (where M = DME, DEGDME, and TEGDME) have been considered in the gas phase as proxy models of concentrated (low n) and diluted (high n) Na^+ concentration limits. Structurally, a maximum six-fold coordination of O donor groups with Na^+ was achieved, and trying to include further amount of molecules in the complex resulted in less O groups participating in the bonding with Na^+ (see the linear, or semi-linear structures in Figure 3.15). Energetically, the coordination numbers in the diluted limit are predicted to be $n = 3$ for DME, $n =$ 2-3 for DEGDME, and $n =$ 1-2 for TEGDME, which agrees with the experimental trend, for the measured

coordination number and calorimetry results, but is quite off the quantitative results, probably because of the limits of the calculation. Those include: not considering second solvation shells and not including the electrostatic and steric contributions of the solvent with implicit models. Simulated IR spectra agreed reasonably well with the experimental one, and it was used to identify the main regions where the IR peaks shifted as a function of salt concentration, which then were used to measure the coordination numbers. Lastly electrochemical tests were performed by experimentalists to compare the cycling performance of the three DME, DEGDME and TEGDME solvents. We conclude that simple charge screening and DN based arguments are not enough to explain the observed differences. Mainly, at low salt concentrations, large n values for DME negatively impact the electrochemical performance. Moreover, steric effects lower the chelating ability of larger solvents at large n values, as discussed using the $n = 3$ structural models for DME and DEGDME obtained with DFT, and therefore desolvation becomes easier in DEGDME, explaining the enhanced cyclability. However, at higher salt concentrations, DME largely improves the cycling performance, which again relates to the coordination structure. In this case, the weaker solvation of the DME through four O donor groups (instead of six O groups of DEGDME), makes it easier to desolvate the species. At high current densities, the viscosity of the solvent dominates the cycling performance, largely improving the results for DME. Lastly, it was not possible to cycle TEGDME, because of the high stability of Na^+, with resulting high solvation/desolvation barriers and the high viscosity of the solvent.

Chapter 4

Simulations on Layered Oxides for Sodium-ion Batteries

This chapter is dedicated to studying Layered Transition Metal Oxides (LTMOs) as systems of interest for cathodes of Na-ion batteries. Particularly we focused on thoroughly examining P $\leftrightarrow$ O transitions in $NaVO_2$ as a case study, providing atomic-level understanding into glide-driven processes in these compounds, by means of DFT calculations. Our results are meant to help to guide research efforts to design LTMOs with enhanced structural stability during battery cycling.

4.1 Introduction

Lately, Na-ion batteries have emerged as a strong contender for large-scale batteries in stationary applications, where cost, safety, and durability are chief requirements [217]. In particular, two main families of cathode materials are currently considered as the most promising for future Na-ion batteries: polyanion-type structures [218] and LTMOs [219]. Sodium-layered oxides are particularly promising due to their high capacities, ease of synthesis, environmental friendliness, and low cost [22]. Structurally, these compounds belong to two main families: On and Pn phases [220]; the letter indicates that Na ions are in either an octahedral (O) or a prismatic (P) environment, while the number n indicates the number of oxide layers in a unit cell. In contrast to Li counterparts, electrochemical Na insertion is feasible for layered oxides based on most of 3d transition metals (TMs). This has motivated extensive research in recent years, aiming at designing compounds with high performance by carefully selecting complex mixtures of TMs that can selectively operate at target voltages. In this quest, the combination of experimental and theoretical insights is a particularly fruitful strategy to understand and improve the

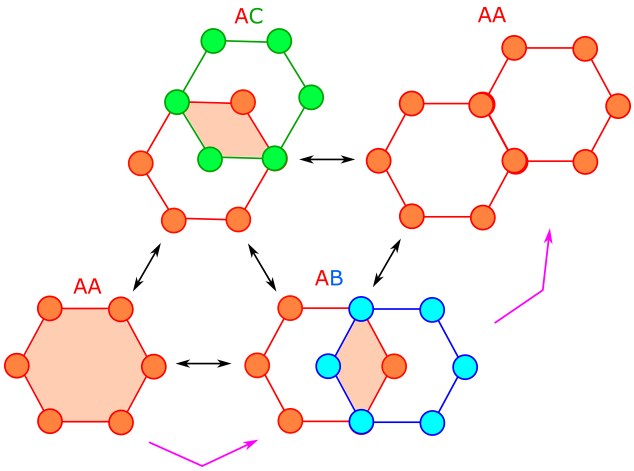

FIGURE 4.1: Stacking sequence changes for graphite. 'A' positions are shown in orange, 'B' positions in blue, and 'C' positions in green. Pink arrows indicate the series of transformations that lead to 'AA' stacking with lattice-invariant shear strain. This Figure is based on the paper by Radin *et. al.* [227].

stability and electrochemical performance of new materials [28, 221, 222].

However, a remaining challenge of LTMOs toward applicability is long-term stability. This is mainly a consequence of phase transitions occurring during Na insertion and extraction cycles, which leads, usually, to structural collapse and significant capacity degradation. In particular, P $\leftrightarrow$ O topotactical transformations are ubiquitous not only during electrochemical operation [223–225], but also during synthetic thermal procedures [223]. Understanding and controlling these structural transformations is therefore of utmost importance to boost the electrochemical performance of LTMOs [226]. Radin *et. al.* [227] have recently proposed that the degradation of the capacity of LTMO cathodes during operations could be due to, amongst other things, the formation of microcracks and accumulation of dislocations, that could find its origin in the so-called lattice invariant shears [228]. In short, lattice invariant shears in layered materials manifest when the reversible, and symmetrically equivalent, pathways between stacking sequence changes form a graph of infinite connectivity. To better illustrate this effect let us consider the case of graphite, as can bee seen in Figure 4.1, which is formed by vertically stacking two-dimensional honeycomb carbon layers. If the lateral position of one of the layers is taken to be 'A', the following layer could be in positions 'A', 'B', or 'C', forming AA and AB stacking (or symmetrically equivalent AC stacking). The lateral positions of the layers can change by sliding the layers with respect to each other, which leads to stacking sequence changes. For instance, AA

$\rightarrow$ AB transformations can occur in three symmetrically equivalent sliding pathways, as there are three different directions in which the lateral positions of the layers can change to form an AB stacking. The reverse transformation, AB $\rightarrow$ AA, also has three symmetrically equivalent pathways. However, only one of these leads back to the original AA stacking. The other two pathways lead to a lattice invariant shear of the original AA phase.

In LTMOs, similar effects occur in P $\leftrightarrow$ O transformations, but the actual mechanism behind these still remain elusive. The process is thought to be facilitated by the presence of partial dislocations in the material. TEM experiments revealed indeed that glissile dislocations can form on $LiCoO_2$ when perfect dislocations dissociate into Shockley partials (that form stacking sequence changes) with the basal {0001} glide plane [229]. Such partial dislocations could then glide on successive lattice planes providing the mechanism for the O3 $\leftrightarrow$ H1-3 $\leftrightarrow$ O1 transformations (H1-3 denotes O1/O3 hybrid phases). However, other materials, such as the Li-rich layered oxide $Li_{1.2}Ni_{0.133}Mn_{0.533}Co_{0.133}O_2$, appear to accumulate dislocations in the {403} planes with Burgers vectors having components along the c-axis (parallel to the layers), during electrochemical charge [230], whose gliding cannot result in a stacking ordering change, but can directly induce such stacking ordering mixtures by simple inclusion of extra half-planes parallel to TM layers.

The aim of this chapter is to gain atomic-level understanding of the mechanism of P $\leftrightarrow$ O topotactical transformations in sodium LTMOs as a function of the Na content. To this end, we used DFT calculations to study a simple system, Na_xVO_2, which has extensively been examined experimentally in recent years [223, 231–235]. And we specifically focused on the early stages of P2 $\leftrightarrow$ O2 transitions during their nucleation as a model to study Pn $\leftrightarrow$ On transitions, in general. In order to model this process, we considered a perfect, uniform gliding of a single slab of TM oxide sandwiched between two blocks of the pristine crystal, meaning that two interfaces are modified during the transformation. We must first note that this idealized process is unlikely to be the actual P $\leftrightarrow$ O transformation mechanism, as a perfect slip generally requires very large shear stresses and, as discussed above for the case of $LiCoO_2$ [229], the transformation can be catalyzed by the diffusion of an edge or screw dislocation. Nonetheless, our idealized model makes it possible to compute nonlinear interfacial potentials, which can roughly inform about the diffusion of such dislocations, and could even be used as inputs of mixed atomic/continuum approaches such as the Peierls-Nabarro model [236, 237], capable of describing the nucleation and mobility of dislocations. Such interfacial potentials encode therefore the impact of the atomic structure in the gliding process [238]. Through the ab initio computations of these interfacial potentials, our work provides atomistic insight into the role of Na content and Na local coordination in such interfacial potentials, and help to further advance our fundamental knowledge of P $\leftrightarrow$ O transformations in LTMOs.

4.2 Computational methods

Spin-polarized DFT calculations were carried out with the VASP code [110–113] using the PAW method [107]. We explicitly treated the Na ($2p^6 3s^1$), V ($3p^6 3d^4 4s^1$), and O ($2s^2 2p^4$) electrons as valence electrons, which were expanded in plane waves with an energy cutoff of 700 eV. We used the recently developed SCAN [66] meta-GGA functional, which, without using empirical corrections, systematically improves the description of diverse types of bonding [239] and yields experimental accuracy in total energies and relative stabilities across main group solid compounds [240]. Additionally, to include the significant effect of vdW forces onto the properties of LTMOs [241], we coupled the SCAN functional with the rVV10 vdW density functional [91–93], which has been proven to outperform the rest of functionals in various systems, including layered materials [239, 240, 242].

Spin polarization was initiated with a high-spin value in a ferromagnetic configuration [243]. For the structural model of $Na_{0.5}VO_2$, we applied the Na/vacancy ordering proposed experimentally [231, 232, 235]. For partially sodiated Na_xVO_2 systems with $x < 0.5$ and $x = 0.667$, due to the lack of available experimental data, we considered low-energy, simple Na/vacancy arrangements proposed theoretically for various LTMOs [244]. Figure 4.2 summarizes all of the supercells and Na/vacancy arrangements considered in this study. Appendix A shows an experimental and theoretical catalogue on Na/vacancy orderings for different sodium based LTMOs. The geometries were fully relaxed until a residual force threshold of 0.01 eV/Å was achieved. For the calculation of layer glidings, we doubled the unit cell in the z-directions, resulting in $\sim$ 20 Å long c-axis. The gliding process is analyzed by translating a single TM layer within the xy plane, perpendicular to the z-axis, as shown in Figure 4.2g. The long c-axis allows creating enough space between the periodic images of the interfaces that are generated because of the gliding, which prevents spurious interactions between them. The interfacial potential is then evaluated as:

$$\Phi[\mathbf{R}, x] = \frac{1}{2A}(E[\mathbf{R}, x] - E[P2]), \tag{4.1}$$

where $\mathbf{R}$ is the translation vector for the gliding of an oxide layer, x is the Na content, and A is the area of the interface that is generated between the pristine crystal and the translated layer. Essentially, $\Phi[\mathbf{R}, x]$ represents how much energy is gained (negative values) or lost (positive values) per unit area in the gliding layer with respect to the P2 phase.

The minimum-energy paths and the transition-state configurations for the gliding of the TM layers were determined using the CI-NEB [128] method as implemented in the transition-state tools for VASP.

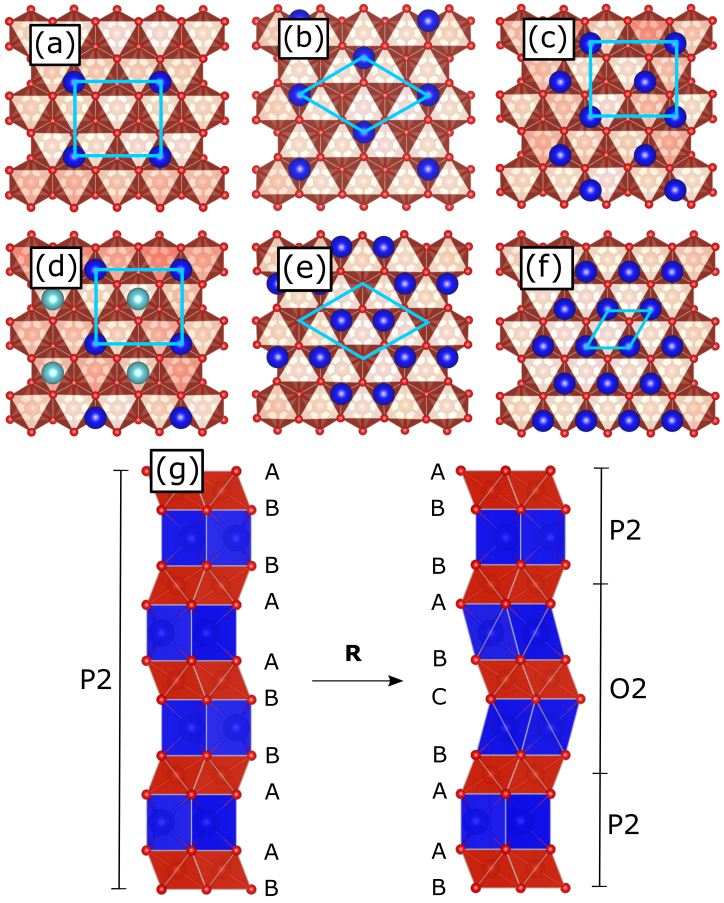

FIGURE 4.2: Top view of considered Na/vacancy orderings for P2-Na_xVO_2 at Na contents x = 0.25 (a), x = 0.333 (b), x = 0.5 (c), x = 0.667 (e), and x = 1 (f), and for O2-Na_xVO_2 only at x = 0.5 (c). The *xy* projections of the unit cells are shown in turquoise, and Na ions and VO_6 octahedra are shown in blue and red, respectively. (d) Na ions at edge- and face-shared prismatic sites in dark and light blue, respectively. (g) Formation of a O2 phase sandwiched between two P2 domains as a result of the gliding of a layer in the pristine P2 phase; note how the initial BA AB oxygen packing of the P2 structure changes to a BA BC stacking in the interface between P2 and O2 domains. Adapted from *ACS Appl. Mater. Interfaces* 2019, 11, 13, 12562-12569 [245]. Copyright 2019 American Chemical Society.

The Madelung potentials were computed using the Fourier method implemented in VESTA [246], assuming formal charges and delocalized fractional

charges on the V atoms for intermediate Na configurations. This means that each V atom in the transition state is assumed to have a fractional formal charge between +3 and +4 to achieve electroneutrality as a function of x in Na_xVO_2, this is to say, $V^{+(4-x)}$. This potential is calculated as:

$$\phi_i = \sum_j \frac{Z_j}{4\pi\epsilon_0 l_{ij}}, \tag{4.2}$$

where Z_j is the formal charge in the ion j, ϵ_0 is the vacuum permittivity, and l_{ij} is the distance between ions i and j. This ϕ_i value represent the electrostatic interaction of the whole crystal onto a given site within that crystal. These potentials give us the opportunity to rationalize the character of the physical properties behind the gliding process.

4.3 Results and discussion

4.3.1 Gliding in VO_2

Under thermodynamical conditions, P → O transitions in LTMOs follow a minimum-energy gliding path, $\Phi_0[\mathbf{R}, x]$, that can be characterized by a set of translation vectors, $\{\mathbf{R_i}\}$. For example, Delmas and co-workers [247, 248] proposed the existence of two equivalent translation vectors [(1/3, 2/3, z) and (2/3, 1/3, z)] for the P2-$Na_{0.7}CoO_2$ → O2-$LiCoO_2$ exchange transition. We first focus on VO_2 to thoroughly examine the topology of $\Phi[\mathbf{R}, 0]$ and identify Φ_0 in the simplest case, where no Na ions are intercalated between the layers. The role of including Na ions is introduced in the next Section 4.3.2. We use Equation 4.1 to compute $\Phi[\mathbf{R}, 0]$ for a complete set of translations ($\mathbf{R}$) that span discrete fractions of the cell vectors **a** and **b** (perpendicular to the largest **c** vector) as can be seen in Figure 4.3. We consider a rather dense grid of 400 translation vectors, where each grid point represents a displaced state of the VO_2 layers. For each grid point, we freeze the x and y coordinates of all of the atoms in the system and only allowed relaxation in the z direction. The approach is similar to that used in the literature to obtain interlayer gliding energy landscapes for two-dimensional materials [249–251].

Figure 4.3 reveals that P2-VO_2 is unstable, with a barrierless transition to a local O2 structure along the (1/3, 2/3, 0) gliding vector (or any other equivalent vector within the C_6 rotational group). We see therefore that, without sodium in the system, VO_2 prefers to form O2 structures, in agreement with other recent DFT calculations [226]. Indeed, P2 structures are thought to undergo phase transitions into O2 structures when approaching full charge. For instance, complete Na extraction from P2-$Na_{0.67}Ni_{0.33}Mn_{0.67}O_2$ results in the transformation into O2-$Ni_{0.33}Mn_{0.67}O_2$ with random stacking faults

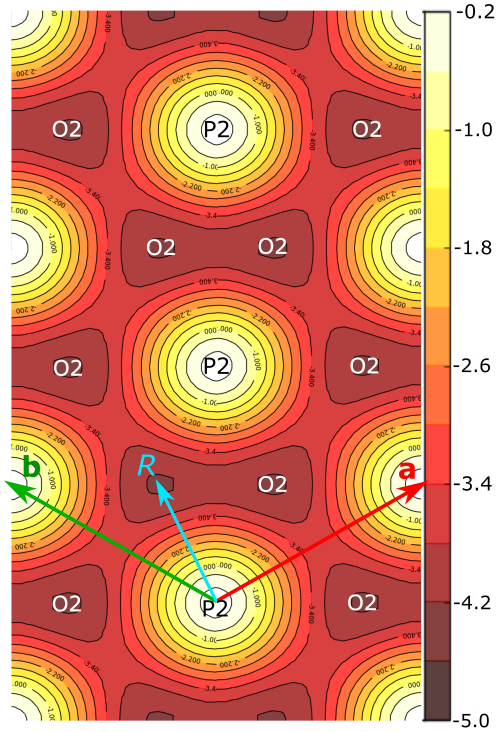

FIGURE 4.3: Computed contour plot of the interfacial potential (in meV/Å^2) for VO_2. The light blue $\mathbf{R} = (1/3, 2/3, 0)$ vector indicates one of the equivalent lowest-energy directions for the P2 $\rightarrow$ O2 transition. **a** (red) and **b** (green) are the translation vectors equivalent to the cell vectors. Heat map color scheme: light (yellow) and dark (brown) colors indicate high- and low-energy translations, respectively. Reprinted from *ACS Appl. Mater. Interfaces* 2019, 11, 13, 12562-12569 [245]. Copyright 2019 American Chemical Society.

[252]. Additionally, the formation of stacking faults is consistent with the existence of multiple equivalent gliding vectors and the barrierless nature of the transformation [227].

4.3.2 Gliding in Na_xVO_2 ($0 < x \leq 1$)

In the previous Section 4.3.1, the O2 phase was shown to be preferred for VO_2. However, upon sodiation, the local coordination of inserted Na ions and

Na/vacancy distributions determines the overall stability of these systems. Typically, in P2 phases, large Na ions prefer to be accommodated in trigonal prismatic sites, so the as-prepared P2 LTMOs tend to adopt this stacking sequence at relatively high Na contents [231, 253, 254], whereas transformation to O2 structures often takes place when charging and reaching low Na contents [255–257]. In addition, preferred Na/vacancy distributions tend to be governed by electrostatics, forming highly symmetric configurations with respect to the exchange of Na and vacancies, and reducing the electrostatic repulsion between Na ions within each layer [258, 259]. However, asymmetric Na/vacancy configurations can also form by stabilizing many-body interactions [244].

These stability considerations are expected to still hold during the out-of-equilibrium gliding process. But the implicit large structural distortions across the gliding direction destroy the existence of Na sites with well-defined octahedral or prismatic local coordinations, especially when approaching transition-state configurations. This allows for a diverse and dynamic environment of distorted Na sites during gliding, which flattens the energy well of ground-state structures and facilitates the formation of low-energy metastable states. Because of this, when following the method used in the case of P2-VO_2, we found that the evaluation of the full $\Phi[\mathbf{R}, x]$ was impractical. Concretely, we observed discontinuities in Φ, related to sudden jumps of Na atoms between sites of similar energy, that were generated when constructing the initial grid of translation vectors. A solution for this problem requires extremely fine grids and the evaluation of different initial geometries for Na/vacancy orderings in each grid point. However, since we are only interested on identifying the minimum energy gliding paths (Φ_0), an alternative approach to computing the full Φ is using the CI-NEB method, concentrating on the structures along the gliding directions (1/3, 2/3, 0) that connects P and O structures as seen in Figure 4.3. This way we can automatically find the TS configurations at different Na contents, while taking into account the full effect of atom relaxation across the gliding process. This is an upgrade with respect to other approaches to calculate interfacial energies between stacking sequence changes, where only vertical atomic relaxation are taken into account (and not lateral ones). Figure 4.4 shows the CI-NEB energy profiles for gliding at different Na contents in Na_xVO_2. In contrast to the barrierless P2 $\rightarrow$ O2 transition (Figure 4.4a) at zero Na content, as discussed also in the previous section, the presence of sodium results in the appearance of at least one energy barrier for the gliding process (Figure 4.4b-f). In other words, we see that Na insertion induces effective friction between the oxide layers.

Also, note that the relative stability between P2 and O2 structures changes with the Na content. The thermodynamic preference of O-type structures at low Na contents (Figure 4.4a-c) continuously decreases upon Na insertion, and at large enough Na contents, P-type structures become preferred (Figure 4.4d-f). The origin of this behavior is that, in O2 structures, Na ions in octahedral

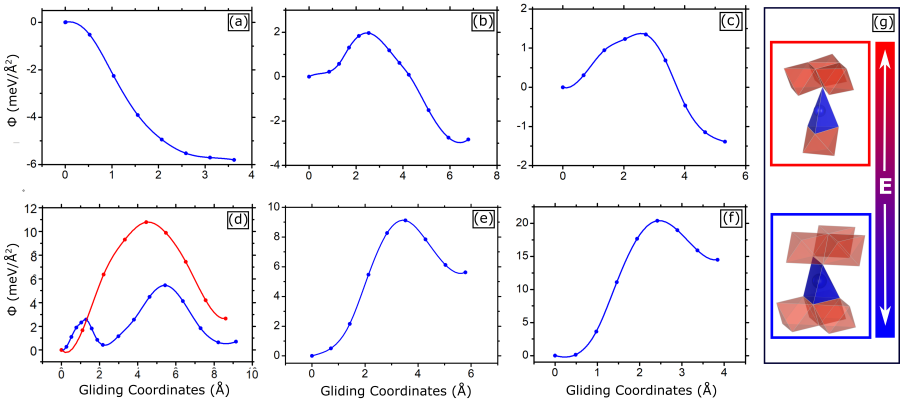

FIGURE 4.4: CI-NEB energy paths for layer gliding in Na_xVO_2: $x = 0$ (a), $x = 0.25$ (b), $x = 0.333$ (c), $x = 0.5$ (d), $x = 0.666$ (e), and $x = 1$ (f). The blue curves in (a)-(f) are associated with transition-state structures, where the local environment of Na ions is a distorted square pyramid, whereas the red curve in (d) corresponds to an alternative high-energy path through tetrahedral-like coordinations. (g) The two different local Na environment of low (blue profile) and high (red profile) energies. Reprinted from *ACS Appl. Mater. Interfaces* 2019, 11, 13, 12562-12569 [245]. Copyright 2019 American Chemical Society.

sites share both edges and faces with neighboring VO_6 octahedra, resulting in too small Na-V distances and consequently destabilizing the O phases with respect to the P ones.

Amongst all the computed curves in Figure 4.4, we find a special case for $x = 0.5$, where the gliding process requires first a reordering of Na ions. The phenomenon is revealed by the presence of two energy barriers in Figure 4.4d. The large energy barrier corresponds to the rigid gliding itself, whereas the small one is associated with the diffusion of Na ions during the Na/vacancy reordering. This provides an important insight into the gliding process at the atomic level, and is thoroughly analyzed in the following.

P2-$Na_{0.5}VO_2$ combines two distinct Na prismatic sites: face- and edge-shared with the VO_6 octahedra (Figure 4.2d). This is in contrast to the rest of investigated compositions, where only edge-shared prisms are present. In fact, face-shared prisms are less stable than edge-shared ones in terms of Na-V repulsive electrostatic interactions; however, face shared prisms allow for larger spacing between Na ions, which also electrostatically repel. In the end, it is the balance between Na-Na and Na-V repulsive interactions that drives the final in-plane Na/vacancy ordering for P2-$Na_{0.5}VO_2$. Considering this

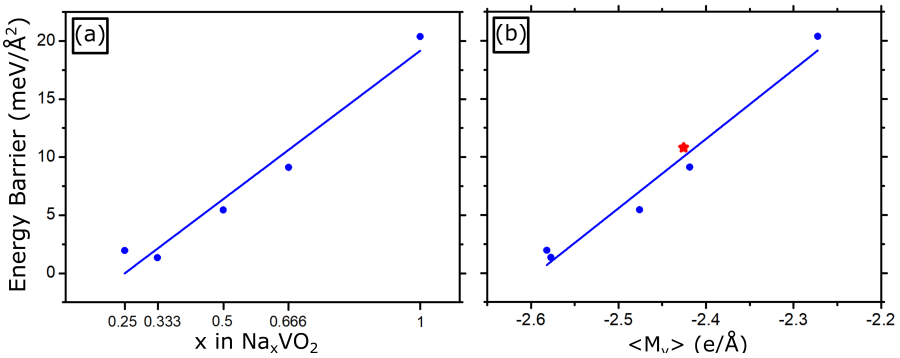

FIGURE 4.5: Energy barrier for gliding of Na_xVO_2 as a function of Na content (a) and mean value of the Madelung potential on the V atoms within the gliding layer (b). The red start in (b) is calculated from the transition-state configuration of the high-energy profile (red curve in Figure 4.4d) for $x = 0.5$. Reprinted from *ACS Appl. Mater. Interfaces* 2019, 11, 13, 12562-12569 [245]. Copyright 2019 American Chemical Society.

mixed Na/vacancy ordering for $x = 0.5$, direct gliding to a corresponding O2-like structure yields an energy barrier of 10.8 eV/Å^2. In contrast, if the Na ions in face-shared prisms are first allowed to diffuse to adjacent edge-shared prisms (Figure 4.2c), the overall barrier of the gliding reduces in half to 5.5 eV/Å^2 (Figure 4.4d). Note that in this two-stage process, the energy barrier for the Na diffusion (2.6 meV/Å^2) is significantly smaller than that for gliding, which indicates that Na/vacancy reordering through Na diffusion is kinetically accessible during the phase transition process of gliding.

Another key observation is that the energy barrier for P $\rightarrow$ O gliding increases linearly with the Na content (Figure 4.5a). To rationalize this trend, in Figure 4.5b, we show the computed energy barriers as a function of the averaged Madelung potential at V atoms ($\langle M_V \rangle$) within the gliding layer in the transition-state structure. This allows us to analyze in a compact way the role of ionic radius, structure, and electrostatics in the underlying physics of this trend. In the case of ionic crystals such as Na_xVO_2, the linear correlation suggests that the gliding process is mainly governed by electrostatic interactions. Concretely, if different gliding paths are allowed, the one with the smallest $\langle M_V \rangle$ will in general be the most favorable one. We can see that this is the case for $Na_{0.5}VO_2$, with computed $\langle M_V \rangle$ for the red(blue) high(low)-energy profile in Figure 4.4d of -2.43(-2.48) e/Å (Figure 4.5b). We conclude from this analysis that the insertion of sodium into Na_xVO_2 enhances the overall repulsive electrostatic interactions at the TS structure for gliding, inducing larger energy barriers.

4.3.3 Effect of local Na coordination

Generally, we observe from the results obtained in the last section that Na ions prefer to avoid tetrahedral-like coordination at the transition state of the gliding process. This only happens when the initial P2 structure has all the Na ions at edge-shared prisms. The process is schematically shown in Figure 4.6, from a top view (e.g. Figure 4.6b), note first that if we consider the projection plane of any edge-sharing prism, the medians of the resulting triangle overlie the directions of the gliding vectors, i.e. the triangle points in the line of gliding. As a rule of thumb, the movement of a Na atom with respect to a fixed TM layer (e.g. TM1 in Figure 4.6a) takes place along these medians and, therefore, follows the direction of gliding (Figure 4.6b). Conversely, with respect to the moving TM layer (TM2), the Na ions remain apparently immovable (Figure 4.6d). To sum up, the local geometry of Na ions in the transition state resembles a deformed square pyramid, as illustrated in Figure 4.6c. Importantly, this mechanism allows Na atoms to avoid tetrahedral coordination along the whole gliding process.

4.3.4 Applied considerations

As pointed out before, avoiding P $\leftrightarrow$ O transformations during cycling is crucial to achieve long-term cyclable electrodes. Even reversible transformations are not desirable because they tend to have a negative impact on capacity retention by inducing stacking faults and lattice volume changes, which will in turn generate lattice invariant shear [227]. Furthermore, P-type phases are generally preferred over O-type ones, because they facilitate Na-ion diffusion and, therefore, yield better rate performance during electrochemical operation [258, 260]. A design strategy for practical LTMO cathodes is, therefore, to block P $\rightarrow$ O transformations. A conventional way to achieve this is to limit the maximum amount of extracted Na ions during electrochemical operation, since, for example, O-type phases tend to appear at low Na contents [255, 257, 261]. However, this approach inevitably lowers the specific capacity that the material can theoretically achieve.

Our study suggests yet another fundamental way of blocking P $\rightarrow$ O gliding. According to the approximate Rice theory, low activation energies on interfacial potentials (energies in the transition-state structures, as calculated in this work) facilitates the nucleation of dislocations [262]. Also, low energy barriers indicate that low stresses are needed to emit such dislocations and can therefore form larger stacking fault regions, which appear to be connected to the stacking ordering changes in LTMOs [229]. Of course this is the simplest possible assumption, and conclusions based only on these barriers should be taken with extreme care as discussed by Juan *et. al.* [263]. In any case, as discussed earlier, direct P $\rightarrow$ O gliding in the presence of Na ions at face-shared

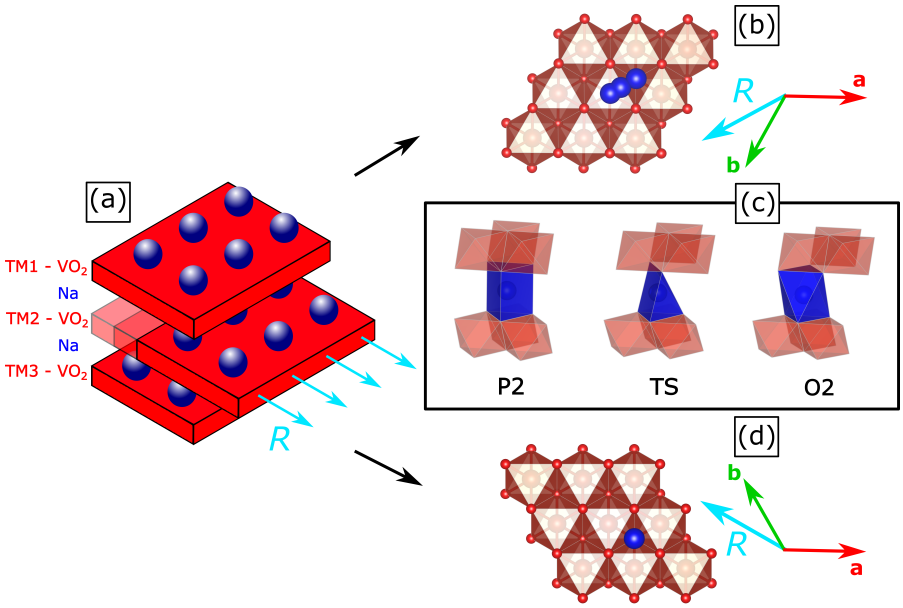

FIGURE 4.6: (a) Schematic representation of the rigid gliding process. Evolution of a Na ion relative to a (b) fixed (TM1-VO_2) or (d) gliding (TM2-VO_2) TM layer. (c) Local geometries of a Na ion in the P2, O2, and transition-state (TS) structures. VO_6 octahedra and Na ions are red and blue, respectively. Reprinted from *ACS Appl. Mater. Interfaces* 2019, 11, 13, 12562-12569 [245]. Copyright 2019 American Chemical Society.

sites is associated with a large energy barrier due to the formation of high-energy tetrahedral environments for Na ions in the transition-state structure. This can be circumvented if all of the Na ions in face-shared prisms diffuse into nearby edge-shared prismatic sites prior to gliding. Such preliminary Na-ion diffusion step is kinetically feasible due to the relatively low energy barrier involved. However, one can expect that intrinsic Na/vacancy disorder will impede the required homogeneous diffusion of Na ions. Consistently with such model, Didier *et. al.* [223] found that the thermally activated O'3 → P'3 (the apostrophe represents that the structure has suffered a monoclinic distortion, either by Jahn-Teller distortion, or concrete Na/vacancy orderings [264]) transition in $Na_{0.5}VO_2$ around 85 °C is irreversible, with P'3-$Na_{0.5}VO_2$ remaining stable even after thermal treatment at 270 °C. Here, we must note that the geometry of prismatic (octahedral) sites in P2 (O2) and P3 (O3) structures does not have equivalent local environments (see Appendix A for details on the local coordination of Na-ions). But our mechanistic insights for P2 ↔ O2 transitions, involving the avoidance of high-energy tetrahedral

environments for Na ions, should qualitatively describe other Pn ↔ On transitions too and, in particular, the discussed experimental results on O3 ↔ P3 transitions in $Na_{0.5}VO_2$. However, further theoretical work still remains desirable to confirm the generalization of this proposal.

At low Na contents, in general, Na ions only occupy edge-sharing prismatic sites because they are lower in energy than face-shared prisms. Indeed, all reported Na/vacancy orderings for $x < 0.5$ in LTMOs only involve the occupancy of edge-shared sites [257, 265]. As a consequence, at low Na contents, rigid gliding becomes facilitated and, in turn, other more realistic stacking-sequence change mechanisms such as partial dislocation propagation. This study put forward that a plausible way to block gliding at high degrees of charge could be to increase the population of face-shared prisms; the presence of Na atoms at these sites creates an effective resistance to gliding and could help prevent undesired P → O transitions. Practically, this can be achieved by modifying Na/vacancy orderings in P-type phases, for instance, by TM substitution by electrochemically inactive elements [266]. Specifically, inducing Na/vacancy disordering seems to improve capacity, rate performance, and cycle life [267, 268]. We hypothesize that because of the disorder, there is a higher probability of finding microstates with occupied face-shared prisms. Ideally, enhancing face-shared prismatic sites populations could be a preferable alternative to inducing TM migration from the oxide to the Na layers [269, 270], since that approach might negatively impact Na mobility as well as volume change and structural stability upon cycling.

4.4 Conclusions

Glide-driven P ↔ O phase transformations contribute to the structural degradation and capacity loss of LTMOs. To investigate the mechanistic insights of such transformations, we have investigated the energetics of idealized rigid plane glides, considering a range of simple Na_xVO_2 ($0 < x \leq 1$) systems and DFT calculations. We observe that energy barriers for gliding increase linearly with the Na content. We rationalize this trend by showing that the increase in sodium in the system increases the electrostatic repulsion between Na and V ions. Validating the generalization of this trend to other LTMOs will require further consideration of more complex systems than Na_xVO_2, specifically accounting for compounds that exhibit TM disordered mixtures, Jahn-Teller distortion, presence of point defects, etc.

Our analysis also reveals another important insights about the role of Na-ion in the process of gliding. Na-ions in P-type layered-oxides occupy either edge- or face-sharing prismatic sites. Yet, during P ↔ O gliding, each individual Na-ion is swept by the moving TM layer and forced into a distorted Na-O coordination environments. We find that low-energy transition-state structures

for such environments involve distorted square pyramids. Such pathways can only take place when all of Na ions are initially occupying edge-sharing prismatic sites. Instead, when Na-ions are occupying face-sharing prisms, they are forced into high energy barrier tetrahedral-like environment. Our calculations show that these high energy barrier pathways might be avoided by allowing Na-ions at face-shared prisms to diffuse into adjacent edge-shared sites before gliding. Additionally, we saw that the corresponding Na-ion diffusion barrier for this preliminary step is smaller than those associated with gliding and, in principle, kinetically accessible. However, we note that this necessity of a collective motion of Na ions from face-sharing to edge-sharing prisms, although energetically favorable, is likely to hinder the phase transformations. This is especially so, when Na/vacancy disorder is favored in the system, as recent experiments suggest. Interestingly, as a consequence of repulsive Na-Na interactions, some Na/vacancy orderings at high Na contents ($x \geq 0.5$) ensure the presence of Na ions at face-sharing prisms, since these orderings allow to increase the mean Na-Na distance, therefore reducing the electrostatic repulsion. Therefore, glide-driven P $\rightarrow$ O transformations can be effectively avoided in high Na contents, which agrees well with the usual experimental practice of limiting the state of charge of the battery to enhance cyclability.

Overall, we rationalize that LTMOs capable of accommodating face-sharing prisms at low Na contents, via, for example, Na/vacancy disorder promotion through TM substitution, could prevent P $\leftrightarrow$ O phase transformations in these materials. We note, however, that a more detailed analysis of such transformations, by means of dislocation emission within the Peierls-Nabarro model, or explicit methods with classical molecular dynamics, still remains desirable.

Chapter 5

Magnetism of Na-ion Cathodes: The Case of $NaFePO_4$

Magnetic properties of maricite (m) and triphlyte (t) polymorphs of $NaFePO_4$ are investigated by combining DFT with a model Hamiltonian approach. For this, a Hubbard-type model is constructed for magnetic $3d$ states of Fe using first principles. Then this model is solved by means of mean field HF approximation and the theory of superexchange interactions briefly introduced in Chapter 3, in order to extract the corresponding interatomic exchange parameters. These calculations help provide microscopic understanding on the competing exchange interactions in m- and t-$NaFePO_4$, which leads to magnetic superstructures that could result in multiferroicity.

5.1 Introduction

In Chapter 4 we investigated one promising family of cathode compounds for Na-ion batteries: layered oxides. Now we move our attention towards another important contender: polyanionic compounds. Polyanionic compounds are based on molecular frameworks that combine tetrahedron anion units $(XO_4)^{n-}$ (with X = S, P, Si, As, Mo, or W), or any other derivative $(X_mO_{3m+1})^{n-}$, and TM polyhedra MO_x. They are relevant cathode materials because of their attractive electrochemical properties for high energy density applications [218]. Particularly, polyanionic compounds show a rich structural diversity, which provides flexibility to best fit different applications. Additionally, inductive effects of $(XO_4)^{n-}$ anion units, which are stronger than those of O^{-2} ions in transition metal oxides, enable higher charge and discharge voltages. This occurs because strong X-O bonds weakens the M-O bond, further splitting the energy gap between their antibonding orbitals, and therefore resulting in higher redox potentials. Lastly, these compounds

usually undergo minimal structural and volume changes during alkaline ion insertion. All these properties create a fertile playground to design suitable cathode materials with outstanding cycling performance, which has triggered a surge of research among the battery community in recent years, leading to the discovery of numerous new polyanionic compounds [271, 272].

Apart from their good electrochemical properties, other aspects of potential interest in polyanionic compounds are, however, less explored. One prominent example is magnetism [271]. In fact, these compounds, show unusual magnetic properties that give rise to a variety of more exotic phenomena, such as magnetoelectricity [273–280] and even multiferroicity [281]. The origin of such rich magnetic behavior is a consequence of the combination of super-exchange and super-super-exchange interactions in these materials, which can induce the emergence of complex magnetic structures. These magnetic properties are interesting for their application in sensors, spintronics, multifunctional devices, among others [282]. Moreover, the impact of such effects in the operational performance of these materials in batteries is unknown, even though the emergence of electric polarization from magnetic fields could lead to undesirable fluctuations in operational voltage, especially in potential applications where battery packs could be exposed to high magnetic fields.

In this chapter, the magnetic properties of sodium iron phosphate ($NaFePO_4$), which is the sodium analogue of lithium iron phosphate ($LiFePO_4$) are analyzed. $LiFePO_4$ is one of the most studied cathode materials for today's Li-ion batteries [283]. However, the high abundance, environmental friendliness and low cost of sodium based electrode materials have made them a topic of high interest [11, 12, 21, 284–288] with an ongoing activity focused on $NaFePO_4$ [289]. $NaFePO_4$ crystallizes in two different polymorphic forms: triphlyte (t) and maricite (m). m-$NaFePO_4$ is the thermodynamically stable phase and shows many similarities with orthorhombically distorted TM perovskite oxides [290, 291], whereas t-$NaFePO_4$ is isostructural to $LiFePO_4$. Avdeev *et. al.* studied both polymorphs by means of neutron powder diffraction (NPD) experiments and magnetic susceptibility measurements [292]. The magnetic properties of $NaFePO_4$ are indeed very interesting and rather complex. According to NPD measurements, t-$NaFePO_4$ forms a simple AFM order, the same as $LiFePO_4$ [293], which is expected to reveal magnetoelectric effect [276]. On the other hand, m-$NaFePO_4$ forms a magnetic superstructure with the propagation vector $\mathbf{q} = (\frac{1}{2}, 0, \frac{1}{2})$ [292], which implies that there exist competing magnetic interactions in the system. This situation is interesting because there are many examples of orthorhombic manganites, where such competition results in the formation of superstructures that would break the inversion symmetry and give rise to multiferroic effects [294–296]. Both polymorphs show very different Neél magnetic transition temperatures, T_N: 13 K for m-$NaFePO_4$ and 50 K for t-$NaFePO_4$. However the Curie-Weiss temperatures, θ, are very similar, about -80 K. Kim *et. al.* theoretically investigated

the magnetic properties of both $NaFePO_4$ polymorphs using very straightforward total-energy differences method based on pure DFT+U calculations, including the Coulomb repulsion U empirically to best fit the experimental data [297]. Their calculations suggest that the magnetic structure of t-$NaFePO_4$ can be understood solely by the isotropic spin exchange interactions. In contrast, in m-$NaFePO_4$ additional mechanisms, such as magnetic anisotropy, appear.

This chapter aims at further understanding the apparently complex magnetic properties of $NaFePO_4$. Instead of stand-alone DFT calculations, the analysis is done by means of effective model Hamiltonians constructed from first-principles DFT calculations in a Wannier functions basis for the set of magnetically active Fe $3d$ bands. This approach provides a more rigorous treatment of the Coulomb interactions when compared to brute-force total energy DFT calculations. Additionally, the model yields in-depth insight into the microscopic origin of the magnetic interactions in such compounds and helps better understand the experimental data and DFT results. Furthermore, this chapter also presents a comparative study comparing two different numerical implementations of the Wannier functions, one based on the maximal localization criteria for extracting MLWF [121, 123, 124], as implemented in the Wannier90 package [122]. And the other based on the projection technique on the minimal basis set of linear muffin-tin orbitals (LMTOs) [298]. In the following, an extended methods section is introduced, which is intended to be self-contained in this chapter, and includes a more detailed extension of some of the methods introduced in Chapter 3.

5.2 Methods and models

This section describes the specific methods used to construct the effective Hamiltonians and solve and extract the corresponding magnetic properties. In addition, the computational details used to calculate the electronic structure of $NaFePO_4$ polymorphs with first-principles are provided.

5.2.1 Crystal structures

Both t- and m-$NaFePO_4$ crystallize in the orthorhombic structure with the space group *Pnma* (No. 62 in the International Tables). Both polymorphs contain four formula units in the primitive cell, with all Fe sites being equivalent by symmetry, as shown in Figure 5.1. The structure of t-$NaFePO_4$ involves corner sharing FeO_6 distorted octahedra and PO_4 tetrahedra that share edges with first-neighbor Fe sites, and corners with the rest of surrounding octahedra, as shown in Figure 5.1a-b. The experimental lattice parameters are

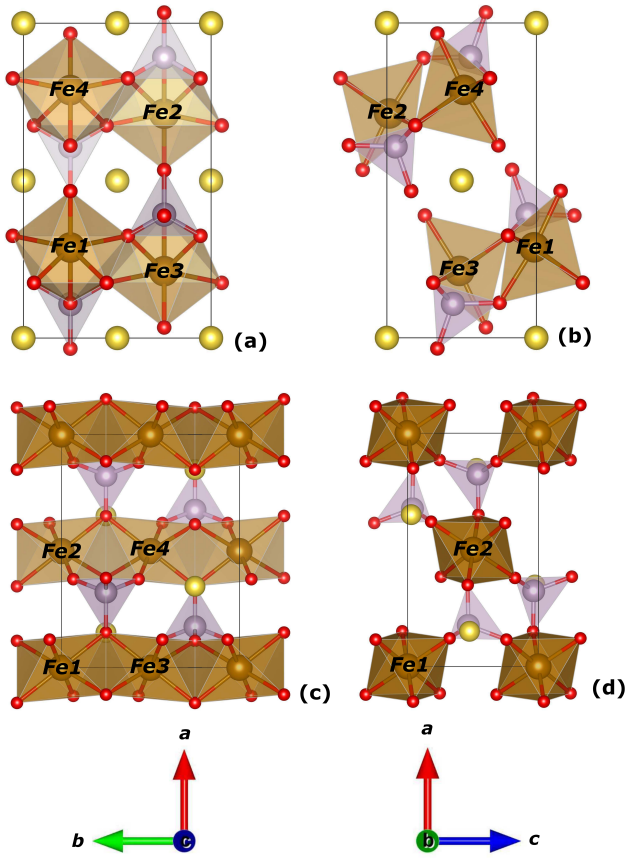

FIGURE 5.1: *ab* and *ac* projections of the bulk crystal structure of t- (a and b) and m-$NaFePO_4$ (c and d). Na, P, Fe, and O atoms are shown in yellow, gray, brown, and red, respectively. Reprinted from *Phys. Chem. Chem. Phys.*, 2018, **20**, 13497 [299]. Licensed under Creative Commons Attribution-NonCommercial 3.0 Unported Licence.

given in Table 5.1. We note that the Fe sites are located away from the positions of the crystal inversion centers, which are occupied by non-magnetic Na atoms. In the m-phase, the distorted FeO_6 octahedra share edges with other equivalent FeO_6 units, forming short Fe-O-Fe contacts in a chain-like fashion. The PO_4 tetrahedra share corners with FeO_6 units, binding the chains together as seen in Figure 5.1c-d. Table 5.1 also shows the experimental lattice parameters [292] for m-$NaFePO_4$. The Fe sites, contrary to the t-phase, are located at the inversion centers.

	m-phase			t-phase		
a (Å)	8.9628			10.3936		
b (Å)	6.8429			6.1979		
c (Å)	5.0283			4.9357		
Fe1	0.0	0.0	0.0	0.2875	0.75	0.9853
Fe2	0.5	0.0	0.5	0.7125	0.25	0.0147
Fe3	0.0	0.5	0.0	0.2125	0.25	0.4853
Fe4	0.5	0.5	0.5	0.7875	0.75	0.5147

TABLE 5.1: Experimental lattice parameters of m- and t-$NaFePO_4$ [292]. Positions of Fe atoms are given in fractional coordinates.

5.2.2 Electronic structure of $NaFePO_4$ in GGA

In order to properly parametrize the effective Hamiltonian, we first need to properly understand the electronic structure of the $NaFePO_4$ polymorphs in the absence of strong Coulomb interactions with the GGA functionals. For this, DFT calculations were performed using the GGA with the PBE exchange correlation functional [57]. The QE (version 6.1) package was used, where the core electrons were replaced with NCPPs, treating the Na ($3s^1$), Fe ($3d^64s^2$), P ($3s^23p^3$), and O ($2s^22p^4$) electrons explicitly as valence states. The plane wave basis set was expanded with a kinetic energy cutoff of 100 Ry (1360 eV) and a charge density cutoff of 400 Ry (5442 eV). A tight energy convergence criteria of 10^{-8} Ry (1.3^{-7} eV) was used with a **k**-point sampling of 4 × 8 × 10 (6 × 8 × 10) for t-(m-)$NaFePO_4$. All these parameters ensure a tight convergence of energy of less than 1 meV per atom.

The calculated GGA DOS for t- and m-$NaFePO_4$ are shown in Figure 5.2. The typical character of insulating TM oxides changes when increasing the atomic number along the Ti-Cu series [300]. Early TM oxides, including Ti, V, and Cr, are normally called Mott insulators, while late oxides exhibit a stronger charge transfer character, because the TM 3*d* states strongly hybridize with the O 2*p* states and, as a consequence, O atoms also contribute to the low-energy properties. Typically, the properties of Mott insulators can be described by a conventional Hubbard-type model. On the other hand, charge transfer insulators require more complex models that include the contribution of the O 2*p* bands. However, as already mentioned, the polyanionic compounds that are being treated here have strong inductive effects because of the PO_4^{-3} anion species. This leads to additional band splittings into the bonding states (mainly formed by the O 2*p* orbitals) and antibonding states (formed by the P 3*p* orbitals). As a consequence, the bonding O 2*p* states are additionally shifted to the low-energy region, which increases their separation from the Fe 3*d* states. Thus, as can be seen in Figure 5.2, the Fe 3*d* states

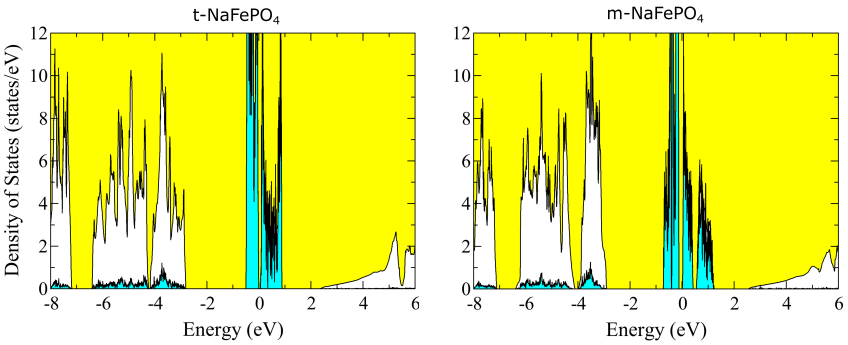

FIGURE 5.2: Total and partial PBE DOS for t- and m-$NaFePO_4$. The shaded blue bands shows contributions from the Fe 3*d* states. The Fermi level is at zero energy. Reprinted from *Phys. Chem. Chem. Phys.*, 2018, **20**, 13497 [299]. Licensed under Creative Commons Attribution-NonCommercial 3.0 Unported Licence.

form a narrow band located near the Fermi level, which is very well separated from both the O 2*p* bands (from below) and P 3*p* bands (from above). Such electronic structures are particularly suitable for applying a low energy Hubbard model exclusively on the Fe 3*d* states, as with Mott insulators.

5.2.3 Construction of the effective low energy Hubbard model

Effective low energy Hubbard models are useful tools to reproduce results of first-principles calculations, further treating the problem of electron correlations beyond what is possible with standard first-principles methods. This type of model Hamiltonians were defined for the particular case of NaO_2 clusters in Chapter 3, but more generally, and compactly, such models are defined here as follows:

$$\hat{H} = \sum_{ij} \sum_{\alpha\beta} t_{ij}^{\alpha\beta} \hat{c}_{i\alpha}^{\dagger} \hat{c}_{j\beta} + \frac{1}{2} \sum_{i} \sum_{\alpha\beta\gamma\delta} U_{\alpha\beta\gamma\delta}^{i} \hat{c}_{i\alpha}^{\dagger} \hat{c}_{i\gamma}^{\dagger} \hat{c}_{i\beta} \hat{c}_{i\delta}, \tag{5.1}$$

where $\hat{c}_{i\alpha}^{\dagger}$ ($\hat{c}_{i\alpha}$) are the creation (annihilation) operators acting at lattice points i, on a MLWF [121, 123, 124] $|w_{i\alpha}\rangle$, that is constructed from the set of magnetically active Fe 3*d* bands in t- and m-$NaFePO_4$ (see Figure 5.2). Here lattice points i (j) are specified by the position of the atomic site in the primitive cell

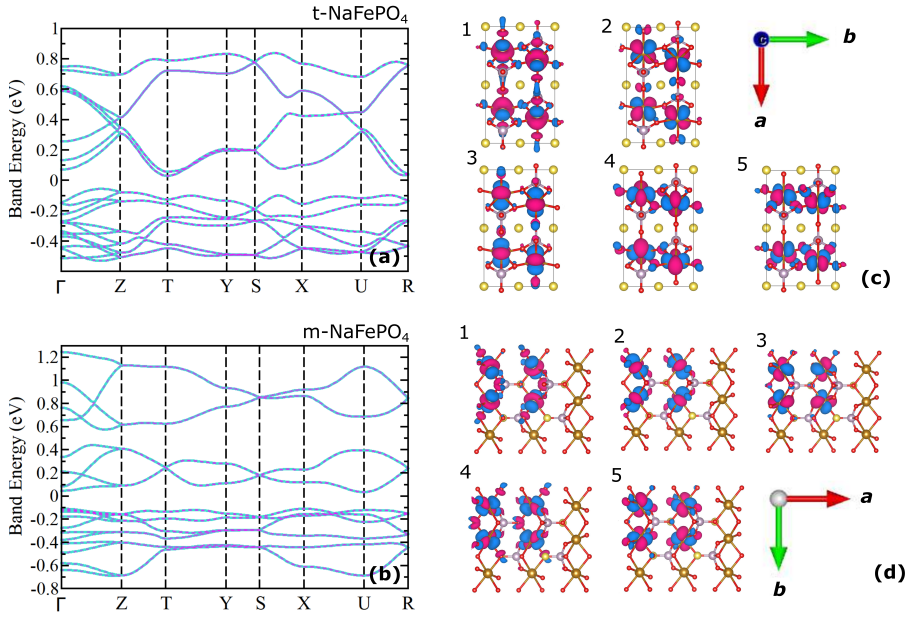

FIGURE 5.3: (a) PBE (turquoise solid lines) and (b) Wannier interpolated (blue dashed lines) band structures for the low-energy Fe 3*d* states as obtained for t- and m-$NaFePO_4$, respectively. The corresponding real-space Wannier functions centered at Fe sites are shown for t-$NaFePO_4$ (c) and m-$NaFePO_4$ (d). Notations of the high symmetry points of the Brillouin zones are taken from ref. [301]. Reprinted from *Phys. Chem. Chem. Phys.*, 2018, **20**, 13497 [299]. Licensed under Creative Commons Attribution-NonCommercial 3.0 Unported Licence.

$\boldsymbol{\tau}$ ($\boldsymbol{\tau'}$) and the lattice translation $\mathbf{R}$. The symbols (α, β, γ, and δ) stand for the combined indices of spin, with σ (σ') = $\uparrow$ or $\downarrow$; and orbitals (a, b, c, and d). For example $\alpha = (\sigma_a, a)$, being $\sigma_a = \sigma$ or σ'. Since the t- and m-$NaFePO_4$ contain four Fe sites per unit cell, the localization procedure yields a total of 20 Wannier orbitals, one for each band in the 3*d* manifold. The resulting Wannier functions are well localized at Fe sites, as shown in the Figure 5.3.

Indeed, for a = 1-5, the individual spreads, $< \mathbf{r}^2 >_a$, are 1.66, 1.04, 1.14, 1.21, and 1.47 Å^2 for t-$NaFePO_4$, and 1.62, 1.15, 1.01, 1.84, and 1.22 Å^2 for m-$NaFePO_4$. Additionally, the *d*-orbital character of the Wannier functions is visually apparent (Figure 5.3c-d). More precisely, it is possible to obtain the expansion of these Wannier orbitals in terms of the original trial cubic harmonics from the $\mathbf{A}^{(\mathbf{k})}$-matrix that is used in the wannierisation procedure

(see, e.g., the review by Marzari *et. al.* [302]) whose matrix elements are defined as:

$$A_{mn}^{(\mathbf{k})} = \langle \psi_{m\mathbf{k}} | g_n \rangle \,, \tag{5.2}$$

where $|\psi_{m\mathbf{k}}\rangle$ are the KS states of our DFT calculations with band index m and k-index $\mathbf{k}$, and $|g_n\rangle$ are the trial localized orbitals in the form of cubic harmonics, where n is the combined index of the sites $\boldsymbol{\tau}$ where such functions are centered, and the type of cubic orbital ($\lambda = xy$, yz, $3z^2 - r^2$, xz, and $x^2 - y^2$). Also, from the wannierization procedure one obtains the unitary matrix $\mathbf{U}^{(\mathbf{k})}$, that rotates the KS states (Bloch type) into the 'smooth' gauge $|\tilde{\psi}_{m\mathbf{k}}\rangle$, as already explained in Section 2.6. One could then equivalently transform the $\mathbf{A}^{(\mathbf{k})}$-matrix to this 'smooth gauge' with the following matrix multiplication:

$$\tilde{\mathbf{A}}^{(\mathbf{k})} = \mathbf{A}^{(\mathbf{k})\dagger} \mathbf{U}^{(\mathbf{k})}. \tag{5.3}$$

And then transform this matrix to the real space representation with a Fourier transform:

$$\tilde{\mathbf{A}}(\mathbf{R}) = \frac{1}{N_k} \sum_{\mathbf{k}} e^{-i\mathbf{k}\mathbf{R}} \tilde{\mathbf{A}}^{(\mathbf{k})}. \tag{5.4}$$

Focusing on the values of the home unit cell $\mathbf{R} = 0$, one can obtain the expansion of the Wannier orbitals extracted from the $3d$ bands of $NaFePO_4$ in terms of the trial orbitals from which they were obtained. These values then must be normalized with the overlap matrix $\mathbf{N}^{(\mathbf{k})} = \mathbf{A}^{(\mathbf{k})\dagger}\mathbf{A}^{(\mathbf{k})}$, which, after Fourier transforming like in Equation 5.3, $\tilde{\mathbf{A}}(\mathbf{R})$ normalizes as:

$$\mathbf{C}(0) = \mathbf{N}(0)^{-1/2} \tilde{\mathbf{A}}(0). \tag{5.5}$$

The matrix $\mathbf{C}(0)$ is a 20x20 matrix whose matrix elements are divided site-wise in 5x5 sub-matrices ($\mathbf{c}^{\boldsymbol{\tau},\boldsymbol{\tau}'}$) and are defined as:

$$c_{\lambda a}^{\boldsymbol{\tau},\boldsymbol{\tau}'} = \langle g_{\lambda\boldsymbol{\tau}} | w_{a\boldsymbol{\tau}'} \rangle \,. \tag{5.6}$$

Then, the site-diagonal sub-matrices ($\boldsymbol{\tau} = \boldsymbol{\tau}'$) give the final expansion of the localized Wannier orbitals in terms of the cubic harmonics as:

$$|w_{a\boldsymbol{\tau}}\rangle = \sum_{\lambda} c_{\lambda a}^{\boldsymbol{\tau},\boldsymbol{\tau}} \, |g_{\lambda\boldsymbol{\tau}}\rangle \,. \tag{5.7}$$

For instance, choosing the Fe1 site for both t- and m-$NaFePO_4$ results into the following expansion. Beginning with t-$NaFePO_4$:

$$\begin{aligned}
|w_{11}\rangle &= 0.98\,|g_{31}\rangle + 0.16\,|g_{41}\rangle - 0.09\,|g_{51}\rangle \\
|w_{21}\rangle &= -0.14\,|g_{31}\rangle + 0.96\,|g_{41}\rangle + 0.22\,|g_{51}\rangle \\
|w_{31}\rangle &= 0.18\,|g_{11}\rangle + 0.98\,|g_{21}\rangle \\
|w_{41}\rangle &= 0.12\,|g_{31}\rangle - 0.20\,|g_{41}\rangle + 0.97\,|g_{51}\rangle \\
|w_{51}\rangle &= 0.98\,|g_{11}\rangle - 0.18\,|g_{21}\rangle
\end{aligned} \tag{5.8}$$

Remember that the order of the cubic harmonics ($|g_{\lambda\boldsymbol{\tau}}\rangle$) is $\lambda = xy$, yz, $3z^2-r^2$, xz, and x^2-y^2. For the m-$NaFePO_4$ the expansion is the following:

$$\begin{aligned} |w_{11}\rangle &= |g_{31}\rangle\,,\ |w_{21}\rangle = |g_{41}\rangle\,,\ |w_{31}\rangle = |g_{21}\rangle \\ |w_{41}\rangle &= |g_{51}\rangle\,,\ |w_{51}\rangle = |g_{11}\rangle \end{aligned} \tag{5.9}$$

From these expressions we therefore confirm the d-orbital character of the extracted Wannier functions, whose stronger contributions are consistent with the Wannier functions represented in Figures 5.3b and 5.3d. Therefore, it is clear that, from 1 to 5, the ordering of the Wannier functions in Figure 5.3 is $3z^2-r^2$, xz, yz, x^2-y^2, and xy.

The second step, after obtaining the basis of Wannier functions $\{|w_{i\alpha}\rangle\}$, is constructing the one-electron part of the model (first term in Equation 5.1), identifying it, as already mentioned in Chapter 3, with the matrix elements of the GGA Hamiltonian in the Wannier basis: $t^{\alpha\beta}_{\boldsymbol{\tau},\boldsymbol{\tau'}+\mathbf{R}} = \langle w_{\boldsymbol{\tau}\alpha}|\hat{H}_{PBE}|w_{\boldsymbol{\tau'}+\mathbf{R}\beta}\rangle$. The construction of such one-electron part is exact, since the Wannier basis is complete for the $3d$ bands, as there is virtually no contribution from the oxygen in the low energy region. And therefore, Fourier transforming $t^{\alpha\beta}_{\boldsymbol{\tau},\boldsymbol{\tau'}+\mathbf{R}}$ back to the reciprocal space and diagonalizing it should result in the exact same band structure as the one obtained from PBE. This is indeed the case as can be seen in Figures 5.3a-b.

The third step is the parametrization of the screened Coulomb interactions (second term in Equation 5.1) in this Wannier basis. Its matrix elements are computed as:

$$U^{\boldsymbol{\tau}}_{\alpha\beta\gamma\delta} = \int\int d\mathbf{r}d\mathbf{r}' w^{\dagger}_{\boldsymbol{\tau}\alpha}(\mathbf{r}) w_{\boldsymbol{\tau}\beta}(\mathbf{r}) v_{scr}(\mathbf{r},\mathbf{r}') w^{\dagger}_{\boldsymbol{\tau}\gamma}(\mathbf{r}') w_{\boldsymbol{\tau}\delta}(\mathbf{r}'). \tag{5.10}$$

The screened Coulomb interaction $v_{scr}(\mathbf{r},\mathbf{r}')$ can be computed with the constrained random-phase approximation (cRPA) [193, 303]. Note that since $v_{scr}(\mathbf{r},\mathbf{r}')$ does not depend on spin variables, then $U_{\alpha\beta\gamma\delta}$ will not either. Therefore, $U^{\boldsymbol{\tau}}_{\alpha\beta\gamma\delta} = U^{\boldsymbol{\tau}}_{abcd}\delta_{\sigma_\alpha\sigma_\beta}\delta_{\sigma_\gamma\sigma_\delta}$.

In principle, it is possible to fully parametrize a multi-orbital Hubbard Hamiltonian with the steps mentioned above. However, there are still some physical considerations to take into account when evaluating the one-electron part of the model Hamiltonian $\hat{t} = [t^{\alpha\beta}_{\boldsymbol{\tau},\boldsymbol{\tau'}+\mathbf{R}}]$. In the following we consider three computation schemes, all related to the treatment of the double counting of the non-sphericity of the Coulomb and xc-potentials in the model.

A. Scheme 1 (s1)

In this scheme, the one-electron part is evaluated 'as is', directly identifying its elements with the matrix elements of the GGA Hamiltonian calculated in the Wannier basis. In this case, $\hat{t}$ already takes into account non-spherical contributions of the Coulomb and xc-potential. Therefore, in order to avoid double counting, we have to remove these contributions from the Coulomb and exchange interactions in the Hubbard model (contained in $U^{\boldsymbol{\tau}}_{abcd}$). For this, instead of considering the full screened Coulomb interactions obtained from cRPA, $\hat{U} = [U_{abcd}]$, a spherical parametrization is used with the on-site Coulomb repulsion $U = F^0$, intra-atomic exchange interaction $J = (F^2 + F^4)/14$, and the 'nonsphericity' $B = (9F^2 - 5F^4)/441$, where F^0, F^2, and F^4 are the screened radial Slater's integrals. This parametrization fully specifies $\hat{U}$ in an spherical atomic environment. Then, when solving the Hubbard Hamiltonian in the mean-field HF approximation (which is going to be introduced in the next Section 5.2.4), U_{aabb} is set to U for any a and b, and $U_{abba} = J$ for $a \neq b$. This ensures that the Coulomb part of the HF potential is spherical, and the exchange part, besides intra-atomic Hund's rule, is responsible for the appearance of a discontinuity term, which is proportional to $U - J$ and missing in ordinary GGA. The rest of the effects are included in $\hat{t}$ which is described at the GGA level. The logic behind this approach consists of assuming that the non-spherical contribution of the d^6 electron configuration of the Fe^{+2} ions of $NaFePO_4$ is, to a certain extent, properly described with GGA. So it is possible to ignore non-spherical effects obtained in cRPA.

B. Scheme 2 (s2)

In the second scheme the matrix elements of the GGA xc-potential are subtracted from $\hat{t}$ in the Wannier basis. First, the xc-potential ($\hat{V}^{xc}$) is obtained in the KS basis. Their matrix elements are written as:

$$V^{xc}_{nm}(\mathbf{k}) = \langle \psi_{n\mathbf{k}} | \hat{V}^{xc} | \psi_{m\mathbf{k}} \rangle \,. \tag{5.11}$$

Rotating to the 'smooth' representation of the Bloch states by considering the following matrix multiplication:

$$\tilde{\mathbf{V}}^{xc}_{(\mathbf{k})} = \mathbf{U}^{(\mathbf{k}\dagger)} \mathbf{V}^{xc}_{(\mathbf{k})} \mathbf{U}^{(\mathbf{k})}. \tag{5.12}$$

And Fourier transforming this matrix by summing over all $\mathbf{k}$-points in the Brillouin zone:

$$\tilde{\mathbf{V}}^{xc}(\mathbf{R}) = \frac{1}{N_k} \sum_{\mathbf{k}} e^{-i\mathbf{k}\mathbf{R}} \tilde{\mathbf{V}}^{xc}_{(\mathbf{k})}. \tag{5.13}$$

In this way it is possible to obtain the GGA xc-potential in the basis of Wannier functions. The basic idea behind this approach is to fully replace the

xc-interactions in GGA by the ones obtained from the Hubbard model. Thus, in the HF calculations the full Coulomb matrix is used $\hat{U} = [U_{abcd}]$, obtained in cRPA without any additional approximations for the exchange part of the HF potential. Simultaneously, the non-sphericity of the Coulomb potential is still expected to be well treated at the GGA level and already included in $\hat{t}$. Therefore, when using the HF method, still the spherical form of $\hat{U}$ is used. Therefore the Coulomb potential is described with a single parameter, $U_{aabb} = U$.

Moreover, two further approximations are considered. Concretely, considering the matrix elements at the home unit cell $\tilde{\mathbf{V}}^{xc}(\mathbf{R} = 0)$, similar to the case of Equation 5.5, we can subdivide the 20x20 matrix site-wise into 5x5 submatrices ($\tilde{\mathbf{v}}^{\boldsymbol{\tau},\boldsymbol{\tau'}}$). In the first approximation, we subtract from $\hat{t}$ only site-diagonal matrix elements of the xc-potential where $\boldsymbol{\tau} = \boldsymbol{\tau'}$. The logic is that since the Hubbard model (Equation 5.1) includes the on-site interactions, only the on-site interactions should be subtracted from GGA, assuming that other (intersite) interactions are described reasonably well at the GGA level. In the second approximation, we subtract both site diagonal and intersite matrix elements, $\tilde{\mathbf{v}}^{\boldsymbol{\tau},\boldsymbol{\tau'}+\mathbf{R}}$.

C. Scheme 3 (s3)

This scheme is based on the LMTO method [298]. The additional atomic-spheres approximation (ASA) in the LMTO method leads to some limitations for treating the electronic structure of $NaFePO_4$. In this scheme the atomic spheres in LMTO were selected so as to reproduce the electronic structure of the more precise QE calculations of the schemes 1 and 2. Nevertheless, the use of the LMTO method provides yet another way of treating the non-spherical on-site Coulomb and xc-interactions in GGA. For instance, in ASA, all these interactions are spherically averaged inside the atomic spheres. Therefore, there is no need to worry about the double counting of this non-sphericity in GGA, and all non-sphericity arises solely from the screened Coulomb and exchange interactions in the Hubbard model. In ASA, one should include additional corrections regarding the non-sphericity of the inter-site Madelung potential, and some extra approximations when dealing with the cRPA calculations in LMTO (the interested reader is encouraged to follow the review by I. V. Solovyev [298]). For instance, instead of constructing a proper Wannier basis, we use the pseudo-atomic LMTO basis to calculate $\hat{U}$. And since atomic orbitals are more localized than Wannier functions, we expect the effective Coulomb interactions to be larger in this scheme, compared to the former two.

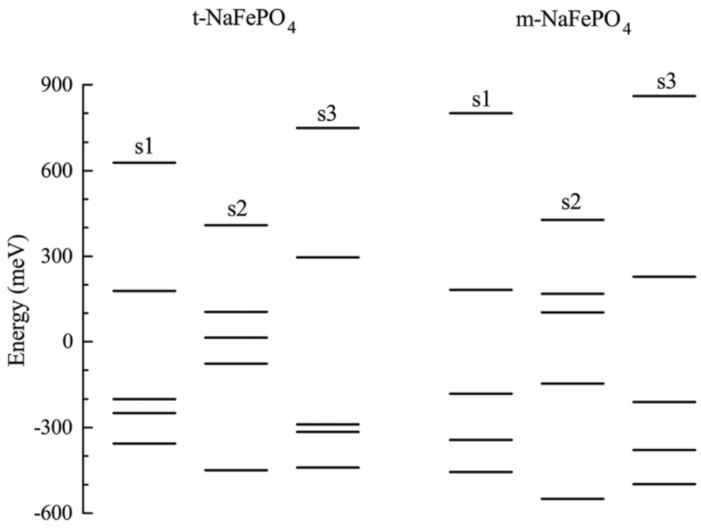

FIGURE 5.4: Crystal-field splitting as obtained from QE with (s2) and without (s1) subtraction of the matrix elements of the GGA xc-potential, and LMTO method (s3) for the Fe 3*d* states of t- and m-$NaFePO_4$. Reprinted from *Phys. Chem. Chem. Phys.*, 2018, **20**, 13497 [299]. Licensed under Creative Commons Attribution-NonCommercial 3.0 Unported Licence.

Crystal field splitting

The corresponding crystal-field (CF) splitting obtained from the diagonalization of the site-diagonal parts of $\hat{t} = [t^{\alpha\beta}_{\tau\tau}]$ is shown in Figure 5.4. In the case of Fe^{+2} ions, for a high-spin configuration (S = 2), the majority-spin electron levels are all occupied while the lowest energy orbital is occupied by the only minority-spin electron. In both LMTO (s3) and QE (s1) the energy splitting between orbitals 1 and 2 is of the order of 100 meV. The subtraction of $\tilde{\mathbf{v}}^{\tau,\tau}$ in s2 additionally splits off the orbital 1, to around 400 meV. The shape of orbital 1 and its orientations between different Fe sites also changes upon s1, s2, or s3 schemes. Its effect will be considered later when discussing the results for m- and t-$NaFePO_4$.

Lastly, one could further include the spin-orbit coupling by directly solving the electronic structure of $NaFePO_4$ in the GGA+SO approximation, and evaluating the Hubbard model (Equation 5.1) in the basis of relativistic Wannier functions. One could also make use of the expressions in Equations 5.8 and 5.9, and add the SO coupling with the form $\zeta \hat{L} \cdot \hat{S}$ which has known matrix elements in the basis of atomic orbitals. Its strength (ζ) can then be extracted

from the additional splitting of the energy levels in Figure 5.4 considering the SO coupling. In cases where SO coupling is small, so that the electronic structure is not largely changed, and relativistic and non-relativistic Wannier functions do not change much, direct comparison between the site-diagonal parts of the GGA and GGA+SO Hamiltonian, in their respective Wannier basis, can directly yield the on-site contributions of the SO potential.

The calculations in this chapter do not include the SO coupling for the most part. Note that if the SO coupling is not included, the transfer integrals do not depend on spin indices and are then further simplified as $\hat{t}_{\boldsymbol{\tau},\boldsymbol{\tau'}+\mathbf{R}} = [t^{ab}_{\boldsymbol{\tau},\boldsymbol{\tau'}+\mathbf{R}}\delta_{\sigma_\alpha\sigma_\beta}]$. However, we acknowledge that further analysis including these effects might be needed to quantitatively analyze other properties, such as the Dzyaloshinskii-Moriya (DM) interactions, or higher order anisotropic magnetic interactions. For instance, the emergence of electric polarization, because of the magnetoelectric effect, is allowed by combining the inversion ($\hat{I}$) and time-reversal ($\hat{T}$) symmetries. In principle, one does not need to include SO interactions in order to stabilize concrete magnetic orderings that break the inversion symmetry. However it is proven that [304], without SO, although lattice inversion is formally broken by the magnetic structure, the emergence of electric polarization is still forbidden. In this case higher order DM and anisotropic magnetic interactions are needed, which arise from the SO coupling, in order to allow for such effects.

This chapter generally describes the process of parametrizing a model Hubbard Hamiltonian. In the following, a simple solution of the model Hamiltonian (Equation 5.1) is described by means of the mean-field HF method. Then, from the solution of such HF methods, further post-processing methods are going to be described in order to calculate the isotropic exchange interactions. We also shortly describe the process of obtaining anisotropic magnetic couplings.

5.2.4 The mean-field HF method

Once the Hubbard model (Equation 5.1) is constructed, it is solved in the mean-field HF approximation, which is the lattice version of the methods introduced in Subsection 2.2.1. This is the simplest approach, which treats the correlation term $\hat{c}^\dagger_{i\alpha}\hat{c}^\dagger_{i\gamma}\hat{c}_{i\beta}\hat{c}_{i\delta}$ as a pair-wise average, neglecting higher order correlation terms (other more refined methods such as the dynamical mean-field theory [305] include further quantum effects). In the case of $NaFePO_4$, the degeneracy of the energy levels is lifted by the heavily distorted octahedral environments of Fe ions, as can be seen in Figure 5.4. In this instance, the ground state wavefunction can be correctly described by a single Slater determinant, which justifies the use of the mean-field HF approximation in these compounds. From this approximation, the one-electron HF equations that are

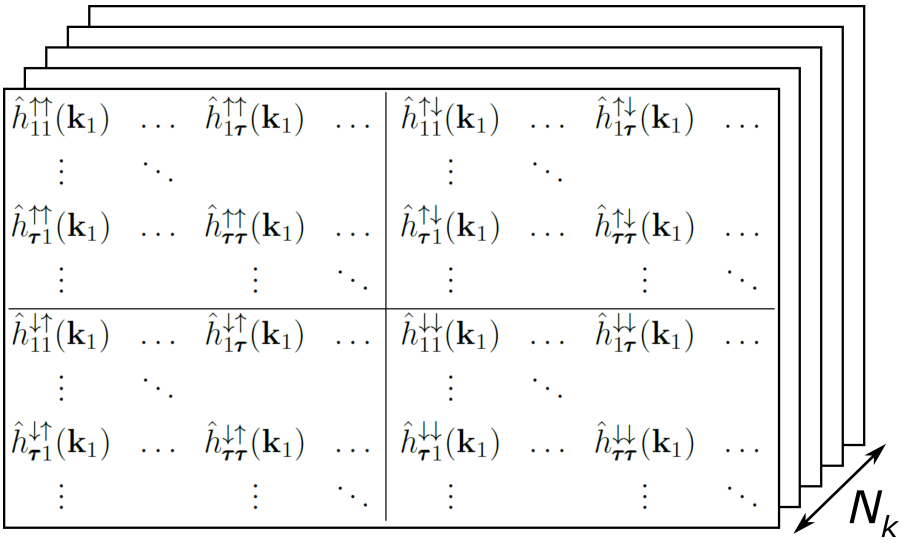

FIGURE 5.5: Shape of the $\hat{H}_{HF}(\mathbf{k})$ matrix. The matrix is divided by spin subspaces and each subspace is divided by the matrices $[h_{\boldsymbol{\tau}\boldsymbol{\tau}'}^{ab,\sigma\sigma'}(\mathbf{k})]$. The third dimension of the matrix represent the $\mathbf{k}$-point in the BZ where $[\hat{t}(\mathbf{k}) + \hat{v}]$ is evaluated.

obtained for the periodic Hubbard model, can be conveniently formulated in the matrix form, in each point of the Brillouin zone (BZ):

$$\hat{H}_{HF}(\mathbf{k}) \left|C_{\nu\mathbf{k}}\right\rangle = \epsilon_{\nu\mathbf{k}} \left|C_{\nu\mathbf{k}}\right\rangle, \tag{5.14}$$

where the matrix $\hat{H}_{HF}(\mathbf{k}) = [\hat{t}(\mathbf{k}) + \hat{v}]$ is composed of submatrices $\hat{h}_{\boldsymbol{\tau}\boldsymbol{\tau}'}^{\sigma\sigma'}(\mathbf{k}) = [h_{\boldsymbol{\tau}\boldsymbol{\tau}'}^{ab,\sigma\sigma'}(\mathbf{k})]$, containing the spin ($\sigma$, σ') and orbital (a and b) indices; and the positions of atomic sites ($\boldsymbol{\tau}$, $\boldsymbol{\tau}'$) in the primitive cell. The diagonalization of these supermatrices for each $\mathbf{k}$ point yields the eigenvectors $|C_{\nu\mathbf{k}}\rangle$ and eigenvalues $\epsilon_{\nu\mathbf{k}}$, where the band index ν also includes the information about the spin. Figure 5.5 shows a schematic representation of the supermatrix $\hat{H}_{HF}(\mathbf{k})$. The elements of the supermatrix $\hat{t}(\mathbf{k})$ are defined directly as the Fourier images of the matrix elements of the GGA Hamiltonian $\hat{t}_{\boldsymbol{\tau},\boldsymbol{\tau}'+\mathbf{R}} = [t_{\boldsymbol{\tau},\boldsymbol{\tau}'+\mathbf{R}}^{\alpha\beta}]$ in the Wannier basis. The supermatrix $\hat{t}(\mathbf{k})$ is then defined from the following matrices:

$$\hat{t}_{\boldsymbol{\tau}\boldsymbol{\tau}'}(\mathbf{k}) = \sum_{\mathbf{R}} \hat{t}_{\boldsymbol{\tau},\boldsymbol{\tau}'+\mathbf{R}} e^{i\mathbf{k}\cdot(\boldsymbol{\tau}'-\boldsymbol{\tau}+\mathbf{R})}, \tag{5.15}$$

$\hat{v} = [v_{ab,\boldsymbol{\tau}}^{\sigma\sigma'}]$ is the self-consistent HF potential, which is diagonal with respect to

site indices $\boldsymbol{\tau}$. It can be obtained by using the screened Coulomb interactions ($U^{\boldsymbol{\tau}}_{abcd}$) and the occupation matrix $\hat{n} = [n^{\sigma\sigma'}_{ab,\boldsymbol{\tau}}]$, whose matrix elements are defined as:

$$n^{\sigma\sigma'}_{ab,\boldsymbol{\tau}} = \frac{1}{N_k}\sum_{\nu}^{occ}\sum_{\mathbf{k}}^{BZ}(C^{a\sigma\boldsymbol{\tau}}_{\nu\mathbf{k}})^* C^{b\sigma'\boldsymbol{\tau}}_{\nu\mathbf{k}}, \tag{5.16}$$

where $C^{a\sigma\boldsymbol{\tau}}_{\nu\mathbf{k}}$ and $C^{b\sigma'\boldsymbol{\tau}}_{\nu\mathbf{k}}$ are the elements of the vector $|C_{\nu\mathbf{k}}\rangle$, the summation runs over all the occupied states first, and then it runs over all $\mathbf{k}$-points in the BZ. Then the matrix elements of the HF potential ($\hat{v}$) are going to be defined as the following, for the diagonal elements with respect to spin indices:

$$v^{\sigma\sigma}_{ab,\boldsymbol{\tau}} = \sum_{cd}(U^{\boldsymbol{\tau}}_{abcd} - J^{\boldsymbol{\tau}}_{abcd})n^{\sigma\sigma}_{cd,\boldsymbol{\tau}} + U^{\boldsymbol{\tau}}_{abcd}n^{\sigma'\sigma'}_{cd,\boldsymbol{\tau}}. \tag{5.17}$$

and the non-diagonal ones:

$$v^{\sigma\sigma'}_{ab,\boldsymbol{\tau}} = -\sum_{cd} J^{\boldsymbol{\tau}}_{abcd}n^{\sigma'\sigma}_{cd,\boldsymbol{\tau}}, \tag{5.18}$$

where $J^{\boldsymbol{\tau}}_{abcd} = U^{\boldsymbol{\tau}}_{adcb}$. As we noted earlier, the non-diagonal elements are produced by the SO coupling and non-collinear magnetic alignments. If SO coupling is not included, one can always select a quantization axis so that the non-diagonal elements are zero (including the elements from Equation 5.18). Therefore, the equations for the spin-up and spin-down channels can be solved separately, and we get separate eigenvectors $|C^{\sigma}_{n\mathbf{k}}\rangle$ and eigenvalues $\epsilon^{\sigma}_{n\mathbf{k}}$ for each spin channel. Similarly, the computed HF potential $\hat{v}$ and occupation matrix $\hat{n}$ will have separate components for both spin channels. Then, this set of equations can be solved self consistently with respect to the total energy. For the general case:

$$E^{HF} = \frac{1}{N_k}\sum_{\nu}^{occ}\sum_{\mathbf{k}}^{BZ}\epsilon_{\nu\mathbf{k}} - \frac{1}{2}\sum_{\sigma\sigma'}\sum_{\boldsymbol{\tau}} Tr\{\hat{v}^{\sigma\sigma'}_{\boldsymbol{\tau}}(\hat{n}^{\sigma\sigma'}_{\boldsymbol{\tau}})^T\}. \tag{5.19}$$

This method is implemented in FORTRAN90, it is stable (as far as I know), and freely available in GitHub (https://github.com/oarcelus/MFHF). The details about the code and the form of usage can be found in Appendix B.

5.2.5 Spin models

The low energy model in Equation 5.1 can be mapped onto a classical spin model of the type:

$$E = -\sum_{i>j} J_{ij}\mathbf{e}_i\cdot\mathbf{e}_j + \sum_{i>j}\mathbf{d}_{ij}\cdot[\mathbf{e}_i\times\mathbf{e}_j] + \sum_{i\geq j}\mathbf{e}_i\cdot\hat{\tau}_{ij}\cdot\mathbf{e}_j, \tag{5.20}$$

where $\mathbf{e}_i$ is the direction of spin at the site i. Remember that i (j) implies a site at position $\boldsymbol{\tau}$ ($\boldsymbol{\tau}' + \mathbf{R}$). The first term represents the isotropic Heisenberg term, with exchange interactions J_{ij}. The second term represents the antisymmetric Dzyaloshinskii-Moriya (DM) interactions. The last term is the symmetric anisotropic interaction whose contribution is neglected on this chapter. Here we will mainly focus in the isotropic Heisenberg term that can be evaluated without the inclusion of SO coupling, and later we will shortly discuss the effect of the SO interaction in the computation of DM interactions. In the following we present two approaches to calculate the magnetic interactions in Equation 5.20.

A. The Green's function approach

The parameters J_{ij}, $\mathbf{d}_{ij}$ can be extracted from a collinear magnetic configuration obtained from HF calculations without the SO coupling, and by considering the perturbations to the HF potential caused by the SO coupling at the zeroth and first order, respectively. From the solution of the HF equations, one can define the one-electron (non-interacting) retarded Green's function in the spectral representation for all the bonds i-j in the system as:

$$\hat{G}^{\sigma}_{ij}(\omega) = \frac{1}{N_k} \sum_{n\mathbf{k}} \frac{|C^{\sigma}_{n\mathbf{k}}\rangle \langle C^{\sigma}_{n\mathbf{k}}|}{\omega - \epsilon^{\sigma}_{n\mathbf{k}} + i\delta} e^{i\mathbf{k}(\boldsymbol{\tau} - \boldsymbol{\tau}' - \mathbf{R})}. \tag{5.21}$$

where δ is a small number. Once we define the Green's function, let us consider the force component of an infinitesimal rotation around a magnetic site i, i.e., $\boldsymbol{f}_i = -\partial E/\partial \mathbf{e}_i$. From Equation 5.20, the force can be written as a sum:

$$\boldsymbol{f}_i = \sum_j \boldsymbol{f}^j_i. \tag{5.22}$$

where

$$\boldsymbol{f}^j_i = [\mathbf{d}_{ij} \times \mathbf{e}_j] + J_{ij}\mathbf{e}_j \tag{5.23}$$

is the force that a spin at site i feels from the effect of the spin at site j.

If we consider the direction of the spin without any SO coupling, $\mathbf{e}^0_j$, the inclusion of the SO coupling will tilt the direction of spins through a correction $\delta\mathbf{e}_j$. So that $\mathbf{e}_j = \mathbf{e}^0_j + \delta\mathbf{e}_j$. And therefore we can construct the following convenient expression:

$$\frac{1}{2}(\boldsymbol{f}^j_i - \boldsymbol{f}^i_j) = [\mathbf{d}_{ij} \times \mathbf{e}^0_j] + \frac{1}{2} J_{ij}(\delta\mathbf{e}_j - \delta\mathbf{e}_i). \tag{5.24}$$

Then, we apply the Lloyd's formula to calculate the changes in single-particle energies as second order perturbations with respect to a given applied potential [306]. This way we are able to map Equation 5.24 with the forces

obtained from the expressions derived from the Lloyd's formula. Particularly, the isotropic magnetic exchange parameters are obtained with the Lichtenstein formula (LF) [307]:

$$J_{ij} = \frac{1}{2\pi} Im \int_{-\infty}^{E_F} d\omega \; Tr_L\{\hat{G}_{ij}^{\uparrow}(\omega)\Delta\hat{v}_j\hat{G}_{ji}^{\downarrow}(\omega)\Delta\hat{v}_i\}. \tag{5.25}$$

Here, $\Delta\hat{v}_i$ is the exchange field derived from the up and down-spin components of the HF potential $\hat{v}_i$ at site i ($\Delta\hat{v}_i = \hat{v}_i^{\uparrow}$ - $\hat{v}_i^{\downarrow}$). The trace (Tr_L) runs the summation over the orbital indices. The force components of Equation 5.24 can be similarly computed as:

$$\frac{1}{2}(\boldsymbol{f}_i^j - \boldsymbol{f}_j^i) = \frac{1}{2\pi} Im \int_{-\infty}^{E_F} d\omega \; Tr\{\hat{\hat{G}}_{ij}(\omega)\delta\hat{v}_j^p\hat{\hat{G}}_{ji}(\omega)\Delta\hat{v}_i\hat{\boldsymbol{\sigma}} - \hat{\hat{G}}_{ij}(\omega)\Delta\hat{v}_j\hat{\boldsymbol{\sigma}}\hat{\hat{G}}_{ji}(\omega)\delta\hat{v}_i^p\}, \tag{5.26}$$

where

$$\hat{\hat{G}}_{ij}(\omega) = \begin{pmatrix} \hat{G}_{ij}^{\uparrow}(\omega) & 0 \\ 0 & \hat{G}_{ij}^{\downarrow}(\omega) \end{pmatrix} \tag{5.27}$$

is constructed from the Green's function without SO coupling. The $\hat{\boldsymbol{\sigma}}$ is a vector of Pauli matrices with x, y, and z components; and the matrix $\delta\hat{v}^p$ is obtained with the self-consistent linear response theory (SCLR) with respect to an external potential ($\delta\hat{v}^{ext}$), which we consider to be the SO interaction. By comparing Equations 5.26 and 5.25, with Equation 5.24, one can obtain $[\mathbf{d}_{ij} \times \mathbf{e}_j^0]$. Then, considering $\mathbf{e}_j^0 = (0, 0, 1)$, we will get the x and y components of $\mathbf{d}_{ij}$. By rotating the spin $\mathbf{e}_j^0$ and re-calculating the expressions above, we obtain the rest of the components for $\mathbf{d}_{ij}$. The whole process of SCLR is explained in detail in the work by I. V. Solovyev [308]. Briefly, the process consists of computing the response tensor from the solution of the HF equations as:

$$\boldsymbol{R}_{ij,abcd}^{\sigma\sigma'} = \frac{1}{N_k}\sum_{m}^{occ}\sum_{l}^{unocc}\sum_{\mathbf{k}}^{BZ} \frac{(C_{m\mathbf{k}}^{a\sigma i})^* C_{l\mathbf{k}}^{b\sigma' i}(C_{l\mathbf{k}}^{c\sigma' j})^* C_{m\mathbf{k}}^{d\sigma j}}{\epsilon_{m\sigma\mathbf{k}} - \epsilon_{l\sigma'\mathbf{k}}} + \frac{(C_{l\mathbf{k}}^{a\sigma i})^* C_{m\mathbf{k}}^{b\sigma' i}(C_{m\mathbf{k}}^{c\sigma' j})^* C_{l\mathbf{k}}^{d\sigma j}}{\epsilon_{m\sigma'\mathbf{k}} - \epsilon_{l\sigma\mathbf{k}}}. \tag{5.28}$$

Then, we compute the total perturbation $\delta\hat{v}^p$, which can be regarded as the 'screened' SO coupling, and derived properties, such as the change in density ($\delta\hat{n}_i$) and the change in the HF potential ($\delta\hat{v}_i$):

$$\delta\hat{v}_i^p = [1 - \hat{\mathbb{U}}_i\hat{\mathbb{R}}_{ij}]^{-1}\delta\hat{v}_j^{ext}; \quad \delta\hat{n}_i = \hat{\mathbb{R}}_{ij}\delta\hat{v}_j^p; \quad \delta\hat{v}_i = \hat{\mathbb{U}}_i\hat{\mathbb{R}}_{ij}\delta\hat{v}_j^p \tag{5.29}$$

where $\hat{\mathbb{U}}_i$ and $\hat{\mathbb{R}}_{ij}$ are the matrices that define the operations between different spin subspaces in a compact way. For instance:

$$\hat{\mathbb{R}}_{ij} = \begin{pmatrix} \hat{\boldsymbol{R}}_{ij}^{\uparrow\uparrow} & 0 & 0 & 0 \\ 0 & 0 & \hat{\boldsymbol{R}}_{ij}^{\downarrow\uparrow} & 0 \\ 0 & \hat{\boldsymbol{R}}_{ij}^{\uparrow\downarrow} & 0 & 0 \\ 0 & 0 & 0 & \hat{\boldsymbol{R}}_{ij}^{\downarrow\downarrow} \end{pmatrix}; \hat{\mathbb{U}}_i = \begin{pmatrix} \hat{\boldsymbol{U}}_i - \hat{\boldsymbol{J}}_i & 0 & 0 & \hat{\boldsymbol{U}}_i \\ 0 & 0 & -\hat{\boldsymbol{J}}_i & 0 \\ 0 & -\hat{\boldsymbol{J}}_i & 0 & 0 \\ \hat{\boldsymbol{U}}_i & 0 & 0 & \hat{\boldsymbol{U}}_i - \hat{\boldsymbol{J}}_i \end{pmatrix} \tag{5.30}$$

and each sub-block is defined as $\hat{\boldsymbol{R}}_{ij}^{\sigma\sigma'} = [\boldsymbol{R}_{ij,abcd}^{\sigma\sigma'}]$, $\hat{\boldsymbol{U}}_i = [U_{abcd}^i]$, and $\hat{\boldsymbol{J}}_i = [J_{abcd}^i]$. The way these matrices operate with $\delta\hat{v}^p$ is easily viewed as a matrix and column vector multiplication, if $\delta\hat{v}^p$ is rearranged as:

$$\delta\hat{v}_j^p = \begin{pmatrix} \delta\hat{v}_j^{p\uparrow\uparrow} \\ \delta\hat{v}_j^{p\downarrow\uparrow} \\ \delta\hat{v}_j^{p\uparrow\downarrow} \\ \delta\hat{v}_j^{p\downarrow\downarrow} \end{pmatrix}. \tag{5.31}$$

The same holds for other quantities, for instance, $\delta\hat{n}_i$ and $\delta\hat{v}_i$.

This method is also implemented as a post-processing tool to the code presented in Appendix B. It is written in FORTRAN90, and freely available at GitHub (https://github.com/oarcelus/HFPP). A general description of the code and its form of usage can be found in Appendix C. More details about the computation of the formulas above, specially the integrals in Equations 5.25 and 5.26, are given in Appendix D.

B. The superexchange theory

Here we briefly explain how to derive the isotropic exchange parameters J_{ij} by using the SE theory (Section 3.2.4 also explains the method in detail for the particular case of $(NaO_2)_n$ clusters). In short, when the transfer integrals, that account for the one-electron part of Equation 5.1 between sites $i-j$, are orders of magnitude smaller than on-site interactions, i.e., $t/U \ll 1$, they can be treated perturbatively. The SE interaction is considered to be the kinetic energy gain acquired by an electron in the process of virtual hoppings between an occupied state at site i and the space of unnocupied states at a site j. This kinetic energy gain can be computed for FM ($T_{ij}^{\uparrow\uparrow}$) and AFM ($T_{ij}^{\uparrow\downarrow}$) configurations in the bond $i-j$, and its difference mapped onto a classical spin Hamiltonian (see Equation 5.20).

The simplest case is just to drop the SO interaction dependent terms in Equation 5.20, and just consider the isotropic J_{ij} interactions. We note that there exist other more convoluted approaches to the theory of SE interactions, were

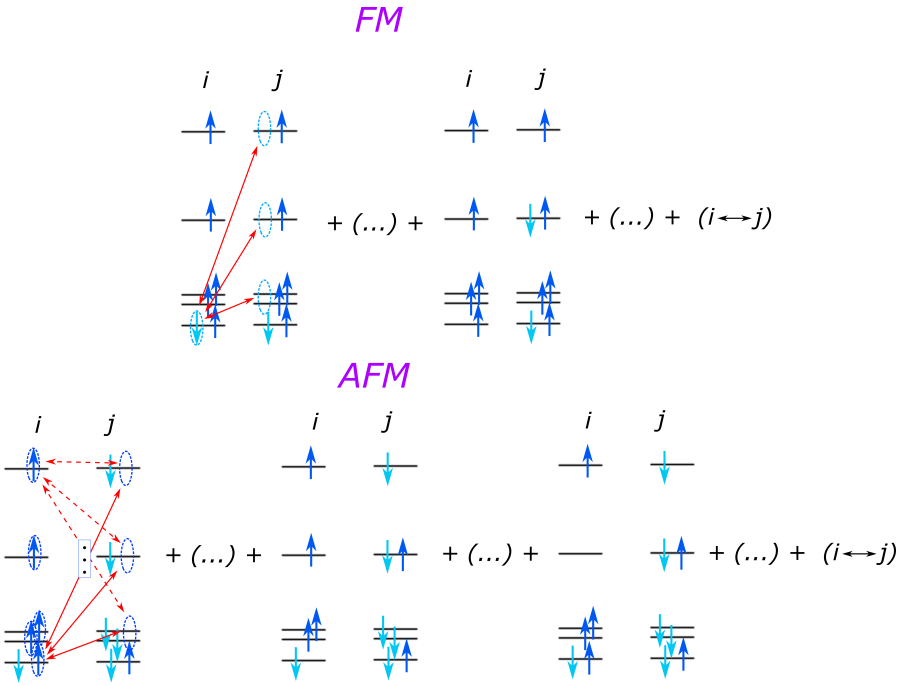

FIGURE 5.6: Scheme representing the process of virtual hoppings between the GS configurations (defined by the CF orbitals) between sites $i - j$ and CF orbitals of Fe^{2+} ions, for FM (top) and AFM (bottom) configurations. Blue (turquoise) arrows represent spin-up (-down) electrons. Red arrows represent all the combinations of hoppings between the space of occupied states in site i to the space of unoccupied states in site j.

many body effects are considered and SO interactions can be included [309]. In this case, a full parameterization of the spin Hamiltonian (Equation 5.20) is possible. In our case, we consider that the ground state (GS) configuration of the bond $i - j$ is defined only by the CF orbitals, obtained by diagonalizing the site-diagonal elements of $\hat{t}$, and defined in Figure 5.4. The virtual hoppings of electrons then occur between these orbitals. For the specific case of $NaFePO_4$, recalling the Equation 3.9, the expression that parametrize the interactions J_{ij} is defined as:

$$J_{ij} = \frac{1}{2}\sum_{b=2}^{5}\frac{(t_{ij}^{1b})^2 + (t_{ij}^{b1})^2}{U - J + \epsilon_b - \epsilon_1} - \frac{1}{2}\sum_{a=1}^{5}\sum_{b=2}^{5}\frac{(t_{ij}^{ab})^2 + (t_{ij}^{ba})^2}{U + 3J + \epsilon_b - \epsilon_a}. \tag{5.32}$$

Here, the first term stands for the FM coupling, caused by the occupation of the lowest energy CF orbital by the minority spin electron. The second term

is the AFM coupling describing the interaction of all majority-spin orbitals at site i (a runs from 1 to 5) with the orbitals at site j, except the lowest energy orbital, which is doubly occupied. Figure 5.6 shows a schematic representation of the virtual hoppings occurring between Fe^{2+} sites in $NaFePO_4$. In this expression, it is assumed that the transfer integrals t_{ij}^{ab} are rotated to the CF representation, which diagonalizes the site-diagonal part of $\hat{t}$. The values of U and J represent the spherical parameterization of the screened Coulomb interactions (as explained in Section 5.2.3), and ϵ_a are the energy eigenvalues of the corresponding CF orbitals.

As we already mentioned, most of the results and discussions that are going to be presented in the following sections are based on the evaluation of isotropic J_{ij}, this is why the more generalized version of the SE interactions, which also includes SO coupling, and is able to extract anisotropic DM parameters ($\mathbf{d}_{ij}$ in Equation 5.20), has not been used. We will stick to the simpler version here, since the effect of the SO coupling is not crucial to the main points of the discussion. Just for purposes of completeness, we will, in the end, shortly discuss the inclusion of the SO coupling by means of the SCLR method.

5.3 Results and discussions

5.3.1 m-$NaFePO_4$

We start our analysis with m-$NaFePO_4$. From the computational viewpoint, this is a somewhat simpler case when compared to t-$NaFePO_4$, since the Fe^{2+} ions are located at the inversion centers, and the computation of the Hamiltonian parameters in the three schemes (s1-s3), resulted to be successful, including the computation of costly and time consuming cRPA calculations of the screened Coulomb interactions.

Figure 5.7 shows the parameters of the effective Coulomb and exchange interactions obtained in cRPA. As expected, the effective Coulomb repulsion calculated with LMTO method is larger than that obtained with QE. For instance, the spherical parameterization in terms of U, J, and B yields values of $U = 3.7$ and 2.9 eV for LMTO and QE, respectively. This is consistent with the initial consideration (see Section 5.2.3) that the effective U in LMTO is evaluated in the basis of pseudo-atomic $3d$ orbitals, which are expected to be more localized than the MLWFs used in QE. In every other respect, the behavior of the matrix elements of $\hat{U}$ is similar in both methods, and the J and B parameters yield very similar results of $J = 0.9$ eV and $B = 0.1$ eV in both QE and LMTO methods.

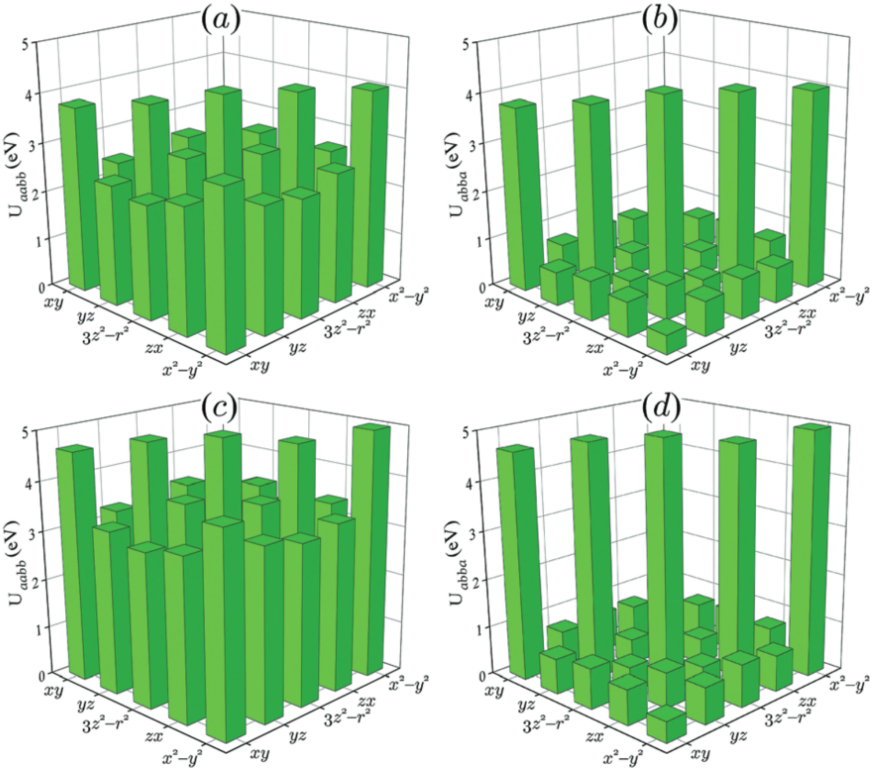

FIGURE 5.7: Matrix elements of Coulomb (a and c) and exchange (b and d) interactions for m-$NaFePO_4$ as obtained in the framework of cRPA in QE (a and b) and LMTO (c and d) calculations. Reprinted from *Phys. Chem. Chem. Phys.*, 2018, **20**, 13497 [299]. Licensed under Creative Commons Attribution-NonCommercial 3.0 Unported Licence.

The behavior of transfer integrals can be illustrated by considering SE interactions, which we explained in Section 5.2.5, specifically in Equation 5.32. The CF orbitals that are occupied by the minority-spin electron, which ultimately controls the form of J_{ij} in the SE theory, are displayed in Figures 5.8a-c, and the corresponding SE interactions in Figures 5.8d-e. The sizeable interatomic exchange interactions spread up to the fifth coordination sphere. The rest of interactions are, for the most part, negligible in all the three schemes that we considered. This tendency is related to the behavior of transfer integrals which is similar in all schemes. As expected, the largest interactions occur between the nearest neighbors. Additionally, schemes s2 and s3 produce very similar results: in both cases, the strong AFM contributions are partly compensated by weaker FM ones. As a consequence, the total interactions remain AFM. It is surprising that the total interactions, as well as the partial contributions,

Method	J_{12}	$J_{33'}$	J_{13}	$J_{34'}$	J_{14}	$J_{14'}$	θ
s1, SE	0.02	-0.05	-0.39	-1.30	-1.61	-0.12	-80.4
s1, LF	-0.11	-0.04	-0.39	-1.31	-1.62	-0.12	-82.1
s2, SE	-3.19	-0.11	-0.11	-0.07	-1.32	-0.13	-76.5
s2, LF	-2.19	-0.12	-0.30	-0.72	-1.54	-0.17	-87.1
s3, SE	-3.54	-0.07	-0.17	-0.66	-0.95	-0.12	-86.5
s3, LF	-3.07	-0.06	-0.18	-0.67	-0.97	-0.12	-87.1

TABLE 5.2: Interatomic exchange interactions (in meV) and corresponding Curie-Weiss temperature (in K) in m-$NaFePO_4$ as obtained in LMTO (s3) and QE calculations with (s2) and without (s1) subtraction of site-diagonal matrix elements of the GGA xc-potential.

are very similar in both s2 and s3 schemes, judging from the radically different orbital orderings obtained from both schemes (Figures 5.8a-c). Nevertheless, the effect of the orbital ordering can, to some extent, be compensated by the transfer integrals, which for such low-symmetry systems mix all five types of orbitals. This orbital mixing can produce similar results of interatomic exchange parameters. The SE interactions obtained in scheme s1 are clearly different. In this case, the AFM contribution is fully compensated by the FM one, resulting in small FM couplings between nearest neighbors. To some extent, the qualitative discrepancies between schemes s1, s2, and s3 can be alleviated by calculating the magnetic interactions with the full-scale HF calculations and the LF (see Equation 5.25), without SE approximation. In this case, results between the three schemes are more consistent, as in all three cases, the nearest neighbor couplings are found to be AFM (see Table 5.2).

Finally, when the SE interactions are obtained in scheme 's2', after the subtraction of both site-diagonal and off-diagonal elements of the GGA xc-potential, they are strongly overestimated as seen in Figure 5.8e. Concretely, the obtained off-diagonal elements of $\tilde{\mathbf{v}}^{\boldsymbol{\tau},\boldsymbol{\tau'}} = [\tilde{v}_{ab}^{\boldsymbol{\tau},\boldsymbol{\tau'}}]$, appear to be large and they strongly change the values of the transfer integrals. As a consequence, the model parameters in this scheme 's2' are clearly unphysical. Then, it is reasonable to assume that, if one tries to correct GGA by adding only on-site electron-electron interactions, it follows that the same should be done when subtracting the xc-potential.

Using the obtained parameters of exchange interactions, one can easily evaluate the Curie-Weiss temperature as:

$$\theta = \frac{1 + 1/S}{3k_B} \sum_j J_{ij}. \tag{5.33}$$

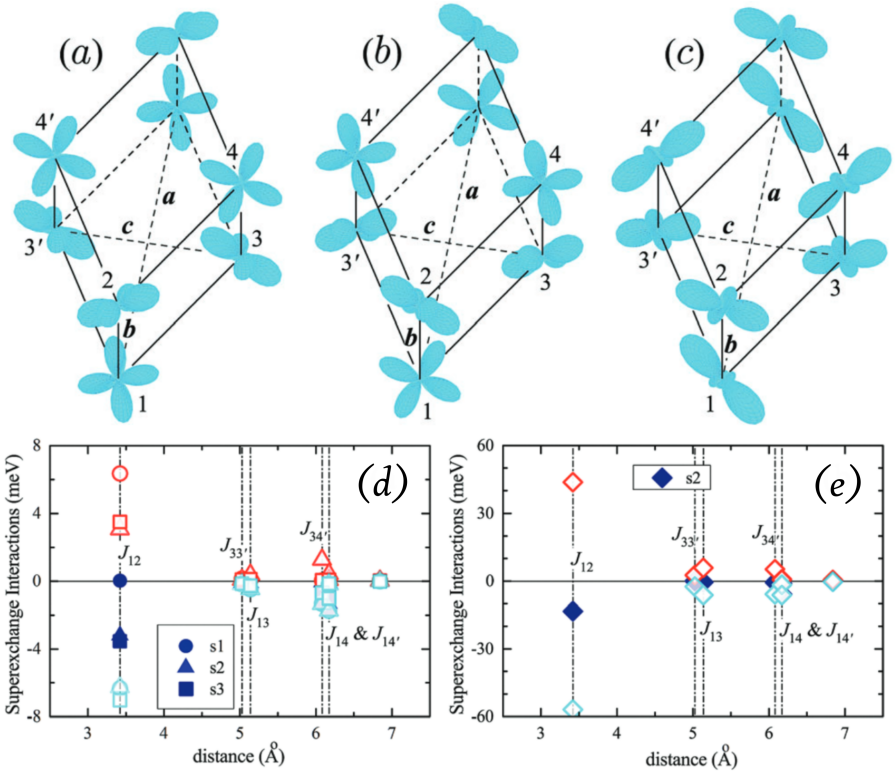

FIGURE 5.8: The electron density of the occupied minority-spin orbital in m-$NaFePO_4$ as obtained in (a) LMTO calculations 's3', (b) QE calculations 's1', and (c) QE calculations 's2'. (d) shows the distance dependent SE interactions as obtained in the three schemes s1-s3. (e) shows the SE interactions in the s2 scheme, but for the case where both site diagonal and off-diagonal elements of the GGA xc-potential are extracted from $\hat{t}$. The FM and AFM contributions are shown by open red and cyan symbols, respectively, and the total contributions are shown by filled symbols. Reprinted from *Phys. Chem. Chem. Phys.*, 2018, **20**, 13497 [299]. Licensed under Creative Commons Attribution-NonCommercial 3.0 Unported Licence.

Depending on the computational scheme (s1-s3) and method to calculate the exchange parameters (SE or LF), θ varies from -77 to -87 K (see Table 5.2), being in fair agreement with the experimental values of -83 K reported by Avdeev *et. al.* [292].

Now that the isotropic exchange parameters are obtained, it is important to see how consistent they are with the experimental magnetic structure of

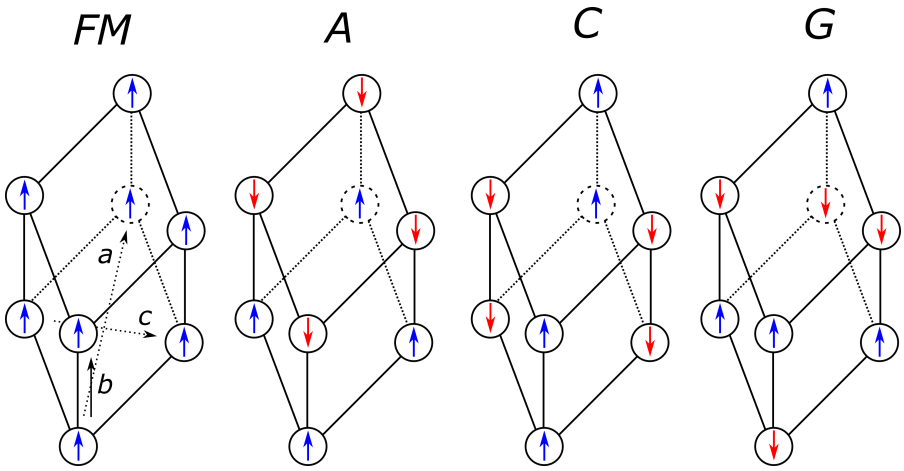

FIGURE 5.9: Schematic representation of the four collinear magnetic orderings common to structures with equivalent symmetries to those of TM perovskite oxides. Blue (Red) arrows represent the spin up (down) magnetization on each site.

m-$NaFePO_4$. We note that, since m-$NaFePO_4$ has the same symmetry as orthorhombic perovskite TM oxides, an appropriate starting point is to compare the energies of FM, A-type AFM (the FM ac layer are antiferromagnetically coupled along b), C-type AFM (FM chains propagating along b and antiferromagnetically coupled in the ac plane), and G-type AFM (AFM coupling between nearest neighbors in all three directions) states, as shown schematically in Figure 5.9.

We found that the A and C states are close in energy, and considerably lower than the FM and G states. The energy difference between A and C states varies from 8 meV per $NaFePO_4$ formula unit in the s3 scheme to 4 meV per $NaFePO_4$ formula unit in the s1 scheme. The A state, which is antiferromagnetically coupled along the b axis, is stabilized by the nearest neighbor AFM interactions J_{12}. The C state in the other hand arises from a joint effect of several long-range interactions, i.e., the AFM J_{13} and J_{14}, which would compete with J_{12} to make the coupling of spins along the nearest-neighbor Fe^{2+} chains (along the b axis) ferromagnetic. We note that the formation of FM chains in the second case is consistent with the experimental data [292]. However, NPD measurements reveal that a more complicated magnetic structure is formed, which is described by the propagation vector $\mathbf{q} = (\frac{1}{2}, 0, \frac{1}{2})$ and corresponds to the AFM coupling between the chains separated by the translations along c and a directions.

In order to explore such possibility, we investigate the stability of the A and

C states with respect to the incommensurate spin-wave excitations. This is to say, we compare the energetics of such A and C states with respect to magnetic orderings with propagation vectors that increase the periodicity of the non-magnetic unit cell, defined for example in Figure 5.8. Namely, we search for eigenvalues ω_l of the 4×4 matrix:

$$\hat{\Omega}(\mathbf{q}) = (1/S)[\tilde{J}_l \delta_{ll'} - \tilde{J}_{ll'}(\mathbf{q})], \tag{5.34}$$

where the dimensionality corresponds to the number of magnetic sublattices in the unit cell. The couplings are set as $\tilde{J}_{ij} = \pm J_{ij}$ for the ferromagnetically $(+)$ and antiferromagnetically $(-)$ coupled bonds. The $\tilde{J}_{ll'}(\mathbf{q})$ is the Fourier image of $\tilde{J}_{ij}$ between sublattices l and l', and $\tilde{J}_l = \sum_{l'} \tilde{J}_{ll'}(0)$. If all $\omega_l(\mathbf{q})$ are positive, the magnetic state, that we are comparing the spin excitations with, is stable. If some of them are negative, the state is unstable with respect to a spin excitation of a given propagation vector $\mathbf{q}$. The results are shown in Figure 5.10, using parameters obtained in the SE theory for the s1 scheme (other schemes provide a similar picture qualitatively). One can see that for the calculated value of U the A state is stable (all ω's are positive), while for the C state, some of the ω's are negative, even for $\mathbf{q} = 0$. Thus, the magnetic ground state is expected to be the A type. This is definitely inconsistent with the experimental data. To some extent, the problem is alleviated by decreasing the value U, which increases the weight of the FM contributions to the exchange coupling J_{12} and eventually makes it ferromagnetic. For instance, the SE interaction J_{12} in the s1 scheme gradually increases from 0.02 meV to 4.58 meV when the Coulomb repulsion decreases from 2.94 eV to 1.47 eV. In reality, the underestimation of the FM contributions to the exchange coupling may be related to the lack of direct interatomic interactions considered in the Hubbard model (see Equation 5.1), since only on-site Coulomb interactions are considered ($U^i_{\alpha\beta\gamma\delta}$) [310]. The inclusion of such interatomic interactions is mimicked by the change of the value U in the expression for the SE interactions. Particularly, when changing from U to $0.5U$, the A state becomes unstable for $\mathbf{q} = 0$, and the C state becomes stabilized. Furthermore, the minimal value of $\omega_l(\mathbf{q}*)$ is obtained for $\mathbf{q}^* \approx (0.36, 0, 0)$, which is close to the Z-point in Figure 5.10. As a result, one could expect the formation of a incommensurate magnetic ground state. We note that for $0.5U$ both A and C states are also unstable with respect to the experimental $\mathbf{q} = (\frac{1}{2}, 0, \frac{1}{2})$, represented in the U-point in Figure 5.10. However, according to the spin-wave analysis, the energy of the experimental ground state is expected to be higher than that of the incommensurate state corresponding $\mathbf{q}^*$. It is true that the energy difference between $\mathbf{q}^*$ and U points is very small (about 1 meV). Yet, the spin-wave dispersion shows a very flat line in the Z-U direction, meaning that there are not sizeable magnetic interactions along the a axis, which would stabilize the experimental $\mathbf{q} = (\frac{1}{2}, 0, \frac{1}{2})$ superstructure. This seems reasonable taking into account that a is the largest while c is the shortest lattice parameter in m-$NaFePO_4$ ($a/b = 1.310$ and $a/c = 1.782$). Therefore, it is fair to expect the existence of strong magnetic interactions which could lead to the formation of

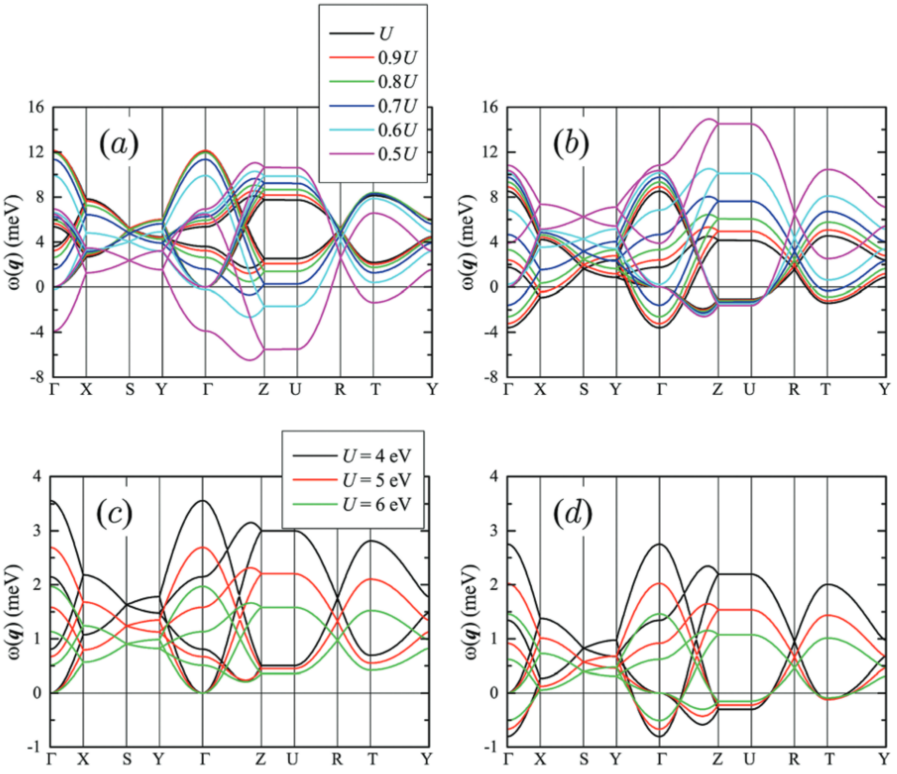

FIGURE 5.10: Spin-wave dispersion with respect to the A- (a and c) and C-type (b and d) AFM state of m-$NaFePO_4$. (a) and (b) are obtained through the SE interaction in the first scheme 's1' and scaling the value of the Coulomb repulsion from $U = 2.94$ eV to $0.5U = 1.47$ eV. (c) and (d) are obtained by using parameters reported in Table 2 of ref. [297]. Reprinted from *Phys. Chem. Chem. Phys.*, 2018, **20**, 13497 [299]. Licensed under Creative Commons Attribution-NonCommercial 3.0 Unported Licence.

superstructures along c axis, but not along the a axis. Additionally, we note that if the magnetic superstructure in m-$NaFePO_4$ was incommensurate with $\mathbf{q^*} \approx (0.36, 0, 0)$, this phase would be multiferroic, similar to the perovskite manganites with the same crystal and magnetic structures [294–296]. It would be interesting to explore this possibility experimentally.

Regarding this apparent disagreement with the NPD data, it is noted that the parameters of the interatomic exchange interactions for m-$NaFePO_4$ were also derived in Ref. [297] by mapping the total energies, obtained for different magnetic structures in the DFT+U approach, onto the spin model of Equation

	$\mathbf{d}_{ij}$ $(s1)$
$\mathbf{d}_{12}$	(-0.04, 0.0, 0.08)
$\mathbf{d}_{33'}$	(0.0, 0.0, 0.0)
$\mathbf{d}_{13}$	(0.01, -0.01, 0.0)
$\mathbf{d}_{34'}$	(-0.02, 0.02, -0.01)
$\mathbf{d}_{14}$	(0.0, 0.0, -0.04)
$\mathbf{d}_{14'}$	(0.0, 0.0, 0.0)

TABLE 5.3: Interatomic DM interactions (in meV) for m-$NaFePO_4$ as obtained QE calculations with (s1).

5.20. This procedure is different from the one used in this work. On the one hand, it takes into account the contributions from the oxygen band, which may be important. On the other hand, it suffers from ambiguities related to the choice of parameters and details of implementation of the DFT+U approach, and the microscopic and mechanistic perspective for the emergence of magnetic couplings gets a bit lost. Nevertheless, their computed parameters lead to the same conclusions as ours. If we use the parameters that were computed in Ref. [297] and perform the spin-wave analysis, we readily obtain that the magnetic ground state is also A and there are no signs of instabilities towards a magnetic superstructure with $\mathbf{q} = (\frac{1}{2}, 0, \frac{1}{2})$. Including the SO coupling can lead to canting of spins due to the DM interactions ($\mathbf{d}_{ij}$), similar to other perovskite TM oxides crystallizing in the centrosymmetric *Pnma* group [298, 311]. However, SO interaction alone cannot lead to the formation of superstructures. Indeed the computed DM interactions with the SCLR method in the s1 scheme for m-$NaFePO_4$ are orders of magnitude smaller than the isotropic exchange couplings (J_{ij}), as seen in Table 5.3. Thus, the microscopic origin of the $\mathbf{q} = (\frac{1}{2}, 0, \frac{1}{2})$ order, reported experimentally, is still puzzling.

5.3.2 t-$NaFePO_4$

When dealing with the t-$NaFePO_4$ phase, computational complications arised, due to problems with the structure of the system. Concretely, we encountered difficulties when dealing with the cRPA calculations and the symmetry of the Wannier functions. Consequently, we only considered two schemes for these calculations, the s1, where the averages of the Coulomb and exchange interactions were those used for the calculations on the m-phase, and s3 (LMTO). Indeed, the averaged cRPA parameters of the effective Coulomb and exchange interactions obtained in the LMTO method, $U = 3.5$ eV, $J = 0.9$ eV, and $B = 0.1$ eV, are very close to those of the m-phase. Therefore, we expect a similar tendency to hold for the QE calculations.

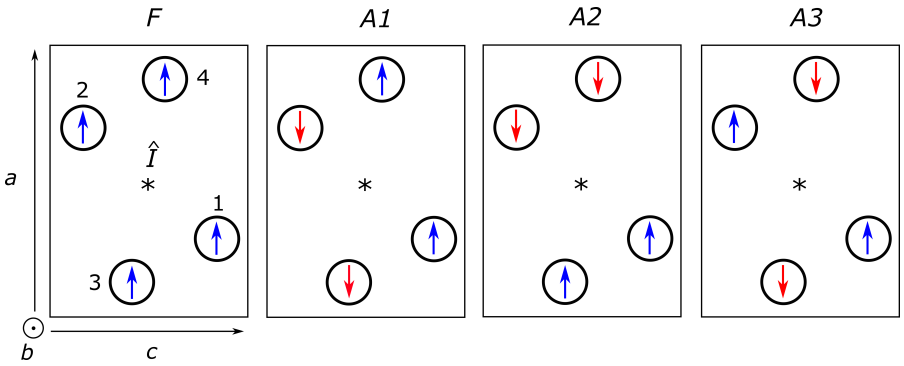

FIGURE 5.11: Schematic representation of the four collinear magnetic orderings in t-$NaFePO_4$. Blue (Red) arrows represent the spin up (down) magnetization on each site. The asterisk represents the inversion center of the system.

Without SO interaction, there are four possible collinear alignments of the Fe^{2+} spins in the primitive cell: ↑↑↑↑ (F), ↑↓↓↑ (A1), ↑↓↑↓ (A2), and ↑↑↓↓ (A3), where the arrows indicate the directions of spins at sites 1-4, as seen in Fig 5.11. Amongst the collinear magnetic orders, F and A3 contain spacial inversion $\hat{I}$ as it is, while in A1 and A2, $\hat{I}$ is combined with time reversal $\hat{T}$. Thus the latter two magnetic phases allow for magnetoelectric effect, when $\hat{I}\hat{T}$ symmetry breaks with a magnetic field. The magnetic ground state is A1, in agreement with the experiments [292]. In the HF approximation, the energy difference between F, A2 and A3 (on the one hand) and A1 (on the other hand) is 16.5 (26.0), 12.6 (22.7), and 2.1 (2.0) meV per $NaFePO_4$ formula unit in s1 (s3), respectively.

The interatomic exchange interactions obtained by using different techniques are summarized in Table 5.4. Similar to m-$NaFePO_4$, we find a consistent description for J_{ij} with both methods SE and LF, even when the orbital ordering substantially changes between different schemes, as can be seen in Figure 5.12

The sizeable interatomic magnetic interactions in the t-phase spread up to the sixth coordination sphere around each Fe^{2+} site. The ↑↓↓↑ AFM order is stabilized mainly by J_{13} and J_{12}. Moreover, we note the existence of the relatively strong AFM interaction $J_{1'1''}$, which tends to form a long-periodic magnetic structure along b.

Therefore, our theoretical calculations for the t-phase correctly reproduce the experimental magnetic ground state ↑↓↓↑ of t-$NaFePO_4$. The theoretical Néel temperature is obtained by using Tyablikov's RPA, from which the following

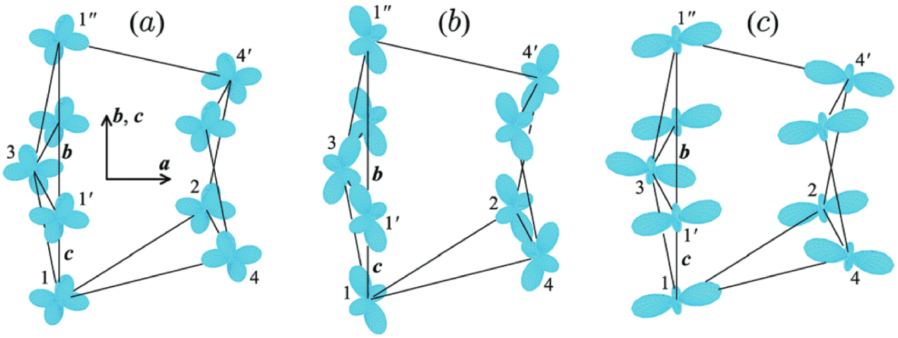

FIGURE 5.12: Orbital ordering (the electron density of the occupied minority-spin orbital) in t-phase of $NaFePO_4$ as obtained in (a) LMTO calculations, (b) QE calculations after subtraction of the GGA xc-potential. The crystallographic b and c axes are located in the plane. Reprinted from *Phys. Chem. Chem. Phys.*, 2018, **20**, 13497 [299]. Licensed under Creative Commons Attribution-NonCommercial 3.0 Unported Licence.

formula is derived:

$$T_N = \frac{nS(S+1)}{3k_B S^2} \left(\sum_{\mathbf{q}} \sum_{l=1}^{n} 1/\omega_l(\mathbf{q}) \right)^{-1}, \tag{5.35}$$

where n is the number of magnetic atoms in the unit cell. The T_N parameters listed in Table 5.4 are on the range of 34-68 K, which is also in fair agreement with the experimental value of 50 K reported in [292]. However, the theoretical Curie-Weiss temperature appears to be systematically overestimated by a

Method	J_{13}	$J_{11'}$	J_{12}	$J_{1'4}$	J_{14}	$J_{1'1''}$	θ	T_N
s1, SE	-3.62	0.14	-1.66	-0.57	0.09	-2.16	-133	34
s1, LF	-3.39	0.07	-1.49	-0.48	0.05	-1.93	-124	34
s3, SE	-4.20	-0.14	-0.94	0.03	-0.14	-1.32	-127	50
s3, LF	-5.92	-0.21	-1.30	-0.08	-0.22	-1.73	-177	68

TABLE 5.4: Interatomic exchange interactions in (meV) and corresponding Curie-Weiss and Néel temperatures (in K) in t-$NaFePO_4$ as obtained from LMTO (s3) and QE calculations without subtraction of site-diagonal matrix elements of the GGA xc-potential (s1). The magnetic couplings are computed in the superexchange 'SE' approach and with the LF.

factor 1.5-2.

5.4 Conclusions

Summing up, we have studied the electronic structure and magnetic properties of triphlyte and maricite orthorhombic polymorphs of $NaFePO_4$. In order to analyze their magnetic properties, we have constructed a realistic Hubbard-type model in the basis of localized Wannier functions, for the magnetically active Fe $3d$ bands and extracted all the parameters from first-principles electronic structure calculations. The basis of Wannier functions that we extracted is complete and perfectly represents the electronic structure of $NaFePO_4$ in the region of Fe $3d$ bands, which allows us to identify the one-electron part of our model Hamiltonian with the matrix elements of the the DFT Hamiltonian in the Wannier basis. After the extraction of the Wannier functions, the screened Coulomb interactions were evaluated by means of constrained RPA. Two numerical implementations were considered, one based on density functional calculations with plane wave basis sets and pseudopotentials, as implemented in QE, and the other based on the minimal basis set LMTO methods. Additional corrections were introduced to deal with the parasitic non-sphericity and the one-electron xc-potential, which appears twice, in DFT and in the Coulomb interactions in the Hubbard-type model. We have found that both schemes provide qualitatively similar pictures, and a consistent description of the magnetic properties of $NaFePO_4$. From the construction of the Hubbard model, electronic and magnetic properties have been simulated in the mean-field HF approximation, and interatomic exchange interactions have been extracted by using the Liechtenstein formula (based on the magnetic local force-theorem), and the theory of SE interactions, again providing a consistent description.

Regarding the type of AFM ordering and the theoretical values of Curie-Weiss and Néel temperatures, we have obtained a fair agreement with the experimental data for t-$NaFePO_4$. In this case, the experimental $\uparrow\downarrow\downarrow\uparrow$ ground state is correctly reproduced, stabilized by the AFM interactions in the Fe-Fe bonds 1-2 and 1-3 (and other symmetry equivalent bonds). Nevertheless, like in the theoretical study by Kim *et. al.* [297], the experimental $\mathbf{q} = (\frac{1}{2}, 0, \frac{1}{2})$ superstructure in m-$NaFePO_4$ could not be reproduced. The experimental magnetic frustration index $|\theta|/T_N$ is significantly larger in m-$NaFePO_4$ when compared to t-$NaFePO_4$ (about 6.4 and 1.7, respectively), this suggests that interatomic magnetic interactions in m-$NaFePO_4$ should be complex, involving several competing AFM interactions connecting Fe sites beyond nearest neighbors. Nevertheless, the theoretical interactions we computed around each Fe site extend practically to the same amount of neighbors in both m- and t-$NaFePO_4$. It appears that some long-range AFM interactions are missing in the electronic structure calculations of m-$NaFePO_4$ and the reason is not at all

clear. Yet the magnetic superstructure along the orthorhombic axis c can be understood by adjusting the value of the on-site Coulomb repulsion U, but the one along the a axis is puzzling. For instance, reducing the value of U makes the theoretical A-type AFM ground state unstable as superstructures along c axis are stabilized. This could be the key point at understanding the origin of the experimental $\mathbf{q} = (\frac{1}{2}, 0, \frac{1}{2})$ order. If the Coulomb repulsion is sufficiently small, the conventional SE theory breaks down and one has to consider additional interactions, appearing at higher orders with respect to the hopping parameters. These interactions operate between intermediate transition-metal sites and are typically referred to as the super-SE interactions. These interactions are long-ranged and are responsible for the formation of long-ranged magnetic structures [312]. However, we still do not know how important these interactions are in the formation of superstructures in m-$NaFePO_4$. In order to explore such possibility, it is important to understand: (i) the physical mechanism, which would reduce the value of the effective Coulomb repulsion U in m-$NaFePO_4$, and (ii) the origin of the orbital ordering, which could assist the super-SE mechanism in stabilizing the AFM coupling along the a axis. These two factors could be behind the origin of the $\mathbf{q} = (\frac{1}{2}, 0, \frac{1}{2})$ superstructure, and further analysis in this regard is highly desirable.

Lastly, we note that the magnetic ground state in t-$NaFePO_4$ allows for the magnetoelectric effect. This would also happen for the predicted incommensurate ground state for small U values in m-$NaFePO_4$, i.e., $\mathbf{q^*} \approx (0.36, 0, 0)$.

Appendix A

Na/vacancy Orderings in LTMOs

In Chapter 4 we calculated the energetics of rigid gliding in LTMOs, that give atomistic information into the process of P $\leftrightarrow$ O transformations. As we discussed, the concrete Na/vacancy orderings strongly affect the energetics of gliding. Therefore, it is helpful to provide here a general catalogue of different experimental and theoretical Na/vacancy orderings for Na-based LTMOs.

A.1 Catalogue of proposed Na/vacancy orderings

Figures A.1, A.2, and A.3 show the different Na/vacancy orderings reported in the bibliography for P2, P3, and O3 phases, respectively. No explicit orderings are found for the O2-phase, probably, because this phase is rarely thermodynamically stable for Na-based compounds. Table A.1 presents the list of compounds for which the pictured Na/vacancy orderings are the GS orderings (or other energetically accessible orderings). We must note that some of these orderings, especially the ones predicted by DFT calculations, are not necessarily going to appear experimentally at room temperature, as disordered phases may be more favorable. Other experimental Na/vacancy orderings are best fits of material models to XRD data.

Additionally, Figure A.4 shows the local Na environments for P2, P3, and O3 phases in LTMOs. Shortly, as already mentioned in Chapter 4, P2 phases show two symmetrically nonequivalent Na sites where Na prisms either share edges (e) or faces (f) with transition metal octahedra (see Figure A.4a-b). In P3 phases, Na ions have the same local coordination with oxygen atoms, with one e-sharing and one f-sharing interface with MO_6 octahedra. This is rigorously different from P2 phases, where only f- or e-sharing prismatic sites exist. Specifically, from a crystallographic viewpoint, Na ions in P3 phases occupy

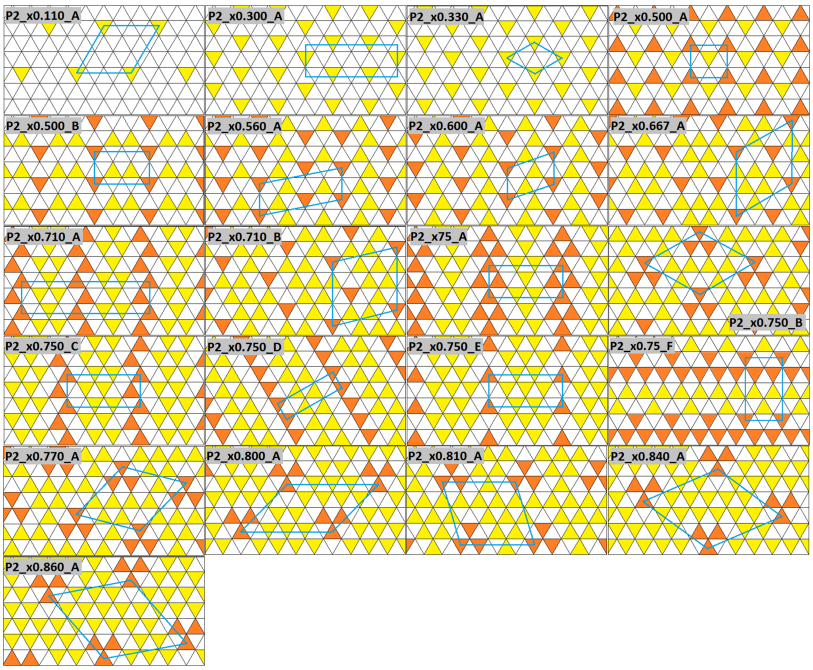

FIGURE A.1: In plane Na/vacancy orderings for P2-type structures. The label of each ordering appears in the insets on each sub-plot. Na prisms that share edges (faces) appear in yellow (orange). The in-plane unit cells are shown in blue.

two symmetrically equivalent sites: one has 'f/e'-sharing prisms (in this order, i.e. one f-shared interface with the MO_6 above and one e-shared interface with the MO_6 below) as seen in Figure A.4c, while the other corresponds to 'e/f'-sharing prisms (see Figure A.4d). Both of these types of prisms are still differentiable locally as shown in Figure A.2. In the case of O3 phases, only one site exists where Na octahedra always share edges with TM octahedra (see Figure A.4e). However, experimentally and theoretically, special cases have been observed (i.e. the O3_x0.625_A ordering) where, due to large structural distortions, it is possible to accommodate Na ions in distorted face sharing octahedra.

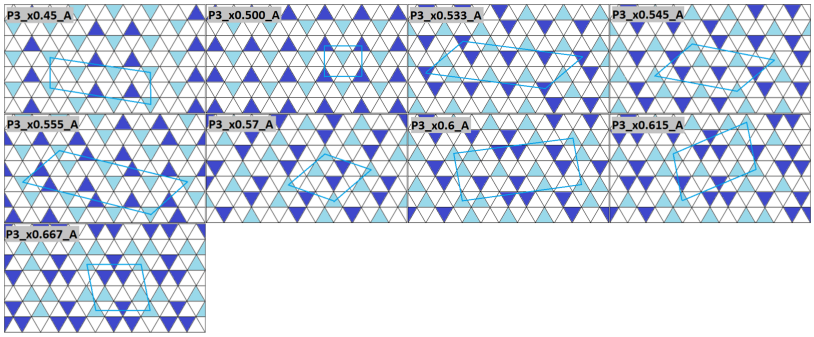

FIGURE A.2: In plane Na/vacancy orderings for P3-type structures. The label of each ordering appears in the insets on each sub-plot. The two distinct in-plane Na-sites (i.e., edge-face 'e/f' or face-edge 'f/e' prisms) appear in turquoise or dark-blue, respectively. The in-plane unit cells are shown in blue.

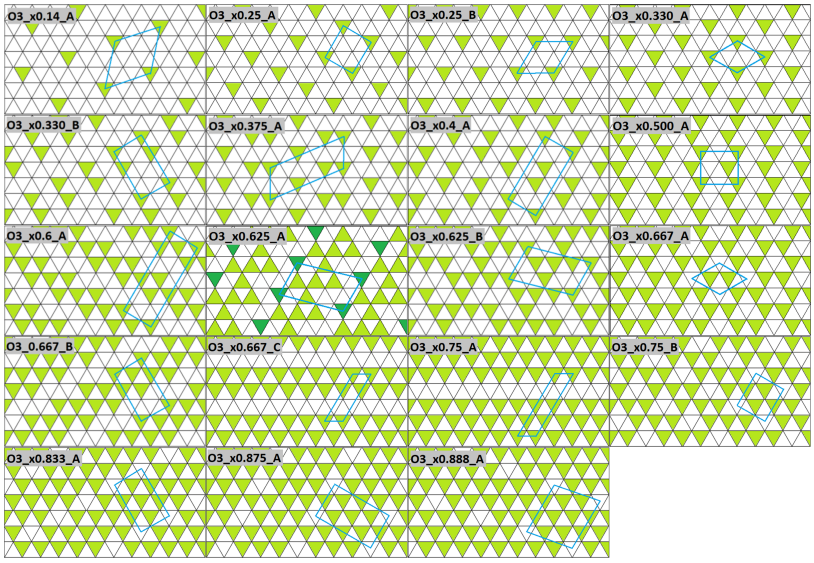

FIGURE A.3: In plane Na/vacancy orderings for O3-type structures. The label of each ordering appears in the insets on each sub-plot. Sodium octahedral environment appears in green. The especial case for ordering O3_x0.625_A also shows octahedral environments that share faces with TM octahedra, and are shown in dark-green. The in-plane unit cells are shown in blue.

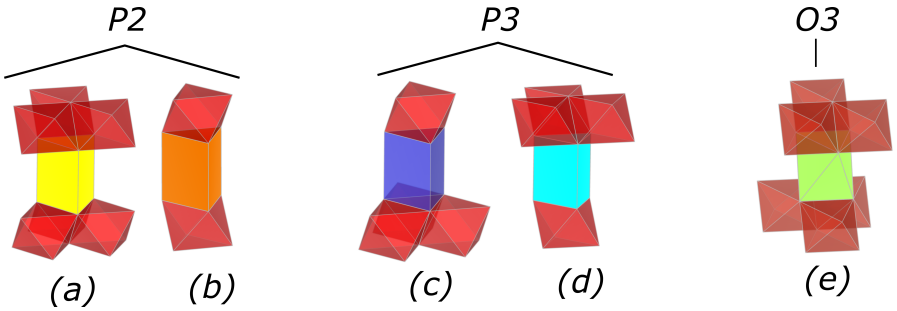

FIGURE A.4: Local coordination of Na ion sites in LTMOs. Yellow (a) and Orange (b) prisms show edge- and face-sharing coordinations in the P2 phase. Dark blue (c) and turquoise (d) prisms show the 'e/f' and 'f/e'-sharing prisms in the P3 phase. Green (e) octahedra shows edge-sharing coordinations in the O3 phase. Red octahedra show the MO_6 octahedra.

Compound	Phase	x	Label	Source	Reference
Na_xTiO_2	O3	0.14	O3_x0.14_A	Th.	[244]
		0.25	O3_x0.25_B	Th.	[244]
		0.33	O3_x0.330_B	Th.	[244]
		0.5	O3_x0.500_A	Th.	[244]
		0.6	O3_x0.6_A	Th.	[244]
		0.666	O3_x0.666_C	Th.	[244]
		0.75	O3_x0.75_A	Th.	[244]
		0.888	O3_x0.888_A	Th.	[244]
Na_xVO_2	P2	0.5	P2_x0.5_A	Exp.	[235]
					[231]
	O3	0.25	O3_x0.25_A	Th.	[244]
		0.333	O3_x0.333_A	Th.	[244]
		0.5	O3_x0.500_A	Th.	[244]
		0.625	O3_x0.625_B	Th.	[244]
		0.666	O3_x0.666_C	Th.	[244]
		0.75	O3_x0.75_A	Th.	[244]
		0.875	O3_x0.875_A	Th.	[244]
	O'3	0.5	O3_x0.500_A	Exp.	[232]
					[223]
Na_xCrO_2	P3	0.5	P3_x0.500_A	Exp.	[313]
	O3	0.14	O3_x0.14_A	Th.	[244]
		0.25	O3_x0.250_A	Th.	[244]
		0.333	O3_x0.333_A	Th.	[244]
		0.4	O3_x0.4_A	Th.	[244]
		0.5	O3_x0.500_A	Th.	[244]

		0.6	O3_x0.6_A	Th.	[244]
		0.666	O3_x0.666_B	Th.	[244]
		0.75	O3_x0.75_A	Th.	[244]
Na_xMnO_2	O3	0.333	O3_x0.333_A	Th.	[244]
		0.5	O3_x0.500_A	Th.	[244]
		0.625	O3_x0.625_A	Th.	[244]
				Exp.	[314]
		0.666	O3_x0.666_A	Th.	[244]
		0.75	O3_x0.75_B	Th.	[244]
Na_xFeO_2	O3	0.25	O3_x0.25_A	Th.	[244]
		0.333	O3_x0.333_A	Th.	[244]
		0.5	O3_x0.5_A	Th.	[244]
Na_xCoO_2	P2	0.110	P2_x0.110_A	Exp.	[265]
		0.3	P2_x0.300_A	Exp.	[265]
		0.333	P2_x0.330_A	Exp.	[265]
		0.5	P2_x0.500_A	Exp.	[315]
					[254]
					[265]
				Th.	[316]
					[317]
		0.56	P2_x0.560_A	Th.	[316]
		0.6	P2_x0.600_A	Th.	[316]
					[317]
		0.667	P2_x0.667_A	Th.	[316]
					[317]
				Exp.	[318]
					[254]
		0.71	P2_x0.710_A	Exp.	[265]
			P2_x0.710_B	Th.	[317]
					[316]
		0.75	P2_x0.75_A	Exp.	[265]
			P2_x0.75_B	Th.	[316]
					[259]
			P2_x0.75_C		[319]
			P2_x0.75_D*		[319]
			P2_x0.75_E*		[319]
			P2_x0.75_F	Th.	[320]
				Exp.	[320]
		0.77	P2_x0.770_A	Th.	[316]
					[317]
		0.80	P2_x0.800_A	Exp.	[259]
		0.81	P2_x0.810_A	Th.	[316]
					[317]
		0.84	P2_x0.840_A	Th.	[316]
					[317]
		0.86	P2_x0.860_A	Th.	[316]

	P3	0.45	P3_x0.45_A	Th.	[321]
		0.5	P3_x0.500_A	Th.	[321]
		0.533	P3_x0.533_A	Th.	[321]
		0.545	P3_x0.545_A	Th.	[321]
		0.555	P3_x0.555_A	Th.	[321]
		0.57	P3_x0.57_A	Th.	[321]
		0.615	P3_x0.615_A	Th.	[321]
		0.667	P3_x0.667_A	Th.	[321]
	O3	0.25	O3_x0.25_B	Th.	[244]
		0.333	O3_x0.330_A	Th.	[244]
		0.375	O3_x0.375_A	Th.	[244]
		0.5	O3_x0.500_A	Th.	[244]
		0.667	O3_x0.667_B	Th.	[244]
		0.833	O3_x0.833_A	Th.	[244]
Na_xNiO_2	O3	0.25	O3_x0.25_A	Th.	[244]
		0.33	O3_x0.330_A	Th.	[244]
		0.4	O3_x0.4_A	Th.	[244]
		0.625	O3_x0.625_A	Th.	[244]
$Na_xNi_{0.33}Mn_{0.66}O_2$	P2	0.333	P3_x0.330_A	Exp.	[257] [267]
		0.5	P2_x0.500_B	Exp.	[257] [267]
		0.667	P2_x0.667_A	Exp.	[257] [267]
$Na_xMn_{0.33}Fe_{0.66}O_2$	P2	0.667	P2_x0.667_A	Th.	[258]
	O3	0.667	O3_x0.667_A	Th.	[258]
$Na_xFe_{0.5}Co_{0.5}O_2$	P'3	0.5	P3_x0.500_A	Exp.	[322]
$Na_xMn_{0.33}Fe_{0.33}Co_{0.33}O_2$	O3	0.333	O3_x0.333_A	Th.	[323]
		0.667	O3_x0.667_A	Th.	[323]
Na_xRhO_2	O'3	0.5	O3_x0.500_A	Exp.	[324]
Na_xMoO_2	O'3	0.333	O3_x0.333_A	Exp.	[325]

TABLE A.1: Catalogue of Na/vacancy orderings, the columns represent the compound, the concrete phase (O or P), the sodium content (x), the labels that are represented pictorically in Figures A.1, A.2, and A.3; whether the source is experimental (Exp.) or theoretical (Th.), and the citation reference.

Appendix B

User's Guide to Mean-Field HF code

B.1 Input files

The implemented mean-field HF method requires first performing DFT calculations, followed by a Wannierization procedure. The general structure of the code and its modules are schematically represented in Figure B.1. The input files needed to run the program are listed bellow:

- `hf.in`

The `hf.in` file contains the main calculation parameters. This file must have the following inputs in this concrete order so that the code reads it properly.

- `# Empty space for description line`
- `logical :: spinorb`

`.true.` if SO coupling is included, `.false.` if not.

- `character(len=50) :: soctype`

If string starts with an `'f'`, the one electron part fully includes the SO coupling. If string starts with an `'s'`, the one electron part of the model does not include the SO coupling. However, the on-site contributions to the SO coupling are read from a separate file and then added to the non-relativistic one electron part.

- `character(len=50) :: bondcoord`

If string starts with `'c'`, means that the bonds in the `hf_ham.in` input file are given in cartesian coordinates. If string starts with `'f'` the bonds are given in fractional (or direct) coordinates.

- `integer :: nelec`

Total amount of electrons in the system.

- `integer :: nscf`

Total number of self-consistency cycles.

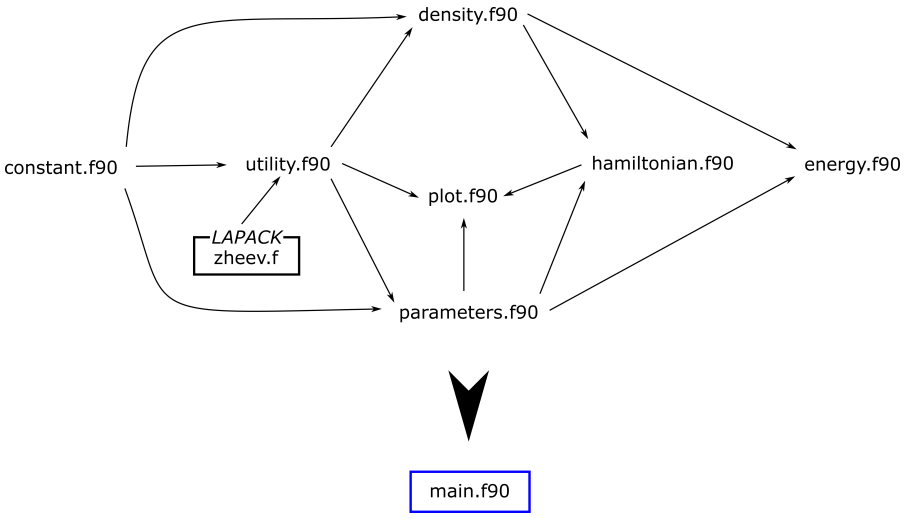

FIGURE B.1: Structure of the module hierarchy, arrows indicate which modules are called in which programs. Some arrows are avoided for the sake of clarity, since the `constant.f90` module is called in almost every other module. Then, all these modules are called in the main program `main.f90` where the self-consistency loop is done.

- `integer :: nener`

Total number of energy points between energy maximun and minimum, for DOS plotting purposes.

- `real*8 :: etemp`

Electronic temperature for smearing in K. This is used to improve convergence by smoothing the occupations of the energy levels with the Fermi-Dirac (FD) distribution function. Using 0 K, the FD becomes a heavyside function and can lead to convergence issues.

- `real*8 :: ediff`

Convergence criteria for the total energy.

- `real*8 :: mix`

Mixing fractions (ξ) for old and new densities in the self-consistent cycles. Defined as $\hat{n}_{new} = (1-\xi)\hat{n}_{old} + \xi\hat{n}_{new}$. For convergence purposes.

- `logical :: dosplot`

`.true.` if DOS is plotted, `.false.` if not.

- `real*8 :: smear`

Smearing of the gaussians for DOS plots.

- `logical :: bandplot`

`.true.` if bands are plotted, `.false.` if not.

- `logical :: lsph`

`.true.` if the spherical parametrization of the screened Coulomb interactions

are used, `.false.` if not.

- `hf_ham.in`

The `hf_ham.in` file contains the one electron part of the Hubbard model, containing the matrix elements of the DFT Hamiltonian in the Wannier basis. In our case the wannier90 code is used to obtain the parameters, which are written to a file called `wannier90_hr.dat`. This file has to be correctly formatted, so that the parameters have an adequate shape like in the definition of $\hat{t}_{\boldsymbol{\tau},\boldsymbol{\tau}'+\mathbf{R}} = [t^{\alpha\beta}_{\boldsymbol{\tau},\boldsymbol{\tau}'+\mathbf{R}}]$. The file `hf_ham.in` should contain the indices of each pair of sites ($\boldsymbol{\tau}$ and $\boldsymbol{\tau}'$), and the shape (a, b) of the each submatrix $\hat{t}_{\boldsymbol{\tau},\boldsymbol{\tau}'+\mathbf{R}}$, all in one line. The following line contains the x, y, and z components of the vector that connects both sites ($\boldsymbol{\tau}' - \boldsymbol{\tau} + \mathbf{R}$). Lastly a number of lines and b number of columns are included, containing the matrix elements of the DFT Hamiltonian involving the Wannier orbitals in the given bond (in eV).

For instance, when no SO coupling is included the matrix $\hat{t}_{\boldsymbol{\tau},\boldsymbol{\tau}'+\mathbf{R}}$ does not depend on spin indices and the `hf_ham.in` has the following form:

```
2 4 5 5
0.000000000000000E+000 -3.42142510415000 0.000000000000000E+000
-4.7653999E-02 -7.0290002E-03 3.8224999E-02 -1.3328000E-02 1.6369000E-02
-7.0290002E-03 -4.7029998E-02 2.0575000E-02 2.0439001E-02 -3.2487001E-02
3.8224999E-02 2.0575000E-02 1.1220000E-03 -5.6885000E-02 1.4934000E-02
-1.3328000E-02 2.0439001E-02 -5.6885000E-02 -0.1151010 3.7037998E-02
1.6369000E-02 -3.2487001E-02 1.4934000E-02 3.7037998E-02 -1.1529000E-02
2 4 5 5
0.000000000000000E+000 3.42142510415000 0.000000000000000E+000
...
...
```

If SO coupling is included, i.e., `spinorb = .true.` and `soctype = 'f'`, the `hf_ham.in` also includes the matrix elements involving all spin subspaces. In this case, as the elements of the Hamiltonian may also be imaginary, two matrices are included for each bond, first the real elements and second the imaginary ones. For example:

```
1 2 6 6
0.000000000000000E+000 0.000000000000000E+000 3.93555000000000
0.0002230 0.0007410 0.0000000 0.0000000 0.0000000 0.0000200
-0.0007410 0.0002230 0.0000000 0.0000000 0.0000000 -0.0000110
0.0000000 0.0000000 -0.0005920 -0.0000100 0.0000140 0.0000000
0.0000000 0.0000000 -0.0000200 0.0002230 0.0007410 0.0000000
0.0000000 0.0000000 0.0000110 -0.0007410 0.0002230 0.0000000
0.0000100 -0.0000140 0.0000000 0.0000000 0.0000000 -0.0005920
```

```
-0.0000500 -0.0002730 0.0000000 0.0000000 0.0000000 -0.0000110
0.0002730 -0.0000500 0.0000000 0.0000000 0.0000000 -0.0000200
0.0000000 0.0000000 -0.0000180 0.0000140 0.0000100 0.0000000
0.0000000 0.0000000 -0.0000110 0.0000500 0.0002730 0.0000000
0.0000000 0.0000000 -0.0000200 -0.0002730 0.0000500 0.0000000
0.0000140 0.0000100 0.0000000 0.0000000 0.0000000 0.0000180
7 5 6 6
0.000000000000000E+000 0.000000000000000E+000 -3.93555000000000
...
...
```

- `hf_soc.in`

If SO is included, i.e., `spinorb = .true.` but `soctype = 's'` instead of `'f'`, the SO potential is read from file `hf_soc.in`. Its format is that of the `hf_ham.in` (when including SO coupling), but only includes site diagonal elements ($\boldsymbol{\tau} = \boldsymbol{\tau}'$).

- `hf_coulomb.in`

The elements of the screened Coulomb parameters in the Wannier basis ($U^{\boldsymbol{\tau}}_{abcd}$) obtained from cRPA calculations are read from file `hf_coulomb.in`. The format of the file includes (`norb*nsite`)^4 lines (where `norb*nsite` is the total amount of Wannier functions in the home unit cell). Each line then contains the indices of the Wannier functions, and the real and imaginary parts of the Coulomb parameters. The code then only takes the on-site contributions to build $U^{\boldsymbol{\tau}}_{abcd}$.

For example,

```
1 1 1 1 3.7422210950 -0.0000000570
1 1 1 2 -0.0022344150 0.0000003589
1 1 1 3 0.0427219367 -0.0000001032
1 1 1 4 0.0409806520 -0.0000001924
1 1 1 5 0.0100683116 0.0000011909
1 1 1 6 -0.0017153231 0.0000000069
1 1 1 7 0.0026091471 0.0000000088
1 1 1 8 -0.0025190860 0.0000000029
1 1 1 9 -0.0001198428 0.0000000191
1 1 1 10 -0.0017945542 0.0000000109
1 1 1 11 0.0105224639 -0.0000000132
1 1 1 12 -0.0023309739 0.0000000022
1 1 1 13 -0.0106370049 0.0000000071
...
...
```

- `hf_mag.in`

Includes `nsite` lines with the initial magnetization that the code uses to initialize the calculation. In the collinear case (no SO coupling included), just one number is provided for the magnetization of each site in units of μ_B (Bohr magnetons). In the non-collinear case, spin-up and spin-down channels are not treated separately; either because we include the SO coupling, or because of magnetic alignments with components perpendicular to the quantization axis z. In this case each line contains the x, y, and z components of the magnetization for each site.

- `hf_kpt.in`

The first line in this file is a general description line. The second line is the total number of **k**-points (`nkpt`). Then next `nkpt` lines include the three components of the **k**-points in direct coordinates with respect to the reciprocal lattice. This file can be easily generated with some of the wannier90 package tools; the `kmesh.pl` script, particularly.

- `hf_struct.in`

The first line is a general description. The next three lines are the cartesian x, y, and z components of cell vectors **a**, **b**, and **c**. The next line contains the label of the sites and the total number of sites in the unit cell (`nsite`). The following `nsite` lines contain the positions of the sites in direct coordinates with respect to the cell vectors.

For instance,

```
New structure
8.9627799988000003 0.0000000000000000 0.0000000000000000
0.0000000000000000 6.8428502082999998 0.0000000000000000
0.0000000000000000 0.0000000000000000 5.0282697678000003
Fe 4
0.0000000000000000 0.0000000000000000 0.0000000000000000
0.5000000000000000 0.0000000000000000 0.5000000000000000
0.0000000000000000 0.5000000000000000 0.0000000000000000
0.5000000000000000 0.5000000000000000 0.5000000000000000
```

- `hf_path.in`

Read in order to plot the bandstructure (`bandplot = .true.`). The first line contains the number of high symmetry points in BZ (`npth`), and the amount of **k**-points (`npnts`) contained in the path between two high symmetry points.

The next `npth` lines contain the coordinates of the high symmetry points in the BZ, in direct coordinates with respect to the reciprocal lattice vectors.

B.2 Output files

These are all the input files that are needed in order to run the program. The calculations are not too heavy and can easily run in a normal machine. A `Makefile` file is provided for the compilation of the program. Once we execute the program, several output files will be generated, which are introduced here.

- `hf.out`

Contains the general information about the calculation parameters and the self-consistency cycle. In the end of the file information about the total HF energy can be found, alongside the site occupations and final magnetization of the system.

For instance,

```
...
...
---------------- Reached required accuracy ----------------
---------------- Ending self-consistent loop ----------------

!  Converged HF energy :  310.20909803 eV

Occupations
------------------------------
Atom:  1 6.0000
Atom:  2 6.0000
Atom:  3 6.0000
Atom:  4 6.0000

Magnetization (bohr magnetons)
------------------------------
Atom:  1 4.0000
Atom:  2 4.0000
Atom:  3 4.0000
Atom:  4 4.0000
```

If SO coupling is included (`spinorb = .true.`), the x, y, and z components of the final magnetizations are given instead.

- `dens.out`

The file contains the converged occupation matrix $\hat{n}$. The file contains the matrix elements of the occupation matrix with respect to spin and site indices. The first line of each block contains the spin and site indices; i_σ, $k_{\boldsymbol{\tau}}$ (when `spinorb = .false.`); and i_σ, $j_{\sigma'}$, $k_{\boldsymbol{\tau}}$ (when `spinorb = .true.`). The next `norb`^{2} lines contain the orbital indices (a, and b), and the real and imaginary parts of the elements of the occupation matrix. The next line is empty, so that elements of $\hat{n}$ of different sites and spin components are given separatedly.

For example, when SO coupling is not included:

```
1 1
1 1 1.00000000000000 0.000000000000000E+000
2 1 5.223183304320345E-016 1.593540548066249E-019
3 1 1.157413778693502E-016 -3.963558669021824E-019
...
3 5 -2.495085764646510E-016 2.436385314115116E-018
4 5 1.936295441969418E-016 8.706242052173861E-019
5 5 1.00000000000000 0.000000000000000E+000

1 2
1 1 1.00000000000000 0.000000000000000E+000
2 1 -5.733865643461239E-017 1.370161755117588E-018
3 1 -4.960982353267559E-017 1.670883165390235E-019
...
```

- `pot.out`

The file contains the converged HF potential $\hat{v}$, the format of the file `pot.out` is identical to that of the `dens.out` file.

- `bond.out`

The file contains geometrical information of all bonds ($\boldsymbol{\tau}$, $\boldsymbol{\tau}' + \mathbf{R}$) in the calculation. The first line contains the amount of bonds (`nrpt`). The next `nrpt` pairs of lines contain the indices of the sites in a given bond ($i_{\boldsymbol{\tau}}$, $j_{\boldsymbol{\tau}'}$) in one line and the x, y, and z components of the vector $\boldsymbol{\tau} - \boldsymbol{\tau}' - \mathbf{R}$ in the next line.

For instance,

```
164
1 3
0.000000000000000E+000 -3.42142510415000 0.000000000000000E+000
4 2
```

```
0.000000000000000E+000 -3.42142510415000 0.000000000000000E+000
1 3
0.000000000000000E+000 3.42142510415000 0.000000000000000E+000
...
4 4
0.000000000000000E+000 0.000000000000000E+000 5.02826976780000
1 1
0.000000000000000E+000 0.000000000000000E+000 5.02826976780000
1 1
0.000000000000000E+000 0.000000000000000E+000 -5.02826976780000
...
```

- `eig.out`

Contains the eigenvalues $\epsilon_{\nu\mathbf{k}}$ obtained from solving the Equation 5.14. If SO is included (`spinorb = .true.`) the format of the file consists of a first line containing the Fermi energy and the following `nkpt` blocks, separated by empty lines, where each block is composed by a first line containing the x, y, and z components of the $\mathbf{k}$-points and the following `norb*nsite*nspin` lines containing the band index ν and the corresponding eigenvalue.

For instance,

```
22.1395502348349
0.000000000000000E+000 0.000000000000000E+000 0.000000000000000E+000
1 17.4418607515576
2 17.5225865687802
3 17.5387831092303
...

0.000000000000000E+000 0.000000000000000E+000 0.124957207392916
1 17.4487271426789
2 17.5247106648669
3 17.5470681512283
...
```

If SO is not included (`spinorb = .false.`), then, as explained in the main text, the eigenvalues are given for the spin-up and spin-down channels separatedly as $\epsilon^{\sigma}_{n\mathbf{k}}$. The `nkpt` blocks then additionally split into `nspin` sub-blocks of `norb*nsite` lines each.

```
22.1530293085132
0.000000000000000E+000 0.000000000000000E+000 0.000000000000000E+000
1
1 17.4749020931288
```

```
2 17.5443771261387
...

2
1 21.1570840556554
2 21.2097782315694
...

0.000000000000000E+000 0.000000000000000E+000 0.124957207392916
1
1 17.4835562554176
2 17.5491541029557
...
```

- `wav.out`

Contains the eigenvectors $|C_{\nu\mathbf{k}}\rangle$ (if `spinorb = .true.`) and $|C^{\sigma}_{n\mathbf{k}}\rangle$ (if `spinorb = .false.`). The first two lines contain the number of **k**-points (`nkpt`) and the amount of lines in each block (if SO coupling is included), or sub-block (if not). The rest of lines have the same format as the `eig.out` file, with the difference that each line contains the real and imaginary parts of the eigenvectors.

- `dos.out`

For plotting the DOS. Only generated if `dosplot = .true.`. It contains `nener*nspin` lines, each line containing an energy value inside a grid between the maximum and minimum eigenvalues $\epsilon_{\nu\mathbf{k}}$, and the number of states at that point smeared by a Gaussian function.

- `bands.out`, `bands.1.out`, and `bands.2.out`

Files for plotting the HF bandstructures. Only generated if `bandplot = .true.`. File `bands.out` is generated if `spinorb = .true.`; and files `bands.1.out` and `bands.2.out` are generated for the spin-up and -down channels, respectively, if `spinorb = .false.`. `bands.out` contains `norb*nsite*nspin` blocks of `npnts` lines each. Each line here contains the accumulated distance done along the path and the energy eigenvalue in the corresponding **k**-point. The files `bands.1.out` and `bands.2.out` contain `norb*nsite` blocks each. The format of each block is identical to that of the `bands.out` file.

- `eigpath.out` and `wavpath.out`

Files contain the eigenvalues $\epsilon_{\nu\mathbf{k}}$ (in `eigpath.out`), and eigenvectors $|C_{\nu\mathbf{k}}\rangle$ (in `wavpath.out`), along the **k**-point path on the `hf_path.in` file. Only generated if `bandplot = .true.`. The format is the same as those of the files `eig.out`

and `wav.out`.

Appendix C

User's Guide to HF Post-Processing Code

C.1 Input files

The method first requires to run the mean-field HF calculations presented in Appendix B without SO coupling. The general structure of the calculation is presented in Figure C.1. And the input files are described in the following.

- `gflr.in`

The `gflr.in` file contains all the calculation parameters. In the same way as the `hf.in` (Appendix B), the parameters must be given in the correct order.

- `# Empty space for description line`
- `integer :: npoles`
Total number of poles included inside the contour $\boldsymbol{L}$ (see Fig D.1d).
- `integer :: npath`
Total number of points included in the arc path $\boldsymbol{C}$ (see Fig D.1d).
- `integer :: sspin`
Spin number S of magnetic sites.
- `real*8 :: fdtemp`
Electronic temperature for the smoothing of the Fermi-Dirac distribution function.
- `integer :: nelec`
Total number of electrons.

- `logical :: lexch`
`.true.` if isotropic exchange interactions (J_{ij}) are calculated through the Liechtenstein formula, `.false.` if not.
- `logical :: lmgnon`
`.true.` if spin-wave excitations are calculated from J_{ij} interactions, `.false.`

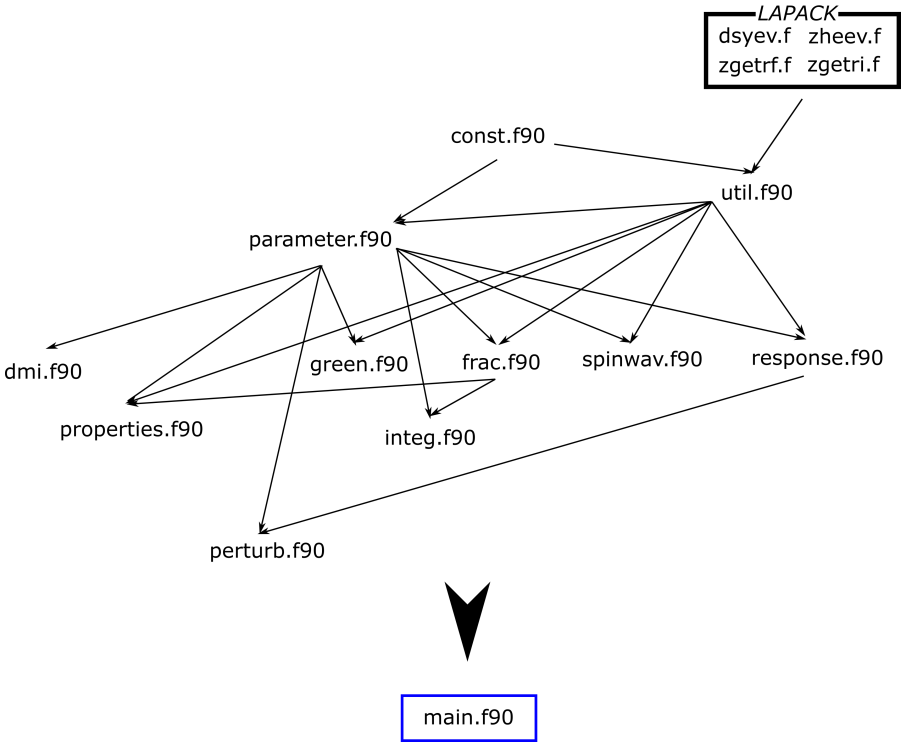

FIGURE C.1: Structure of the module hierarchy, arrows indicate which modules are called in which programs. The module `constant.f90` is called in every other module so only the first module dependencies are shown. Then, all these modules are called in the main program `main.f90` where the SCLR calculations are done, and the Liechtenstein formula and forces are solved.

if not.

- `# Empty line`
- `logical :: lsclr`

`.true.` to activate the SCLR modules, `.false.` otherwise. If `lsclr = .true.` the code will read the following lines in this order.

- `logical :: lsph`

`.true.` if spherical parameters are used in the HF calculations, and are going to be used in the SCLR calculations too. `.false.` if not. These subroutines are still not very well implemented, and the values of the spherical Coulomb interactions are set by hand. This feature needs polishing.

- `logical :: lorb`

`.true.` if the orbital moment operators $\hat{\mathbf{L}} = (\hat{L}_x, \hat{L}_y, \hat{L}_z)$ are read, and the orbital magnetic moment calculated. `.false.` otherwise. Of course, for this

we must exactly know the shape of the orbital moment operators in the basis of the Wannier basis used. This feature must be used with extreme care.
- `logical :: ldmi`
`.true.` if DM interactions are calculated.
- `character(len=50) :: soctype`
If string starts with an `'r'`, the on-site part of the SO potential ($\delta\hat{v}^{ext}$) is calculated from the difference between DFT+SO and DFT Hamiltonians in the Wannier basis. If it starts with and `'f'`, the SO potential is read from an external file.
- `real*8 :: th, phi`
Gives the values of θ and ϕ that define the angles of the direction of the magnetization off the quantization axis z, for SCLR calculations. The magnetization direction is defined as $\mathbf{e} = (\cos\phi\sin\theta, \sin\phi\sin\theta, \cos\theta)$.

- `wav.out, eig.out, bond.out, pot.out,` and `dens.out`
All these files are outputs of the mean-field HF code, which the post-processing code uses as inputs. The format of these files is already explained in Appendix B.

- `struct.in`
This file contains the structural parameters of the calculations. It has the same format as the file `hf_struct.in` (see Appendix B).

- `bandpath.in`
This file contains the high-symmetry **k**-points that define the paths in order to obtain spin-wave excitations. It has the same format as the file `hf_path.in`, used to calculate bandstructures in the Mean-Field HF method (see Appendix B).

- `maglatt.in`
Defines the magnetic sub-lattice with which to compare the spin-wave excitations. The format is that of the `hf_mag.in` file with collinear configuration of spins. However it only contains integer +1 or -1 numbers. This means that all spins defined by a sublattice (repeated periodic images of a single site in the home unit cell), are spin-up (+1) or spin-down (-1). So bonds (+1)-(+1) and (-1)-(-1) are FM; while (+1)-(-1) and (-1)-(+1) are AFM.

- `sclr_ham.in` and `sclr_hamso.in`
These two0 files contain the one electron part of the Hubbard model with (`sclr_hamso.in`) and without (`sclr_ham.in`) SO interaction. Their formats are the same as for the `hf_ham.in` files, as explained in Appendix B. These files are read when `soctype = 'r'` so as to take the difference between their site diagonal parts.

- `sclr_u.in`

This file contains the Coulomb interaction matrix elements in the Wannier basis, obtained in cRPA. With the same format as `hf_coulomb.in` (see Appendix B).

- `sclr_vso.in`

This file contains the on site SO potential matrix elements, with the same format as `hf_soc.in` (see Appendix B). This file is read if `soctype = 'f'`.

- `sclr_l.in`

This file contains the matrix elements of the orbital moment operators $\hat{\mathbf{L}} = (\hat{L}_x, \hat{L}_y, \hat{L}_z)$. It is read if `lorb = .true.`. The format contains a first descriptive line, then, two matrices are provided, separated by another empty line, with a amount of lines and b number of columns (where a, b = `norb`) containing the real and imaginary matrix elements of $\hat{L}_x = [L_x^{ab}]$. The same structure holds in the following lines for $\hat{L}_y$ and $\hat{L}_z$.

```
x-dir
0.0 0.0 0.0
0.0 0.0 0.0
0.0 0.0 0.0

0.0 0.0 1.0
0.0 0.0 0.0
-1.0 0.0 0.0

y-dir
0.0 0.0 0.0
...
...
```

C.2 Output files

Similar to the mean-field HF code, a `Makefile` is provided to compile the program. The calculations generate the following output files:

- `gf.out`

The standard output file contains the general information about the calculation parameters. It also prints the Curie-Weiss temperature if the corresponding file that contains the exchange interactions J_{ij} is found in the working directory.

- `lf.dat`

Contains the isotropic exchange interactions J_{ij} as a result of solving the Liechtenstein formula (see Equation 5.25). This file is only generated if `lexch = .true.`. It has `nrpt` lines, each line showing the indices of the sites at a given bond ($i_{\boldsymbol{\tau}}$, $j_{\boldsymbol{\tau}'}$), the vector connecting both sites at a given bond $\boldsymbol{\tau}$ - $\boldsymbol{\tau}' - \mathbf{R}$ and the exchange parameters (in meV).

```
 ...
1 1 -6.7992 0.0000 0.0000 0.219419
1 1 6.7992 0.0000 0.0000 0.219419
1 1 -3.3996 5.8883 0.0000 0.199414
...
```

- `spinwav.dat`

Contains the energies of the spin-wave excitations (with respect to a given magnetic ordering), along the paths that connect high symmetry **k**-points. The format of this file is the same as the `bands.out` (see Appendix B), but only contains `nsite` blocks of `npnts` lines each.

- `sclr.out`

Generated if the modules for SCLR are activated (`lsclr = .true.`). It contains general system properties on first or second orders of perturbation with the SO coupling. For example, the correction to the spin magnetization ($\boldsymbol{\mu}_S$) and the orbital magnetization ($\boldsymbol{\mu}_L$ if `lorb = .true.`); or the correction of the SO coupling to the total energy.

- `sclr_r.out`

Contains the matrix elements of the response tensor $\boldsymbol{R}^{\sigma\sigma'}_{ij,abcd}$ (see Equation 5.28). Generated if (`lsclr = .true.`). The file has $\texttt{norb}^4\texttt{nsite}^2\texttt{nspin}^2$ lines, where each line shows the indeces of the orbitals a, b, and their corresponding site $i_{\boldsymbol{\tau}}$; the indeces c, d, and their site $j_{\boldsymbol{\tau}'}$; the spin index, which goes from 1

to 4, for spin sub-spaces ↑↑, ↓↑, ↑↓, and ↓↓; and lastly the real and imaginary values of the response tensor for the corresponding indices.

```
1 1 1 1 1 1 1 -1.9199890015E-01 1.4742515531E-19
1 1 1 1 2 1 1 4.4152432590E-06 -1.2793147587E-06
1 1 1 1 3 1 1 -3.9968333874E-03 6.1345296398E-07
1 1 1 2 1 1 1 4.4152432590E-06 1.2793147586E-06
1 1 1 2 2 1 1 9.6086799699E-02 7.0330204402E-20
1 1 1 2 3 1 1 -2.3506337552E-07 -2.3261899204E-07
1 1 1 3 1 1 1 -3.9968333874E-03 -6.1345296398E-07
...
...
```

- `forces_x.dat`, `forces_y.dat`, and `forces_z.dat`

Contains the force components, calculated with Equation 5.26, when the magnetic moments are aligned in the x, y, and z directions, respectively. Only written if `ldmi = .true.` and `lsclr = .true.`. The format of each of the files is the following. The first `nsite` lines show the x, y, and z components of $\delta\mathbf{e}$ (the difference between the directions of the magnetization with and without correcting for SO coupling). Then an empty line, and the following `nrpt` lines has the indices of the sites at a given bond ($i_{\boldsymbol{\tau}}$, $j_{\boldsymbol{\tau}'}$), the vector connecting both sites at a given bond $\boldsymbol{\tau}$ - $\boldsymbol{\tau}' - \mathbf{R}$ and the corresponding x, y, and z force components of $\boldsymbol{f}_i^j - \boldsymbol{f}_j^i$ (in meV).

```
-0.000000 0.000000 0.000000

...
1 1 -3.3996 5.8883 0.0000 -0.000015 -0.006084 0.077530
1 1 3.3996 5.8883 0.0000 -0.000015 0.006113 -0.077522
1 1 3.3996 -5.8883 0.0000 0.000015 0.006084 -0.077530
...
```

- `dmi.dat`

Contains `nrpt` lines with the indices of the sites at a given bond ($i_{\boldsymbol{\tau}}$, $j_{\boldsymbol{\tau}'}$), the vector connecting both sites at a given bond $\boldsymbol{\tau}$ - $\boldsymbol{\tau}' - \mathbf{R}$ and the corresponding x, y, and z components of the Dzyaloshinskii-Moriya interactions. Only generated if `ldmi = .true.` and `lsclr = .true.`; and the if the files `lf.dat`, `forces_x.dat`, `forces_y.dat`, and `forces_z.dat` are generated and present in the working directory.

```
...
1 1 -6.7992 0.0000 0.0000 0.000000 -0.153043 0.006770
1 1 6.7992 0.0000 0.0000 0.000000 0.153043 -0.006770
1 1 -3.3996 5.8883 0.0000 -0.135743 -0.077533 -0.006084
...
```

C.3 A few notes

In the following, we give a few notes about the program usage. First of all, the calculation of J_{ij} can sometimes take hours to complete, specially when `nrpt` is large (this will depend on the parameters of the Wannierisation with wannier90). One could manually set a cutoff distance for the MFHF calculations so no unnecessary transfer integrals are considered, because the amplitude of the transfer integrals fastly decays with interatomic distance. This can ease up the calculation a lot. Also, for the calculation of the spin-wave excitations, the program must be run twice, first to generate the `lf.dat` file, and then to calculate the spin-wave excitations. Please make sure that the `lf.dat` is completed and all `nrpt` bonds are present.

For the calculation of DM interactions and other properties with SCLR, we must take into account that the method (explained in detail in the work by I.V. Solovyev [308]) requires from correcting certain instabilities in the response tensor $\boldsymbol{R}^{\sigma\sigma'}_{ij,abcd}$, which are corrected just for the case where the magnetic moments are aligned in the z axis. In this case, we will first execute the program just to compute the corrected response tensor and print it to file `sclr_r.out`, for the case of $\theta = 0$ and $\phi = 0$. Then, once the response tensor is printed, we can run the program again, to compute other properties for any other value of θ and ϕ.

For the calculation of DM interactions, after generating the file `sclr_r.out`, and setting `ldmi = .true.` and `lsclr = .true.`, we have to execute the program three times. Each time we run the program we must set the values of θ and ϕ so that the magnetization is exactly aligned in the x ($\theta = 90$ and $\phi = 0$), y ($\theta = 90$ and $\phi = 90$) and z ($\theta = 0$ and $\phi = 0$) directions, one for each run. If other values are given, the program will stop immediately. This way we will generate the files `forces_x.dat`, `forces_y.dat`, and `forces_z.dat`, to finally compute the DM interactions.

Appendix D

Computation of Complex Integrals

D.1 Liechtenstein formula and related integrals

Equations 5.25 and 5.26 involve the integration of Green's functions. The integrals themselves have the following form:

$$I = \int_{-\infty}^{E_F} d\omega \; \eta(\omega), \tag{D.1}$$

where the function $\eta(\omega)$ is strongly structured (has poles) along the real ω axis. This would require a very large amount of integration points along the real axis. A more elegant way of solving this integral resides in evaluating an arbitrarily shaped contour integral that extends the ω energies to the imaginary axis, where $\eta(\omega)$ is analytical and does not have poles. For now we will change the variables $\omega \rightarrow z$, where $z = \Re e(\omega) + i \; \Im m(\omega)$.

$$I = \int_{-\infty}^{E_F} dz \; \eta(z). \tag{D.2}$$

The bounds of this integral can be expanded by using the Fermi-Dirac distribution function:

$$I = \int_{-\infty}^{\infty} dz \; f(z - E_F)\eta(z), \tag{D.3}$$

where

$$f(z - E_F) = \frac{1}{e^{(z-E_F)/k_B T} + 1}. \tag{D.4}$$

The inclusion of $f(z - E_F)$ ensures that the summation is zero above E_F. However, it introduces extra poles (Matsubara energies) in the complex plane, which will be included into the complex integration as residues. It is known that the value of the complex integral converges slowly with the number of

Matsubara energies included as residues inside the contour line. The calculation could still run perfectly like this, but for the sake of efficiency we implemented the approximate form of the Fermi-Dirac function in the continuous fraction representation [326]. This method approximates $f(z - E_F)$ as:

$$f(z - E_F) \simeq \tilde{f}(z - E_F) = \frac{1}{2} + \sum_{p}^{N} \frac{k_B R_p T}{z - E_F - i\gamma_p k_B T} + \sum_{p}^{N} \frac{k_B R_p T}{z - E_F + i\gamma_p k_B T}. \tag{D.5}$$

The computation of R_p and γ_p is straightforward (see the work by Ozaki [326] for full details), owing to the properties of symmetrical tridiagonal matrices and its equivalency with the continuous fraction representation of $f(z - E_F)$. Equation D.5 also has poles at values $z_p = E_F \pm i\gamma_p k_B T$ where $(p = 1, ..., N)$. However, the interesting property of such poles is that its separation increases non-uniformly along the imaginary axis, different to the Matsubara energies $E_m = E_F \pm i\pi(2p - 1)k_B T$ where $(p = 1, ..., N)$, whose separation between neighboring poles remains a constant $(2\pi k_B T)$ along the whole imaginary axis as can be seen in Figure D.1a. As a consequence, the convergence of the value of integrals is much faster with the amount of poles N included as residues. On the one hand, as shown in Figure D.1b-c the continuous fraction approximant resembles the shape of the analytical expression of $f(\omega - E_F)$ along the real axis, for much smaller values of N, when compared to the Matsubara summation, which is defined as:

$$\frac{1}{e^x + 1} = \frac{1}{2} + \sum_{p}^{N} \frac{-2x}{x^2 + \pi^2(2p - 1)^2}, \tag{D.6}$$

where $x = (z - E_F)/k_B T$. On the other hand the Greens functions in $\eta(z)$ become increasingly smooth the further they separate from the real axis, and this pairs well with the fact that the poles z_p increase their separation in the complex plane.

The value of the contour integral of a function that is analytical along a closed contour which has no poles inside is zero, because of the Cauchy's Integral Theorem. So, in the case of the contour $\bar{\boldsymbol{L}}$ in Figure D.1d:

$$\oint_{\bar{\boldsymbol{L}}} dz\ \tilde{f}(z - E_F)\eta(z) = 0. \tag{D.7}$$

Considering the integral over the contour $\boldsymbol{L}$ the Cauchy's Theorem does not apply as the function has poles $z_p = E_F + i\gamma_p k_B T$ inside the contour. Note that we dropped the negative values of the poles, as they are outside the contour we defined. Additionally, the integral over the contour $\bar{\boldsymbol{L}}$ can be separated in the contributions of line integrals along $\boldsymbol{L}$ and the contours $\bar{z}_p$ around poles

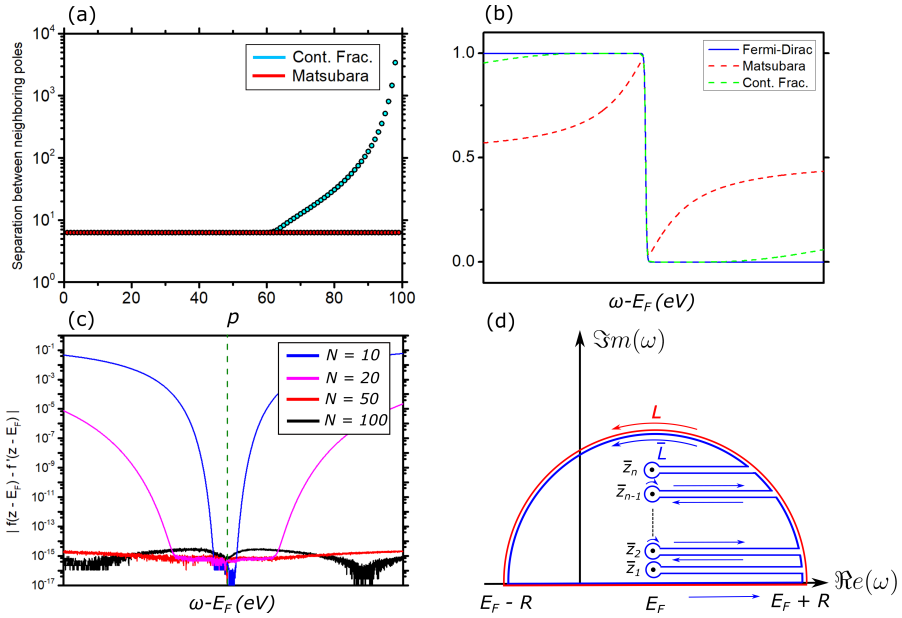

FIGURE D.1: (a) Shows the separation between adjacent poles in the continuous fraction approximation (turquoise) and Matsubara energies (red). (b) Is the Fermi-Dirac distribution function (solid blue line), the Matsubara summation (dashed red line), and the continuous fraction approximation (dashed green line) with $N = 10$ sums. (c) Value of $|f(z-E_F) - f(z-E_F)|$, with $N = 10$ (blue), $N = 20$ (purple), $N = 50$ (red), and $N = 100$ (black). (d) The path for the contour integration, $\bar{\boldsymbol{L}}$ denotes the whole path (blue line), the lines $\bar{z}_p$ ($p = 1, ..., N$), are the smaller contours that surround the poles z_p. The outer part of the path (red line) is denoted as $\boldsymbol{L}$. The separation of the horizontal lines connecting each pole is infinitesimally small so that the line integration along each pairs of lines cancel out. The radius of the semi-sphere is large ($R \simeq 10^8$).

z_p, such that:

$$\oint_{\bar{\boldsymbol{L}}} = \oint_{\boldsymbol{L}} - \sum_{p}^{N} \oint_{\bar{z}_p} = 0 \implies \oint_{\boldsymbol{L}} = \sum_{p}^{N} \oint_{\bar{z}_p} . \tag{D.8}$$

The integral over $\boldsymbol{L}$ can be further divided in the arc line ($\boldsymbol{C}$) and the real axis line.

$$\oint_{\boldsymbol{L}} = \oint_{\boldsymbol{C}} + \int_{E_F - R}^{E_F + R} . \tag{D.9}$$

The radius of this semi-circle is very large so we can approximate the integral along the real axis with the one of Equation D.3. In this way, the integrals can be evaluated as:

$$\int_{-\infty}^{\infty} \simeq \int_{E_F-R}^{E_F+R} = -\oint_{\boldsymbol{C}} + \sum_{p}^{N} \oint_{\tilde{z}_p}, \tag{D.10}$$

Using the Cauchy's Residues Theorem, the contour integral of a function that is analytical around a close contour, but contains a pole inside, is defined as:

$$\oint_{\tilde{z}_p} dz\ \tilde{f}(z-E_F)\eta(z) = 2\pi i\ Res[\tilde{f}(z-E_F)\eta(z)]_{z=z_p}. \tag{D.11}$$

where $Res[\tilde{f}(z-E_F)\eta(z)]_{z=z_p}$ is the residue of the function around the pole z_p. The computation of this residue is straightforward for simple functions, for example, when

$$\frac{f(z)}{z-z_0}, \quad where\ f(z)\ is\ analytical\ at\ z_0. \tag{D.12}$$

The residue is computed as:

$$Res[f(z)]_{z=z_0} = f(z_0). \tag{D.13}$$

Going back to our case, the function $\eta(z)$ is analytical at the pole z_p. In the same way, and taking into account that the poles inside $\boldsymbol{L}$ have positive imaginary values (see Figure D.1d), the Cauchy's Integral Theorem can be applied for the first and third terms of Equation D.5. This is to say, the only non-zero contribution to the contour integral of the function $\tilde{f}(z-E_F)\eta(z)$ around a pole z_p is the following:

$$\oint_{\tilde{z}_p} dz\ \tilde{f}(z-E_F)\eta(z) = \oint_{\tilde{z}_p} dz\ \frac{k_B R_p T\eta(z)}{z-E_F-i\gamma_p k_B T}. \tag{D.14}$$

And recalling Equations D.12 and D.13,

$$\oint_{\tilde{z}_p} dz\ \frac{k_B R_p T\eta(z)}{z-E_F-i\gamma_p k_B T} = 2\pi i k_B R_p T\ \eta(E_F+i\gamma_p k_B T). \tag{D.15}$$

Therefore, the integral that we are interested to compute in order to obtain the isotropic exchange parameters or force components for DM interactions (see 5.25 and 5.26), is evaluated as:

$$\int_{-\infty}^{\infty} dz\ \tilde{f}(z-E_F)\eta(z) = -\oint_{\boldsymbol{C}} dz\ \tilde{f}(z-E_F)\eta(z) + \sum_{p}^{N} 2\pi i k_B R_p T\ \eta(E_F+i\gamma_p k_B T), \tag{D.16}$$

where the integral over $\boldsymbol{C}$ is evaluated by using the very simple rectangle rule,

along the path. So by dividing the $\boldsymbol{C}$ line into N segments, we evaluate the integral like:

$$\oint_{\boldsymbol{C}} dz\ \tilde{f}(z - E_F)\eta(z) = \sum_{n}^{N-1} \Delta z_n\ \tilde{f}(z_n - E_F)\eta(z_n), \tag{D.17}$$

where z_n is a point in $\boldsymbol{C}$ and $\Delta z_n = z_{n+1} - z_n$.

Bibliography

(1) BP Energy Outlook: 2019 Edition.

(2) Stephens, E.; Ross, I. L.; Mussgnug, J. H.; Wagner, L. D.; Borowitzka, M. A.; Posten, C.; Kruse, O.; Hankamer, B. *Trends in Plant Science* **2010**, *15*, 554–564.

(3) Kerr, R. A. *Science* **1998**, *281*, 1128–1131.

(4) ipcc Climate Change 2014: Synthesis Report.

(5) A global snapshot of the ait pollution-related health impacts of transportation sector emissions in 2010 and 2015.

(6) aqli: Pollution Facts.

(7) DeCarolis, J. F.; Keith, D. W. *Energy Policy* **2006**, *34*, 395–410.

(8) Laine, H. S.; Salpakari, J.; Looney, E. E.; Savin, H.; Peters, I. M.; Buonassisi, T. *Energy and Environmental Science* **2019**, 2706–2716.

(9) Masquelier, C.; Croguennec, L. *Chemical Reviews* **2013**, *113*, 6552–6591.

(10) Nazar, L. F.; Cuisinier, M.; Pang, Q. *MRS Bulletin* **2014**, *39*, 436–442.

(11) Yabuuchi, N.; Kubota, K.; Dahbi, M.; Komaba, S. *Chem. Rev.* **2014**, *114*, 11636–11682.

(12) Landa-Medrano, I.; Li, C.; Ortiz-Vitoriano, N.; Ruiz de Larramendi, I.; Carrasco, J.; Rojo, T. *The Journal of Physical Chemistry Letters* **2016**, *7*, 1161–1166.

(13) Choi, J. W.; Aurbach, D. *Nature Reviews Materials* **2016**, *1*, 16013.

(14) Hwang, J.-Y.; Myung, S.-T.; Sun, Y.-K. *Chemical Society Reviews* **2017**, *46*, 3529–3614.

(15) Kubota, K.; Komaba, S. *Journal of The Electrochemical Society* **2015**, *162*, A2538–A2550.

(16) Goodenough, J. B.; Park, K.-S. *Journal of the American Chemical Society* **2013**, *135*, 1167–1176.

(17) Goodenough, J. B.; Kim, Y. *Chemistry of Materials* **2010**, *22*, 587–603.

(18) Blomgren, G. E. *Journal of The Electrochemical Society* **2017**, *164*, A5019–A5025.

(19) Manthiram, A. *ACS Central Science* **2017**, *3*, 1063–1069.

(20) Noh, H. J.; Youn, S.; Yoon, C. S.; Sun, Y. K. *Journal of Power Sources* **2013**, *233*, 121–130.

(21) Palomares, V.; Serras, P.; Villaluenga, I.; Hueso, K. B.; Carretero-González, J.; Rojo, T. *Energy and Environmental Science* **2012**, *5*, 5884–5901.

(22) Han, M. H.; Gonzalo, E.; Singh, G.; Rojo, T. *Energy and Environmental Science* **2015**, *8*, 81–102.

(23) Hartmann, P.; Bender, C. L.; Vračar, M.; Dürr, A. K.; Garsuch, A.; Janek, J.; Adelhelm, P. *Nature Materials* **2013**, *12*, 228–232.

(24) Xu, X.; Zhou, D.; Qin, X.; Lin, K.; Kang, F.; Li, B.; Shanmukaraj, D.; Rojo, T.; Armand, M.; Wang, G. *Nature Communications* **2018**, *9*, 3870.

(25) Hueso, K. B.; Armand, M.; Rojo, T. *Energy and Environmental Science* **2013**, *6*, 734–749.

(26) Hong, S. Y.; Kim, Y.; Park, Y.; Choi, A.; Choi, N.-S.; Lee, K. T. *Energy and Environmental Science* **2013**, *6*, 2067–2081.

(27) McCloskey, B. D.; Garcia, J. M.; Luntz, A. C. *The Journal of Physical Chemistry Letters* **2014**, *5*, 1230–1235.

(28) Jain, A.; Shin, Y.; Persson, K. A. *Nature Reviews Materials* **2016**, *1*, 1–13.

(29) Urban, A.; Seo, D. H.; Ceder, G. *npj Computational Materials* **2016**, *2*, 16002.

(30) Islam, M. S.; Fisher, C. A. *Chemical Society Reviews* **2014**, *43*, 185–204.

(31) Groß, A. *Topics in Current Chemistry* **2018**, *376*, 1–22.

(32) Meng, Y. S.; Arroyo-De Dompablo, M. E. *Energy and Environmental Science* **2009**, *2*, 589–609.

(33) Born, M; Oppenheimer, R *Annalen der Physik* **1927**, *389*, 457–484.

(34) Roothaan, C. C. J. *Reviews of Modern Physics* **1951**, *23*, 69–89.

(35) Parr, R. G.; Yang, W., *Density-Functional Theory of Atoms and Molecules*; International Series of Monographs on Chemistry; Oxford University Press: 1994.

(36) Szabo, A; Ostlund, N. S., *Modern Quantum Chemistry: Introduction to Advanced Electronic Structure Theory*; Macmillan: 1982.

(37) Roos, B. O.; Taylor, P. R.; Sigbahn, P. E. M. *Chemical Physics* **1980**, *48*, 157–173.

(38) Malrieu, J. P.; Caballol, R.; Calzado, C. J.; de Graaf, C.; Guihéry, N. *Chemical Reviews* **2014**, *114*, 429–492.

(39) Angeli, C.; Cimiraglia, R.; Malrieu, J.-P. *Chemical Physics Letters* **2001**, *350*, 297–305.

(40) Angeli, C; Cimiraglia, R; Evangelisti, S; Leininger, T; Malrieu, J.-P. *The Journal of Chemical Physics* **2001**, *114*, 10252–10264.

(41) Angeli, C.; Cimiraglia, R.; Malrieu, J.-P. *The Journal of Chemical Physics* **2002**, *117*, 9138–9153.

(42) Andersson, K.; Malmqvist, P.; Roos, B. O. *The Journal of Chemical Physics* **1992**, *96*, 1218–1226.

(43) Andersson, K.; Malmqvist, P. A.; Roos, B. O.; Sadlej, A. J.; Wolinski, K. *The Journal of Physical Chemistry* **1990**, *94*, 5483–5488.

(44) Friesner, R. A. *Proceedings of the National Academy of Sciences of the United States of America* **2005**, *102*, 6648 –6653.

(45) Lyakh, D. I.; Musiał, M.; Lotrich, V. F.; Bartlett, R. J. *Chemical Reviews* **2012**, *112*, 182–243.

(46) Sauri, V.; Serrano-Andrés, L.; Shahi, A. R. M.; Gagliardi, L.; Vancoillie, S.; Pierloot, K. *Journal of Chemical Theory and Computation* **2011**, *7*, 153–168.

(47) Thomas, L. H. *Mathematical Proceedings of the Cambridge Philosophical Society* **1927**, *23*, 542–548.

(48) Dirac, P. A. M. *Mathematical Proceedings of the Cambridge Philosophical Society* **1930**, *26*, 376–385.

(49) Fermi, E *Zeitschrift für Physik* **1928**, *48*, 73–79.

(50) Kohn, W; Sham, L. J. *Physical Review* **1965**, *140*, A1133–A1138.

(51) Ceperley, D. M.; Alder, B. J. *Physical Review Letters* **1980**, *45*, 566–569.

(52) Vosko, S. H.; Wilk, L; Nusair, M *Canadian Journal of Physics* **1980**, *58*, 1200–1211.

(53) Perdew, J. P.; Wang, Y. *Physical Review B* **1992**, *45*, 13244–13249.

(54) Lee, C.; Yang, W.; Parr, R. G. *Physical Review B* **1988**, *37*, 785–789.

(55) Becke, A. D. *Physical Review A* **1988**, *38*, 3098–3100.

(56) Perdew, J. P.; Chevary, J. A.; Vosko, S. H.; Jackson, K. A.; Pederson, M. R.; Singh, D. J.; Fiolhais, C. *Physical Review B* **1992**, *46*, 6671–6687.

(57) Perdew, J. P.; Burke, K.; Ernzerhof, M. *Physical Review Letters* **1996**, *77*, 3865–3868.

(58) Zhao, Y.; Truhlar, D. G. *The Journal of Chemical Physics* **2006**, *125*, 194101.

(59) Wang, Y.; Jin, X.; Yu, H. S.; Truhlar, D. G.; He, X. *Proceedings of the National Academy of Sciences* **2017**, *114*, 8487 –8492.

(60) Peverati, R.; Truhlar, D. G. *The Journal of Physical Chemistry Letters* **2012**, *3*, 117–124.

(61) Peverati, R.; Truhlar, D. G. *Physical Chemistry Chemical Physics* **2012**, *14*, 13171–13174.

(62) Yu, H. S.; He, X.; Truhlar, D. G. *Journal of Chemical Theory and Computation* **2016**, *12*, 1280–1293.

(63) Tao, J.; Perdew, J. P.; Staroverov, V. N.; Scuseria, G. E. *Physical Review Letters* **2003**, *91*, 146401.

(64) Perdew, J. P.; Ruzsinszky, A.; Csonka, G. I.; Constantin, L. A.; Sun, J. *Physical Review Letters* **2009**, *103*, 26403.

(65) De Silva, P.; Corminboeuf, C. *The Journal of Chemical Physics* **2015**, *143*, 111105.

(66) Sun, J.; Ruzsinszky, A.; Perdew, J. *Physical Review Letters* **2015**, *115*, 36402.

(67) Kim, K; Jordan, K. D. *The Journal of Physical Chemistry* **1994**, *98*, 10089–10094.

(68) Stephens, P. J.; Devlin, F. J.; Chabalowski, C. F.; Frisch, M. J. *The Journal of Physical Chemistry* **1994**, *98*, 11623–11627.

(69) Heyd, J.; Scuseria, G. E.; Ernzerhof, M. *The Journal of Chemical Physics* **2003**, *118*, 8207–8215.

(70) Krukau, A. V.; Vydrov, O. A.; Izmaylov, A. F.; Scuseria, G. E. *The Journal of Chemical Physics* **2006**, *125*, 224106.

(71) Neumann, M. A.; Perrin, M.-A. *The Journal of Physical Chemistry B* **2005**, *109*, 15531–15541.

(72) Moellmann, J.; Grimme, S. *The Journal of Physical Chemistry C* **2014**, *118*, 7615–7621.

(73) Klimeš, J.; Michaelides, A. *The Journal of Chemical Physics* **2012**, *137*, 120901.

(74) Liu, W.; Filimonov, S. N.; Carrasco, J.; Tkatchenko, A. *Nature Communications* **2013**, *4*, 2569.

(75) Carrasco, J.; Santra, B.; Klimeš, J.; Michaelides, A. *Physical Review Letters* **2011**, *106*, 26101.

(76) Liu, W.; Carrasco, J.; Santra, B.; Michaelides, A.; Scheffler, M.; Tkatchenko, A. *Physical Review B* **2012**, *86*, 245405.

(77) Grimme, S.; Hujo, W.; Kirchner, B. *Physical Chemistry Chemical Physics* **2012**, *14*, 4875–4883.

(78) Lage-Estebanez, I.; del Olmo, L.; López, R.; García de la Vega, J. M. *Journal of Computational Chemistry* **2017**, *38*, 530–540.

(79) Lin, I.-C.; Seitsonen, A. P.; Tavernelli, I.; Rothlisberger, U. *Journal of Chemical Theory and Computation* **2012**, *8*, 3902–3910.

(80) DiStasio, R. A.; Santra, B.; Li, Z.; Wu, X.; Car, R. *The Journal of Chemical Physics* **2014**, *141*, 84502.

(81) Møgelhøj, A.; Kelkkanen, A. K.; Wikfeldt, K. T.; Schiøtz, J.; Mortensen, J. J.; Pettersson, L. G. M.; Lundqvist, B. I.; Jacobsen, K. W.; Nilsson, A.; Nørskov, J. K. *The Journal of Physical Chemistry B* **2011**, *115*, 14149–14160.

(82) Marini, A.; García-González, P; Rubio, A. *Physical Review Letters* **2006**, *96*, 136404.

(83) Harl, J.; Kresse, G. *Physical Review B* **2008**, *77*, 45136.

(84) Harl, J.; Kresse, G. *Physical Review Letters* **2009**, *103*, 56401.

(85) Spanu, L.; Sorella, S.; Galli, G. *Physical Review Letters* **2009**, *103*, 196401.

(86) Dahlen, N. E.; van Leeuwen, R.; von Barth, U. *Physical Review A* **2006**, *73*, 12511.

(87) Rydberg, H; Dion, M; Jacobson, N; Schröder, E; Hyldgaard, P; Simak, S. I.; Langreth, D. C.; Lundqvist, B. I. *Physical Review Letters* **2003**, *91*, 126402.

(88) Rydberg, H.; Lundqvist, B. I.; Langreth, D. C.; Dion, M. *Physical Review B* **2000**, *62*, 6997–7006.

(89) Dion, M; Rydberg, H; Schröder, E; Langreth, D. C.; Lundqvist, B. I. *Physical Review Letters* **2004**, *92*, 246401.

(90) Lee, K.; Murray, É. D.; Kong, L.; Lundqvist, B. I.; Langreth, D. C. *Physical Review B* **2010**, *82*, 81101.

(91) Vydrov, O. A.; Van Voorhis, T. *Journal of Chemical Physics* **2010**, *133*, 244103.

(92) Sabatini, R.; Gorni, T.; De Gironcoli, S. *Physical Review B* **2013**, *87*, 4–7.

(93) Vydrov, O. A.; Van Voorhis, T. *Physical Review Letters* **2009**, *103*, 63004.

(94) Michaelides, J. K.; Bowler, D. R.; Angelos *Journal of Physics: Condensed Matter* **2010**, *22*, 22201.

(95) Grimme, S. *Journal of Computational Chemistry* **2004**, *25*, 1463–1473.

(96) Grimme, S. *Journal of Computational Chemistry* **2006**, *27*, 1787–1799.

(97) Grimme, S.; Antony, J.; Ehrlich, S.; Krieg, H. *The Journal of Chemical Physics* **2010**, *132*, 154104.

(98) Tkatchenko, A.; Scheffler, M. *Physical Review Letters* **2009**, *102*, 73005.

(99) Ashcroft, N. W.; Mermin, N. D., *Solid State Physics*; HRW international editions; Holt, Rinehart and Winston: 1976.

(100) Hellmann, H *The Journal of Chemical Physics* **1935**, *3*, 61.

(101) Hellmann, H; Kassatotschkin, W *The Journal of Chemical Physics* **1936**, *4*, 324–325.

(102) Laasonen, K.; Pasquarello, A.; Car, R.; Lee, C.; Vanderbilt, D. *Physical Review B* **1993**, *47*, 10142–10153.

(103) Laasonen, K.; Car, R.; Lee, C.; Vanderbilt, D. *Physical Review B* **1991**, *43*, 6796–6799.

(104) Vanderbilt, D. *Physical Review B* **1990**, *41*, 7892–7895.

(105) Hamann, D. R.; Schlüter, M; Chiang, C *Physical Review Letters* **1979**, *43*, 1494–1497.

(106) Kresse, G; Joubert, D *Physical Review B* **1999**, *59*, 1758–1775.

(107) Blöchl, P. E. *Physical Review B* **1994**, *50*, 17953–17979.

(108) Baroni, P. G. et al. *Journal of Physics: Condensed Matter* **2017**, *29*, 465901.

(109) Wentzcovitch, P. G.; Baroni, S.; Bonini, N.; Calandra, M.; Car, R.; Cavazzoni, C.; Ceresoli, D.; Chiarotti, G. L.; Cococcioni, M.; Dabo, I.; Corso, A. D.; de Gironcoli, S.; Fabris, S. *Journal of Physics: Condensed Matter* **2009**, *21*, 395502.

(110) Kresse, G; Hafner, J *Physical Review B* **1994**, *49*, 14251–14269.

(111) Kresse, G; Hafner, J *Physical Review B* **1993**, *47*, 558–561.

(112) Kresse, G; Furthmüller, J *Physical Review B* **1996**, *54*, 11169–11186.

(113) Kresse, G; Furthmüller, J *Computational Materials Science* **1996**, *6*, 15–50.

(114) Huhn, W. P.; Blum, V. *Physical Review Materials* **2017**, *1*, 33803.

(115) Levchenko, S. V.; Ren, X.; Wieferink, J.; Johanni, R.; Rinke, P.; Blum, V.; Scheffler, M. *Computer Physics Communications* **2015**, *192*, 60–69.

(116) Lederer, A. M.; Blum, V; Johanni, R; Havu, V; Lang, B; Auckenthaler, T; Heinecke, A; Bungartz, H.-J.; H *Journal of Physics: Condensed Matter* **2014**, *26*, 213201.

(117) Scheffler, X. R.; Rinke, P.; Blum, V.; Wieferink, J.; Tkatchenko, A.; Sanfilippo, A.; Reuter, K.; Matthias *New Journal of Physics* **2012**, *14*, 53020.

(118) Havu, V; Blum, V; Havu, P; Scheffler, M *Journal of Computational Physics* **2009**, *228*, 8367–8379.

(119) Blum, V.; Gehrke, R.; Hanke, F.; Havu, P.; Havu, V.; Ren, X.; Reuter, K.; Scheffler, M. *Computer Physics Communications* **2009**, *180*, 2175–2196.

(120) Wannier, G. H. *Physical Review* **1937**, *52*, 191–197.

(121) Marzari, N.; Vanderbilt, D. *Physical Review B* **1997**, *56*, 12847–12865.

(122) Mostofi, A. A.; Yates, J. R.; Pizzi, G.; Lee, Y.-S.; Souza, I.; Vanderbilt, D.; Marzari, N. *Computer Physics Communications* **2014**, *185*, 2309–2310.

(123) Marzari, N.; Mostofi, A. A.; Yates, J. R.; Souza, I.; Vanderbilt, D. *Reviews of Modern Physics* **2012**, *84*, 1419–1475.

(124) Souza, I.; Marzari, N.; Vanderbilt, D. *Physical Review B* **2001**, *65*, 35109.

(125) Feynman, R. P. *Physical Review* **1939**, *56*, 340–343.

(126) Henkelman, G.; Jónsson, H. *The Journal of Chemical Physics* **1999**, *111*, 7010–7022.

(127) Henkelman, G.; Uberuaga, B. P.; Jónsson, H. *The Journal of Chemical Physics* **2000**, *113*, 9901–9904.

(128) Henkelman, G.; Jónsson, H. *The Journal of Chemical Physics* **2000**, *113*, 9978–9985.

(129) Jónsson, H.; Mills, G.; Jacobsen, K. W. In *Classical and Quantum Dynamics in Condensed Phase Simulations*; World Scientific: 1998, pp 385–404.

(130) Armand, M; Tarascon, J.-M. *Nature* **2008**, *451*, 652.

(131) Tarascon, J.-M.; Armand, M In *Materials for Sustainable Energy*; Co-Published with Macmillan Publishers Ltd, UK: 2010, pp 171–179.

(132) Energy Future: Think Efficiency.

(133) Li, Y.; Lu, J. *ACS Energy Letters* **2017**, *2*, 1370–1377.

(134) Luntz, A. C.; McCloskey, B. D. *Chemical Reviews* **2014**, *114*, 11721–11750.

(135) Girishkumar, G; McCloskey, B; Luntz, A. C.; Swanson, S; Wilcke, W *The Journal of Physical Chemistry Letters* **2010**, *1*, 2193–2203.

(136) Christensen, J.; Albertus, P.; Sanchez-Carrera, R. S.; Lohmann, T.; Kozinsky, B.; Liedtke, R.; Ahmed, J.; Kojic, A. *Journal of The Electrochemical Society* **2012**, *159*, R1.

(137) Freunberger, S. A.; Chen, Y.; Peng, Z.; Griffin, J. M.; Hardwick, L. J.; Bardé, F.; Novák, P.; Bruce, P. G. *Journal of the American Chemical Society* **2011**, *133*, 8040–8047.

(138) Black, R.; Oh, S. H.; Lee, J.-H.; Yim, T.; Adams, B.; Nazar, L. F. *Journal of the American Chemical Society* **2012**, *134*, 2902–2905.

(139) McCloskey, B. D.; Speidel, A; Scheffler, R; Miller, D. C.; Viswanathan, V; Hummelshøj, J. S.; Nørskov, J. K.; Luntz, A. C. *The Journal of Physical Chemistry Letters* **2012**, *3*, 997–1001.

(140) Liu, Y.; Wang, L.; Cao, L.; Shang, C.; Wang, Z.; Wang, H.; He, L.; Yang, J.; Cheng, H.; Li, J.; Lu, Z. *Materials Chemistry Frontiers* **2017**, *1*, 2495–2510.

(141) Yao, X.; Dong, Q.; Cheng, Q.; Wang, D. *Angewandte Chemie International Edition* **2016**, *55*, 11344–11353.

(142) Carboni, M.; Marrani, A. G.; Spezia, R.; Brutti, S. *Journal of The Electrochemical Society* **2018**, *165*, A118–A125.

(143) Peng, Z.; Freunberger, S. A.; Chen, Y.; Bruce, P. G. *Science* **2012**, *337*, 563 –566.

(144) Viswanathan, V; Nørskov, J. K.; Speidel, A; Scheffler, R; Gowda, S; Luntz, A. C. *The Journal of Physical Chemistry Letters* **2013**, *4*, 556–560.

(145) Liu, T.; Leskes, M.; Yu, W.; Moore, A. J.; Zhou, L.; Bayley, P. M.; Kim, G.; Grey, C. P. *Science* **2015**, *350*, 530 –533.

(146) Wang, L.; Pan, J.; Zhang, Y.; Cheng, X.; Liu, L.; Peng, H. *Advanced Materials* **2017**, *30*, 1704378.

(147) Asadi, M. et al. *Nature* **2018**, *555*, 502.

(148) Ren, X.; Wu, Y. *Journal of the American Chemical Society* **2013**, *135*, 2923–2926.

(149) Kang, S.; Mo, Y.; Ong, S. P.; Ceder, G. *Nano Letters* **2014**, *14*, 1016–1020.

(150) Ortiz-Vitoriano, N.; Batcho, T. P.; Kwabi, D. G.; Han, B.; Pour, N.; Yao, K. P. C.; Thompson, C. V.; Shao-Horn, Y. *The Journal of Physical Chemistry Letters* **2015**, *6*, 2636–2643.

(151) Kim, J.; Lim, H.-D.; Gwon, H.; Kang, K. *Physical Chemistry Chemical Physics* **2013**, *15*, 3623–3629.

(152) Jian, Z.; Chen, Y.; Li, F.; Zhang, T.; Liu, C.; Zhou, H. *Journal of Power Sources* **2014**, *251*, 466–469.

(153) Liu, W.; Sun, Q.; Yang, Y.; Xie, J.-Y.; Fu, Z.-W. *Chemical Communications* **2013**, *49*, 1951–1953.

(154) Riyadi, S.; Zhang, B.; de Groot, R. A.; Caretta, A.; van Loosdrecht, P. H. M.; Palstra, T. T. M.; Blake, G. R. *Physical Review Letters* **2012**, *108*, 217206.

(155) Kováčik, R.; Werner, P.; Dymkowski, K.; Ederer, C. *Physical Review B* **2012**, *86*, 75130.

(156) Kim, M.; Min, B. I. *Physical Review B* **2014**, *89*, 121106.

(157) Nandy, A. K.; Mahadevan, P.; Sen, P.; Sarma, D. D. *Physical Review Letters* **2010**, *105*, 56403.

(158) Ylvisaker, E. R.; Singh, R. R. P.; Pickett, W. E. *Physical Review B* **2010**, *81*, 180405.

(159) Kim, M.; Kim, B. H.; Choi, H. C.; Min, B. I. *Physical Review B* **2010**, *81*, 100409.

(160) Solovyev, I. V.; Pchelkina, Z. V.; Mazurenko, V. V. *CrystEngComm* **2014**, *16*, 522–531.

(161) Hartmann, P.; Bender, C. L.; Sann, J.; Dürr, A. K.; Jansen, M.; Janek, J.; Adelhelm, P. *Physical Chemistry Chemical Physics* **2013**, *15*, 11661–11672.

(162) Johnson, L.; Li, C.; Liu, Z.; Chen, Y.; Freunberger, S. A.; Ashok, P. C.; Praveen, B. B.; Dholakia, K.; Tarascon, J.-M.; Bruce, P. G. *Nature Chemistry* **2014**, *6*, 1091.

(163) Radin, M. D.; Rodriguez, J. F.; Tian, F.; Siegel, D. J. *Journal of the American Chemical Society* **2012**, *134*, 1093–1103.

(164) Alkauskas, A.; Broqvist, P.; Pasquarello, A. *Physica Status Solidi (b)* **2011**, *248*, 775–789.

(165) Franchini, C. *Journal of Physics: Condensed Matter* **2014**, *26*, 253202.

(166) He, J.; Franchini, C. *Physical Review B* **2012**, *86*, 235117.

(167) Conesa, J. C. *The Journal of Physical Chemistry C* **2012**, *116*, 18884–18890.

(168) Skone, J. H.; Govoni, M.; Galli, G. *Physical Review B* **2014**, *89*, 1–12.

(169) Radin, M. D.; Siegel, D. J. *Energy and Environmental Science* **2013**, *6*, 2370–2379.

(170) Yang, S.; Siegel, D. J. *Chemistry of Materials* **2015**, *27*, 3852–3860.

(171) Wriedt, H. *Bulletin of Alloy Phase Diagrams* **1987**, *8*, 234–246.

(172) Solovyev, I. V.; Pchelkina, Z. V.; Mazurenko, V. V. *CrystEngComm* **2014**, *16*, 522–531.

(173) Lee, B.; Seo, D.-H.; Lim, H.-D.; Park, I.; Park, K.-Y.; Kim, J.; Kang, K. *Chemistry of Materials* **2014**, *26*, 1048–1055.

(174) Hartmann, P.; Heinemann, M.; Bender, C. L.; Graf, K.; Baumann, R.-P.; Adelhelm, P.; Heiliger, C.; Janek, J. *The Journal of Physical Chemistry C* **2015**, *119*, 22778–22786.

(175) Kang, S.; Mo, Y.; Ong, S. P.; Ceder, G. *Nano Letters* **2014**, *14*, 1016–1020.

(176) Lee, B.; Kim, J.; Yoon, G.; Lim, H. D.; Choi, I. S.; Kang, K. *Chemistry of Materials* **2015**, *27*, 8406–8413.

(177) Xia, C.; Black, R.; Fernandes, R.; Adams, B.; Nazar, L. F. *Nature Chemistry* **2015**, *7*, 496–501.

(178) Lutz, L.; Yin, W.; Grimaud, A.; Alves Dalla Corte, D.; Tang, M.; Johnson, L.; Azaceta, E.; Sarou-Kanian, V.; Naylor, A. J.; Hamad, S.; Anta, J. A.; Salager, E.; Tena-Zaera, R.; Bruce, P. G.; Tarascon, J.-M. *The Journal of Physical Chemistry C* **2016**, *120*, 20068–20076.

(179) Morasch, R.; Kwabi, D. G.; Tulodziecki, M.; Risch, M.; Zhang, S.; Shao-Horn, Y. *ACS Applied Materials & Interfaces* **2017**, *9*, 4374–4381.

(180) Lutz, L.; Dachraoui, W.; Demortière, A.; Johnson, L. R.; Bruce, P. G.; Grimaud, A.; Tarascon, J. M. *Nano Letters* **2018**, *18*, 1280–1289.

(181) Das, U.; Lau, K. C.; Redfern, P. C.; Curtiss, L. A. *The Journal of Physical Chemistry Letters* **2014**, *5*, 813–819.

(182) Arcelus, O.; Suaud, N.; Katcho, N. A.; Carrasco, J. *The Journal of Chemical Physics* **2017**, *146*, 184301.

(183) Henkelman, W. T.; Sanville, E; G *Journal of Physics: Condensed Matter* **2009**, *21*, 84204.

(184) Sanville, E.; Kenny, S. D.; Smith, R.; Henkelman, G. *Journal of Computational Chemistry* **2007**, *28*, 899–908.

(185) Henkelman, G.; Arnaldsson, A.; Jónsson, H. *Computational Materials Science* **2006**, *36*, 354–360.

(186) Yu, M.; Trinkle, D. R. *The Journal of Chemical Physics* **2011**, *134*, 64111.

(187) Kanamori, J. *Progress of Theoretical Physics* **1963**, *30*, 275–289.

(188) Solovyev, I. V.; Imada, M *Physical Review B* **2005**, *71*, 45103.

(189) Gunnarsson, O; Andersen, O. K.; Jepsen, O; Zaanen, J *Physical Review B* **1989**, *39*, 1708–1722.

(190) Anisimov, V. I.; Gunnarsson, O *Physical Review B* **1991**, *43*, 7570–7574.

(191) Gunnarsson, O *Physical Review B* **1990**, *41*, 514–518.

(192) Cococcioni, M.; de Gironcoli, S. *Physical Review B* **2005**, *71*, 35105.

(193) Aryasetiawan, F; Imada, M; Georges, A; Kotliar, G; Biermann, S; Lichtenstein, A. I. *Physical Review B* **2004**, *70*, 195104.

(194) Anderson, P. W. *Physical Review* **1959**, *115*, 2–13.

(195) Boilleau, C.; Suaud, N.; Bastardis, R.; Guihéry, N.; Malrieu, J. P. *Theoretical Chemistry Accounts* **2010**, *126*, 231–241.

(196) Labèguerie, P.; Boilleau, C.; Bastardis, R.; Suaud, N.; Guihéry, N.; Malrieu, J.-P. *The Journal of Chemical Physics* **2008**, *129*, 154110.

(197) Neese, F. *Wiley Interdisciplinary Reviews: Computational Molecular Science* **2012**, *2*, 73–78.

(198) Aquilante, F. et al. *Journal of Computational Chemistry* **2016**, *37*, 506–541.

(199) Ben Amor, N.; Maynau, D. *Chemical Physics Letters* **1998**, *286*, 211–220.

(200) Dunning, T. H. *The Journal of Chemical Physics* **1989**, *90*, 1007–1023.

(201) Roos, B. O.; Lindh, R.; Malmqvist, P.-Å.; Veryazov, V.; Widmark, P.-O. *The Journal of Physical Chemistry A* **2004**, *108*, 2851–2858.

(202) Roos, B. O.; Veryazov, V.; Widmark, P.-O. *Theoretical Chemistry Accounts* **2004**, *111*, 345–351.

(203) Pradines, B.; Suaud, N.; Malrieu, J.-P. *The Journal of Physical Chemistry A* **2015**, *119*, 5207–5217.

(204) Maurice, R.; de Graaf, C.; Guihéry, N. *Physical Chemistry Chemical Physics* **2013**, *15*, 18784–18804.

(205) Kwabi, D.; Ortiz-Vitoriano, N.; Freunberger, S.; Chen, Y.; Imanishi, N.; Bruce, P.; Shao-Horn, Y. *MRS Bulletin* **2014**, *39*, 443–452.

(206) Bryantsev, V. S.; Giordani, V.; Walker, W.; Blanco, M.; Zecevic, S.; Sasaki, K.; Uddin, J.; Addison, D.; Chase, G. V. *Journal of Physical Chemistry A* **2011**, *115*, 12399–12409.

(207) Becke, A. D. *The Journal of Chemical Physics* **1993**, *98*, 5648–5652.

(208) Rajput, N. N.; Qu, X.; Sa, N.; Burrell, A. K.; Persson, K. A. *Journal of the American Chemical Society* **2015**, *137*, 3411–3420.

(209) Ong, S. P.; Andreussi, O.; Wu, Y.; Marzari, N.; Ceder, G. *Chemistry of Materials* **2011**, *23*, 2979–2986.

(210) Okoshi, M.; Yamada, Y.; Yamada, A.; Nakai, H. *Journal of the Electrochemical Society* **2013**, *160*, A2160–A2165.

(211) In, Nocedal, J., Wright, S. J., Eds.; Springer New York: New York, NY, 2006, pp 529–562.

(212) Callsen, M.; Sodeyama, K.; Futera, Z.; Tateyama, Y.; Hamada, I. *The Journal of Physical Chemistry B* **2017**, *121*, 180–188.

(213) Sun, Y.; Hamada, I. *The Journal of Physical Chemistry B* **2018**, *122*, 10014–10022.

(214) Okamoto, Y.; Kubo, Y. *The Journal of Physical Chemistry C* **2013**, *117*, 15940–15946.

(215) Lutz, L.; Alves Dalla Corte, D.; Tang, M.; Salager, E.; Deschamps, M.; Grimaud, A.; Johnson, L.; Bruce, P. G.; Tarascon, J.-M. *Chemistry of Materials* **2017**, *29*, 6066–6075.

(216) *Scientific Reports* **2017**, *7*, 17635.

(217) Delmas, C. *Advanced Energy Materials* **2018**, *8*, 1703137.

(218) Ni, Q.; Bai, Y.; Wu, F.; Wu, C. *Advanced Science* **2017**, *4*, 1600275.

(219) Wang, P. F.; You, Y.; Yin, Y. X.; Guo, Y. G. *Advanced Energy Materials* **2018**, *8*, 1–23.

(220) Delmas, C; Fouassier, C; Hagenmuller, P *Physica B+C* **1980**, *99*, 81–85.

(221) Yao, H.-R.; Wang, P.-F.; Gong, Y.; Zhang, J.; Yu, X.; Gu, L.; OuYang, C.; Yin, Y.-X.; Hu, E.; Yang, X.-Q.; Stavitski, E.; Guo, Y.-G.; Wan, L.-J. *Journal of the American Chemical Society* **2017**, *139*, 8440–8443.

(222) Yao, H.-R.; Wang, P.-F.; Wang, Y.; Yu, X.; Yin, Y.-X.; Guo, Y.-G. *Advanced Energy Materials* **2017**, *7*, 1700189.

(223) Didier, C.; Guignard, M.; Suchomel, M. R.; Carlier, D.; Darriet, J.; Delmas, C. *Chemistry of Materials* **2016**, *28*, 1462–1471.

(224) Mortemard de Boisse, B.; Liu, G.; Ma, J.; Nishimura, S.-i.; Chung, S.-C.; Kiuchi, H.; Harada, Y.; Kikkawa, J.; Kobayashi, Y.; Okubo, M.; Yamada, A. *Nature Communications* **2016**, *7*, 11397.

(225) Delmas, C.; Braconnier, J.-J.; Fouassier, C.; Hagenmuller, P. *Solid State Ionics* **1981**, *3-4*, 165–169.

(226) Sun, Y.; Guo, S.; Zhou, H. *Energy and Environmental Science* **2018**, 825 –840.

(227) Radin, M. D.; Alvarado, J.; Meng, Y. S.; Van der Ven, A. *Nano Letters* **2017**, *17*, 7789–7795.

(228) Bhattacharya, K.; Conti, S.; Zanzotto, G.; Zimmer, J. *Nature* **2004**, *428*, 55.

(229) Gabrisch, H.; Yazami, R.; Fultz, B. *Electrochemical and Solid-State Letters* **2002**, *5*, A111.

(230) Singer, A et al. *Nature Energy* **2018**, *3*, 641–647.

(231) Guignard, M.; Didier, C.; Darriet, J.; Bordet, P.; Elkaïm, E.; Delmas, C. *Nature Materials* **2013**, *12*, 74–80.

(232) Didier, C.; Guignard, M.; Darriet, J.; Delmas, C. *Inorganic Chemistry* **2012**, *51*, 11007–11016.

(233) Szajwaj, O.; Gaudin, E.; Weill, F.; Darriet, J.; Delmas, C. *Inorganic Chemistry* **2009**, *48*, 9147–9154.

(234) Didier, C.; Guignard, M.; Denage, C.; Szajwaj, O.; Ito, S.; Saadoune, I.; Darriet, J.; Delmas, C. *Electrochemical and Solid-State Letters* **2011**, *14*, A75.

(235) Guignard, M.; Carlier, D.; Didier, C.; Suchomel, M. R.; Elkaïm, E.; Bordet, P.; Decourt, R.; Darriet, J.; Delmas, C. *Chemistry of Materials* **2014**, *26*, 1538–1548.

(236) Nabarro, F. R. N. *Proceedings of the Physical Society* **1947**, *59*, 256–272.

(237) Peierls, R *Proceedings of the Physical Society* **1940**, *52*, 34–37.

(238) Kamimura, Y; Edagawa, K; Iskandarov, A. M.; Osawa, M; Umeno, Y; Takeuchi, S *Acta Materialia* **2018**, *148*, 355–362.

(239) Sun, J.; Remsing, R. C.; Zhang, Y.; Sun, Z.; Ruzsinszky, A.; Peng, H.; Yang, Z.; Paul, A.; Waghmare, U.; Wu, X.; Klein, M. L.; Perdew, J. P. *Nature Chemistry* **2016**, *8*, 831–836.

(240) Zhang, Y.; Kitchaev, D. A.; Yang, J.; Chen, T.; Dacek, S. T.; Sarmiento-Pérez, R. A.; Marques, M. A.; Peng, H.; Ceder, G.; Perdew, J. P.; Sun, J. *npj Computational Materials* **2018**, *4*, 9.

(241) Carrasco, J. *The Journal of Physical Chemistry C* **2014**, *118*, 19599–19607.

(242) Peng, H.; Yang, Z.-H.; Sun, J.; Perdew, J. P. *Physical Review X* **2015**, *041005*, 1–15.

(243) Jain, A.; Hautier, G.; Moore, C. J.; Ping Ong, S.; Fischer, C. C.; Mueller, T.; Persson, K. A.; Ceder, G. *Computational Materials Science* **2011**, *50*, 2295–2310.

(244) Toumar, A. J.; Ong, S. P.; Richards, W. D.; Dacek, S.; Ceder, G. *Physical Review Applied* **2015**, *4*, 1–9.

(245) Arcelus, O.; Carrasco, J. *ACS Applied Materials & Interfaces* **2019**, *11*, 12562–12569.

(246) Momma, K.; Izumi, F. *Journal of Applied Crystallography* **2011**, *44*, 1272–1276.

(247) Tournadre, F.; Croguennec, L.; Saadoune, I.; Carlier, D.; Shao-Horn, Y.; Willmann, P.; Delmas, C. *Journal of Solid State Chemistry* **2004**, *177*, 2790–2802.

(248) Tournadre, F.; Croguennec, L.; Willmann, P.; Delmas, C. *Journal of Solid State Chemistry* **2004**, *177*, 2803–2809.

(249) Marom, N.; Bernstein, J.; Garel, J.; Tkatchenko, A.; Joselevich, E.; Kronik, L.; Hod, O. *Physical Review Letters* **2010**, *105*, 1–4.

(250) Blumberg, A.; Keshet, U.; Zaltsman, I.; Hod, O. *Journal of Physical Chemistry Letters* **2012**, *3*, 1936–1940.

(251) Hod, O. *Physical Review B* **2012**, *86*, 1–8.

(252) Lu, Z.; Dahn, J. R. *Journal of The Electrochemical Society* **2001**, *148*, A710.

(253) Kim, D.; Kang, S.-H.; Slater, M.; Rood, S.; Vaughey, J. T.; Karan, N.; Balasubramanian, M.; Johnson, C. S. *Advanced Energy Materials* **2011**, *1*, 333–336.

(254) Berthelot, R.; Carlier, D.; Delmas, C. *Nature Materials* **2011**, *10*, 74–80.

(255) Yoshida, J.; Guerin, E.; Arnault, M.; Constantin, C.; Mortemard de Boisse, B.; Carlier, D.; Guignard, M.; Delmas, C. *Journal of the Electrochemical Society* **2014**, *161*, A1987–A1991.

(256) Jung, Y. H.; Christiansen, A. S.; Johnsen, R. E.; Norby, P.; Kim, D. K. *Advanced Functional Materials* **2015**, *25*, 3227–3237.

(257) Lee, D. H.; Xu, J.; Meng, Y. S. *Physical Chemistry Chemical Physics* **2013**, *15*, 3304–3312.

(258) Katcho, N. A.; Carrasco, J.; Saurel, D.; Gonzalo, E.; Han, M.; Aguesse, F.; Rojo, T. *Advanced Energy Materials* **2017**, *7*, 1–9.

(259) Roger, M.; Morris, D. J.; Tennant, D. A.; Gutmann, M. J.; Goff, J. P.; Hoffmann, J. U.; Feyerherm, R.; Dudzik, E.; Prabhakaran, D.; Boothroyd, A. T.; Shannon, N.; Lake, B.; Deen, P. P. *Nature* **2007**, *445*, 631–634.

(260) Delmas, C.; Maazaz, A.; Fouassier, C.; Réau, J.-M.; Hagenmuller, P. *Materials Research Bulletin* **1979**, *14*, 329–335.

(261) Wang, H.; Yang, B.; Liao, X.-Z.; Xu, J.; Yang, D.; He, Y.-S.; Ma, Z.-F. *Electrochimica Acta* **2013**, *113*, 200–204.

(262) Rice, J. R.; Beltz, G. E. *Journal of the Mechanics and Physics of Solids* **1994**, *42*, 333–360.

(263) Juan, Y. M.; Kaxiras, E. *Philosophical Magazine A: Physics of Condensed Matter, Structure, Defects and Mechanical Properties* **1996**, *74*, 1367–1384.

(264) Yao, H.-R.; Lv, W.-J.; Yin, Y.-X.; Ye, H.; Wu, X.-W.; Wang, Y.; Gong, Y.; Li, Q.; Yu, X.; Gu, L.; Huang, Z.; Guo, Y.-G. *ACS Applied Materials & Interfaces* **2019**, *11*, 22067 –22073.

(265) Zandbergen, H. W.; Foo, M.; Xu, Q.; Kumar, V.; Cava, R. J. *Physical Review B* **2004**, *70*, 1–8.

(266) Zheng, C.; Radhakrishnan, B.; Chu, I. H.; Wang, Z.; Ong, S. P. *Physical Review Applied* **2017**, *7*, 1–12.

(267) Wang, P.-F.; Yao, H.-R.; Liu, X.-Y.; Yin, Y.-X.; Zhang, J.-N.; Wen, Y.; Yu, X.; Gu, L.; Guo, Y.-G. *Science Advances* **2018**, *4*.

(268) Gutierrez, A.; Dose, W. M.; Borkiewicz, O.; Guo, F.; Avdeev, M.; Kim, S.; Fister, T. T.; Ren, Y.; Bareño, J.; Johnson, C. S. *The Journal of Physical Chemistry C* **2018**, *122*, 23251 –23260.

(269) Talaie, E.; Kim, S. Y.; Chen, N.; Nazar, L. F. *Chemistry of Materials* **2017**, *29*, 6684–6697.

(270) Silván, B.; Gonzalo, E.; Djuandhi, L.; Sharma, N.; Fauth, F.; Saurel, D. *Journal of Materials Chemistry A* **2018**, *6*, 15132–15146.

(271) Rousse, G; Tarascon, J. M. *Chemistry of Materials* **2014**, *26*, 394–406.

(272) Masquelier, C.; Croguennec, L. *Chemical Reviews* **2013**, *113*, 6552–6591.

(273) Reynaud, M.; Rodríguez-Carvajal, J.; Chotard, J.-N.; Tarascon, J.-M.; Rousse, G. *Physical Review B* **2014**, *89*, 104419.

(274) Lander, L.; Reynaud, M.; Rodríguez-Carvajal, J.; Tarascon, J.-M.; Rousse, G. *Inorganic Chemistry* **2016**, *55*, 11760–11769.

(275) Lander, L.; Rousse, G.; Abakumov, A. M.; Sougrati, M.; van Tendeloo, G.; Tarascon, J.-M. *Journal of Materials Chemistry A* **2015**, *3*, 19754–19764.

(276) Scaramucci, A; Bousquet, E; Fechner, M; Mostovoy, M; Spaldin, N. A. *Physical Review Letters* **2012**, *109*, 197203.

(277) Li, J.; Tian, W.; Chen, Y.; Zarestky, J. L.; Lynn, J. W.; Vaknin, D. *Physical Review B* **2009**, *79*, 144410.

(278) Toft-Petersen, R.; Andersen, N. H.; Li, H.; Li, J.; Tian, W.; Bud'ko, S. L.; Jensen, T. B. S.; Niedermayer, C.; Laver, M.; Zaharko, O.; Lynn, J. W.; Vaknin, D. *Physical Review B* **2012**, *85*, 224415.

(279) Van Aken, B. B.; Rivera, J.-P.; Schmid, H.; Fiebig, M. *Nature* **2007**, *449*, 702.

(280) Bousquet, E.; Spaldin, N. A.; Delaney, K. T. *Physical Review Letters* **2011**, *106*, 107202.

(281) Rousse, G.; Rodríguez-Carvajal, J.; Wurm, C.; Masquelier, C. *Physical Review B* **2013**, *88*, 214433.

(282) Ortega, N; Kumar, A.; Scott, J. F.; Katiyar, R. S. *Journal of Physics: Condensed Matter* **2015**, *27*, 504002.

(283) Wang, J.; Sun, X. *Energy and Environmental Science* **2015**, *8*, 1110–1138.

(284) Pan, H.; Hu, Y.-S.; Chen, L. *Energy and Environmental Science* **2013**, *6*, 2338–2360.

(285) Saracibar, A; Carrasco, J; Saurel, D; Galceran, M; Acebedo, B; Anne, H; Lepoitevin, M; Rojo, T; Casas Cabanas, M *Physical Chemistry Chemical Physics* **2016**, *18*, 13045–13051.

(286) Kim, H.; Kwon, J. E.; Lee, B.; Hong, J.; Lee, M.; Park, S. Y.; Kang, K. *Chemistry of Materials* **2015**, *27*, 7258–7264.

(287) Kim, H.; Kim, H.; Ding, Z.; Lee, M. H.; Lim, K.; Yoon, G.; Kang, K. *Advanced Energy Materials* **2016**, *6*, 1600943.

(288) Nitta, N.; Wu, F.; Lee, J. T.; Yushin, G. *Materials Today* **2015**, *18*, 252–264.

(289) Fang, Y.; Zhang, J.; Xiao, L.; Ai, X.; Cao, Y.; Yang, H. *Advanced science* **2017**, *4*, 1600392.

(290) Matsumoto, G. *Journal of the Physical Society of Japan* **1970**, *29*, 606–615.

(291) Elemans, J. B. A. A.; Van Laar, B; Van Der Veen, K. R.; Loopstra, B. O. *Journal of Solid State Chemistry* **1971**, *3*, 238–242.

(292) Avdeev, M.; Mohamed, Z.; Ling, C. D.; Lu, J.; Tamaru, M.; Yamada, A.; Barpanda, P. *Inorganic Chemistry* **2013**, *52*, 8685–8693.

(293) Li, J.; Garlea, V. O.; Zarestky, J. L.; Vaknin, D. *Physical Review B* **2006**, *73*, 24410.

(294) Kimura, T *Annual Review of Materials Research* **2007**, *37*, 387–413.

(295) Cheong, S.-W.; Mostovoy, M. *Nature Materials* **2007**, *6*, 13.

(296) Tokura, Y.; Seki, S. *Advanced Materials* **2010**, *22*, 1554–1565.

(297) Kim, H. H.; Yu, I. H.; Kim, H. S.; Koo, H.-J.; Whangbo, M.-H. *Inorganic Chemistry* **2015**, *54*, 4966–4971.

(298) Solovyev, I. V. *Journal of Physics: Condensed Matter* **2008**, *20*, 293201.

(299) Arcelus, O.; Nikolaev, S.; Carrasco, J.; Solovyev, I. *Physical Chemistry Chemical Physics* **2018**, *20*, 13497–13507.

(300) Zaanen, J; Sawatzky, G. A.; Allen, J. W. *Physical Review Letters* **1985**, *55*, 418–421.

(301) Aroyo, M. I.; Kirov, A.; Capillas, C.; Perez-Mato, J. M.; Wondratschek, H. *Acta Crystallographica Section A* **2006**, *62*, 115–128.

(302) Marzari, N.; Mostofi, A. A.; Yates, J. R.; Souza, I.; Vanderbilt, D. *Reviews of Modern Physics* **2012**, *84*, 1419–1475.

(303) Springer, M; Aryasetiawan, F *Physical Review B* **1998**, *57*, 4364–4368.

(304) Solovyev, I. V. *Physical Review B* **2013**, *87*, 144403.

(305) Georges, A.; Kotliar, G.; Krauth, W.; Rozenberg, M. J. *Reviews of Modern Physics* **1996**, *68*, 13–125.

(306) Drittler, B; Weinert, M; Zeller, R; Dederichs, P. H. *Physical Review B* **1989**, *39*, 930–939.

(307) Liechtenstein, A. I.; Katsnelson, M. I.; Antropov, V. P.; Gubanov, V. A. *Journal of Magnetism and Magnetic Materials* **1987**, *67*, 65–74.

(308) Solovyev, I. V. *Physical Review B* **2014**, *90*, 24417.

(309) Solovyev, I. V. *New Journal of Physics* **2009**, *11*, 93003.

(310) Solovyev, I. V.; Kashin, I. V.; Mazurenko, V. V. *Physical Review B* **2015**, *92*, 144407.

(311) Solovyev, I.; Hamada, N.; Terakura, K. *Physical Review Letters* **1996**, *76*, 4825–4828.

(312) Solovyev, I. *Journal of the Physical Society of Japan* **2009**, *78*, 54710.

(313) Yabuuchi, N.; Ikeuchi, I.; Kubota, K.; Komaba, S. *ACS Applied Materials & Interfaces* **2016**, *8*, 32292–32299.

(314) Li, X.; Ma, X.; Su, D.; Liu, L.; Chisnell, R.; Ong, S. P.; Chen, H.; Toumar, A.; Idrobo, J. C.; Lei, Y.; Bai, J.; Wang, F.; Lynn, J. W.; Lee, Y. S.; Ceder, G. *Nature Materials* **2014**, *13*, 586–592.

(315) Huang, Q; Foo, M. L.; Lynn, J. W.; Zandbergen, H. W.; Lawes, G; Wang, Y.; Toby, B. H.; Ramirez, A. P.; Ong, N. P.; Cava, R. J. *Journal of Physics: Condensed Matter* **2004**, *16*, 5803–5814.

(316) Hinuma, Y.; Meng, Y. S.; Ceder, G. *Physical Review B* **2008**, *77*, 1–16.

(317) Meng, Y. S.; Hinuma, Y.; Ceder, G. *Journal of Chemical Physics* **2008**, *128*, 1–8.

(318) Platova, T. A.; Mukhamedshin, I. R.; Alloul, H; Dooglav, A. V.; Collin, G. *Physical Review B* **2009**, *80*, 224106.

(319) Meng, Y. S.; Van Der Ven, A.; Chan, M. K. Y.; Ceder, G. *Physical Review B* **2005**, *72*, 4–7.

(320) Geck, J.; Zimmermann, M. V.; Berger, H.; Borisenko, S. V.; Eschrig, H.; Koepernik, K.; Knupfer, M.; Büchner, B. *Physical Review Letters* **2006**, *97*, 2–5.

(321) Kaufman, J. L.; Van der Ven, A. *Physical Review Materials* **2019**, *3*, 15402.

(322) Kubota, K.; Asari, T.; Yoshida, H.; Yaabuuchi, N.; Shiiba, H.; Nakayama, M.; Komaba, S. *Advanced Functional Materials* **2016**, *26*, 6047–6059.

(323) Su, J.; Pei, Y.; Yang, Z.; Wang, X. *Computational Materials Science* **2015**, *98*, 304–310.

(324) Verger, L.; Guignard, M.; Delmas, C. *Inorganic Chemistry* **2019**, *58*, 2543–2549.

(325) Vitoux, L.; Guignard, M.; Darriet, J.; Delmas, C. *Journal of Materials Chemistry A* **2018**, *6*, 14651–14662.

(326) Ozaki, T. *Physical Review B* **2007**, *75*, 1–9.